Fall 12-2019

Development of Finite Element Techniques to Simulate Concrete-Filled Fiber-Reinforced Polymer Tube Structures

Hakeem S. Majeed
hakeem.majeed@maine.edu

DEVELOPMENT OF FINITE ELEMENT TECHNIQUES TO SIMULATE CONCRETE-FILLED FIBER-REINFORCED POLYMER TUBE STRUCTURES

By

Hakeem Salih Majeed

B.A. Alnahrain University, 2003

M.A. Alnahrain University, 2007

A DISSERTATION

Submitted in Partial Fulfillment of the

Requirements for the Degree of

Doctor of Philosophy

(in Civil Engineering)

The Graduate School

The University of Maine

December 2019

Advisory Committee:

William G. Davids, Professor and Chair of Civil and Environmental Engineering, Chair

Eric N. Landis, Professor of Civil and Environmental Engineering

Roberto Lopez-Anido, Professor of Civil and Environmental Engineering

Edwin Nagy, Lecturer of Civil and Environmental Engineering

Andrew J. Goupee, Assistant Professor of Mechanical Engineering

DEVELOPMENT OF FINITE ELEMENT TECHNIQUES TO SIMULATE CONCRETE-FILLED FIBER-REINFORCED POLYMER TUBE STRUCTURES

By Hakeem S. Majeed

Dissertation Advisor: Dr. William G. Davids

An Abstract of the Dissertation Presented
in Partial Fulfillment of the Requirements for the
Degree of Doctor of Philosophy
(in Civil Engineering)
December 2019

This dissertation presents the development of finite-element (FE) techniques to simulate the behavior of concrete-filled fiber reinforced polymer (FRP) tubes (CFFTs) in support of more effective structural design and analysis methods for buried composite arch bridges (BCABs) that use CFFT arches as main structural members. The research includes three specific topics to make contributions in different aspects of the investigation of these complex structures.

The first topic is the nonlinear three-dimensional FE modeling of steel-free CFFT splices. For model validation, comparisons were made between the model predictions and control beam and spliced beams with and without internal collars tested by others. The modeling was complex due to the need to capture the nonlinear constitutive response of the confined concrete, simulate concrete-FRP interaction, and explicitly incorporate the splice components. Therefore, the numerical analysis utilized the Abaqus/CAE software package with a modified damage concrete plasticity model to idealize the concrete-fill.

The second topic of this research is the development of a computationally efficient structural FE analysis technique for the second-order inelastic behavior of these CFFT arches that includes initial arch curvature. A curved, planar, corotational, flexibility-based (FB), layered frame element is employed to handle geometric and material nonlinearities. An FRP-confined concrete stress-strain model that explicitly considers the effect of dilation of the concrete core and confinement provide by the FRP tube is

implemented. Verification of the FB formulation was carried out for elastic-plastic analysis of a beam and elastic post-buckling analysis of a circular arch. The measured flexural responses of different isolated CFFT arches available in the literature were used to verify the proposed model. The model was shown to accurately predict the load-carrying capacity and ductility of the tested CFFT arches. The model captured arch collapse mechanisms arising from FRP rupture and concrete crushing at the apex of the arches.

The third topic is an extension of the planar FB model to three-dimensions and incorporation of a soil-spring model to simulate soil-structure interaction using a recently developed horizontal earth pressure model. The model rigorously incorporates the interaction between axial load and bending effects in the arches and permits the examination of out-of-plane stability and arch deformations due to bridge skew. Parametric studies were conducted to assess the effect of abutment skew angle on the behavior of CFFT arch bridge components, an important practical design consideration.

DEDICATION

This dissertation is dedicated to the October 2019 demonstrations in Iraq:

To all the heroic patriots who took part in those demonstrations;

To the Tuk-Tuk drivers, who are members of marginalized groups and who became the symbol of resistance;

To the martyrs who fell in Altahrir Square in the center of Baghdad and other protesting arenas throughout the country.

الإهداء

إلى كل أبطال وبَطَلات إنتفاضة تشرين الوطنية العراقية.

إلى أيقونة الثورة، إلى سائقي التُكتُك وأهاليهم من المضطهدين والمهمشين الأزليين.

إلى أرواح الشهداء الذين سقطوا في ساحة التحرير وباقي ميادين التظاهر في محافظات أخرى.

ACKNOWLEDGEMENTS

Foremost, I would like to thank my advisor, Dr. Bill Davids, for offering me the honor to work under his supervision, for all his guidance, patience and dedication over the past few years, challenging me and encouraging me to be the best researcher, writer and critical thinker possible.

I would like to express my sincere appreciation to my country, Iraq, represented by the Higher Committee for Education Development in Iraq for their financial support throughout my Ph.D. program.

I would like to thank the members of my advisory committee, Dr. Eric Landis, Dr. Roberto Lopez-Anido, Dr. Edwin Nagy, and Dr. Andrew J. Goupee for their support, advice and suggestions throughout my Ph.D. work.

I would like to acknowledge all my friends in Iraq and at the University of Maine. This dissertation could not have been completed without their help, support and encouragement.

Finally, I would like to thank and acknowledge my family both in Iraq and here in Maine for their constant support and encouragement throughout my academic journey. My mother, my brothers, my wife and my children, Hasan, Hussain and Zahraa. Without their love, smiles and little voices, I would not have made it this far. I wish I had the opportunity to thank my father, who passed away ten years ago. I wish I could tell him: “Dad, your son became a Doctor.”

TABLE OF CONTENTS

LIST OF TABLES

LIST OF EQUATIONS

LIST OF FIGURES

CHAPTER 1

INTRODUCTION

1.1 Problem Description

In the past three decades, the use of concrete-filled fiber-reinforced polymer (FRP) tubes (CFFTs) has been explored as an alternative to steel-reinforced concrete structural members because of the high strength-to-weight ratio and excellent durability of FRP. Several infrastructure applications have been investigated, including bridge girders (Burgueño 1999; Karbhari et al. 2000), marine piles (Fam et al. 2003a), bridge piers (Fam et al. 2003b), deep beams (Ahmad et al. 2008), and bridge columns for multi-hazard resilience (Echevarria et al. 2016). Prior studies were conducted on a range of topics including flexural behavior (Fam and Rizkalla 2002; Mohamed and Masmoudi 2010), shear behavior (Ahmed 1999), fatigue behavior (Helmi et al. 2006; Zhu et al. 2009), the magnitude of strains at rupture (Abdelkarim and ElGawady 2015), and dynamic behavior (Qasrawi et al. 2016). In the CFFT system, the FRP tube provides confinement and protection of the concrete core and also serves as the concrete formwork and reinforcement for cast-in-place or precast elements (Dagher et al. 2012). The concrete core prevents local buckling failure of the FRP and increases the strength and stiffness of the CFFT member (Fam and Rizkalla 2002).

A specific application that has seen significant investigation is the use of CFFT arches in the buried composite arch bridge (BCAB) system developed at the University of Maine (Bannon 2009; Demkowicz 2011; Walton 2011, 2015). This type of bridge has become an advantageous and attractive alternative to short-span bridges with spans under 20 m because of its environmentally durable, cost-effective and easy-to-skew superstructure. In the BCAB, FRP arch tubes are often fabricated from a combination of an inner layer of E-glass fiber braid and two outer layers of carbon fiber braid. The hybrid FRP braided tube is inflated and impregnated with a thermoset resin using a modified vacuum-assisted resin transfer molding (VARTM) process. This rigidified combination of glass and carbon fiber reinforcement provide

confinement, tension, and shear reinforcement to the concrete core with no need for additional steel rebar while remaining cost-effective, easily fabricated, and lightweight.

These hollow lightweight FRP arches having a diameter range of 300-380 mm and a span range of 7-18 m are typically shipped to the field after rigidification. In the BCAB construction shown in Figure 1-1, multiple parallel composite arch tubes are placed alongside the roadway, cast into concrete footings, and then filled with self-consolidating concrete. FRP transverse corrugated decks are fixed on the top side of these CFFT arches to stabilize them before concrete filling and to support the granular backfill applied before paving. It is important to note that the CFFT arches function as the main structural members of the bridge, carrying combined bending and axial loads, and must support the wet weight of the concrete fill and the decking weight prior to curing of the concrete fill. To date, more than 30 BCABs have been designed and constructed in accordance with AASHTO LRFD design specifications (2012, 2017) by Advanced Infrastructure Technologies (AIT), a company based in Orono, Maine that has commercialized UMaine's CFFT technology. Figure 1-1 illustrates the elements of the BCAB system.

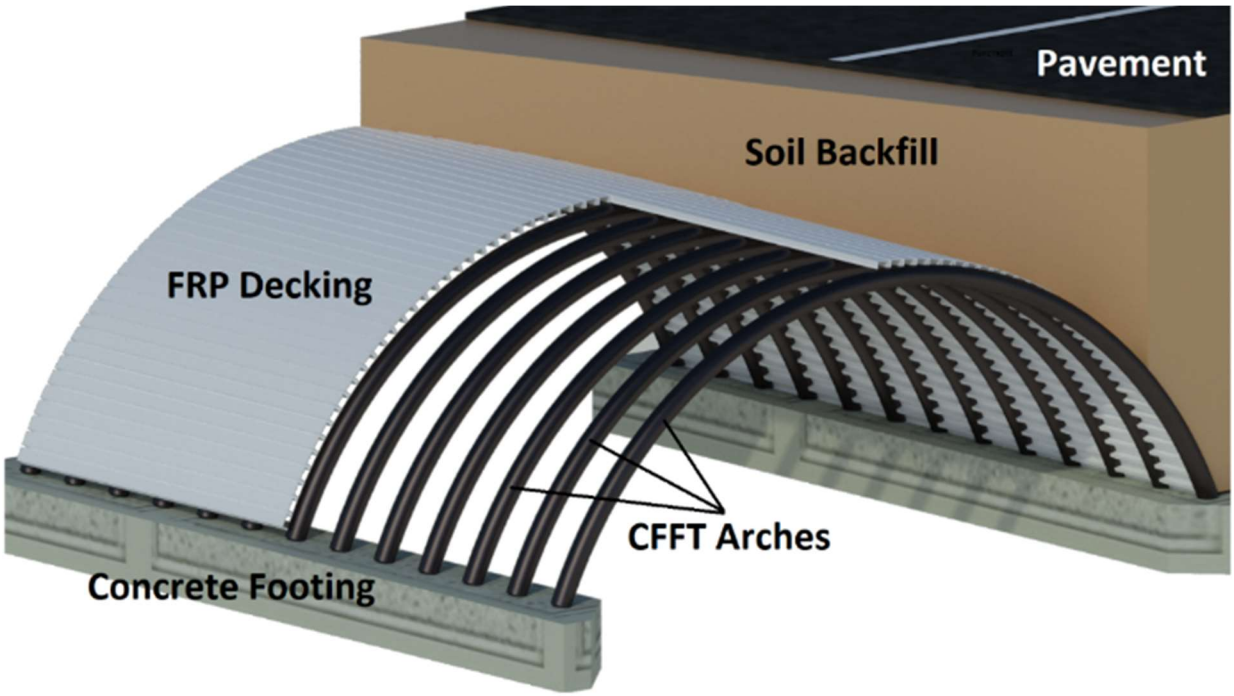

Figure 1-1. Main Components of the Buried Composite Arch Bridge

Researchers at the University of Maine have conducted experimental and numerical studies at different scales and on various configurations of CFFT beams and arches as well as material constituents to develop an understanding of CFFT arch response under loading. The first systematic study focused on utilization of CFFT arches technology and its constructability through the fabrication method of FRP tube and the development of the manufacturing process and design of CFFT arches. Bannon (2009) carried out structural testing on full scale isolated arch specimens, and four-point bending tests of CFFT beam specimens to investigate the bending response of these members and provide a useful tool for structural design using the CFFT members. Through laboratory tests, Demkowicz (2011) performed a comprehensive environmental durability study and evaluated the maintenance requirements of such FRP tube arches. Walton (2011) experimentally examined and numerically simulated the behavior and capacity of these arches as formwork during filling with wet concrete.

Dagher et al. (2012) developed a beam-based finite element (FE) model to simulate the structural response of CFFT arches, based on a small strain, and small displacement, 2-noded two-dimensional (2D) Euler beam. Parry (2013) developed a field splice for the arches to mitigate the challenges of shipping long spans of arches. The splice proved to be structurally feasible, exhibiting a moment capacity similar to that of a control arch with no splice, however, it was aesthetically unappealing and difficult to install. In a subsequent study, Burns (2016) developed a steel-free and easily constructed splice through an experimental investigation into the flexural response of spliced CFFT beams and arches. To expand understanding beyond isolated arch performance, Walton et al. (2016a) conducted laboratory testing of buried arch bridges to evaluate their response to soil backfilling and live-loading in a controlled laboratory environment that mimicked construction of an actual bridge. Walton et al. (2016b) also developed beam-based FE modeling techniques for simulating soil-structure interaction (SSI) and response of buried arches. The model relies on conventional 2D Euler beam-based elements with nonlinear horizontal spring elements to represent the soil backfill. While effective and innovative in its treatment of SSI and construction

sequence, the model of Walton et al. (2016b) requires a high mesh density and does not rigorously couple axial and bending effects.

1.2 Dissertation Objective

The main objective of this dissertation is to develop and validate FE element techniques for advanced simulation of CFFT arches to more effectively perform structural analyses, increase the design efficiency, and develop assessment tools for the BCAB. These numerical procedures attempt to more accurately quantify the behavior of the CFFT arches as a main component. The research includes three specific components: evaluation and simulation of the structural behavior of the field CFFT splice tested by Burns (2016), development of a general fiber-section beam FE employing the flexibility (force-based or FB) approach tailored specifically for modeling CFFTs, and extending the FB beam FE model to the three-dimensional (3D) simulation of BCABs including SSI with an examination of the effect of abutment skew on arch response. One challenge common to all three topics is the implementation of a general FRP-confined concrete constitutive model that captures the combined bending and axial load effects present in BCABs. Further, the 3D FB models will more rigorously incorporate the interaction between axial load and bending effects than was done in previous displacement-based modeling.

1.3 Organization of the Dissertation

This dissertation contains four additional chapters. Chapters 2, 3, and 4 are each a separate manuscript that has been written relatively independently for publication as a journal article and reformatted here according to the requirements of Graduate School, University of Maine. The paper based on Chapter 2 is in print, the paper based on Chapter 3 is currently in review, and the paper based on Chapter 4 will be submitted after the defense of this dissertation. Each journal paper presents one component of this dissertation.

Chapter 2 addresses the nonlinear 3D modeling of control and spliced CFFT structural beams. For model validation, spliced beams with/without collars tested by Burns (2016) were selected to enhance our understanding of the splice structural response and failure mechanisms. For comparison, a numerical investigation is also conducted on the control beam tested by Bannon (2009) and reported by Dagher et al. (2012). The modeling was complex due to the need to capture the nonlinear constitutive response of the confined concrete, model the concrete-FRP interaction, and explicitly incorporate the splice including the internal CFCC reinforcement, FRP collar, and the cohesive bond between the collar and shell. Therefore, the numerical analysis in this topic utilized the Abaqus/CAE software package to investigate the nonlinear flexural response of spliced CFFT beams because of its flexibility and extensive library of material models.

Chapter 3 addresses the development of a second-order, 2D FB fiber-section curved beam-column FE. Since CFFT arches undergo significant nonlinear effects arising from both large deformations (geometric nonlinearity) and material nonlinearity in all their constituents, they are good candidates for modeling using FB FE models. Large displacement geometric nonlinearity is accurately handled at the element level (P-Δ effect) utilizing the corotational formulation and at section level (p-δ effect) using a geometrically nonlinear FB frame element. The FB element's curvature also is handled at the section level as initial bowing. The fiber section technique is equipped to trace the inelastic uniaxial stress-strain relationships of each fiber on the selected cross-sections. MATLAB will be the main software environment used for development of the numerical code for this topic. To-date, the general model formulation and implementation have been validated using conventional structural studies (i.e., elastic-plastic beam, inelastic frame, column elastic buckling, and circular arch elastic post-buckling). Then, results of the CFFT tests including the control beam and arch test of Bannon (2009) and the short and tall arch testes of Walton et al. (2016a) were used to assess the ability of the model to simulate CFFT structures.

In Chapter 4, an efficient structural analysis technique is presented to analyze an entire BCAB using a newly-developed FE model with only two types of elements. Initially, the FE technology described in Chapter 3 is expanded to 3D. A soil-spring element used to idealize the soil with a series of one-dimensional

nonlinear axial-only springs. Following the formulation of both elements and their constituents' material models, solution strategy, and backfilling multistage simulation, the FE analysis method is verified using results measured during laboratory tests of straight buried steel arch bridges from the literature. A parametric study is undertaken on a generic, two-lane BCAB to investigate the effect of bridge skew on bridge capacity. Several BCAB models with skew angles ranging from 0° to 50° increasing of 10° were analyzed for different loading stages. The bridges were subjected to factored (ultimate) loads defined by AASHTO (2017) for the Strength I load cases including AASHTO HL-93 design live loading as surface patch loads distributed through the soil plus applicable dead loads. Critical positions of vehicles along the bridge were chosen to maximize bending in the arches and quantify the expected increase in demand on the arches due to abutment skew.

Chapter 5 closes this dissertation with a discussion of future research needs and potential extensions of the work presented in Chapters 2-4.

CHAPTER 2

CONTINUUM FE SIMULATION OF SPLICE RESPONSE

2.1 Introduction

In the BCAB construction, the lightweight FRP arches are often shipped to the field by trucks. Shipping long spans of these FRP arches can be expensive and challenging due to road width, vehicle height limits, and escort cost. To mitigate the challenges of shipping long spans of arches, splicing two or more smaller segments to form a longer span has been investigated. Relatively few prior studies have been conducted on flexural behavior of spliced CFFTs. Zhu et al. (2006) studied splices of CFFT beams in flexure, testing four types of splices, i.e., internal splices with grouted steel bars, grouted FRP bars, unbonded post-tensioned bars, and a fourth splice using an FRP socket similar to that used in the piping industry. The beams were initially stiffer than a control beam that had no splice, but none of the beams was stronger than the control beam, showing that continuity of the FRP provides greater strength than a discontinuous splice. The four beams were tested in flexure, but Zhu et al. (2006) noted that adding axial compression would theoretically improve a beam's stiffness and the strength of the joint. As part of a wide study on CFFT piles, Helmi et al. (2005) investigated the flexural behavior of three spliced CFFT beams by using a splice consisting of two thick steel circular plates and eight steel bars with threaded ends screwed into those plates. In general, these spliced specimens were 7% stronger in flexure than the un-spliced tubes that were also tested for comparison.

Parry (2013) developed a field splice for the arches that was fabricated from two main parts based on loading type. An external E-glass fiber-reinforced collar was designed to withstand short-term construction and concrete filling loads and held the two arch segments together using mechanical fasteners. The splice also contained conventional steel reinforcing to resist long-term loading that includes forces from the granular backfill, pavement, other superimposed dead loads, and vehicular live loads. The splice proved to be a feasible solution, exhibiting a moment capacity similar to that of a control arch with no splice. The collar developed by Parry (2013) successfully carried both short and long-term loads but had a

few shortcomings. The external splice was aesthetically unappealing, and the mechanical fasteners proved to be difficult to install on the circular surface of the arch. The steel reinforcing also had the potential to corrode and shorten the lifespan of the CFFT, negating one of its advantages.

To develop a steel-free and easily constructed splice, Burns (2016) conducted experimental work to investigate the nonlinear flexural response of spliced CFFT beams and arches (Figure 2-1). While similar in concept to the splice of Parry (2013), the splice presented by Burns (2016) differed in several important ways. It consisted of an internal FRP collar bonded to the FRP shell with a high-strength urethane adhesive to withstand the short-term construction loads and carbon fiber composite cable (CFCC) longitudinal bars and a spiral to withstand permanent and live loads. The CFCC material was produced by Tokyo Rope, Inc. (2017) and can be used for concrete tensile and shear reinforcement. Experimental characterization included testing spliced CFFT beams and arches in flexure as well as tests to determine the adhesive bond strength and CFCC development lengths.

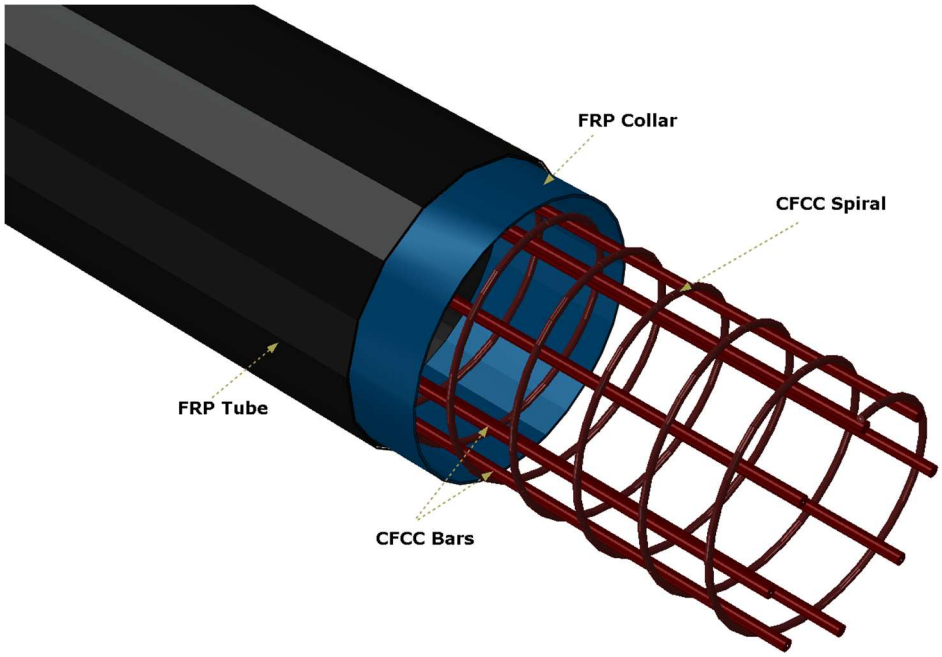

Figure 2-1 Splice Elements Installed into an FRP Tube Segment

This chapter documents the first research contribution of this dissertation. The main objective is to develop a nonlinear 3D modeling of control and spliced CFFT structural beams. For model validation, spliced beams with/without collars tested by Burns (2016) were selected to enhance our understanding of the splice structural response and failure mechanisms. For comparison, a numerical investigation is also conducted on the control beam tested by Bannon (2009) and reported by Dagher et al. (2012). The modeling was complex due to the need to capture the nonlinear constitutive response of the confined concrete, model the concrete-FRP interaction, and explicitly incorporate the splice including the internal CFCC reinforcement, FRP collar, and the cohesive bond between the collar and shell. Therefore, the numerical analysis in this topic utilized the Abaqus/CAE software package (Simulia Inc. 2017) to investigate the nonlinear flexural response of spliced CFFT beams because of its flexibility and extensive library of material models.

2.2 Review of Prior Experimental Work of Burns (2016)

2.2.1 CFFT Specimen Construction

The tubes considered here were fabricated with a combination of an inner layer of E-glass fiber braid and two outer layers of Toray T-700 carbon fiber braid. The three fiber layers of the spliced specimens were impregnated with Derakane 610C vinyl ester thermoset resin (Alshand Inc 2016) while the control specimens, tested by Bannon (2009), were impregnated with Derakane 8084 vinyl ester thermoset resin using the modified VARTM process. These two resins possess similar chemical and mechanical properties, and their use was based on availability at the time of specimen fabrication. Table 2-1 shows the elastic properties of the fiber and matrix materials. The percentage of fiber volume in the entire volume of hybrid braided laminate, fiber volume fraction (V_f), was taken as 50%, according to Bannon (2009) and Walton (2011). More details regarding this hybrid FRP tube and the fiber angle, lamina thickness, and sequence are reported in Section 2.3.2.3.

Table 2-1. Fibers and Matrix Parameters of FRP Tube Components

Material	Elastic Modulus, E (MPa)	Poisson's Ratio v	Shear Modulus G (MPa)
E-Glass Fiber	72,400	0.230	29,600
T-700 Carbon Fiber	234,000	0.200	27,500
Derakane 8084	2,900	0.35	1,100
Derakane 610C	3,530	0.35	1,300

2.2.2 Splice Description and Design

Material cost and availability, fabrication complexity, and collar practicality were considered when developing the splice concept. All materials (FRP collar, adhesive, and self-tapping screws) can be easily procured and installed in the field. Figure 2-1 shows the elements of the splice. An FRP arch can be fabricated to be slightly longer than the design length so that the end can be cut off and used as a collar, which maintains the same radius of curvature as the arch. This approach ensured an accurate fit within the arch for any reasonable collar length and evenly distributed the shear stresses on the collar-to-arch adhesive connection. A longitudinal gap in the collar was created by cutting a longitudinal slit down the collar (Figure 2-2), which, when closed, gave the splice a slightly smaller diameter and allowed insertion into the end of the CFFT tube being spliced. Self-tapping screws were used to hold the collar tightly against the inside of the CFFT tube to evenly disperse the adhesive and provide clamping pressure while the adhesive cured.

This splice design required analysis for two loading conditions, i.e., short-term construction loads and a design combination of permanent and service live loads. The internal FRP collar bonded to the FRP shell with a high-strength urethane adhesive was designed to withstand the short-term construction loads up to and including decking and concrete filling. The CFCC-reinforced concrete core was designed to

withstand the permanent dead load due to soil backfilling, paving, etc. as well as live loads. The splice design assumed a typical BCAB geometry, having circular segment arches each with a 305-mm cross-sectional diameter, 9.75-m horizontal span, and 4.87-m radius of curvature. The ultimate design loads were a bending moment of 46.3 kN-m, a shear load of 39 kN, and an axial compression load of 552 kN. The arches were supplied by Advanced Infrastructure Technology, a company located in Orono, Maine, USA that has commercialized the BCAB technology. Short-term concrete filling and construction service loads carried by the FRP shell before the concrete cured were calculated for this case by Parry (2013) as a moment of 4.9 kN-m, a shear load of 2.2 kN, and an axial load of 7.1 kN.

Figure 2-2 32-mm Longitudinal Slit in Collar

2.2.2.1 Adhesive Shear Strength Determination

Ashland Pliogrip 7770, a high-strength urethane adhesive for composite materials, was used to bond the collar to the CFFT shell. The technical data sheet for Pliogrip 7770 indicated a tensile strength of 29 MPa, Young's modulus of 1184 MPa and a Poisson's ratio of 0.429 but no published shear strength

(Ashland Inc 2016). The missing shear strength was required for the design of the internal collar. Therefore, lap shear tests were conducted on coupons made of the same composite lay-up used for spliced CFFT beam specimens, following a modified procedure of ASTM D5868 (2008).

Two sections of FRP hollow tube were bonded together using the same lay-up as the splice. Prior to bonding, the surfaces were thoroughly sanded as recommended by the manufacturer. After sanding, the coupons were cleaned with alcohol, the adhesive was applied, and the surfaces were fixed in contact. After 24 hours, upon a full adhesive cure, 25.4-mm wide coupons were cut that were 75 mm longer than the bond lines. The ends of the coupons were also coated with adhesive to ensure that the coupons had the same end thickness and that the shear plane would remain consistent within the bonded region. Finally, the coupons were loaded in tension using a servo-hydraulic testing frame with a 100-kN load cell at a displacement rate of 1.27 mm/min. This displacement rate was slower than the ASTM D5868 standard rate (12.7 mm/min) and was selected to mimic the concrete filling process. Load and position were recorded to assess the strength of the adhesive when bonded to the FRP.

The average shear strength of the 76.2-mm-long bond line was 4.87 MPa with a standard deviation of 0.80 MPa (CoV of 16.4%). The average shear strength of the 25.4-mm-long bond line was 8.02 MPa with a standard deviation of 1.25 MPa (CoV of 15.5%). The failure mode of the 76.2-mm bond line tests was interlaminar shear failure between the two layers of carbon, and the failure mode of the 25.4-mm bond lines was interlaminar shear failure between the carbon and E-glass fiber layers. A possible explanation for the different failure modes and failure stresses are inconsistent specimen fabrication and/or different shear and peeling stress distributions for the two different bond lengths. However, because the FRP failed before the adhesive, the collar can be safely designed using this adhesive. In order to be conservative, the 4.87-MPa average shear strength of the 76.2-mm bond line was taken as the ultimate capacity of the adhesive. As will be discussed later, this strength is more than sufficient for splice design.

2.2.2.2 FRP Collar Fabrication and Installation

A collar length of 305 mm (152.5 mm on each side of the splice) was chosen since it was a workable length for collar installation and provided excess capacity based on the lap shear test data. Once the collar was cut from the FRP arch tube, a 32-mm-wide slit was longitudinally cut as shown in Figure 2-2. This slit width was determined to give a bond-line thickness within the range of acceptable values recommended by the adhesive manufacturer (Ashland Inc 2016). The adhesive was then applied to half of the collar, which was inserted into the end of the first arch segment. Self-tapping screws were installed every 102 mm, starting from the side opposite the slit, and installed in an alternating pattern to ensure that the adhesive dispersed evenly. The second half of the arch was installed in the same manner. Before installing the collar into the second half of the arch, the CFCC reinforcement cage was fabricated and placed inside. Figure 2-3 shows one-half of the collar fully installed into one segment of the FRP tube.

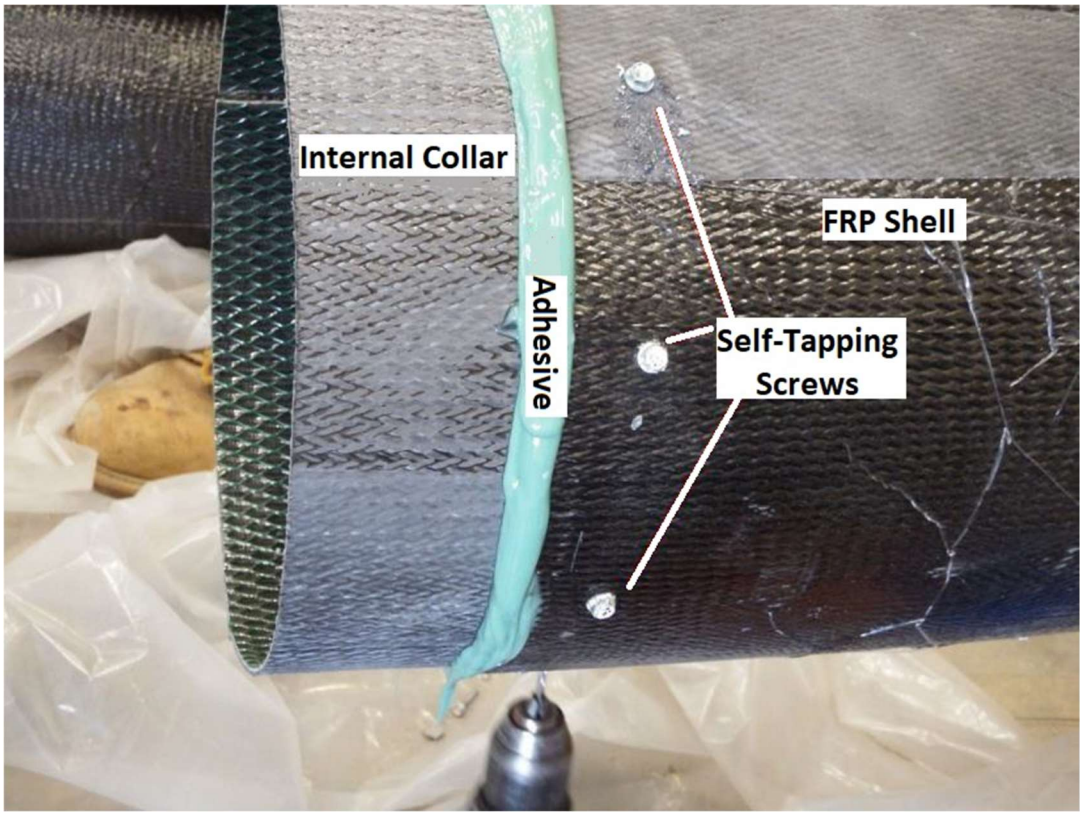

Figure 2-3. One-Half of FRP Collar Fully Installed

2.2.2.3 Internal CFCC Reinforcement

Longitudinal CFCC bars and a CFCC spiral were designed as a cage to reinforce the concrete core for the long-term loads carried by the spliced arch. The longitudinal bars were used to resist bending and axial forces, and the spiral was used to resist shear forces. Axial load-bending interaction diagrams were created to determine the required CFCC longitudinal reinforcing, and conventional shear design concepts were used to determine the required spiral reinforcing. Both ACI 440 (2015) and AASHTO (2012) standards were followed for these calculations. Ultimately, eight longitudinal bars were used along with a spiral having a 76-mm pitch. This spiral pitch is much less than required for shear strength but meets the maximum pitch requirement in AASHTO (2012). Figure 2-1 shows the CFCC reinforcing bars inside the CFCC spiral.

2.2.3 Internal CFCC Reinforcement Pullout Testing

CFCC is a promising reinforcement option to withstand the bending moment, axial force, and shear force at the splice of CFFTs. However, information on development length and pullout strength was not available and was essential to ensure that the required splice capacity could be developed. Therefore, pullout tests were conducted to determine the relationship between the embedment length and the capacity of CFCC by using a modified version of ASTM C900 (2015). The design of these pullout tests was guided by the ACI 440.1R-15 guide (2015).

CFCC bars with diameters of 12.5 mm, 15.2 mm, and 17.2 mm were chosen for testing because they were expected to be the most suitable sizes for the most commonly used FRP tubes. As shown in Figure 2-4, the CFCC specimens were vertically placed into a formwork with a width of 610 mm, a length of 914 mm, and a height of the CFCC length plus an extra 153 mm to provide concrete cover on the bottom of the block. A CFCC spiral was placed off-center within the formwork with a 76.2-mm pitch to mimic the splice, and the straight CFCC bar was located inside and in contact with the spiral. Steel rebar cages were

placed on each of the six sides of the formwork to ensure that the concrete blocks would not fail in tension, and a concrete mix identical to that used to fill CFFTs was cast into the formwork.

The tensile elastic modulus of CFCC straight bars and spiral was 155000 MPa, and the 28-day compressive strength of the concrete was 56.4 MPa based on 150-mm cylinder tests. The CFCC reinforcing had a 1x7 configuration, consisting of a single carbon strand that has six other strands wrapped helically around it. Actual CFCC reinforcing cross-sectional areas were 76 mm^2, 115.6 mm^2, and 151.1 mm^2 for 12.5-mm, 15.2-mm, and 17.2-mm CFCC diameters, respectively. Table 2-2 shows a summary of CFCC pullout test results including the measured maximum pullout loads and the averages for different embedded lengths for each tested diameter of CFCC. According to a compilation of the averages of the maximum pullout loads versus the embedment lengths, an interpolation to find the pullout strength for a given development length was used to design the internal reinforcement of the splice.

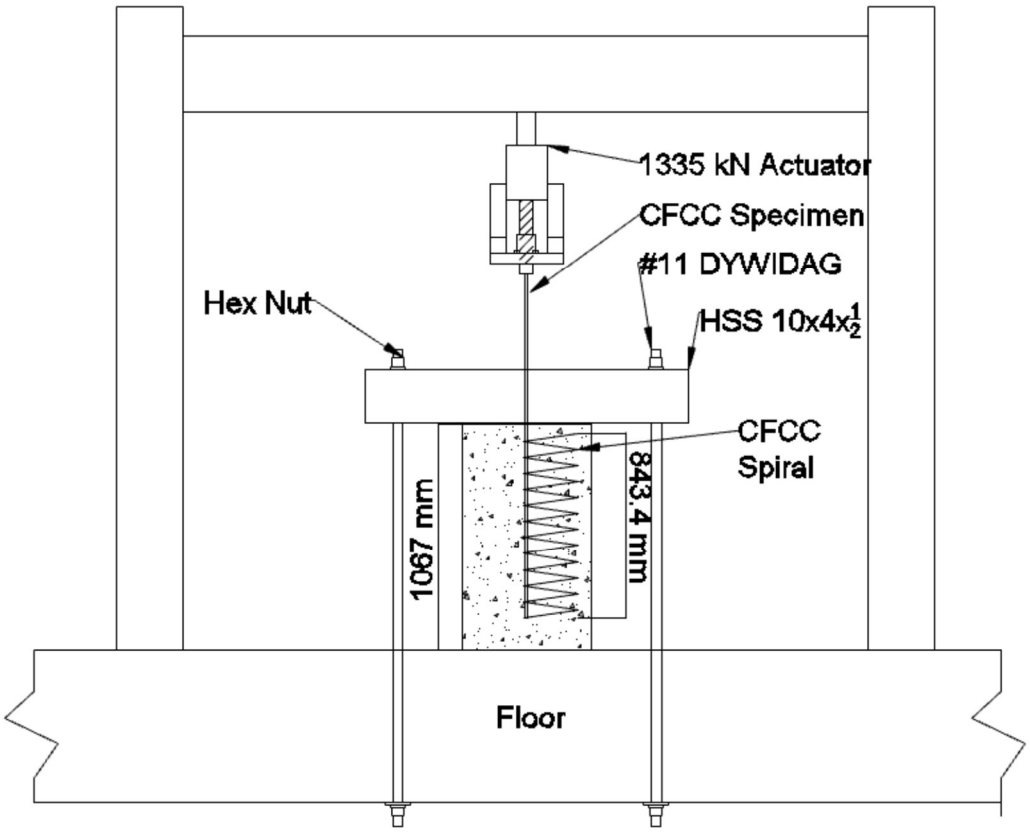

Figure 2-4. CFCC Pullout Test Setup

Table 2-2. Summary of CFCC Pullout Tests

Diameter (mm)	Embedment Length (mm)	Maximum pullout load (kN)	Average (kN)
12.5	254	71.1	75.0
12.5		76.9	
12.5		77.0	
12.5	445	119.4	129.0
12.5		140.6	
12.5		127.1	
12.5	660	165.0	167.8
12.5		157.4	
12.5		181.1	
15.2	305	105.0	112.4
15.2		100.6	
15.2		131.7	
15.2	533	157.4	166.4
15.2		168.9	
15.2		172.9	
15.2	813	204.5	213.9
15.2		204.7	
15.2		232.6	
17.2	343	146.8	146.8
17.2	610	227.7	227.7
17.2	914	348.3	348.3

2.2.4 Flexural Tests of Spliced Beams

2.2.4.1 Specimen, Instrumentation and Test Setup Description

In order to assess the spliced beam capacity, bending tests were conducted on straight CFFT spliced beams including five specimens with internal collars and two specimens without collars. These beams, with the internal reinforcement detailed in Section 2.2.2.3, were filled with concrete. Two CFCC reinforcing configurations were used, including eight longitudinal 12.5-mm-diameter CFCC bars surrounded by a 7.5-mm CFCC spiral and six 15.2-mm-diameter CFCC bars surrounded by a 7.5-mm CFCC spiral. Both the bars and the spiral were embedded 457 mm on either side of the splice for a total reinforcement length of 914 mm. These embedment lengths and bar configurations corresponded to a 61.2 kN-m calculated flexural strength for the concrete specimen if the FRP shell is neglected with eight 12.5-mm CFCC bars, and 66.0 kN-m with six 15.2-mm CFCC bars. Results from tests by Bannon (2009) on three control beams and initially reported by Dagher et al. (2012) are also given here for comparison with spliced beam results. The specimens are given identification codes C, S, and Sc to indicate control, spliced with no collar, and splice with collar specimens, respectively. Table 2-3 presents a summary of the beam specimen properties including the concrete compressive strength $f_c^{'}$ and the nominal moment capacities M_n determined as described previously.

Four-point bend tests were performed to examine the CFFT beams in a region of a constant moment and zero shear force. Figure 2-5 shows the beam test setup. The CFFT beam specimens had an outer diameter of 305 mm. The total thickness of the shell was approximately 2.5 mm and further details of the thickness of each braided layer, and fiber bias angles are described later in this chapter. During filling with the concrete, the beams were placed on their ends. Saddles were used to support the ends of the beams and to apply loads to achieve the simply supported boundary conditions (Figure 2-6).

Table 2-3. CFFT Beam Specimens

Specimen ID	Failure Moment kN-m	M_n kN-m	f_c' MPa	Span Length (Total Length) mm	Splice		
C1	161.1	156	41.0	3660 (3960)	No		
C2	154.2						
C3	140.4						
S1	71.1	61.2	45.5	2845 (3200)	Yes	Without Collar	8 CFCCs of 12.5 mm
S2	49.5						
Sc1	63.1	66.8	33.8	2845 (3200)	Yes	With Collar	6 CFFCs of 15.2 mm
Sc2	53.0						
Sc3	42.4						
Sc4	60.4						
Sc5	61.9						

Cross-sectional strains were measured at the top and the bottom face of specific sections to estimate the maximum tension and compression strains as well as to calculate the curvature. Three sets of strain gages (SG), SG1-3, SG4-6, and SG7-9, were used in this test. Each gage had a 50.8-mm gage length and 120-ohm resistance. The SG1-3 and SG4-6 sets were installed within the constant moment region for each specimen, and the SG7-9 set was installed outside that region for each spliced specimen. A third SG was placed at mid-height to verify the assumption of a linear strain distribution through the depth. Vertical displacement was evaluated at the supports, load points, and mid-span with linear variable differential transducers (LVDTs). The beams were loaded with a 490-kN hydraulic actuator (Figure 2-5 and Figure 2-6).

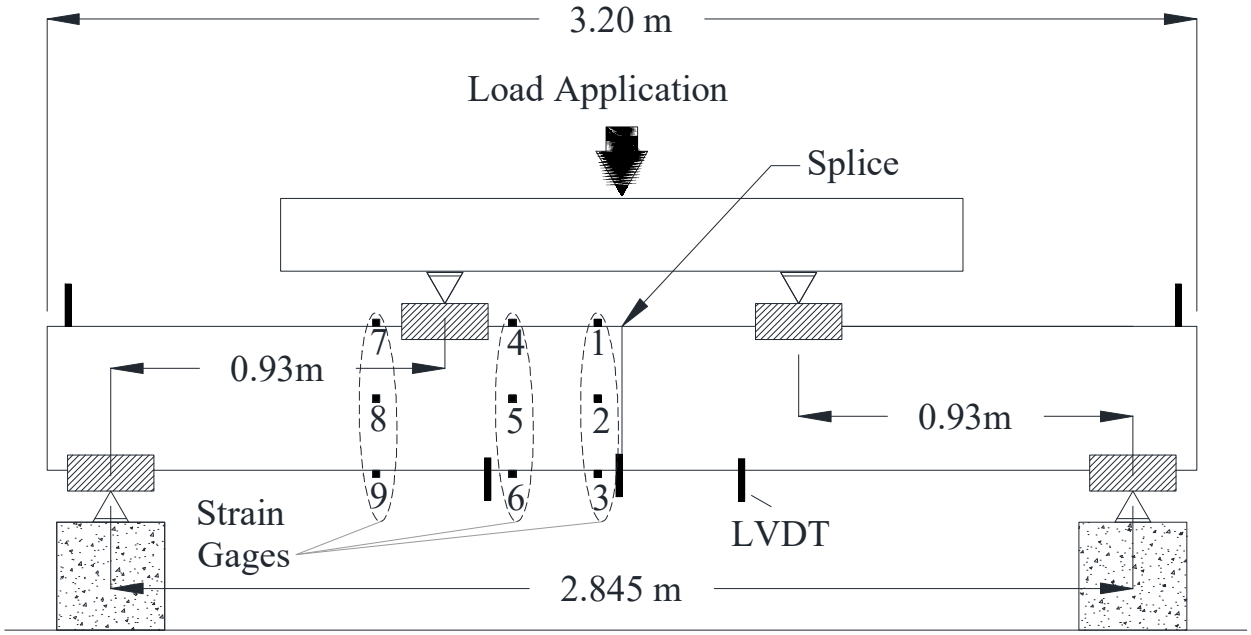

Figure 2-5. Setup of Four-Point Bending Test of Spliced Beam

Figure 2-6. Four-Point Bend Test of Control Beam, (Dagher et al. 2012)

2.2.4.2 Test Results

All the spliced beams with no collar failed via separation of the FRP and concrete (Figure 2-7a), which led to a loss of composite action. This was followed by rupture of the FRP shell on the tension face and buckling of the FRP shell on the compression face. The spliced specimens with collars exhibited separation in the FRP collar to shell interface (Figure 2-7b) as well as separation of the FRP and concrete and damage in the FRP shell. Only one side of the splice debonded, and the same side exhibited both compressive buckling at the load head and tensile rupture below the load head. Signs of FRP rupture and buckling occurred in the FRP shell near the ends of CFCC reinforcing cage that may be indicative of high-stress concentrations where the reinforcing ends. S1, S2, and Sc5 specimens debonded on the same side as the strain gauges, while the other beams debonded on the side opposite the gauges. The side that debonded appears arbitrary and could be influenced by a small difference in applied load, a minor defect in the FRP shell on one side, or an uneven distribution of adhesive for beams with internal collars. This failure mode differs from the tensile rupture of the continuous FRP shell observed in the control beam tests of Dagher et al. (2012) as shown in Figure 2-7c.

The maximum experimentally observed moments for each specimen are given in Table 2-3 for comparison with nominal expected capacities. The spliced beams with no collar had an average experimental capacity of 60.2 kN-m, and spliced beams with collar had an average experimental capacity of 56.2 kN-m. The control specimens tested by Dagher et al. (2012) under nominally identical conditions exhibited an average failure moment of 152 kN-m, implying that the spliced beams with no collar achieved 40% of the control beam capacity, and the spliced beams with collar achieved 37% of the control beam capacity. Clearly, the discontinuity of the reinforcing shell played a significant role in beam failure. However, the beams with and without collar exhibited 84% and 99% of their computed nominal capacity, respectively. The observed failure mode of the spliced beams involving debonding of the shell adjacent to the splice likely affected observed capacity

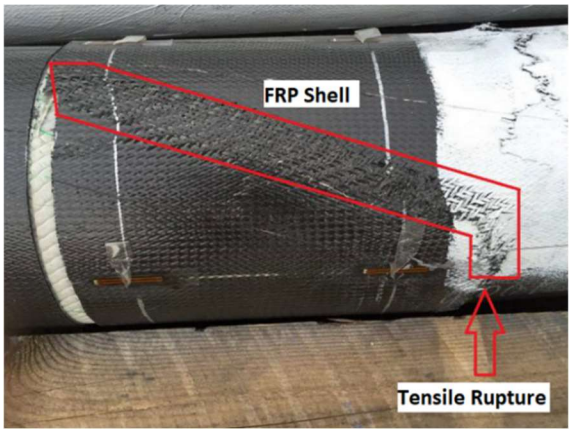

(a) Spliced Beam with no Collar: FRP Shell Damage Propagating from Point of Tensile Rupture

(b) Spliced Beam with Collar: FRP Shell Debonding

(c) Control Beam: Typical Specimen Failure Mode

Figure 2-7. Failure Modes of Beam Specimens

Load versus mid-span deflection plots give a visual representation of the stiffness of the CFFT beam as shown in Figure 2-8 and Figure 2-9. Figure 2-8 shows the mid-span load-deflection response of the control beams (for further details see Dagher et al. (2012)). For the spliced beams with a collar, the load-deflection results exhibited four distinct points as shown in Figure 2-9a. Point 1 shows initial concrete cracking occurring at an average load of approximately 34.4 kN. This initial cracking occurred before the cracking moment due to high-stress concentrations at the end of the CFCC reinforcing cage occurred and was caused by the termination of reinforcing in the tension zone. Point 2 shows concrete cracking occurring in the load span at an average load of approximately 57.3 kN. Point 3 shows the initiation of FRP debonding, where the maximum strain in SG3 occurred at an average load of approximately 97.8 kN. Point 4 shows the maximum average load that the beam withstood, which was approximately 135.4 kN. Spliced beams with no collar exhibited similar load-deformation response as the spliced beams with a collar but did not have a distinct Point 3 corresponding with FRP debonding (Figure 2-9b). The absence of a Point 3 is likely because the splice has no collar, and FRP debonded from the concrete more gradually than from the FRP internal collar.

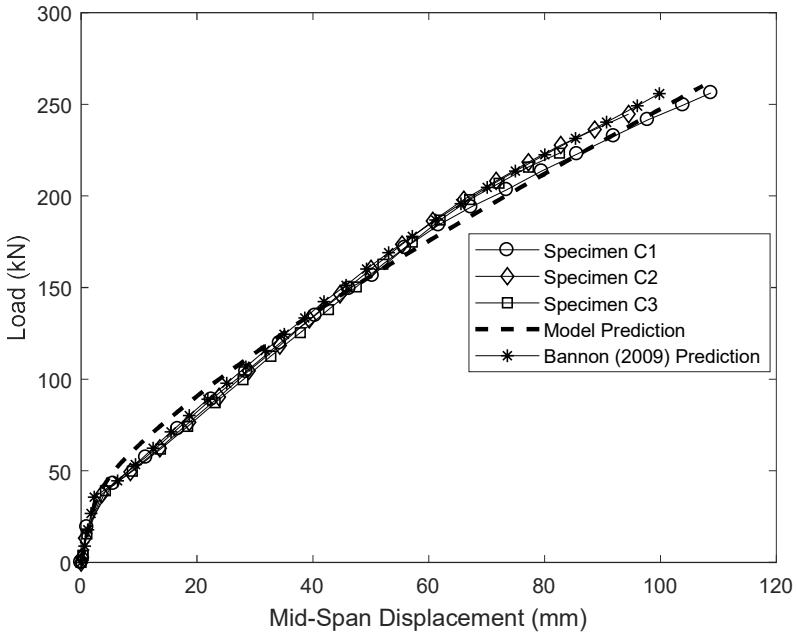

Figure 2-8. Control Beam Mid-Span Load-Deflection Response

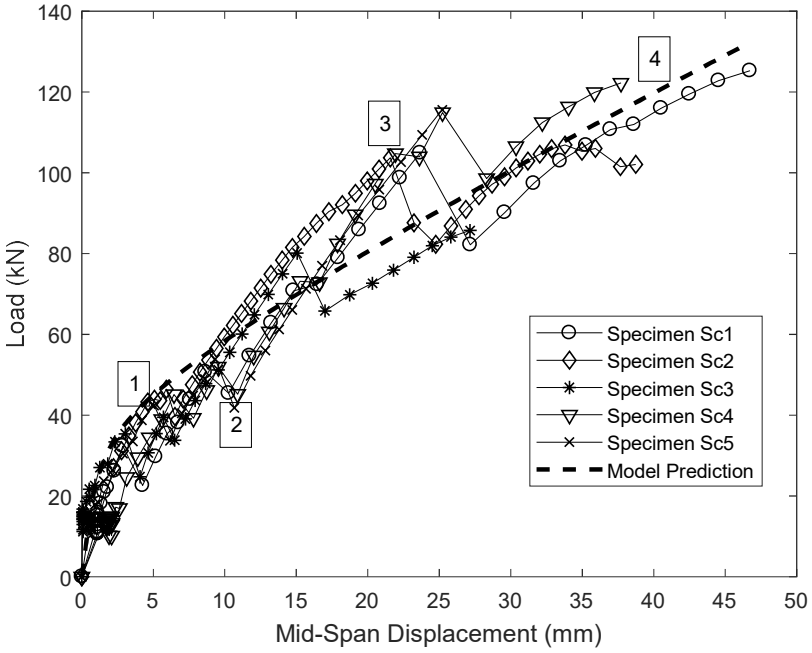

(a) Spliced Beams with Collar

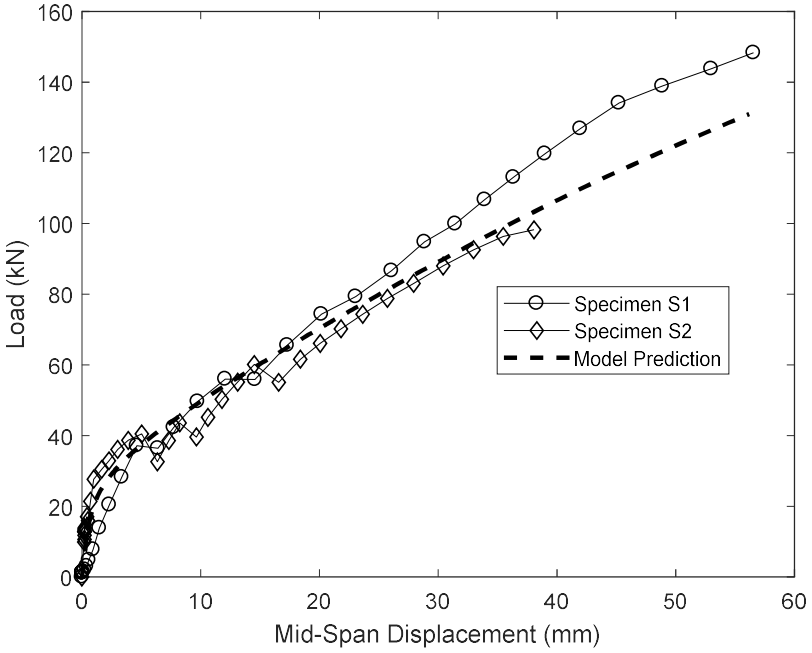

(b) Spliced Beams without Collar

Figure 2-9. Spliced Beam Mid-Span Load-Deflection Response

Figure 2-10 shows the measured strains for typical spliced specimens plotted against the moment in the pure bending region obtained from the applied load, (SG1-9 as illustrated in Figure 2-5). In the spliced beams with no collar, SG3 showed a slight increase in tensile stresses until just beyond the cracking moment and then tended back towards zero strain (Figure 2-10a). The point where it began tending towards zero strain was likely where the debonding of FRP from the concrete core initiated. Spliced beams with a collar showed similar behavior to that of spliced beams with no collar (Figure 2-10b). The main difference was indicated by the gauge on the tension face closest to the splice (SG1-3), which accumulated higher strains before either tending towards zero or breaking. The maximum strain nearest the splice on the tension face was analyzed to characterize when the FRP shell lost composite action by debonding. The average debonding moment for beams without collar was 20.34 kN-m and for beams with collar was 48.26 kN-m. This higher moment capacity before debonding indicated that the internal collar helped resist long-term loading and that stresses transferred from one side of the FRP shell to the other via the internal collar helped reduce stress concentrations in the FRP shell at the splice.

The depth to the neutral axis (NA) was calculated using strain compatibility and the strain gauge readings in the pure bending region away from the splice (SG4-6) to avoid the effect of stress concentrations near the collar before debonding. A best-fit line through the three gages SG4, SG5 and SG6 was used to estimate the NA location, and measured strain values indicated a nearly linear strain distribution throughout the cross-section depth. Figure 2-11 shows the NA depth as a function of the applied moment for the spliced beam with collar. Plotting the NA location gave a visual representation of the damage state of the concrete as it was loaded. Before concrete cracking, the section was linearly elastic, and the NA was expected to be at the mid-height of the section. Upon concrete cracking, the neutral axis shifted towards the compression face to maintain equilibrium, and the CFCC reinforcement was further engaged.

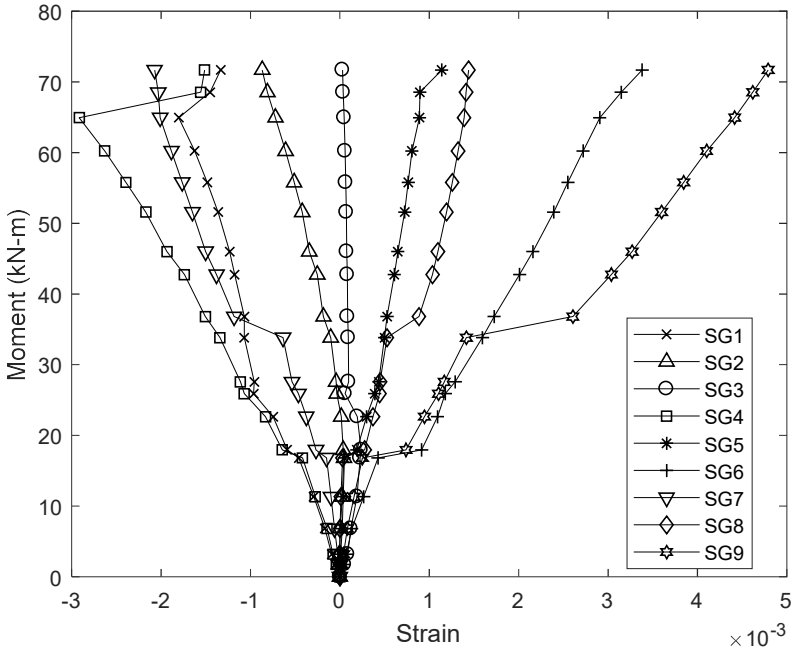

(a) Moment vs. Strain for S1 Specimen

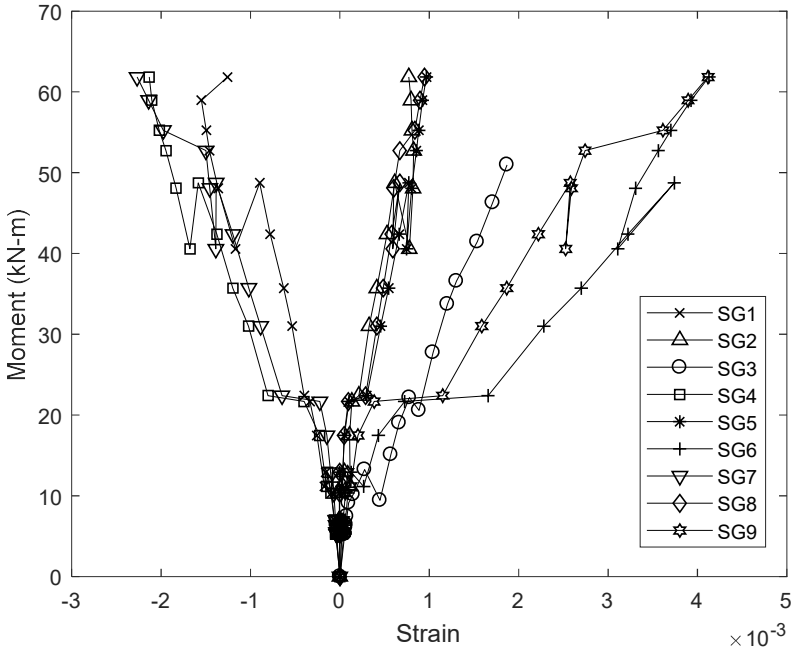

(b) Moment vs. Strain for Sc1 Specimen

Figure 2-10. Measured Beam Strains (for strain gages lay-out see Figure 2-5)

The curvature was calculated as the angle of the strain distribution using the simple geometry of the SG4-6 best-fit line through the depth as shown in Figure 2-12. Figure 2-12 shows the moment-curvature plots of the tested spliced beams with collars. Curvature for beams with no collar showed an initial linear region followed by a rapid increase in curvature at moments between 15 and 18 kN-m, which was where concrete cracking occurred. As shown in Figure 2-12, the spliced specimens with a collar had a distinct region where curvature increased substantially with a decrease in moment. The sudden increase in curvature was due to concrete cracking and occurred at moments between 25 and 30 kN-m, which were close to the expected cracking moment. A smaller increase in curvature was seen around 15–20 kN-m, which aligned with the first shift in the NA (see Figure 2-11). That increase corresponded with an initial cracking that likely occurred in concrete located in the pure bending zone but outside of the reinforced area.

Cracking moment values were estimated via moment-curvature diagrams (Figure 2-12) with the cracking moment taken as the point at which a substantial increase in curvature was paired with a decrease in the moment. The larger moment at which point this curvature began was considered the cracking moment. However, there was likely also initial cracking outside of the reinforced zone that may have propagated in toward the splice. This initial cracking was believed to have occurred due to high-stress concentrations at the end of the CFCC reinforcing cage caused by the termination of reinforcing in the tension zone. The average experimental cracking moment in the S beams was 28.3 kN-m and 25.5 kN-m in the Sc beams. These results were consistent with the lower average concrete compressive strength in the Sc beams compared to the S beams.

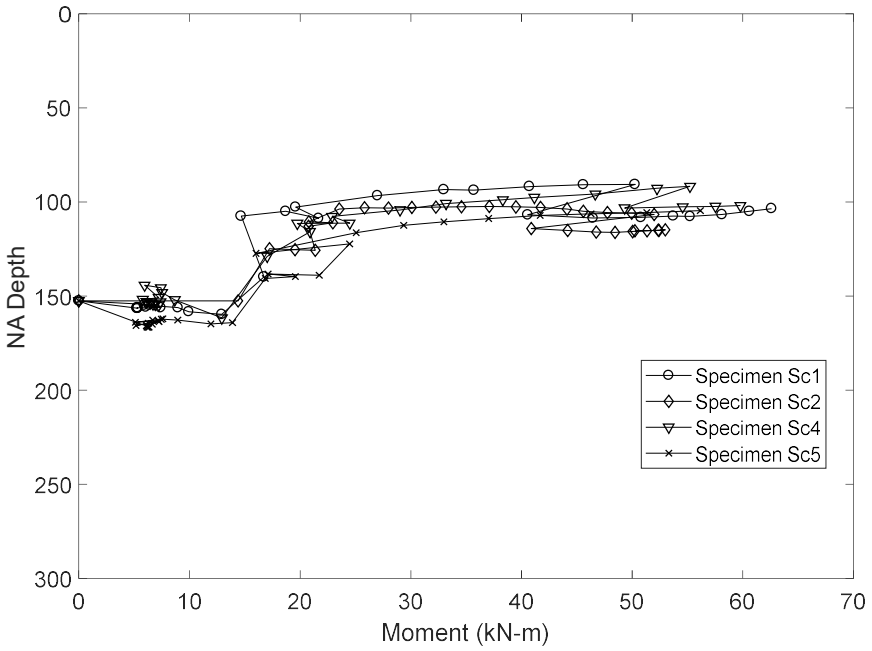

Figure 2-11. Neutral Axis Analysis for Spliced Beams

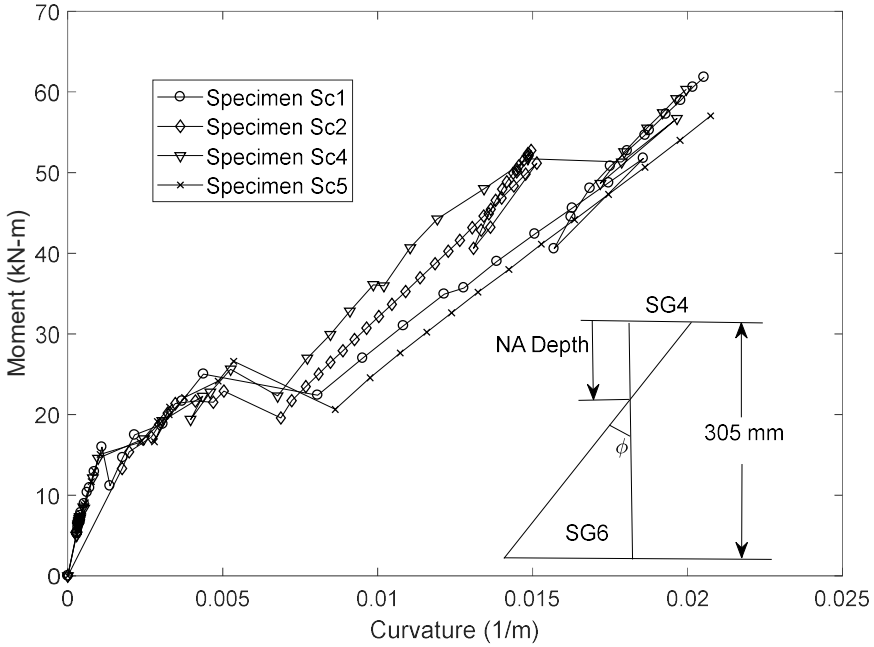

Figure 2-12. Moment versus Curvature for Spliced Beams with Collars

2.3 Finite Element Simulation

2.3.1 Methodology and Simulation Techniques

Previously, Dagher et al. (2012) conducted numerical modeling to investigate the flexural response of CFFT control beams tested by Bannon (2009) using beam elements and an iterative algorithm to predict the moment-curvature relationship for the entire section of the CFFT. Dagher et al. (2012) assumed the FRP laminate had the same ultimate failure strain in tension and compression, full composite action between the FRP tube and the concrete core, and the concrete had no tensile strength. The technique for developing the moment-curvature relationship was initially established by Burgueño (1999) and included a variable confinement model for concrete in compression. In contrast, this study investigated the structural design of a CFFT splice using a fully 3D FE analysis that accounted for concrete confinement, cracking, and construction details of the splice. The FE package Abaqus/CAE was used for all simulations. For comparison, the response of a control beam nominally identical to the three specimens tested by Dagher et al. (2012) was also simulated. A zero-thickness cohesive surface was assumed to capture bond failure at the FRP-concrete interface. The ultimate failure strains of the FRP laminate in tension and compression were treated independently. Based on the symmetry geometry, material properties, loads and boundary conditions about x and z-axes (Figure 2-13), a quarter-symmetric FE model was built for each of the tested beams to minimize the total number of elements/nodes in order to save computational time (Figure 2-14).

2.3.2 Constitutive Model and Mesh

Standard eight-node, fully integrated, 3D linear stress/displacement continuum brick elements were used for modeling the concrete core and saddles. Four-node general-purpose shell elements with reduced integration, hourglass control, finite membrane strains were used for modeling the FRP tube and internal collar. Standard, linear space, shear-flexible beam elements were used to model the CFCC longitudinal and spiral cage reinforcements. Based on a mesh convergence study conducted for the control beam, CFFT specimens were meshed such that maximum global element size was approximately 15 mm (Figure 2-15).

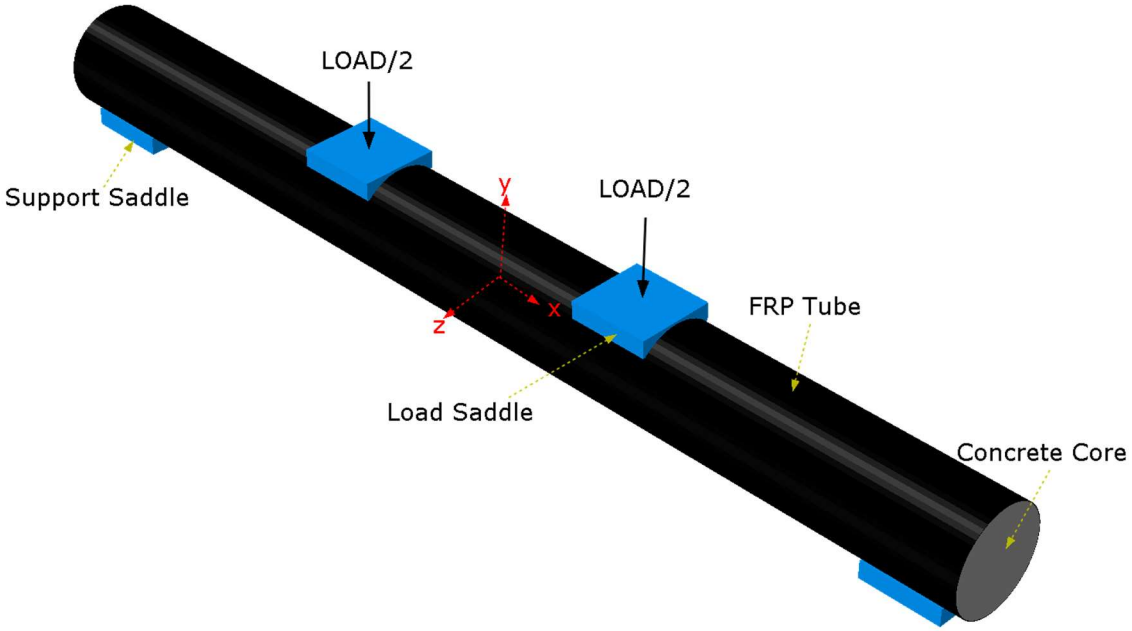

Figure 2-13. Entire Assembled CFFT Specimen

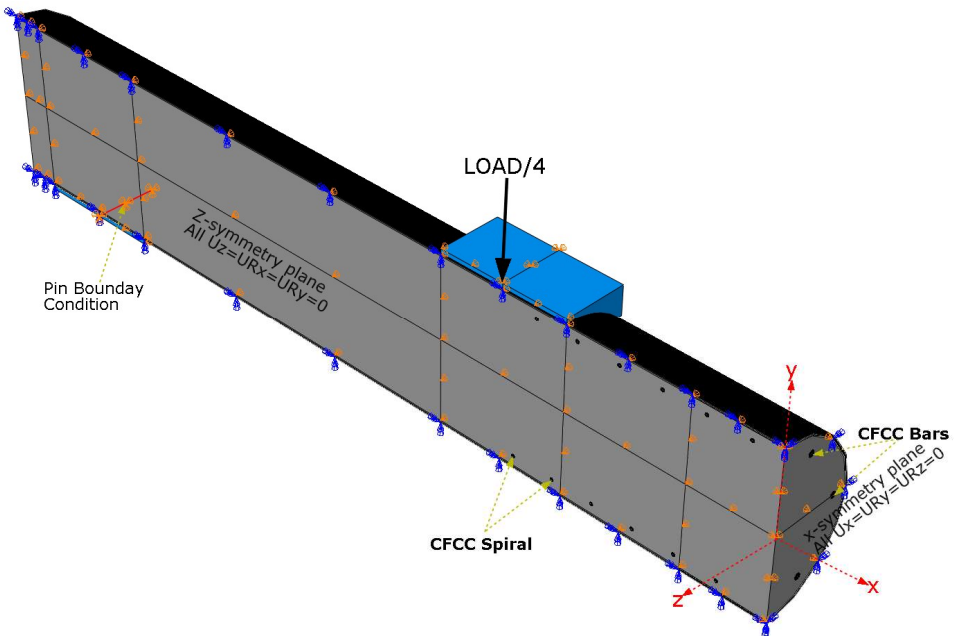

Figure 2-14. Spliced Beam: Boundary Conditions and Applied Loads for Quarter Symmetry

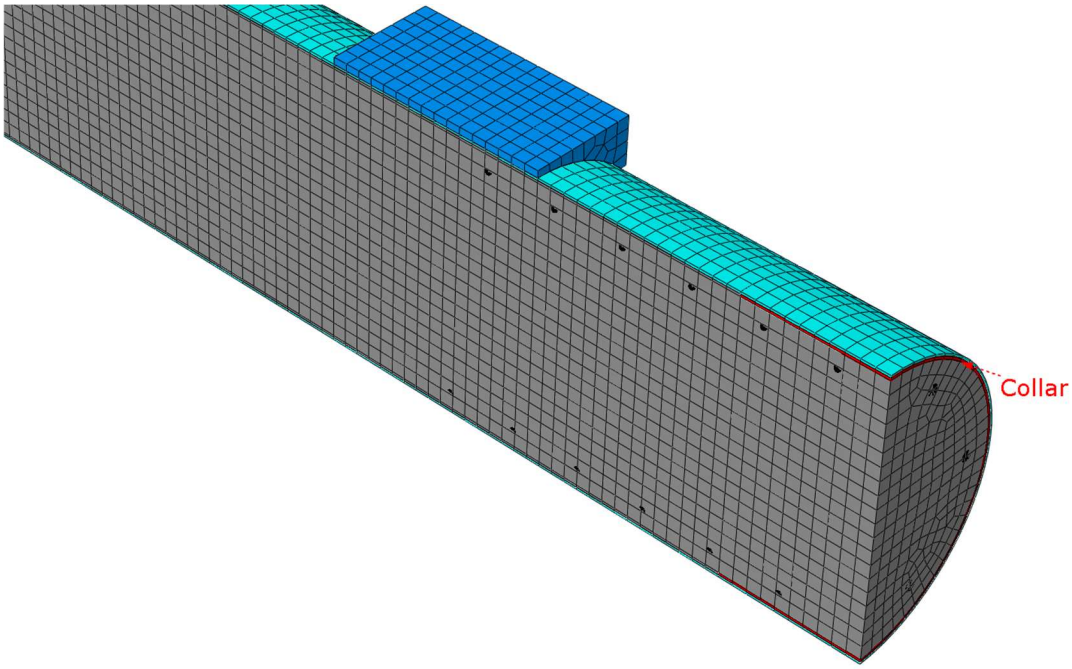

Figure 2-15 FE Model of Spliced Beam: Mesh with 15-mm Global Element Size

2.3.2.1 Modified Concrete Damaged Plasticity Model

Experimental investigations described previously have shown that CFFTs behave nonlinearly under pure bending or combined axial and bending loading. Most of that nonlinearity is due to damage and plasticity of the concrete core including cracking in tension and crushing under compression. Therefore, a nonlinear FE framework for FRP-confined concrete was implemented. Four main inelastic models are provided by Abaqus/CAE that can simulate constitutive behavior for most concrete types and predict failure, i.e., (1) the smeared crack concrete model, (2) the Drucker-Prager plasticity model, (3) the brittle crack concrete model, and (4) the concrete damaged plasticity model (CDPM).

None of these models are specifically designed to simulate FRP-confined concrete. However, the CDPM is appropriate for simulating FRP-confined concrete because it is based on a constitutive model developed by Yu et al. (2010a) which has been directly implemented in the Abaqus/CAE package with no need for a user-defined material subroutine. The model of Yu et al. (2010a) describes the compressive

elastic-plastic behavior of FRP-confined concrete including the damage parameters, the yield criterion, the hardening/softening rule, and the flow rule. It also adopts the cracking and crushing of concrete as the main two failure mechanisms by using the concepts of isotropic damage in combination with isotropic tensile and compressive plasticity. Further, as demonstrated by Tao and Chen (2015), CDPM can simulate debonding of the FRP tube from the concrete core, which is the typical failure mode in the spliced beams. Crack propagation is modeled within the CDPM using continuum damage mechanics and stiffness degradation (Simulia Inc. 2017).

To accurately simulate concrete response, the CDPM implemented in Abaqus/CAE needs: (1) a tensile stress-strain relationship with its damage parameters, (2) a compressive stress-strain relationship with or without its damage parameters, (3) values of the isotropic elastic parameters, including elastic modulus and Poisson's ratio, and (4) additional parameters that define the strain hardening-softening and flow rules including the dilation angle, the flow potential eccentricity, the ratio of initial biaxial compressive yield stress to initial uniaxial compressive yield stress, the ratio of the second stress invariant on the tensile meridian to that on the compressive meridian, and the viscosity parameter that defines viscoelastic regularization, (Simulia Inc. 2017). In general, for unconfined concrete, the recommended values of the last four parameters are the default values given in the Abaqus/CAE documentation, i.e., 0.1, 1.16, 0.667, and 0.00, respectively. Allowable values of the dilation angle are between 0^o and 56^o, where the larger angle produces a stiffer response (Yu et al. 2010a).

Yu et al. (2010a; b) recommend the compressive strain-stress relationship of Teng et al. (2007) be adopted because it explicitly represents the concrete/FRP-shell interaction and the inelastic strains and their corresponding damage parameters are evaluated using the same iterative algorithm. By treating the lateral strain-axial strain relationship as the key to an accurate confinement model for FRP-confined concrete, Teng et al. (2007) presented an analysis-oriented model for FRP-confined concrete in compression where the concrete and the FRP shell responses in addition to their interaction are explicitly considered. In order to provide context, a brief overview is provided in Section 2.3.2.2; for further details, see Teng et al. (2007).

The effect of FRP confinement on the flexural tensile strength of concrete has not been extensively investigated, and almost all FRP-confined concrete models found in the literature simulate only the effect of confinement on compressive strength. In CFFTs under flexural loading, the tensile strength of the concrete is small relative to the confined compressive strength, and the tensile stress will not instantaneously drop to zero because of the tension stiffening phenomenon. The tension stress-strain relationship implemented in this study was assumed to be linear with brittle fracture occurring at the modulus of rupture f_t using the empirical relationship $f_t = 0.7\sqrt{f'_c}$ (ACI Committee 318 2014).

In addition to the adopted tensile stress-strain relationship and the analysis-oriented model (Section 2.3.2.2), other parameters were required for the adopted modified CDPM. Poisson's ratio was assumed to be 0.20, and E_c was computed from the unconfined concrete strength using the empirical relationship $E_c = 4700\sqrt{f'_c}$ (ACI Committee 318 2014). Yu et al. (2010a) assumed a non-associated flow rule in the CDPM and found that the material dilation angle depended on the yield potential function parameters which were adopted by Yu et al. (Yu et al. 2010b). The values of dilation angle, flow potential eccentricity, and the ratio of the second stress invariant on the tensile meridian to that on the compressive meridian were estimated according to methods and assumptions given by Yu et al. (2010a; b) and Teng et al. (2007) giving values of 53°, 0, and 0.725 respectively. The ratio of initial biaxial compressive yield stress to initial uniaxial compressive yield stress and the viscosity parameter were set to the default values recommended by Abaqus/CAE, (Simulia Inc. 2017).

2.3.2.2 FRP-Confined Concrete in Compression

In FRP-confined concrete, the lateral confining pressure is affected by the stiffness of the FRP-shell. The confining pressure σ_l is directly proportional to the hoop strain of the FRP shell. The confining pressure supplied by the FRP shell is given by Equation 2.1.

$$\sigma_l = \frac{E_{frp}.t.\varepsilon_h}{R} \qquad \text{Equation 2.1}$$

E_{frp} is the elastic modulus of the FRP in the hoop direction; t is the thickness of the FRP shell; R is the radius of the confined concrete, and ε_h is the hoop strain of FRP shell, which is assumed to be the negative of the concrete lateral strain.

Teng et al. (2007) reported many experimental studies of actively-confined and FRP-confined concrete that were conducted with different confinement ratios. Based on observation of the results of these tests, the authors concluded that the axial strain at a given lateral strain is highly reliant on the ratio between the lateral confining pressure and the unconfined compressive strength of the concrete. Therefore, Equation 2.2 was proposed as a particular lateral strain-axial strain relationship, which applies to unconfined, actively confined, and FRP-confined concrete and includes that confinement ratio as a parameter.

$$\frac{\varepsilon_c}{\varepsilon_{c0}} = \left(1 + 8\frac{\sigma_l}{f'_{c0}}\right) 0.85 \left\{\left[1 + 0.75\left(\frac{\varepsilon_h}{\varepsilon_{c0}}\right)\right]^{0.7} - exp\left[-7\left(\frac{\varepsilon_h}{\varepsilon_{c0}}\right)\right]\right\} \qquad \text{Equation 2.2}$$

In Equation 2.2, f'_{c0} and ε_{c0} are the unconfined cylindrical compressive strength and its corresponding axial strain, respectively; and ε_c is the uniaxial compressive axial strain. The axial stress-strain relationship of FRP-confined concrete given by Equation 2.3 can be used. In which, $f'_{cc}{}^{*}$ and $\varepsilon_{cc}{}^{*}$ are the peak axial stress and the corresponding axial strain of concrete under a specific constant confining pressure, respectively, and σ_c is the axial stress of concrete. The constant r accounts for the brittleness of concrete and is computed according to Equation 2.4, where E_c is the elastic modulus of concrete

$$\frac{\sigma_c}{f'_{cc}{}^{*}} = [\left(\frac{\varepsilon_c}{\varepsilon_{cc}{}^{*}}\right).r]/[r - 1 + \left(\frac{\varepsilon_c}{\varepsilon_{cc}{}^{*}}\right)^r] \qquad \text{Equation 2.3}$$

$$r = E_c/(E_c - \frac{f'_{cc}{}^{*}}{\varepsilon_{cc}{}^{*}}) \qquad \text{Equation 2.4}$$

For estimating the values for $f'_{cc}{}^{*}$ and $\varepsilon_{cc}{}^{*}$, Teng et al. (2007) assumed that the axial stress of FRP-confined concrete at a given axial strain and confining pressure is equal to that of actively-confined concrete with the same confining pressure and axial strain. The stress-strain curve of FRP-confined concrete can be predicted as a set of points on a series of curves of actively-confined concrete; at these points, both the FRP-confined concrete and the actively-confined concrete have the same confining pressure. The locations of these interception points, however, depends on the stiffness of the FRP shell. In the present model, Equation 2.5 and Equation 2.6 proposed to define the failure surface of the actively confined concrete.

$$\frac{f'_{cc}{}^{*}}{f'_{c0}} = 1 + 3.5\frac{\sigma_l}{f'_{c0}} \qquad \text{Equation 2.5}$$

$$\frac{\varepsilon_{cc}{}^{*}}{\varepsilon_{c0}} = 1 + 17.5\frac{\sigma_l}{f'_{c0}} \qquad \text{Equation 2.6}$$

An iterative algorithm was used to generate the axial stress–axial strain curve of FRP-confined concrete. With the specified axial strain and all material properties as well as the CFFT cross-sectional dimensions, the FRP shell hoop strain was estimated using Equation 2.1 and Equation 2.4 Once the FRP shell hoop strain was available, the confining pressure supplied by the FRP shell could be determined without difficulty using Equation 2.1, then the calculation of axial stress was a straightforward process. By using the same algorithm, the inelastic strain and its corresponding damage parameter were evaluated taking the input variables, which were estimated according to the flow rule and to the softening-hardening rule of Yu et al. (2010b). Figure 2-16 shows the final confined compressive stress-strain model used in this study compared with the unconfined concrete curve using the same unconfined cylindrical compressive strength and its corresponding axial strain.

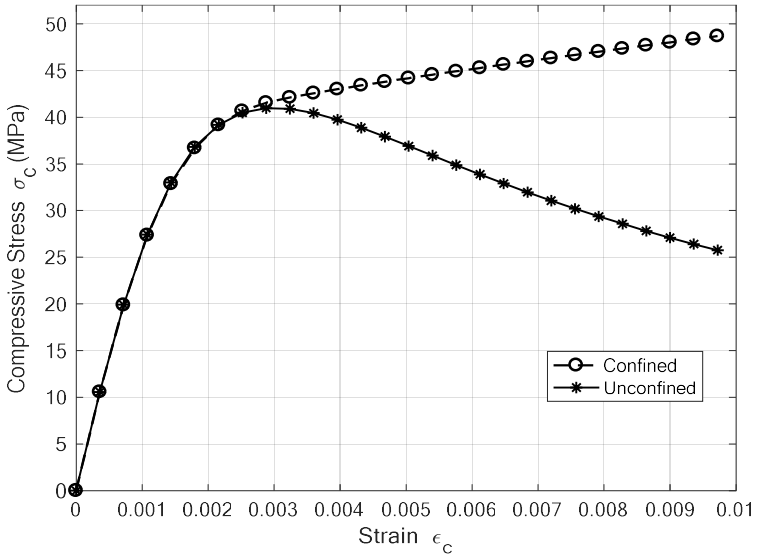

Figure 2-16. Confined and Unconfined Compressive Stress-Strain Model of Concrete

2.3.2.3 FRP Tube and Internal Collar

For many engineering structures, textile or woven fabric composites provide symmetric and balanced properties. A braided composite is a unique form of a textile composite with continuous reinforcement architecture such that the fiber tows are mechanically interlocked with one another, (Ayranci and Carey 2008). Unlike the characterization of unidirectional laminates, which is controlled by the mechanical properties of constituents, fiber angles, and ply thicknesses, analyses of textile composites are complex and depend on the undulation and cross-section geometry of the warp and fill tows as well as the spacing between these tows. The smallest element of the braided composite specimen that includes all the repetitive features is called the repetitive unit cell (RUC), (Barbero 2011). Several analytical models for braided composites are presented in the literature, most of which are reviewed by Ayranci and Carey (2008). Soykasap (2011) and Barbero (2011) satisfactorily estimated the mechanical properties of a braided textile composite by using different micromechanical models, including the rule of mixtures, one-dimensional composite beam, and two-dimensional mosaic models. However, each of these models has some limitations and applying these analytical models requires all the parameters that describe the RUC.

Neither the control nor spliced beam experiments reported all required RUC parameters; therefore, the unidirectional ply micromechanics approach adopted by Barbero (2011) in conjunction with the Tow-Waviness Knockdown Factor (TWKF) given by Cox and Flanagan (1997) was used in this study. Here, each braided composite layer with fiber orientation [±θ] is modeled as two [+θ/-θ] unidirectional plies, with a longitudinal modulus factored by the TWKF. The use of the TWKF accounts for the reduction in stiffness due to the straightening of undulating tows when loads are applied. The TWKT is a geometry-dependent factor, and it approximately equals 0.7 for the braided composites used in this study, (Bannon 2009). Therefore, the hybrid braided FRP tubes and collar were treated as a composite shell section created from three elastic orthotropic laminae with the corresponding braid thicknesses. Table 2-4 shows the micromechanics-predicted elastic properties of the braided laminae with the corresponding braided fiber angle and thickness. These transversely isotropic elastic properties are the model lamina parameters of the FRP shell. The subscript symbols x and y in Table 2-4 refer to longitudinal and hoop directions of FRP tubes, respectively.

This characterization of the braided composite laminate was validated with the coupon-level moduli results of laminate testing conducted by Bannon (2009). That test was carried out on a single layer of (T-700 Carbon/Derakane 8084) braided FRP coupons prepared with different fiber orientation [±22.5°], [±27.5°], [±45.0°], and [±67.5°]. The model predicted values of E_x and ν_{xy} for the braided carbon laminate were in good agreement with experimental data as shown in Figure 2-17.

The failure mechanisms of the braided FRP are complex due to the unique characteristics of textile composites. In order to minimize the uncertainty in the prediction of strength properties, Barbero (2011) recommend back-calculating them from experimentally measured composite properties by using micromechanics formulas. Therefore, the ultimate failure and damage parameters of the braided FRP tube are not considered in this research due to the lack of experimental data at the lamina level.

Table 2-4 Micromechanics Predicted Elastic Properties of Braided Laminas

Braided Lamina	Carbon T-700 Derakane 8084	E-glass Derakane 8084	Carbon T-700 Derakane 610	E-glass Derakane 610
θ (+/-) degree	20	81	22.5	75
V_f (%)	50	50	50	50
Thickness (mm)	0.78	0.94	0.86	1.02
E_x (MPa)	57,171	9,646	50,984	10,967
E_y (MPa)	7,373	25,376	8,108	23,614
v_{xy}	1.111	0.126	1.145	0.182
G_{xy} (MPa)	11,109	3,890	12,799	4,638
G_{yz} (MPa)	3,034	2,404	3,006	2,430
G_{xz} (MPa)	2,474	3,102	2,488	3,064

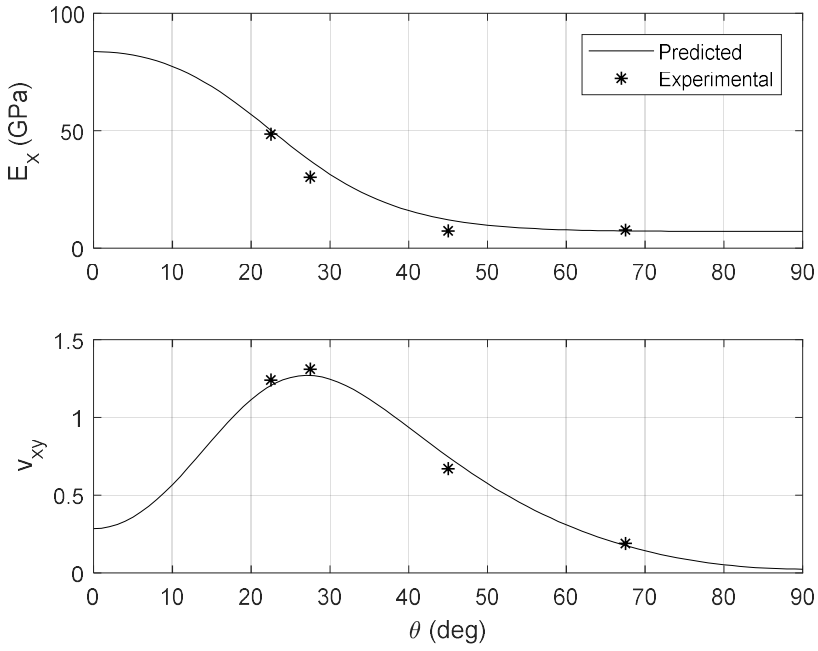

Figure 2-17. E_x and v_{xy} vs. Fiber Angle, Predicted and Experimental in Coupon-Level

2.3.2.4 CFFC Cage

The CFCC longitudinal and spiral reinforcement were assumed to be linear elastic B31 elements with an embedded region constraint in the concrete core. The mechanical properties provided by the manufacturer, (Tokyo Rope Inc 2017) were the tensile elastic modulus of 137,000 MPa, Poisson's ratio of 0.3, and ultimate tensile strain of 1.8%.

2.3.3 Surface Interaction

The FRP-to-concrete interface is usually assumed to exhibit full composite action in un-spliced CFFT simulations, (Chung et al. 2010; Dagher et al. 2012; Fam and Rizkalla 2002). However, in the simulation of spliced CFFT response, the assumption of full composite action produced an overestimated stiffness and did not capture the debonding failure observed experimentally. In their study on segmental CFFT piers, ElGawady and Dawood (2012) represented the FRP-to-concrete interface as a combination of a Coulomb friction model to transmit the shear stress and hard contact to transmit the normal stress. The stiffness predictions and the predicted debonding failure using this combined model were in good agreement for all CFFT beams. However, this model showed an obvious slippage at the end of the CFFT beam which was not observed experimentally.

In order to construct the cylindrical interface between the FRP and concrete, this study simulated a surface-based cohesive interface using the traction-separation law implemented in Abaqus/CAE. This model showed good agreement in both control and spliced beam simulations with no slippage at the ends and captured the debonding failure at the splice. The constitutive law for the fictitious cohesive interface was obtained by back-calculating the stiffness parameters K_{nn}, K_{ss}, and K_{tt} in the normal and two shear directions respectively based only on the response of the control beam. This method started by assuming arbitrary values of these three stiffness parameters, then compared the model-predicted and experimentally-determined mid-span deflection and maximum strains at failure load. The values of these parameters that

gave the best results for the control beams were used for modeling the spliced beams. The value of K_{nn} was found to be 100 N/mm^3 while the values of K_{ss} and K_{tt} were 0.16 N/mm^3.

The lap joint between the FRP tube and FRP internal collar was also represented as a surface-based cohesive behavior. The mechanical parameters of the traction-separation law for this lap joint were determined from the technical sheet of the Pliogrip 7770 adhesive provided by Ashland Inc. (Ashland Inc 2016) and from modeling the lap shear test discussed in Section 2.2.2.1 to determine the effective shear stiffness. Both FRP-to-concrete and FRP-to-FRP behaviors were assumed as a surface-to-surface contact with only slave nodes initially in contact.

2.3.4 Loading Steps and Boundary Conditions

One general-static loading step was adopted in this study. To accurately mimic the CFFT nonlinear flexural response, a reasonable number of automatic time steps were used for the static loading analysis with specific initial, maximum, and minimum increment sizes. If the solution did not converge at a given time step, especially when the concrete tensile cracking occurred, it was resolved with a reduced time step. Abaqus/CAE repeated this procedure until reaching convergence within each increment.

Symmetry boundary conditions about the longitudinal x- and y-axes were implemented for all nodes at the planes of symmetry as shown in Figure 2-15. The test boundary conditions were mimicked by restraining the displacement degrees of freedom for all nodes at the lines of contact on the bottom surface of the support saddles. Frictionless contact between the beam and the top surface of the support saddles was simulated. The load was applied as two concentrated point loads acting on the center of the top surface of the load saddles, and frictionless contact was also assumed between the load saddles and the beam (Figure 2-13 through Figure 2-15).

2.4 Model Predictions

Overall, the model predictions were relatively consistent with the experimental results. Figure 2-8 and Figure 2-9 show the mid-span load-deflection responses obtained from the FE model and experimental tests. The model-predicted load-deflection curves showed linear response up to abrupt softening occurring at a load of approximately 35 kN. This point was attributed to concrete cracking at the bottom of the beam in the load span. Beyond that point, a significant softening and nonlinear response occurred due to the progress of concrete cracking.

The load-deflection response of the control beam was predicted more accurately than the responses of spliced beams due to other sources of nonlinearity caused by the splice and the relative complexity required to model the spliced beam. As shown in Figure 2-8, the FE model slightly overestimated the stiffness of the control specimens after the cracking moment up to the initiation of the debonding. That discrepancy was likely due to the assumption of a constant cohesive behavior between the concrete core and the FRP shell along the length of model regardless of the level of confinement. Nevertheless, it was observed that the simulations of the FRP-to-concrete interface, confined concrete, and hybrid braided FRP tube (an inner layer of E-glass fiber braid and two outer layers of carbon fiber) as three transversely isotropic laminas with zero fiber orientation showed satisfactory results for the predicted deflection.

Figure 2-18 and Figure 2-19 show the predicted strains at the pure bending region plotted against their corresponding experimental strains up to failure. The moment-strain response of the spliced beams, away from the splice (corresponding to SG4-6) shown in Figure 2-18, was similar to that of the control beams, (310-mm away from mid-span) shown in Figure 2-19. The significant difference between the response of the spliced and control beams was indicated by the gauge on the tension face closest to the splice (SG3).

The models did not explicitly predict failure since damage parameters of the braided FRP tube were not incorporated in the simulations. Furthermore, the model did not consider the strength and damage

mechanism of the cohesive FRP-to-concrete assumed in this study. However, the results obtained from the model of the control beam showed that the predicted applied load at a tensile strain of 0.0155 corresponding to longitudinal tensile rupture of the FRP shell that was 258.3 kN (Figure 2-19). This strain of 0.0155 was the average peak tensile strain measured by tension-face gauges at 310-mm away from mid-span (Dagher et al. 2012). The 258.3-kN load was 2.9% greater than the average failure load of 251.0 kN reported by Dagher et al. (2012) with a standard deviation of 17.35 kN and coefficient of variation of 6.91%. Likewise, the results obtained from the model of the spliced beam with collar showed that the applied load corresponding to the maximum longitudinal strain measured by SG4-6 (Figure 2-18) and SG7-9 was 128.7 kN, which is 13.8 % greater than the average failure load of 113.1 kN with a standard deviation of 16.8 kN. These reasonably accurate predictions of strain at failure indicated that the model was capturing the behavior of both spliced and control beams reasonably well.

The maximum predicted axial force in the longitudinal CFCC bar was 70 kN which was less than the minimum average capacity determined from the pullout testing explained in Section 2.2.3. Figure 2-20 and Figure 2-21 show the models of the spliced beams' deformed shapes obtained from the FE analysis at the maximum simulated load. The FE models predicted the general deformed shape, and local debonding of FRP interface at the splice is evident, which was also observed experimentally (see Figure 2-7).

In general, the reasonably accurate prediction of the concrete cracking level, displacements, capacities, debonding, and strains compared with the experimental results indicated that the presented model was capable of predicting and analyzing the nonlinear response of un-spliced and spliced CFFT.

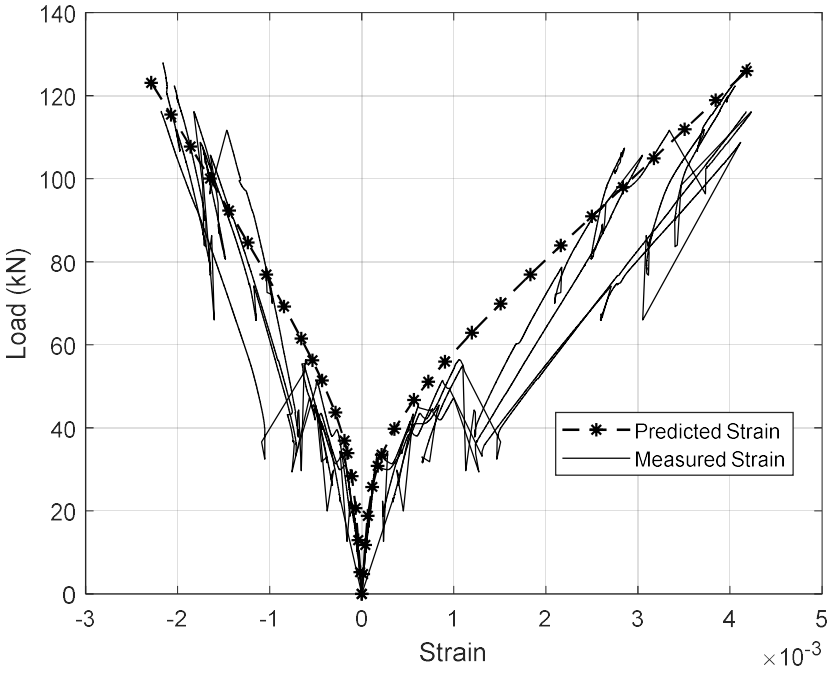

Figure 2-18. Predicted Stains vs. Measured Strains: Spliced Beam with Collar for SG4 and SG6

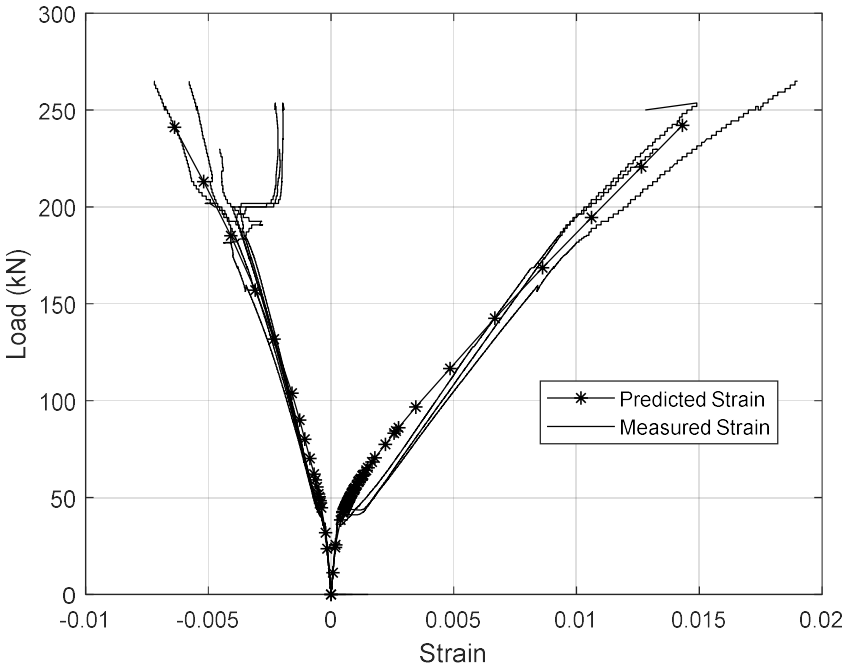

Figure 2-19. Predicted Stains vs. Measured Strains: Control Beam 310 mm away from mid-span

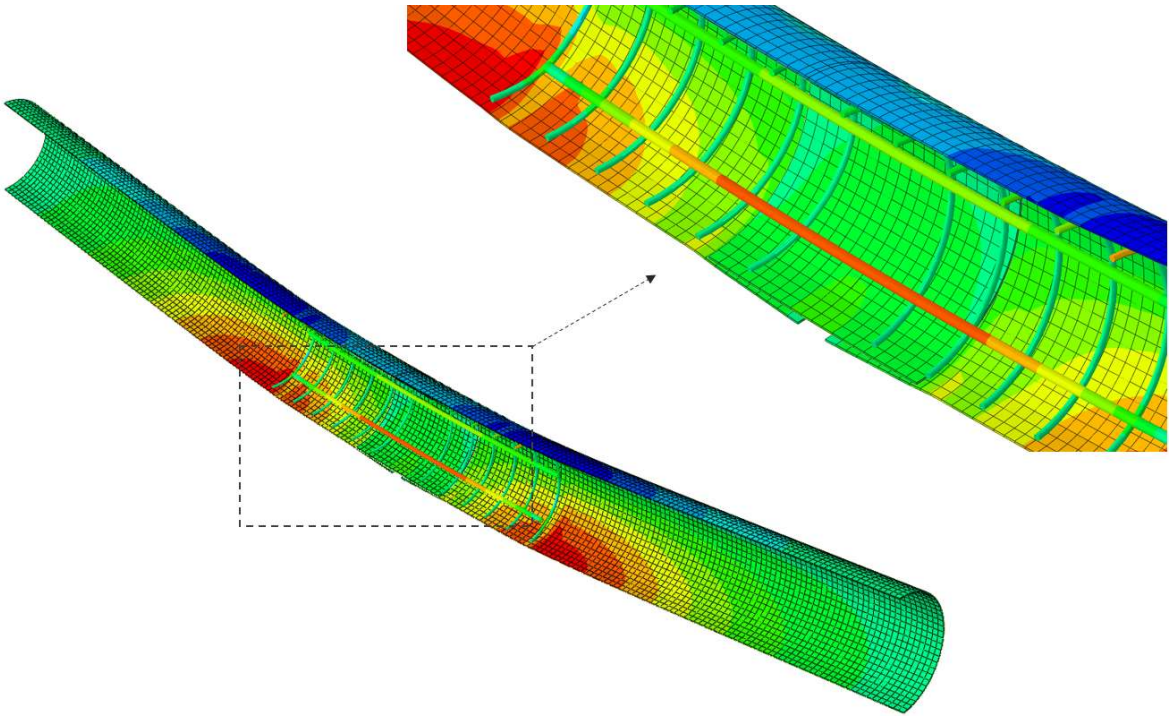

Figure 2-20. Deformed Shape of the Spliced Beam with Collar

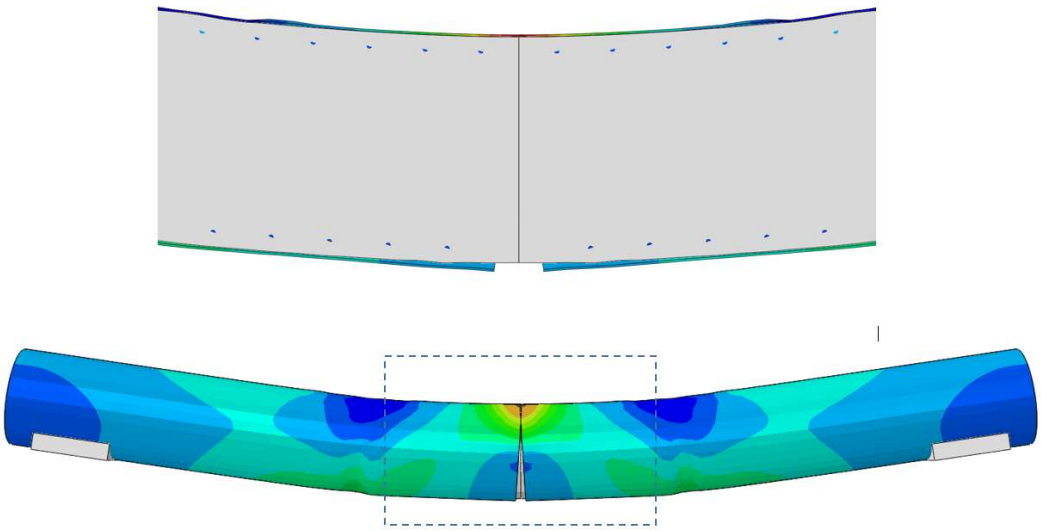

Figure 2-21. Deformed Shape of the Spliced Beam with no Collar

2.5 Summary

Structural development and investigation of a field-installed CFFT splicing for bridge construction have been presented. This splice consisted of an internal FRP collar bonded to the FRP shell with a high-strength urethane adhesive to withstand the short-term construction loads and CFCC longitudinal bars and spiral to withstand permanent and live loads. This chapter has detailed the fabrication, structural testing and FE simulation of spliced CFFT beams. Also included were results of pullout testing of CFCC necessary to design the splice. The following conclusions and findings were drawn from this study.

- Pullout testing of CFCC showed there was a direct correlation between the embedment length and the pullout capacity. Further, relatively short development lengths developed significant CFCC tensile capacity.
- The splice design presented here appears to be a viable option for field-splicing CFFTs. While moment capacity of the spliced beams was, on average, 38% of the moment capacity of the un-spliced beams, spliced beam capacity was, on average, 88% of the computed splice strength which accounted for the internal reinforcing and neglected the FRP collar. In a field application of this technology, splices can be located in regions of the structure with lower applied moments. However, while the adhesive used to attach the collar is also employed to attach adjacent sections of FRP decking during construction of BCABs, the successful field application of the adhesive in a splice may need to be verified through NDE or other techniques.
- The presence of an internal collar may have increased the moment capacity of a spliced beam beyond that of a spliced beam without an internal collar. This was likely due to FRP debonding occurring at higher moments compared to beams with no internal collar. However, only two beams were tested with an internal collar, and significant spread in capacities was observed.
- Debonding of the FRP shell from the concrete core was a pre-cursor to FRP tensile rupture in the spliced beams, and matrix damage propagated from the point of tensile rupture to the splice. Tensile rupture and compressive buckling also occurred for all specimens at the termination of the CFCC

reinforcing. The internal collar did not prevent the FRP from debonding but increased the moment required to debond the shell by a factor of almost 2.4.

- More bending tests could be conducted to better characterize FRP debonding and the resulting effect of loss of concrete confinement. These tests could have varying internal collar lengths to assess if a longer internal collar increases the splice's capacity before debonding. Additional tests employing different lengths and termination points of the CFFT reinforcing cage would also be valuable to help assess the significance of the termination point of the CFFT.
- The nonlinear FE models of this study provided a better understanding of the general performance of the control and spliced CFFT beams as well as the effect of the internal collar. The models gave reasonable predictions of stiffness and strength of the spliced beams, and very good predictions of strains and load-deflection response of the un-spliced control beam.

CHAPTER 3

EFFICIENT FE SIMULATION OF CFFT ARCHES

3.1 Introduction

In 1995, Mirmiran and Shahawy pioneered the use of CFFTs as compression members, (Mirmiran and Shahawy 1997). Thereafter, a large amount of experimental work has been conducted to investigate the structural performance of CFFTs in different configurations, with and without reinforcement, and under different types of loading. Davol et al. (2001) carried out bending tests on CFFT beams to characterize their flexural and shear response as well as the FRP hoop and the concrete dilation behavior. Fam and Rizkalla (Fam and Rizkalla 2002) extensively investigated the flexural behavior of large-scale CFFT beams by demonstrating the effects of various parameters such as concrete filling and placement of an internal hole. Cole and Fam (2006) and Mohamed and Masmoudi (2010) attempted to enhance the flexural response of the CFFTs by reinforcing them with either steel or FRP.

In order to help understand experimentally observed response of CFFTs, provide insight into their structural performance, and design structures supported by CFFT beams and arches, numerical simulations are necessary. The traditional fiber cracked section analysis has been applied to predict CFFT bending response based on the concepts of equilibrium and strain compatibility along with the experimental work as in the literature cited above (Cole and Fam 2006; Davol et al. 2001; Fam and Rizkalla 2002; Mohamed and Masmoudi 2010). FE studies have also been conducted to numerically predict CFFT system response and components (Hany et al. 2016; Hussein Abdallah et al. 2017; Kabir and Shafei 2012; Mirmiran et al. 2000; Qasrawi et al. 2016; Son and Fam 2008; Youssf et al. 2014; Yuan et al. 2017). However, most of those analyses have utilized both solid-based and shell-based elements of commercial software packages such as Abaqus/CAE and have typically been developmentally and computationally demanding. Few researchers have developed simple beam-based, i.e., (either DB or FB), FE analyses to simulate CFFT structural members. Dagher et al. (2012) investigated the bending response of CFFTs using 2D DB FE analysis proposed by as discussed later. Hu and Barbato (2014) adopted a geometrically linear FB element

using a previously-established MATLAB-based program called FEDEASLab to model the structural response of reinforced concrete circular columns confined with externally-bonded FRP, specifically.

Of particular interest in this dissertation are BCABs, where CFFT arches act as the main structural members and must carry combined axial load and bending. Dagher et al. (2012) carried out structural testing on full scale isolated arch specimens along with four-point bending tests of CFFT beam specimens to investigate the flexural response. The authors also developed a DB beam model to simulate the structural response of CFFT arches based on small strains and small displacements using two-noded, 2D Euler beam elements. The authors adopted an iterative algorithm that pre-defines the nonlinear moment-curvature response of an arch cross-section and accounts for concrete cracking and FRP confinement effects on the concrete for the entire section of the CFFT using the concrete constitutive model of Burgueño (1999).

CFFT arches present unique modeling challenges due to the effect of confinement of the concrete core on its stiffness and ductility as well as the importance of large deformations. The arches undergo significant nonlinear effects arising from both geometric and material nonlinearities; however, they have rarely been investigated by a simple, efficient, second-order nonlinear approach. Therefore, CFFT arches are good candidates for simulation using FB beam-column (frame) elements, which permit accurate nonlinear structural simulations with relatively few elements compared to conventional DB analysis (Spacone et al. 1996). With FB element force interpolation functions exactly satisfy the equilibrium in the deformed configuration, although an iterative procedure is required at the element level to verify the compatibility at element integration points.

This chapter documents the second research contribution of this dissertation and presents an efficient method for structural modeling of CFFT arches. The main objective is to develop and validate a general, second-order, layered-section, curved frame element employing the FB approach that is tailored specifically for modeling CFFT members. This will allow more efficient design of CFFT arches and more accurately quantify the behavior of these structures. Large displacements and geometric nonlinearity are accurately

handled at the element level (P-Δ effect) utilizing a corotational formulation and at the section level (p-δ effect) using a geometrically nonlinear FB frame element. The initial curvature of the CFFT arch is incorporated in the formulation. The layered section technique is equipped to trace the elastic behavior of the FRP tube and the inelastic uniaxial stress-strain relationship of the FRP-confined concrete. The MATLAB programming environment (2018) was used to implement the FB element and solver. To the best of the authors' knowledge, this study employs for the first time a second-order inelastic FB curved frame FE to simulate the structural response of CFFT arches. The general model formulation and its implementation are verified using three case studies including elastic-plastic analysis of a beam, elastic buckling analysis of a column and elastic post-buckling analysis of a circular arch. A bending test was performed on isolated CFFT arches spanning 6.1 m and having different rises to compare their response with model predictions. Results of CFFT arch and beam tests reported by Dagher et al. (2012) were also used to additionally assess the ability of the model to simulate CFFT behavior and failure modes. The results of the FB modeling approach are shown to compare well with the experimental results.

3.2 Development of Analysis Methodology

A methodology for performing a FB planar FE analysis on isolated CFFT structural members considering the effect of FRP confinement on the constitutive response of the concrete core is presented. The element geometry within the corotational framework, material constitutive relationship that accounts for the FRP confinement effect on the concrete, element state-determination process, and global incremental-iterative solver are detailed.

3.2.1 Coordinate Systems and Geometry

A curved, planar, FB frame element is adopted with two nodes (*I* and *J*) and six degrees of freedom in the global coordinate system (*X*, *Y*) as shown in Figure 3-1a. The global end displacement including the

rigid body modes $\widehat{\mathbf{D}}$ and their corresponding force components $\widehat{\mathbf{P}}$ are illustrated in Figure 3-1 and grouped in Equation 3.1 and Equation 3.2, respectively.

$$\widehat{\mathbf{D}} = [\widehat{D}_1, \widehat{D}_2, \widehat{D}_3, \widehat{D}_4, \widehat{D}_5, \widehat{D}_6]^T \qquad \text{Equation 3.1}$$

$$\widehat{\mathbf{P}} = \left[\hat{P}_1, \hat{P}_2, \hat{P}_3 \hat{P}_4, \hat{P}_5, \hat{P}_6\right]^T \qquad \text{Equation 3.2}$$

To avoid singularity of the element stiffness matrix due to the rigid body modes, the nodal displacements are transformed to the local element (basic) coordinate (x, y) system using the corotational formulation. The corotational formulation allows accurate handling of large rigid body motions of an element and system-level geometric nonlinearity in a small strain framework de Souza (2000). Furthermore, the element and geometric stiffness matrices, along with the element forces, can then be transformed from the local to the global coordinate system including all translational and rotational degrees of freedom for assembly into the global stiffness matrix and internal force vector, respectively. Further details on the formulation and derivation of the corotational formulation are omitted here but are thoroughly covered by others (Crisfield 1990; de Souza 2000).

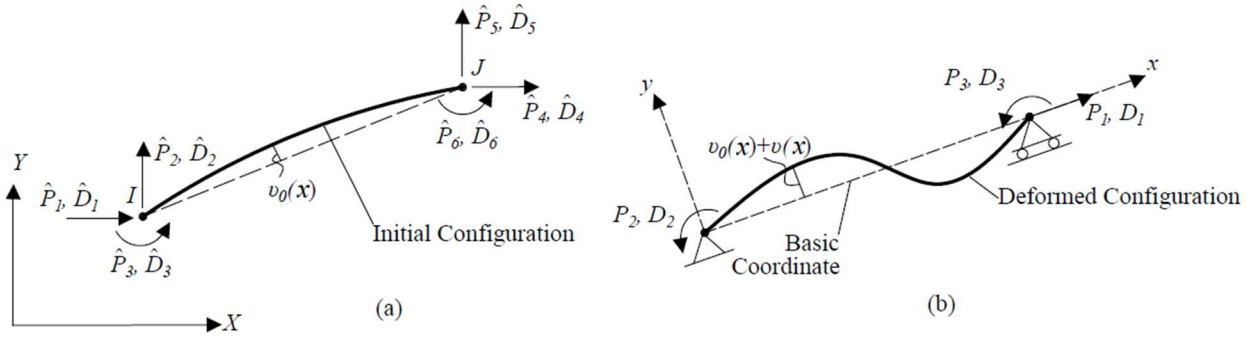

Figure 3-1. (a) Global Coordinate System, (b) Basic Coordinate System

In the basic coordinate system, the frame element has three DOFs including one axial displacement and two rotations relative to the chord. These three degrees of freedom are the minimum number of geometrical variables required to illustrate the deformable mode of the element and must be updated at

every global iteration. The local nodal displacements **D** and the corresponding forces **P** are illustrated in Figure 3-1b and grouped in Equation 3.3 and Equation 3.4, respectively.

$$\mathbf{D} = [D_1, D_2, D_3]^T \quad \text{Equation 3.3}$$

$$\mathbf{P} = [P_1, P_2, P_3]^T \quad \text{Equation 3.4}$$

3.2.2 Element Formulation

Based on Bernoulli- Euler theory, the deformations at each cross-section $\mathbf{d}(x)$ of the adopted frame element are described by defining two degrees of freedom including the axial strain at the reference axis $\varepsilon_0(x)$ and the curvature of the cross-section $\kappa(x)$, as grouped in Equation 3.5. The corresponding section forces or the stress resultant vector $\mathbf{S}(x)$ consists of the axial force, $N(x)$, and the bending moment, $M(x)$, as illustrated in Figure 3-2 and grouped in Equation 3.6.

$$\mathbf{d}(x) = [\ \varepsilon_0(x)\ \kappa(x)]^{\ T} \quad \text{Equation 3.5}$$

$$\mathbf{S}(x) = [N(x)\ M(x)]^T \quad \text{Equation 3.6}$$

Each element is further divided into a number of sections that are subdivided into layers (e.g., for CFFT, there are FRP and confined concrete fibers at each layer as shown in Figure 3-2). The strain $\varepsilon(x, y)$ at any layer i is constant and related to the sectional deformation $\mathbf{d}(x)$ as $\varepsilon(x, y) = \mathbf{a}(y)\mathbf{d}(x)$, where $\mathbf{a}(y)$ is the compatibility matrix that relates the generalized section deformations with the strain at any section, as shown in Equation 3.7.

$$\mathbf{a}(y) = [1\ -y] \quad \text{Equation 3.7}$$

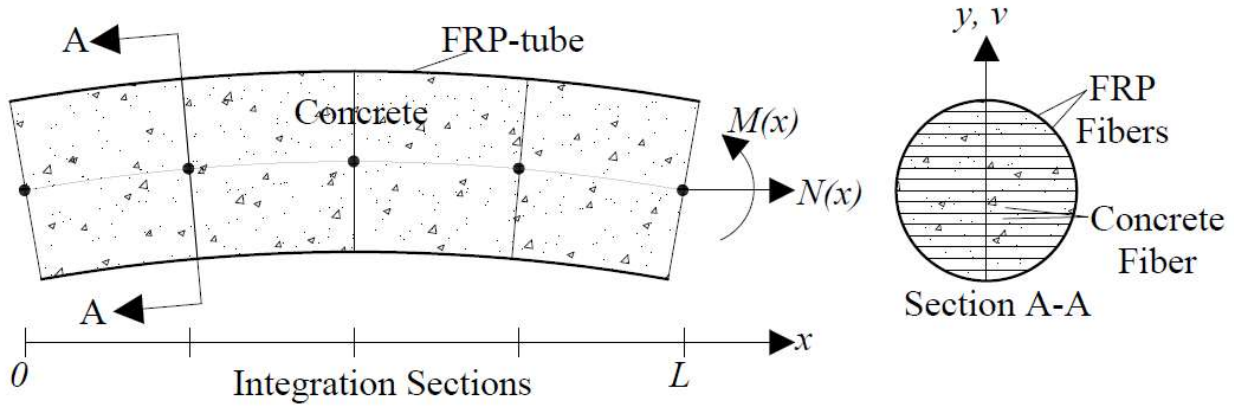

Figure 3-2. Layered-Section Discretization and Distributed Plasticity Technique

To satisfy equilibrium at any section in the deformed element of length L, the force interpolation function $\mathbf{b}(x, v_x)$ in Equation 3.8 proposed by Neuenhofer and Filippou (1998) was adopted to relate the section forces $\mathbf{S}(x)$ to the element end forces $\mathbf{P}$ by Equation 3.9.

$$\mathbf{b}(x, v_x) = \begin{bmatrix} 1 & 0 & 0 \\ v_x & x/L - 1 & x/L \end{bmatrix} \quad \text{Equation 3.8}$$

$$\mathbf{S}(x) = \mathbf{b}(x, v_x)\mathbf{P} \quad \text{where} \quad v_x = v(x) + v_0(x) \quad \text{Equation 3.9}$$

Because this interpolation function strictly satisfies equilibrium in the deformed shape, there is no discretization error but only a numerical error in the FB element analysis (Neuenhofer and Filippou 1997). The lateral displacement $v(x)$ (Figure 3-1) is employed to accurately capture the geometric nonlinearity in the section level caused by the interaction between the axial force and bending moment. In Equation 3.9, $v_0(x)$ is the initial curvature of the FB element, and can be used to capture the curvature of CFFT arches as in the present study or member imperfections (Du et al. 2017).

The weak form of compatibility is enforced through the application of the Principle of Virtual Forces, which in the case of the FB frame element takes the form in Equation 3.10.

$$\int_0^L \delta \mathbf{S}(x)^T \mathbf{d}(x) d(x) = \delta \mathbf{P}^T \mathbf{D} \quad \text{Equation 3.10}$$

According to Du et al. (2017), Equation 3.11 represents the relations between the virtual section forces $\delta \mathbf{S}(x)$ and virtual end forces $\delta \mathbf{P}$ obtained using the composite matrix $\mathbf{b}^*(x, v_x^*)$ in Equation 3.12.

$$\delta \mathbf{S}(x) = \mathbf{b}^*(x, v_x^*) \delta \mathbf{P} \quad \text{where} \quad v_x^* = 0.5 * v(x) + v_0(x) \quad \text{Equation 3.11}$$

$$\mathbf{b}^*(x, v_x^*) = \begin{bmatrix} 1 & 0 & 0 \\ v_x^* & x/L - 1 & x/L \end{bmatrix} \quad \text{Equation 3.12}$$

After substitution of Equation 3.11 in Equation 3.10 and elimination of $\delta \mathbf{P}^T$ based on the arbitrariness argument, the element end displacement in terms of the section deformation along the element is shown in Equation 3.13.

$$\mathbf{D}^{ele} = \int_0^L \mathbf{b}^*(x, v_x^*) \mathbf{d}(x) d(x) \quad \text{Equation 3.13}$$

3.2.3 Fiber Section Model and Element Flexibility matrix

Following Bernoulli-Euler theory, at any cross-section of Figure 3-2 only normal stress $\sigma(x, y)$ acts on each one-dimensional element fiber, and the corresponding material tangent modulus is $E_t(x, y) = \frac{\partial \sigma(x,y)}{\partial \varepsilon(x,y)}$. The stress resultants $\mathbf{S}(x)$ at that cross-section (integration point) can be calculated by stress integration over the whole section area A as in Equation 3.14, which is applicable to both elastic and inelastic materials.

$$\mathbf{S}(x) = \int_0^A \mathbf{a}(y)^T \sigma(x, y) dA \quad \text{Equation 3.14}$$

Therefore, considering distributed plasticity by using the layered-section technique makes the FB elements more efficient than the DB elements in the geometrically nonlinear inelastic analysis (Du et al. 2017). Furthermore, using the layered-section technique in FB elements can assist in capturing plastic hinges along the elements with reduced computation time due to the adopting of exact force interpolation function $\mathbf{b}(x, v_x)$.

According to de Souza (2000), the resulting expressions for the section tangent stiffness matrix $\mathbf{k}^{\boldsymbol{sec}}(x)$ and flexibility matrix $\mathbf{f}^{\boldsymbol{sec}}(x)$ are obtained from Equation 3.15 and Equation 3.16, respectively.

$$\mathbf{k}^{\boldsymbol{sec}}(x) = \int_0^A \mathbf{a}(y)^{\boldsymbol{T}} E_t(x,y)\mathbf{a}(y)dA = \begin{bmatrix} \int_0^A E_t(x,y)dA & -\int_0^A yE_t(x,y)dA \\ -\int_0^A yE_t(x,y)dA & \int_0^A y^2E_t(x,y)dA \end{bmatrix} \quad \text{Equation 3.15}$$

$$\mathbf{f}^{\boldsymbol{sec}}(x) = \mathbf{k}^{\boldsymbol{sec}}(x)^{-\mathbf{1}} \quad \text{Equation 3.16}$$

The section constitutive law is written in Equation 3.17.

$$\mathbf{d}(x) = \mathbf{f}^{\boldsymbol{sec}}(x)\mathbf{S}(x) \quad \text{Equation 3.17}$$

The element flexibility matrix $\mathbf{F}^{\boldsymbol{ele}}$ can be obtained by taking the derivative of the end nodal displacements $\mathbf{D}^{\boldsymbol{ele}}$ (Equation 3.13) with respect to the end nodal forces $\mathbf{P}$. Due to the existence of lateral displacement term $v(x)$ in the matrix $\mathbf{b}^*(x, v_x^*)$, the flexibility matrix evaluation is complicated and leads to Equation 3.18.

$$\mathbf{F}^{ele} = \frac{\partial \mathbf{D}}{\partial \mathbf{P}} = \int_0^L \{\mathbf{b}^*(x, v_x^*)^{\boldsymbol{T}} \mathbf{f}^{\boldsymbol{sec}}(x)[\mathbf{b}(x, v_x) + \mathbf{h}(\mathbf{P}, v_x)] + \mathbf{g}(\mathbf{P}, v_x)\} d(x) \quad \text{Equation 3.18}$$

Finally, the element stiffness matrix without rigid body modes is given by Equation 3.19.

$$\mathbf{K}^{ele} = \mathbf{F}^{ele^{-1}} \qquad \text{Equation 3.19}$$

The matrices **h** and **g** are defined in Equation 3.20.

$$\mathbf{h}(\mathbf{P}, v_x) = P_1 \begin{bmatrix} 0 & 0 & 0 \\ \frac{\partial v(x)}{\partial P_1} & \frac{\partial v(x)}{\partial P_2} & \frac{\partial v(x)}{\partial P_3} \end{bmatrix}, \quad \mathbf{g}(\mathbf{P}, v_x) = \frac{\kappa(x)}{2} \begin{bmatrix} \frac{\partial v(x)}{\partial P_1} & \frac{\partial v(x)}{\partial P_2} & \frac{\partial v(x)}{\partial P_3} \\ 0 & 0 & 0 \\ 0 & 0 & 0 \end{bmatrix} \qquad \text{Equation 3.20}$$

The term $\frac{\partial v(x)}{\partial \mathbf{P}} = [\frac{\partial v(x)}{\partial P_1} \quad \frac{\partial v(x)}{\partial P_2} \quad \frac{\partial v(x)}{\partial P_3}]$ in Equation 3.20 is evaluated using a technique primarily developed by Neuenhofer and Filippou (1998) called Curvature Based Displacement Interpolation (CBDI). In the CBDI technique, the displacements $v(x)$ need to be obtained from the curvature field $\kappa(x)$ evaluated at *n* integration points using a Lagrangian polynomial. The procedure is mathematically summarized in Appendix A. Further details on the derivation of element flexibility matrix $\mathbf{F}^{ele}$ and the formulation of CBDI technique are omitted here but are thoroughly covered by de Souza (2000).

In addition to the use of the layered-section technique to capture the stiffness degradation due to concrete cracking in the tension face of the cross-section and along the CFFT arch element as shown in Figure 3-2, Gauss-Lobatto numerical integration is used to numerically evaluate Equation 3.13 and Equation 3.18. This scheme is more accurate than conventional Gauss integration when solving nonlinear problems because it always includes the end sections of the integration field (Spacone et al. 1996). Element loads are concentrated at the ends, which experience the most substantial nonlinear behavior.

3.2.4 CFFT Constitutive Model

Most of the nonlinear response of the CFFT arches is due to damage and plasticity of the concrete core, including tensile cracking. The compressive strength and the ultimate strain of concrete can be significantly enhanced by FRP confinement. Therefore, an important aspect in the simulation of CFFT arches is to use a compressive stress-strain model that explicitly considers the response of the concrete core and its dilation as well as the FRP tube and its confining effect on the concrete core. The stress-strain,

analysis-oriented model for FRP-confined concrete used in this study was originally proposed by Teng et al. (2007) based on an interpretation of the lateral deformation characteristics of concrete with different levels of FRP confinement. This model has demonstrated good predictive capabilities in 3D continuum shell simulation of spliced and unspliced CFFT beams in Chapter 2 of this dissertation. To provide context, a brief overview is provided in Section, 2.3.2.2; for further details, see Teng et al. (2007).

An iterative algorithm was generated to illustrate the compressive axial stress–axial strain curve of FRP-confined concrete up to the ultimate axial compressive strain (enhanced crushing strain), the maximum value of which is typically taken as 0.01 in accordance with ACI Committee 440 (2017). With a given axial strain and all material properties as well as the CFFT cross-sectional dimensions, the FRP shell hoop strain was estimated using Equation 2.1 and Equation 2.2. In Equation 2.2, the strain at peak stress ε_{c0} is calculated as $\varepsilon_{c0} = 9.37 \times 10^{-4} \sqrt[4]{f_{c0}}$ based on Teng et al. (2009). Once the FRP shell hoop strain was known, the confining pressure supplied by the FRP shell was determined using Equation 2.1, and the calculation of the concrete axial stress σc (illustrated in Figure 2-16) was a straightforward process using Equation 2.3 through Equation 2.6.

The effect of FRP confinement on the tensile strength of the concrete core in CFFT system has not been extensively investigated relative to the confined compressive strength. As a brittle material, the plain concrete is usually considered to have no tensile strength as assumed in the CFFT analytical and numerical investigations by Davol et al. (2001) and Dagher et al. (2012). This assumption is slightly conservative for analysis purposes and consistent with the ACI design recommendation of neglecting the tensile strength for members with a non-normal percentage of steel reinforcement (ACI Committee 318 2008). In a study of characterization and design of BCABs, Burgueño (1999) adopted an approximate linear stress-strain relationship for concrete in tension with a strength taken from the ACI recommendation for cracking strength and neglected the phenomenon of tension stiffening.

In the CFFT system, however, the tensile stress in the concrete core will not instantaneously drop to zero due to the presence of the FRP shell (Fam and Rizkalla (2002) and Son and Fam (2008)). Furthermore, Fam and Rizkalla (2002) found that the value of cracking strength of CFFTs is slightly higher than the value given by the ACI recommendation. Herein, the concrete in tension was treated as shown in Figure 3-3 with a modulus of rupture f_t calculated in accordance with the ACI equation as $f_t = 0.6.\sqrt{f'_{c0}}$ (ACI Committee 318 2014), and stress relaxation multiplier T_c of 0.6 as the default value (Son and Fam 2008). The FRP shell was treated as a linearly elastic material in both longitudinal and transverse (hoop) directions. Longitudinal and hoop elastic moduli and rupture strains were determined based on coupon tension tests as discussed later. Finally, full composite action was assumed between the FRP shell and the concrete interface, which is consistent with observed experimental behavior and design of the CFFT members (Dagher et al. 2012).

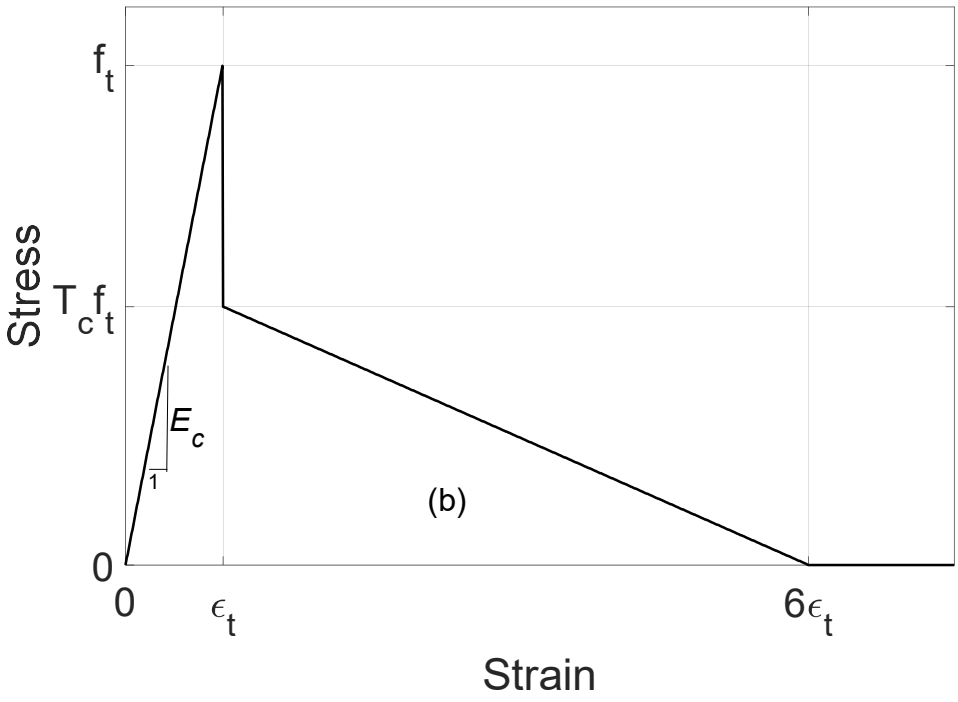

Figure 3-3. Concrete Stress-Stain Relationship in Tension

3.2.5 Nonlinear Solution Procedure

The FB method is very efficient for analyzing nonlinear structural problems because it strictly satisfies force equilibrium at the element level. However, one of its main drawbacks is the difficulty of numerical implementation, especially in general DB FE programs. In FB methods, the determination of element internal forces and deformations is not a straightforward procedure and requires an iterative method at the element level due to the interpolation of the unknown forces as well as the existence of lateral displacement in the interpolation function of those forces. Thus, an element state determination procedure is employed to determine the trial end forces calculated by the end displacements and then used for force interpolation.

Initially, however, the unknown end displacements need to be calculated at each global load increment using the corresponding global stiffness matrix. Therefore, using the FB elements in an incremental-iterative second-order nonlinear analysis requires a trial-and-error procedure which involves two levels of iteration: a global iteration for an incremental-iterative numerical solution (e.g., Newton-Raphson method, Arc-length method, or the Generalized-Displacement Control (GDC) method) as well as local iteration.

The GDC method proposed by Yang et al. (2007) was adopted in this study because of its robustness and effectiveness in solving nonlinear problems with multiple critical points. According to Leon et al. (2011), the GDC method has been used for large deflection analysis with complex nonlinear behavior because of its general numerical stability and efficiency compared with other nonlinear solution schemes (e.g., Load-Control, Displacement-Control, Arc-Length or Work-Control method). Furthermore, the GDC method considers the variation of the structural stiffness and an automatically reversed direction to determine the load increment.

The equilibrium equation for each iteration at any global incremental loading step is performed as in Equation 3.21.

$$\widehat{\mathbf{K}}_0 \Delta \mathbf{U} = \lambda \widehat{\mathbf{Q}} + \mathbf{R}_0 \qquad \text{Equation 3.21}$$

Here, $\widehat{\mathbf{K}}_0$ is the tangent system stiffness matrix from the previous converged state, $\Delta\mathbf{U}$ is the current displacement increment vector, $\widehat{\mathbf{Q}}$ is the total applied load vector, $\mathbf{R}_0$ is the unbalanced force vector from the previous converged state, and λ is the load increment parameter. Equation 3.21 can be decomposed into Equation 3.22 and Equation 3.23.

$$\widehat{\mathbf{K}}_0 \Delta \widehat{\mathbf{U}} = \widehat{\mathbf{Q}} \qquad \text{Equation 3.22}$$

$$\widehat{\mathbf{K}}_0 \Delta \overline{\mathbf{U}} = \mathbf{R}_0 \qquad \text{Equation 3.23}$$

The displacement increment vector $\Delta\mathbf{U}$ can be computed according to Equation 3.24.

$$\Delta \mathbf{U} = \lambda \Delta \widehat{\mathbf{U}} + \Delta \overline{\mathbf{U}} \qquad \text{Equation 3.24}$$

Moreover, the total displacements $\mathbf{U}$ and the corresponding external applied loads $\mathbf{Q}$ of the structure at the end of each iteration can be accumulated using Equation 3.25 and Equation 3.26.

$$\mathbf{U} = \Delta \mathbf{U} + \mathbf{U}_0 \qquad \text{Equation 3.25}$$

$$\mathbf{Q} = \lambda \widehat{\mathbf{Q}} + \mathbf{Q}_0 \qquad \text{Equation 3.26}$$

Here, $\mathbf{U}_0$ and $\mathbf{Q}_0$ are the vectors of total structure displacements and the corresponding total external applied loads from the previous converged state. The unknown load increment factor λ can be determined from a constraint condition based on Generalized Stiffness Parameter (GSP) as follows. For the first iteration step at any increment, λ is determined according to Equation 3.27, and for all other iterations using Equation 3.28 where $\lambda_1$is the first load increment and GSP is computed according to Equation 3.29.

$$\lambda = \lambda_1 \sqrt{|\mathrm{GSP}|} \qquad \text{Equation 3.27}$$

$$\lambda = (\Delta\widehat{\mathbf{U}}_0{}^T \Delta\overline{\mathbf{U}})/(\Delta\widehat{\mathbf{U}}_0{}^T \Delta\widehat{\mathbf{U}}) \quad \text{Equation 3.28}$$

$$\text{GSP} = (\Delta\widehat{\mathbf{U}}_1{}^T \Delta\widehat{\mathbf{U}}_1)/(\Delta\widehat{\mathbf{U}}_0{}^T \Delta\widehat{\mathbf{U}}) \quad \text{Equation 3.29}$$

In the above approach, $\Delta\widehat{\mathbf{U}}_0$ is the displacement increment generated by the reference load $\hat{\mathbf{F}}$ at the first global iteration of the previous incremental step, and $\Delta\widehat{\mathbf{U}}_1$ is the displacement increment generated by the reference load $\hat{\mathbf{F}}$ at the first global iteration of the first incremental step. $\Delta\widehat{\mathbf{U}}$ and $\Delta\overline{\mathbf{U}}$ are the displacement increments generated by the reference load and unbalanced force vectors, respectively. The simplified step-by-step algorithm of the GDC nonlinear iterative-incremental solver used in this study is detailed in Appendix B.

At each load step corresponding to the application of load increment, the global incremental end displacements $\Delta\widehat{\mathbf{D}}$ are extracted from the global displacement increment vector and total end displacements $\widehat{\mathbf{D}}$ are computed using Equation 3.30, where $\widehat{\mathbf{D}}_0$ is the total end element displacements from the previous converged state.

$$\widehat{\mathbf{D}} = \widehat{\mathbf{D}}_0 + \Delta\widehat{\mathbf{D}} \quad \text{Equation 3.30}$$

For each element in the structure, the element displacements $\mathbf{D}$ are obtained from the corotational formulation. At this step of corotational formulation computations, one can evaluate a 3x6 force transformation matrix $\mathbf{T}$ and three 6x6 matrices $\mathbf{G}_i$ $(i = 1,2,3)$ needed to calculate the element geometric stiffness matrix $\mathbf{K}_G{}^{ele}$, the element global forces $\widehat{\mathbf{P}}$, and the element global stiffness matrix $\widehat{\mathbf{K}}^{ele}$ as shown in Equation 3.31, Equation 3.32, and Equation 3.33, respectively. For further details on the formulation and derivation of the corotational formulation see de Souza (2000).

$$\mathbf{K}_G{}^{ele} = \sum_{i=1}^{3} \mathbf{G}_i P_i \quad \text{Equation 3.31}$$

$$\widehat{\mathbf{P}} = \mathbf{T}^{-1}\mathbf{P} \qquad \text{Equation 3.32}$$

$$\widehat{\mathbf{K}}^{ele} = \mathbf{T}^{T}\mathbf{K}^{ele}\mathbf{T} + \mathbf{K}_{G}{}^{ele} \qquad \text{Equation 3.33}$$

The element resisting force increments $\mathbf{\Delta P}$ are calculated by Equation 3.34 using the current element displacements, the element displacements from the previous iteration $\mathbf{D_0}$, and the previous element stiffness matrix $\mathbf{K_0^{ele}}$.

$$\mathbf{\Delta P} = \mathbf{K_0^{ele}}(\mathbf{D} - \mathbf{D_0}) \qquad \text{Equation 3.34}$$

The local iterative form of the element state determination for second-order nonlinear is required for each element. Before performing the main steps of the element state determination in the framework of the overall analysis, initial variables need to be stored for each element before any local iteration is performed based on the previous converged state. These initial variables include total end forces $\mathbf{P}_0$, force interpolation matrices $\mathbf{b}_0$, section forces $\mathbf{S}_0$, section stiffness matrices $\mathbf{k}_0^{sec}$ and section deformations $\mathbf{d}_0$. These quantities must be defined at all integration points. Iterations at the element level were performed such that the residual displacements fall below a specified tolerance within each global iteration. The simplified iterative procedure is accomplished following the state determination algorithm in accordance with Du et al. (2017) as presented in Appendix C.

3.3 Verification of Element Formulation

3.3.1 Distributed Plasticity Analysis of a Fixed-Fixed Beam

A 6.0 m-long W16x31 steel beam (Figure 3-4) was considered as a good candidate to verify the proposed FB element formulation. Similar models can be found in the literature and have been analytically and numerically investigated by others (see Du et al. (2017), for example). The fixed-end beam is fully braced against lateral torsional buckling and has a point load applied at 1.5 m from the left-hand support. For comparison, the analytical solution was also developed by employing a step-wise elastic approximation

accounting for plastic hinges at critical points. Using the basic beam mechanics formulas, the fixed-fixed beam was initially loaded up to the development of the initial plastic hinge at left-hand support (Figure 3-4a). Then, the resulting fixed-hinged beam was loaded until a new plastic hinge occurred under the point load, and finally, the beam was loaded to collapse when hinging occurred at the right-hand support.

Here, Young's modulus and yield stress of the steel were taken as 200 GPa and 345 MPa, respectively and the cross-section was taken as the I shape defined in Figure 3-4b. The equilibrium path obtained using the proposed force-based element is compared against the analytical equilibrium path (Figure 3-5). Four elements, each with four Gauss-Lobatto integration points, were used to discretize the beam. For the numerical integration, the I-section was discretized into 404 layers having an equal thickness of 1 mm using the exact depth of each web and flanges. The model showed robustness and high accuracy even when a coarse FE mesh is used. The elastic-plastic simulation results using the proposed element are in good agreement with the analytical solutions.

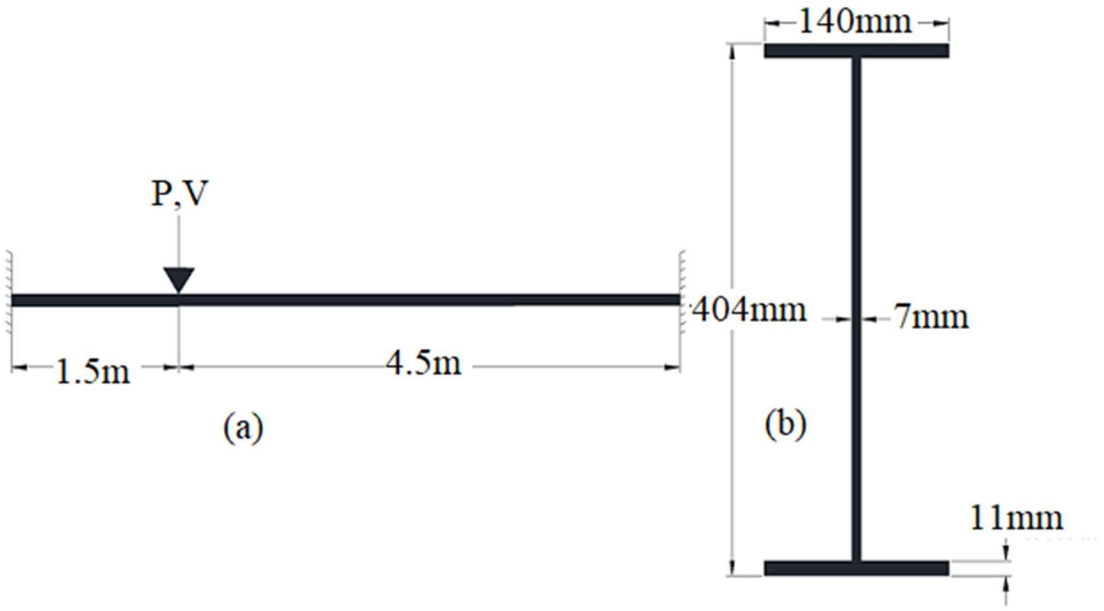

Figure 3-4. Fixed-Fixed Beam with Section Analyzed as Elastic-Plastic

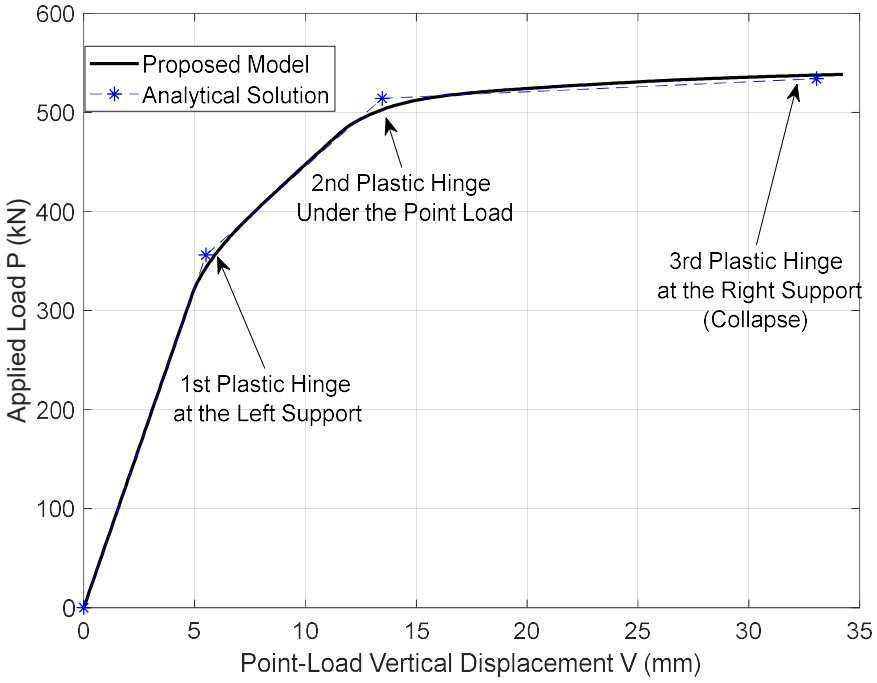

Figure 3-5. Equilibrium Bath for the Fixed-fixed Beam

3.3.2 Elastic Buckling of Columns

A single general pinned-pinned column subjected to an axial load P with very small eccentricity e (Figure 3-6) was analyzed using the proposed element to verify the ability and accuracy of the model to simulate large deformations. For generality and direct comparison with Euler buckling theory, an arbitrary elastic constant cross-section (A, I and E), with an arbitrary length (L) and e of $L/10^7$ were assumed in this analysis, where A, I, E are the cross-sectional area, moment of inertia and Young's modulus, respectively.

Generalized applied load (P/Pcr) vs. generalized axial shortening (V/Vcr) is plotted in Figure 3-7, where $Pcr = \pi^2 EI/L$ and $Vcr = PcrL/EA$ are the Euler buckling load and its corresponding axial shortening, respectively. The load deflection response is plotted for any slenderness ratio $\lambda = L/r$ where $r = \sqrt{I/A}$ is the radius of generation.

Generally speaking, the results predicted by the proposed force-based element agree well with the theoretical results and demonstrate the accuracy of the model for various magnitudes of slenderness ratio. It can be seen from Figure 3-7 that the elastic buckling load predicted by the FB elastic analysis is less than the classical Euler buckling load due to the influence of the load eccentricity.

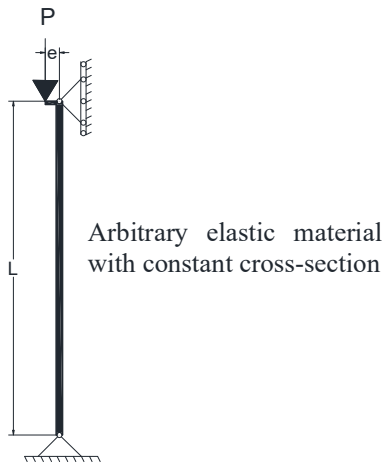

Figure 3-6. A Pinned-Pinned Column under Eccentric Axial load

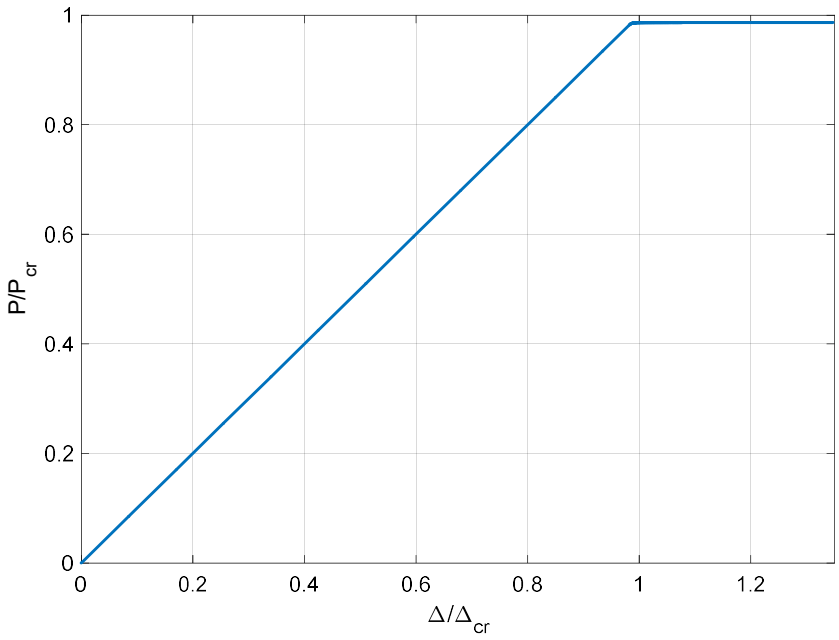

Figure 3-7. A Generalized Load-Deflection Curve for a General Pinned-Pinned Elastic Column

3.3.3 Elastic Postbuckling Analysis of a Circular Arch

The following example is presented to verify the capability of the proposed model to predict postbuckling behavior and large deformations as well as to verify the use of initially curved elements. A postbuckling elastic analysis of a pinned-pinned semi-circular arch has been studied by several researchers for different aims (Jafari et al. 2009; Li 2006; Yang et al. 2007; Yang and Shieh 1990). The arch shown in Figure 3-8 has a major diameter L of 254 mm, a moment of inertia of 416000 mm^4, Young's modulus of 1.38 MPa, and a cross-sectional area of 6452 mm^2.

The arch was represented by 16 circular-segment elements of equal length. A point load was applied at the apex with an eccentricity e of 80 mm (Figure 3-8) to investigate the post-buckling of that arch. The load-deflection curve has been plotted in Figure 3-9 for the imperfect loading. The figure shows that the buckling and postbuckling behavior of this arch is quite complicated, and there exist several snap-back points and multiple loops. At the snap-back points, these load-deflection curves are in a good agreement with the result obtained by Li (2006), who used 25, three-noded beam elements and an isoparametric, mixed element formulation. This simulation verifies the ability of the proposed curved FB element to predict large displacements and rotations.

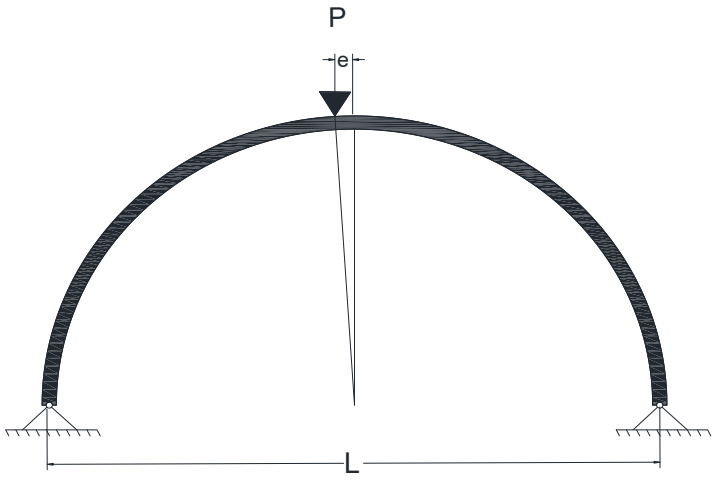

Figure 3-8. Hinged Deep Circular Arch

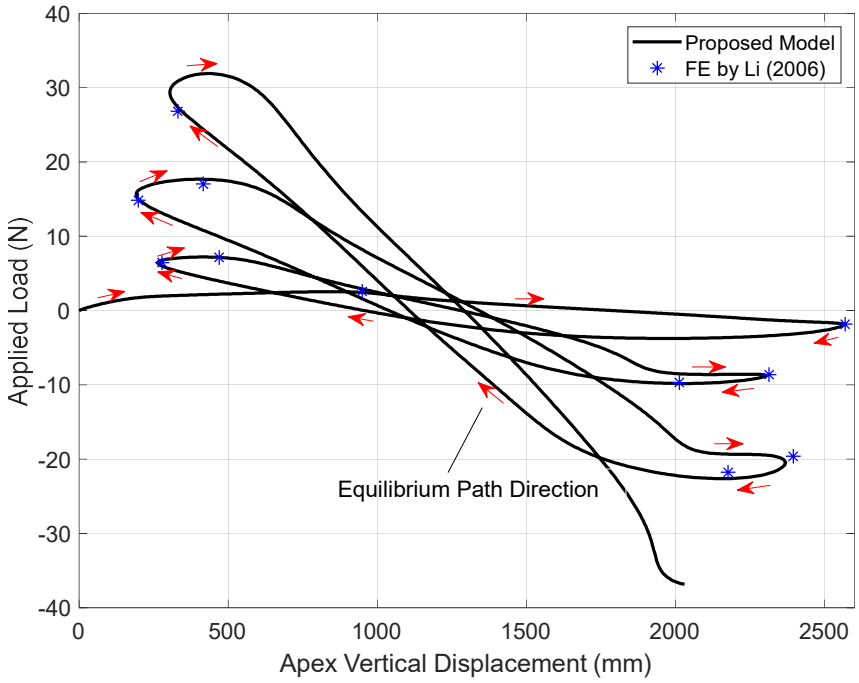

Figure 3-9. Response of the Arch under Eccentric Point Load

3.4 Analysis of CFFT Arches and Beams

An important step in the development of the FB FE analysis for CFFT arches is a comparison with laboratory tests and previously validated analysis techniques due to the complexity of the constitutive response of the confined concrete core and hybrid nature of the arch. In this section, the FB modeling techniques developed in this study are applied to the analysis of two fixed-fixed isolated subscales CFFT arches having the same span length but different rises. In addition, full-scale CFFT arches investigated by Dagher et al. (2012) are modeled using the proposed FB. The models were computationally efficient, relying on a small number of elements and integration points, but proved accurate. In the following analysis, a particular thickness for the section layers is chosen to use a minimum number of layers and to discretize the exact thickness each of the FRP tube and concrete core. Based on a mesh convergence study conducted for the pinned-pinned CFFT arches, the following CFFT arches were meshed with 10 elements per half of the structure and 5 integration points per element.

3.4.1 Laboratory Tests of CFFT arches of Walton (2015)

The load-deformation and load-strain response of two subscale CFFT arches subjected to a central point load were experimentally assessed. Circular segment CFFT arches with spans of 6.1 m and span-to-rise ratios of 5:1 and 8:3 were manufactured and prepared for test specimens in this research. The specimens are referred to as the short arch (1.22-m rise) and tall arch (2.29-m rise). The specimens had an FRP shell with a nominal diameter of 110 mm and a total thickness of 2 mm fabricated from two layers of braided E-glass fiber with an inner layer bias angle of ± 81° and an outer layer bias angle of ± 21°. The braid bias angle is measured relative to the longitudinal axis of the tube; the inner layer with a larger bias angle largely provides shear and confinement reinforcing, and the outer layer provides longitudinal tension reinforcing. The arches were infused with Derakane 610C resin from two ports located at the apex. The infused FRP shell had experimentally determined moduli of 13.8 GPa in the longitudinal direction and 19.4 GPa in the hoop direction, and tensile strengths of 313 MPa longitudinally and 374 MPa in the hoop direction. The coupon-level FRP strength and stiffness characterization were carried out by Walton (2015) and followed the procedures outlined by Bannon (2009) and Demkowicz (2011) based on ASTM D3039 (2008).

The FRP arch tubes were positioned upside down in custom wooden trusses which fully supported the arches while being filled with self-consolidating concrete from the arch ends. The arch specimens were filled with an expansive concrete mix of a nominal compressive design strength of 34.5 MPa. The tall arches and short arches were cast separately along with other specimens used for evaluating SSI of subscale buried arch bridge tests by Walton et al. (2016a). The truss formwork was also used to fully support the filled arches when they were flipped upright and cast into concrete foundations. The arches were cast into 1.52 m wide, 0.91 m long, and 0.46 m deep footings that were fixed to the facility reaction floor to provide full moment restraint at the arch ends.

Figure 3-10 shows the arch test setup. During testing, the arch footings were tied to the concrete floor of the laboratory with four 19 mm diameter rods and further braced against the out-of-plane

movement. Three groups of Omega 12.7 mm foil SGs were installed at 200 mm from the apex and both shoulders to measure bending and axial strains. At each cross-section, SGs were installed at the top, mid-height and bottom, which are referred to as SG_{top}, SG_{mid}, and SG_{bot}, respectively (Figure 3-10). The SG_{mid} was used to verify the assumption of a linear strain distribution through the depth. Deflections were measured vertically at the apex and shoulders and horizontally at shoulders. For the tall arch, vertical displacements were measured with +/-127 mm LVDTs, and the horizontal displacements were measured with 635 mm string potentiometers. The short arch had Celesco SP2 string potentiometers for all five displacements. Both arches were loaded in deflection control at a rate of 12.7 mm/min. A 100 kN load cell was used to measure the applied load on the tall arch, and a 50 kN load cell was used for the short arch. Wooden saddles were used to apply loads produced by the hydraulic actuator. Transverse bracing faced with low-friction plastic was located at the third points of the span to prevent out-of-plane deflections. Figure 3-11 shows a photo of the tests.

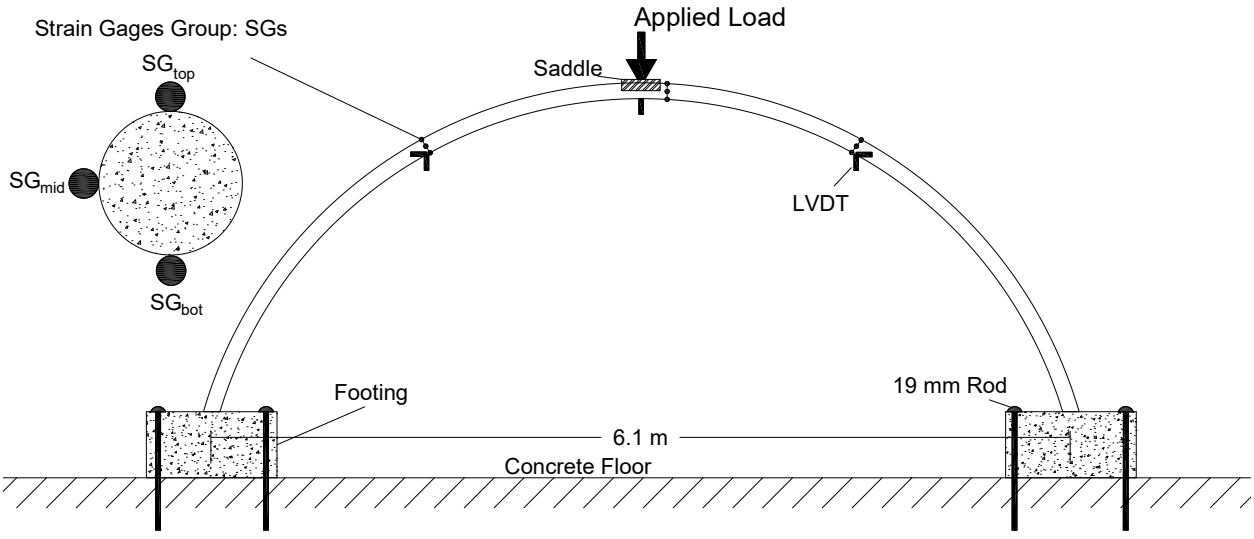

Figure 3-10. Arch Test Setup

Figure 3-11. Photo of Arch in Test Device

3.4.2 Arch test results

Both arches failed by a sudden tensile rupture of the FRP shell with significant crushing of the concrete occurring at the apex as shown in Figure 3-12. The capacity of the short arch was 15.55 kN, and the capacity of the tall arch was 12.15 kN. The maximum tensile strain in the FRP measured by tension gage SG_{bot} of the apex at peak load for the short arch was 1.27%. The tension gage SG_{bot} at the apex of the tall arch went out of range prior to ultimate load, and measured strain at failure was not available. However, the maximum failure tensile strain of 1.14% was estimated based on the linear strain distribution through the depth using readings from the remaining gages SG_{top} and SG_{mid} at failure. Figure 3-13 shows experimentally measured strains at the apex of the tall arch at loads of 4 kN, 6 kN, 8 kN, and failure; also shown are the best-fit linear strain distributions based on these measured values.

The load-deflection response at the apex of each arch gives a visual representation of the stiffness and strength as illustrated in Figure 3-14 and Figure 3-15 for short and tall arches, respectively. It is obvious

that the short arch is stiffer than the tall arch. Figure 3-16 through Figure 3-19 show the measured strains plotted against the apex applied load at the apex and shoulders of both arch specimens.

3.4.3 Model Predictions of Tested CFFT Arches

Each arch was simulated with clamped ends and a point load applied at the apex using the FB element formulation detailed previously. The model was run using 10 elements per half of the structure. For each element, 5 Gauss-Lobatto integration points were used with 114 layers (1 mm thick each) used to discretize the cross-section. The effect of FRP-confinement on concrete was implemented using the model presented in Section 3.2.4. The model-predicted load-deflection responses with and without considering the effect of confinement are plotted with the experimentally-determined responses shown in Figure 3-14 and Figure 3-15. The model-predicted load-strain responses are shown in. Figure 3-16 through Figure 3-19.

Taking advantage of the GDC solver used in this study, the proposed FB model explicitly predicts the failure loads corresponding to longitudinal tensile rupture strains measured at the FRP shell tension face of the apex. After rupture of the FRP shell, a singular stiffness matrix occurs at the apex cross-section along with crushing and cracking of the concrete. The model-predicted failure load for the short arch 17.1 kN, which exceeds the experimental value by 10%. For the tall arch, the model-predicted failure load was 12.4 kN, which is 2% higher than the experimentally measured failure load. While the model predicted arch capacities reasonably accurately, displacements were under-predicted for the short arch by 4.5% at failure and over-predicted by 26% for the tall arch at failure. Neglecting FRP confinement of the concrete core had an insignificant effect on arch stiffness but did reduce the predicted failure load by 10% for the short arch and 7% for the tall arch (Figure 3-14 and Figure 3-15). The importance of accurately modeling that confinement is more clearly demonstrated by the low failure load and low ductility predicted by the unconfined analysis of the full-scale CFFT arches analyzed in the next section. The model was able to accurately predict the strain at the apex and shoulders of both arches for different loading increments before and after the cracking of concrete (Figure 3-16 through Figure 3-19).

Figure 3-12. Apex Failure Mode

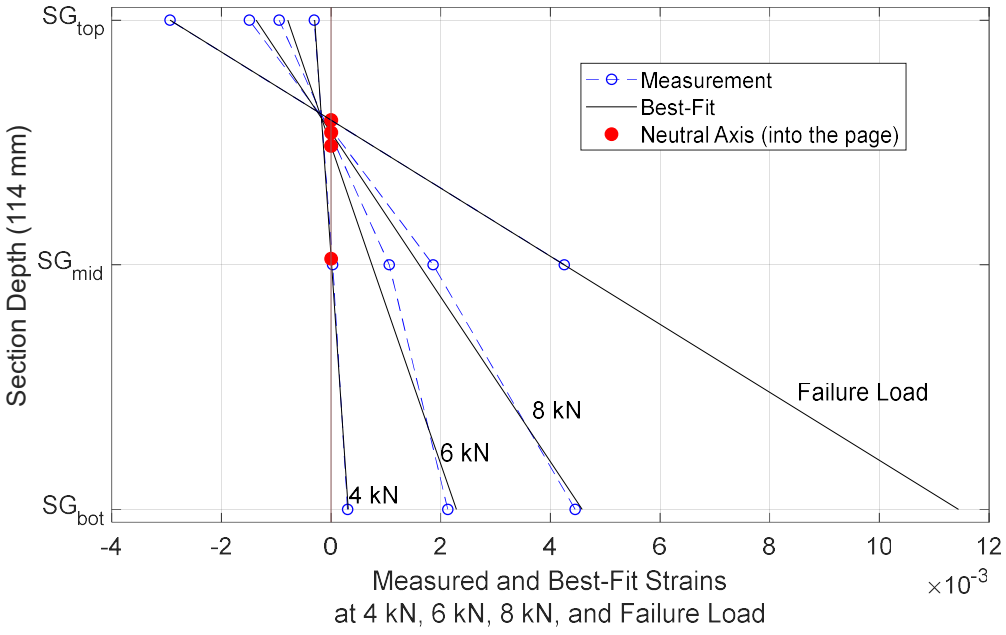

Figure 3-13. Tall Arch: Apex Cross-Sectional Strain-Profile

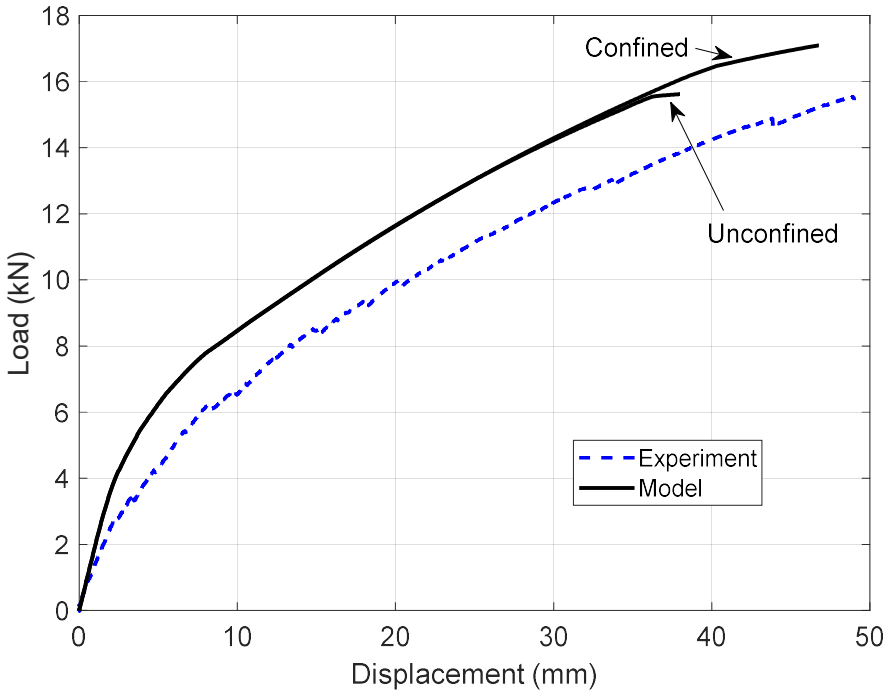

Figure 3-14. Short Arch: Load-Deflection Response at the Apex

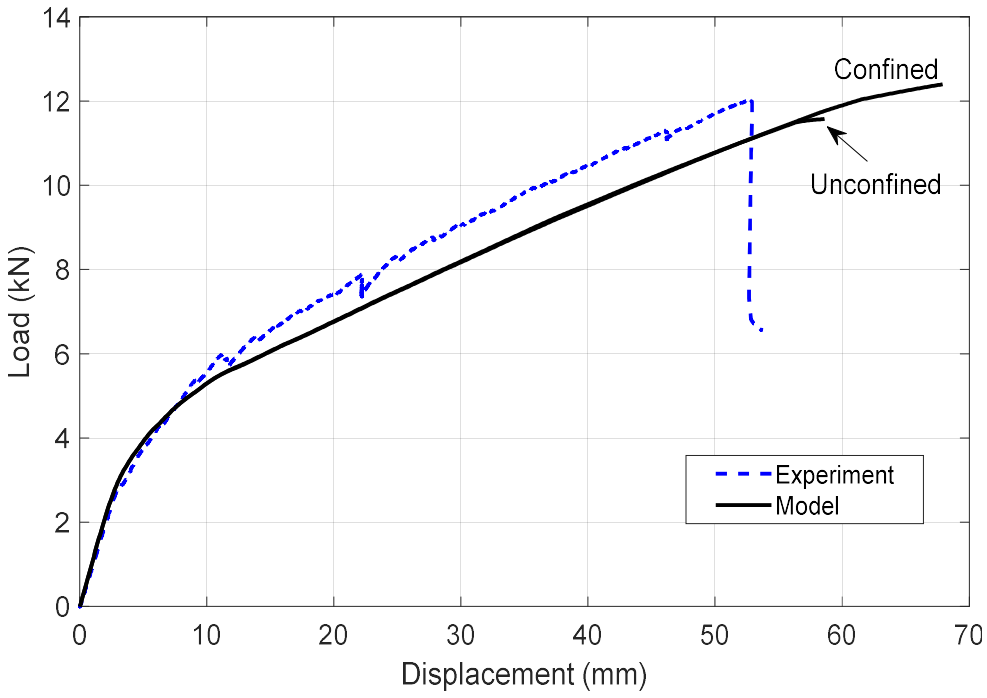

Figure 3-15. Tall Arch: Load-Deflection Response at the Apex

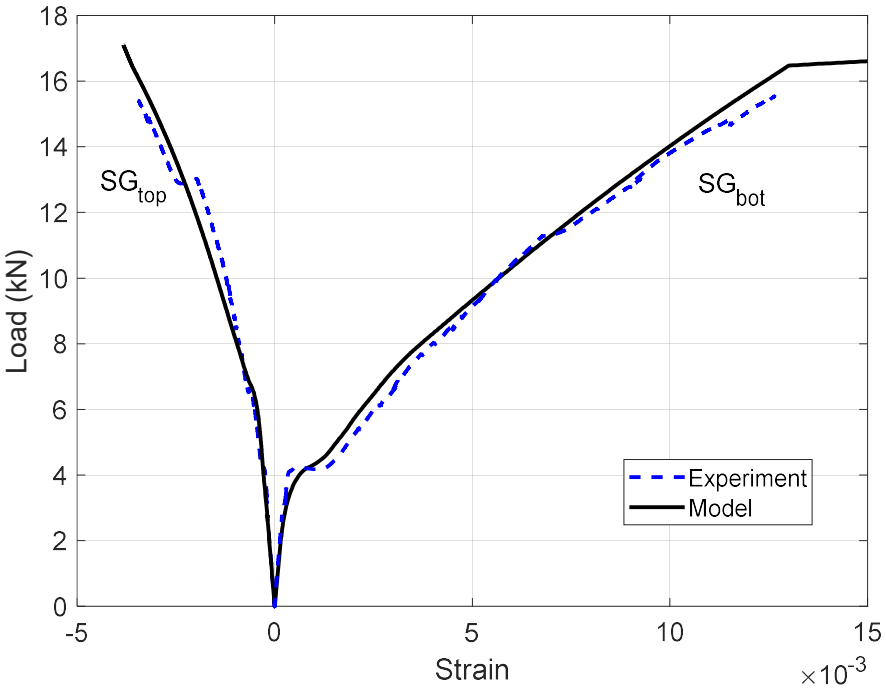

Figure 3-16. Short Arch: Load-Strain Response at the Apex

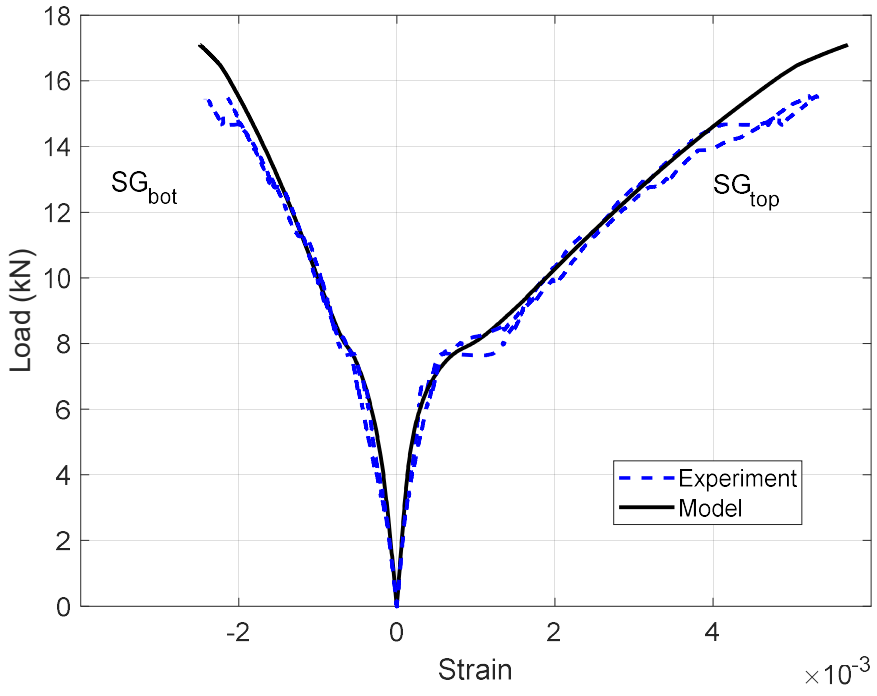

Figure 3-17. Short Arch: Load-Strain Response at the Shoulders

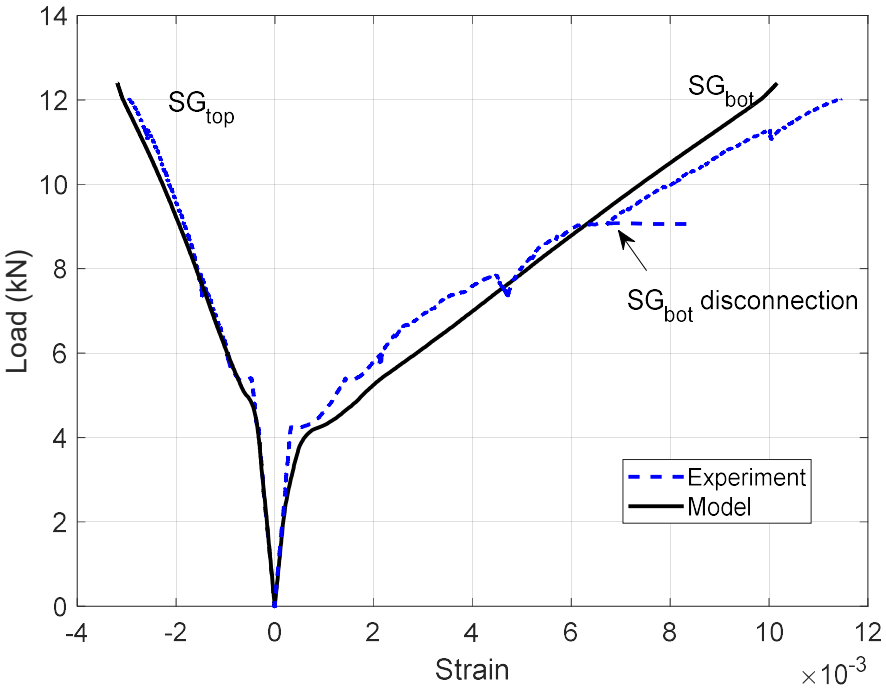

Figure 3-18. Tall Arch: Load-Strain Response at the Apex

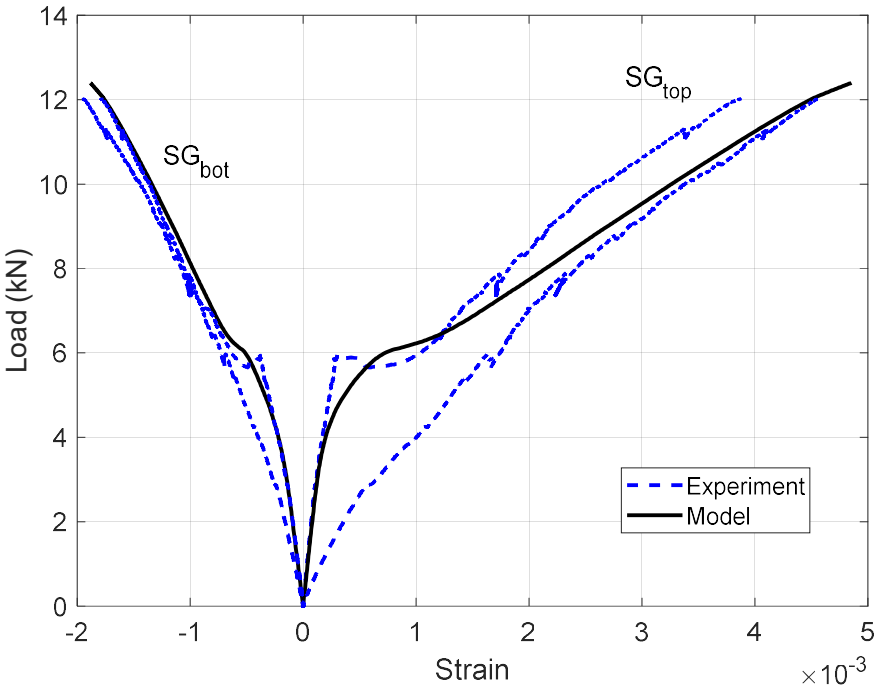

Figure 3-19. Tall Arch: Load-Strain Response at the Shoulders

3.4.4 Simulation of Pinned-Pinned CFFT Arches of Dagher et al. (2012)

The response of four identical CFFT arches tested by Dagher et al. (2012) was simulated to further validate the proposed model. These arches differ significantly from those detailed previously with different braid angles, a much smaller ratio of span to cross-sectional diameter, and different boundary conditions. Each arch specimen had a nominal diameter of 300 mm, a constant radius of 3.96 m, a span of 6.71 m, and a 28-day compressive strength f_c' of 27 MPa based on cylinder tests. The hybrid FRP shell was fabricated with a total wall thickness of 2.5 mm, a longitudinal elastic tensile modulus of 42.7 GPa, and a transverse modulus of 14.3 GPa. The arches were cast in reinforced concrete footings that were detailed as pinned connections. A single load was applied vertically downward at the arch apex. The arches failed at the apex, the location of maximum moment, which resulted in a hinge at that location. The load-deflection response for the arch apex and the load-curvature response for a section 457 mm from the apex are plotted up to failure in Figure 3-20 and Figure 3-21, respectively.

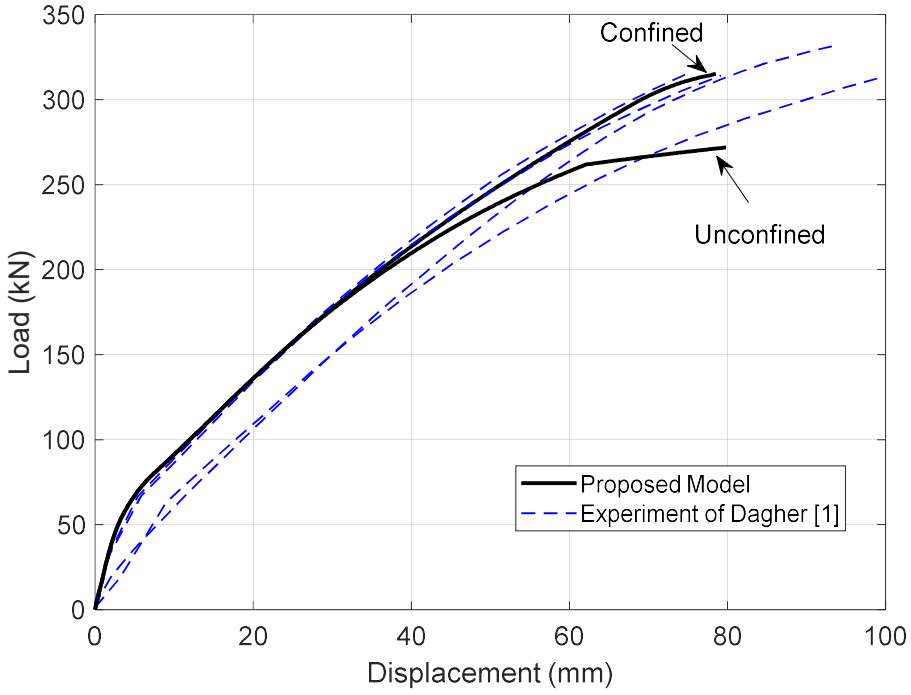

Figure 3-20. Pinned-Pinned Arch: Load-Deflection Response at the Apex

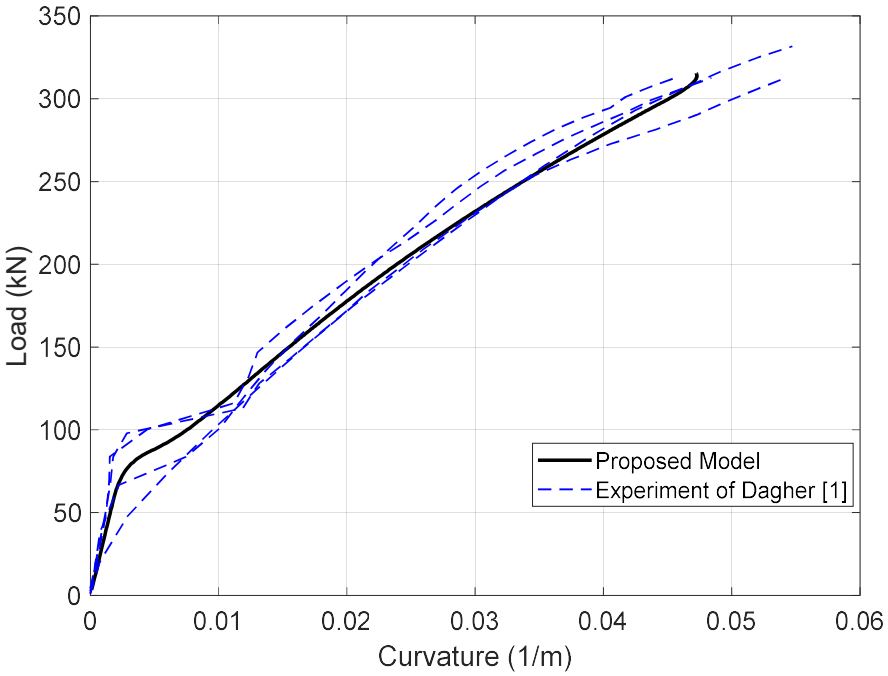

Figure 3-21. Pinned-Pinned Arch: Load-Curvature Response 457 mm away from the Apex

The predicted load-deflection response is also illustrated in Figure 3-20 for comparison. The model was run using ten curved elements per half of the structure and one rigid link (high stiffness element) to simulate the footing mechanism. For each element, 5 Gauss-Lobatto integration points were used with 244 layers used to discretize the cross-section (1.25 mm thick each). The effect of FRP-confinement on concrete was implemented using the model presented in Section 3.2.4. The predicted load-deflection response using the proposed model without considering the effect of confinement is also illustrated in Figure 3-20 to demonstrate the significance of confinement. The predicted load-curvature from the proposed model is plotted versus the experimental load-curvature response reported by Dagher et al. (2012) as shown in Figure 3-21. The proposed FB model explicitly predicts the failure loads corresponding to longitudinal tensile rupture of the FRP shell at the tension face of the apex at an FRP strain of 0.017, the value experimentally determined from coupon tests of this braid as reported by Dagher et al. (2012). After rupture of the FRP shell, a singular stiffness matrix occurs at the apex cross-section along with crushing and cracking of the concrete (Figure 3-22a). The predicted applied loads, corresponding to the experimentally observed apex

failure mode shown in Figure 3-22b, are 315.1 and 261.5 kN for the analyses with and without confinement, respectively. The predicted maximum load accounting for concrete confinement was within 1.5% of the average failure load of 320 kN reported Dagher et al. (2012). The importance of accurately modeling confinement of the concrete core is demonstrated by the low failure load of 261.5 kN predicted by the unconfined analysis.

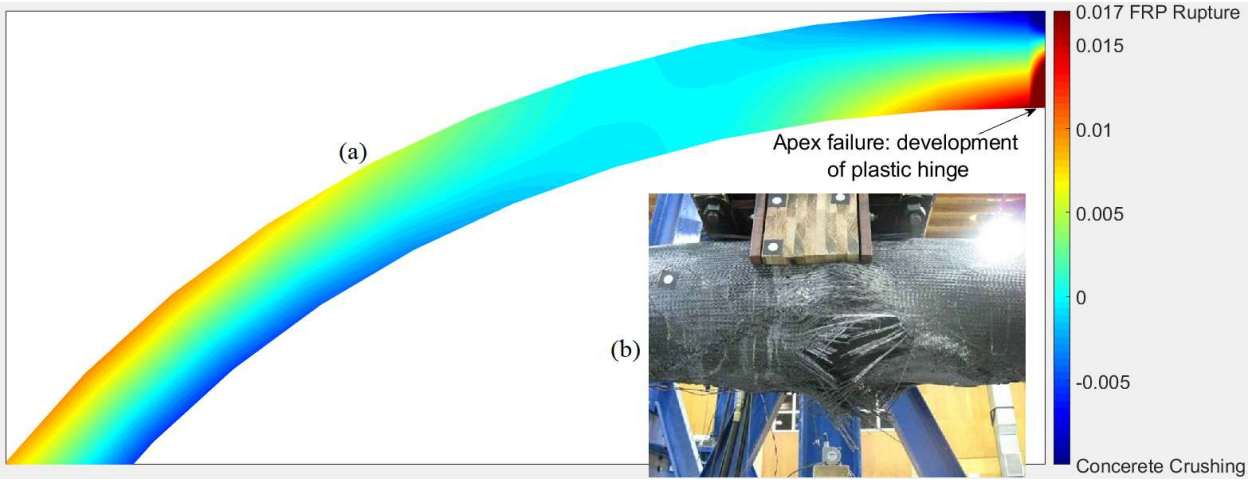

Figure 3-22. Pinned-Pinned Arch: Development of a Plastic-Hinge at the Apex

(a) Model-Predicted Strains at the Failure Load, (b) Typical Apex Failure (Dagher et al. 2012)

3.4.5 Simulation of CFFT Beams of Dagher et al (2012)

The response of three identical CFFT beams tested by Dagher et al. (2012) was simulated to further validate the proposed model. These straight beams of an overall length of 3.96 m had the same FRP-shell materials, properties, and dimensions as did the arches described in Section 3.4.4, and were filled with concrete with a 41 MPa compressive strength based on tests of 150 mm diameter cylinders. The specimens were tested in a four-point bending configuration such that the centerline of length 3.66 m was divided into three equal lengths using wood saddles for support and load application. The beams failed via tensile rupture of the FRP shell within the middle third of the span. The load-deflection response for mid-span and the load-strain response for a section 305 mm from mid-span are plotted up to failure in Figure 3-23 and Figure 3-24, respectively.

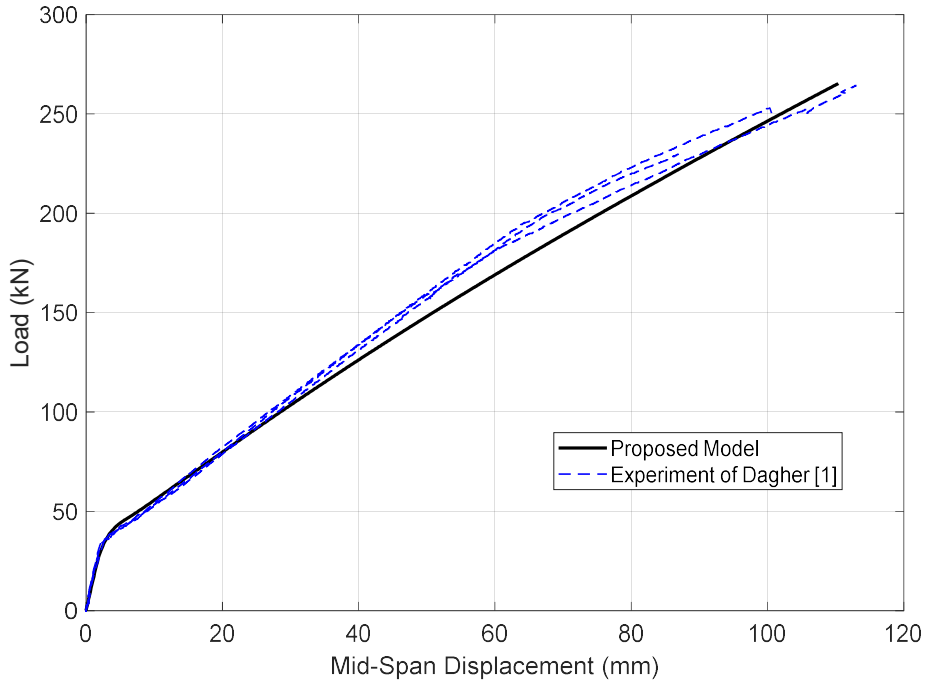

Figure 3-23. Beam: Mid-Span Load-Deflection Response

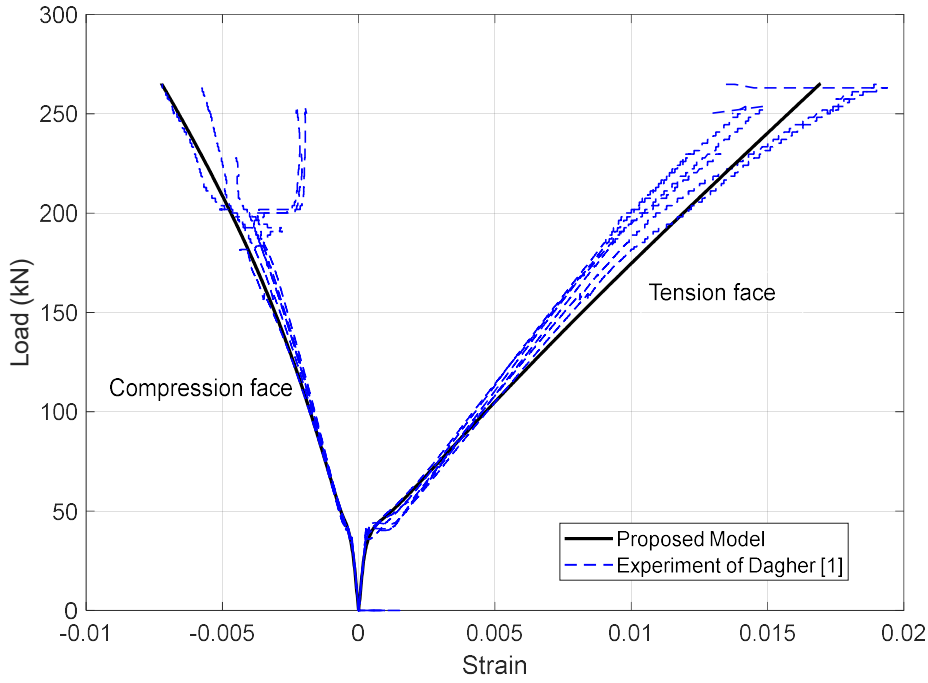

Figure 3-24. Beam: 305 mm away from Mid-Span Load-Strain Response

The predicted load-deflection response is also illustrated in Figure 3-23 for comparison. The model was run using 14 straight elements per half of the structure as illustrated in Figure 3-25a. For each element, five Gauss-Lobatto integration points were used with 244, 1.25 mm layers used to discretize the cross-section. The load-strain response predicted by the model is plotted versus the experimental load-strain response reported by Dagher et al. (2012) in Figure 3-24. The proposed FB model explicitly predicts the failure loads corresponding to longitudinal tensile rupture of the FRP shell within the middle third of the span at an FRP strain of 0.017, the value experimentally determined from coupon tests of this braid as reported by Dagher et al. (2012). The predicted applied load corresponding to the experimentally observed mid-span failure mode shown in Figure 3-25b is 265.4 kN. The predicted maximum load was 5.9% greater than the average failure load of 251.0 kN reported by Dagher et al. (2012) with a standard deviation of 17.35 kN and coefficient of variation of 6.91%. The predicted strain on the tension face at 305-mm section away from the mid-span is 0.0169, which is 9% greater than the average peak tensile strain of 0.0155 measured by the tension-face gauges (Dagher et al. 2012).

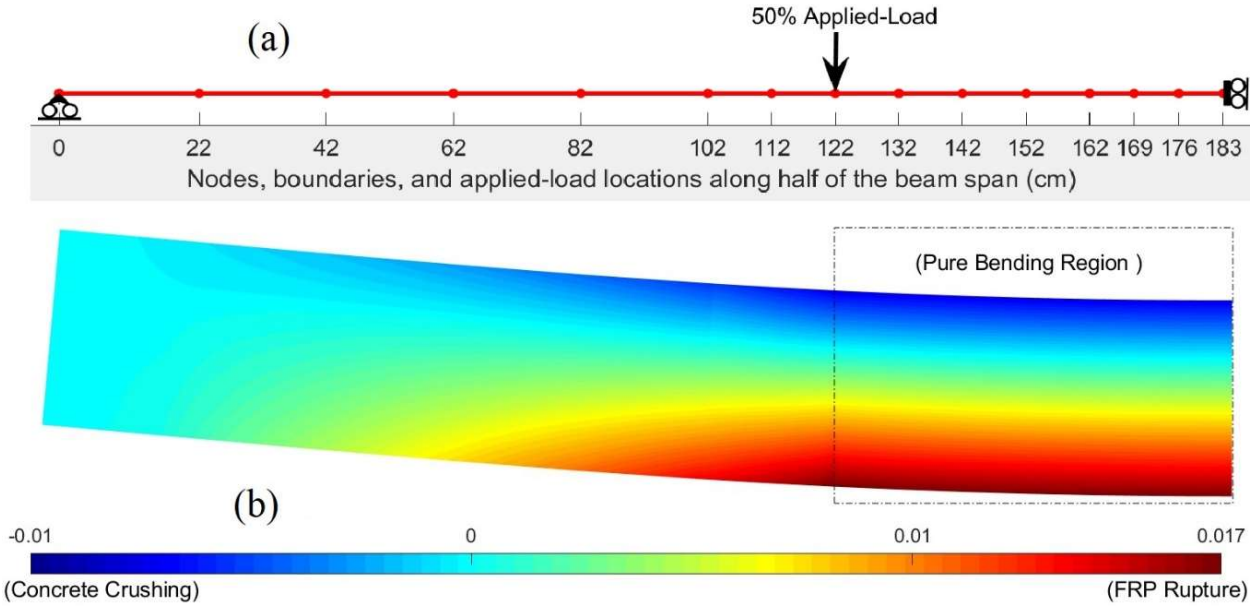

Figure 3-25. Beam: (a) Schematic of FE Model, (b) Strain Profile Corresponding to Maximum Load

3.5 Summary

A computationally efficient, second-order, inelastic FE simulation procedure for the analysis of CFFT arches and beams has been developed. The model uses a curved, planar, layered-frame FB element employing the corotational formulation to address geometric nonlinearity, and a layered-section discretization and distributed plasticity technique to capture material nonlinearity. Second-order effects at the section level and the curvature of the CFFT arch (as initial bowing) are incorporated using a nonlinear force interpolation that strictly satisfies equilibrium in the deformed shape. An FRP-confined concrete compressive stress-strain model that explicitly considers the effect of dilation of the concrete core and confinement provided by the FRP tube, and a bilinear concrete tensile stress-strain that considering the tension stiffening phenomenon and after-cracking concrete relaxation, have been implemented. A full nonlinear FE procedure using the GDC method as a robust and effective incremental-iterative global solver and the element state determination as a trial-and-error iterative local algorithm is outlined.

Following the FB element formulation and the FE nonlinear solution strategy, the implementation was verified by carrying out an elastic-plastic analysis of a beam and an elastic post-buckling analysis of a circular arch. Bending tests were performed on CFFT arches to compare their behavior with the proposed model predictions. Additional comparisons are made with other CFFT beam and arch bending tests available in the literature. The model accurately predicts the load-carrying capacity and ductility of the tested CFFT arches and beams. The model is able to capture the collapse mechanism due to FRP rupture and concrete crushing at the apex of the arches. The model results demonstrate the effect of confinement on the ductility of CFFT arches and beams.

The main contribution of this chapter is the combination and implementation of existing modeling tools into a robust, nonlinear frame finite-element and associate solution strategy that enable engineers to model the mechanical behavior of CFFT arches in an accurate and computationally efficient fashion. While the research reported here represents an important step in the development of a FB analysis and design tool

for CFFT arches, additional developments will be required to extend the FB formulation into a design tool for BCABs. Specifically, an extension of the FB formulation to model more general 3D CFFT framed structures and methods to accurately capture SSI arising from the staged backfilling and the progressive change in soil restraint with increasing deformation and overburden stresses are required. Progressive multistage simulations will also be necessary to capture the effect of alternating stages of soil backfilling as well as the effect of the application of surface live loads.

CHAPTER 4

3D SIMULATION OF SKEWED, BURIED, COMPOSITE ARCH BRIDGES INCORPORATING SSI

4.1 Introduction

The United States has 615,002 bridges, of which 8.9% are considered structurally deficient (FHWA 2018). In the State of Maine, there are 2,458 bridges, of which 13.3% are structurally deficient, and over 200 bridges have been built between 2008-2018 (ARTBA 2018). About half of these bridges are classified as skewed. As national infrastructure facilities, these bridges are experiencing rapid deterioration as they age. The growth in the maintenance, repair, or replacement of old bridges and construction of new bridges calls structural engineers' attention to exploring new materials and bridge types. The high performance, durable, and cost-effective buried composite arch bridge (BCAB) has become an attractive alternative, especially for short-span bridges with spans under 20 m in aggressive environments. The bridge superstructure can be rapidly constructed and shows promise as an integral part of the national railway and highway network. The American Association of State Highway and Transportation Officials (AASHTO) (2012) has published guidelines for the design of the CFFTs as the main structural components of BCABs.

Over 60% of the constructed BCABs have been skewed to some extent. Site inspection and monitoring were carried out on some bridges under service load (Goslin et al. 2015). Figure 4-1 shows a completed BCAB having 11-m span, 3.7-m rise, 17.7-m width, and 56^{o}-skew angle in Lagrange, Maine, USA, which is considered as one of the largest skewed arch bridge in the world (AIT 2019; MaineDOT 2018). Researchers initially focused on understanding the responses of standalone components of BCABs by investigating the structural capacity of CFFT beams and arches of different scales and configurations (Dagher et al. 2012), material constituent durability (Demkowicz 2011), and the effect of concrete filling on the FRP wall local buckling (Walton 2011). The structural design of spliced CFFT was also investigated by Parry (2013) and Burns (2016) to ease shipping of long-span CFFT arches. Wang et al. (2019)

investigated the dynamic responses under blast loading of four scaled CFFT arches with different FRP strengthening ratios and concrete strength.

Figure 4-1. B&A Overhead Bridge in Lagrange, Maine, USA (consists of 13 CFFTs)

However, improvements in structural analysis procedures for the BCAB is warranted due to the soil embedment around the superstructure that both loads the arches and provides additional structural support. Following the earlier research on standalone components of BCABs, Walton et al. (2016a) investigated soil-structure interaction (SSI) in BCABs through laboratory testing of subscale buried steel arch bridges. The authors experimentally evaluated the response of soil backfilling of two buried steel arch bridges of the same geometry. Walton et al. (2016b) also developed a nonlinear soil-spring model to investigate SSI numerically and predict the bending moments during backfilling and service live loads. A structure consisting of a single arch with a tributary width of soil equal to the arch spacing is modeled with conventional displacement-based (DB) 2-noded 2D Euler beams and horizontal axial spring elements that represent soil. While effective and innovative in its treatment of SSI and construction sequence, the model of Walton et al. (2016b) requires a high mesh density to adequately predict the response of the arch system

during backfilling and apex loadings. Moreover, the model accuracy decreased when the 2D arch was subjected to loads offset from the arch apex. Furthermore, the conventional 2D DB model does not rigorously couple axial and bending effects and cannot account for abutment skew angle. Skew may increase flexural demands on the arches, influence SSI, and reduce the load carrying capacity of the bridge. Further, the FRP decking that is placed over the arches and supports the soil acts as a diaphragm. This decking is mechanically fastened to the arches, and in a skewed bridge, these fasteners may be subject to increased shear forces that are not currently considered in the design of BCABs. Consequently, a 3D FE numerical code is required to analyze the behavior of skewed BCABs while considering the actual 3D geometry of the bridges and the effect of the soil backfill. Such numerical procedures need to provide useful information and guidance to BCABs design engineers and can also help establish rational methods of load rating.

This chapter documents the third research contribution of this dissertation. The main objective is to present a computationally efficient structural analysis technique using a newly-developed FE model to analyze an entire BCAB while accounting for abutment skew. The model consists of two types of elements that capture complexities in the structural response arising from the nonlinear behavior of the CFFT arches, the SSI, and transversal effects induced by geometry and load eccentricity in skewed BCABs. The first element is a spatial, co-rotational, flexibility-based (FB), fiber-frame element employed to discretize each of the arches, decking and foundation elements. The third chapter of this dissertation showed the superiority and efficiency of the FB element for the analysis of CFFT arches that helps resolve unique modeling challenges due to the effect of confinement of the concrete core on its stiffness and ductility as well as the importance of large deformations. The second element is a soil-spring element used to idealize the soil with a series of one-dimensional, nonlinear, axial-only springs. All required code was written using MATLAB programming environment (MathWorks Inc 2018), including an FRP-confined concrete compressive stress-strain model and a bilinear concrete tensile stress-strain as well as the nonlinear SSI model based on a recent displacement-dependent lateral earth pressure model. The FE procedures also simulate the staged

backfilling process. This study investigates for the first time the effects of skew angle on BCAB load capacity. The analysis is initially verified by comparison with results measured during laboratory tests of straight (no skew) buried steel arch bridges found in the literature. A parametric study is then conducted using a generic two-lane BCAB of 12 m span and 9 m width shown in Figure 4-2 to investigate the effect of bridge skew on the capacity of the bridge. Case studies of 10°, 20°, 30°, 40°, and 50° skew angles were carried out using AASHTO HL-93 design truck loading distributed through the soil. Critical positions of trucks along the bridge were chosen to produce maximum bending in the arches.

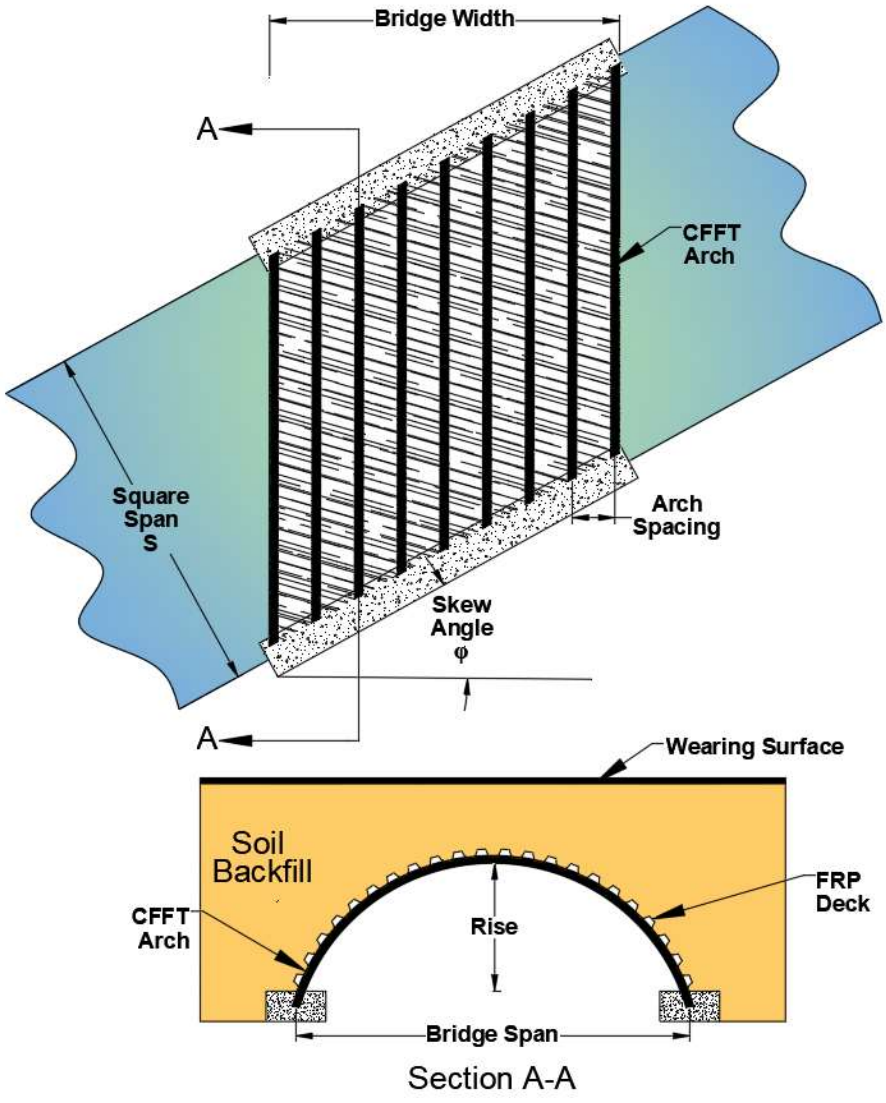

Figure 4-2. Description of Skewed BCAB

4.2 Development of Analysis Methodology

A methodology for performing a combination of spatial FB and one-dimensional soil-spring FE analysis on an entire skewed BCAB considering the effect of the nonlinear response of the CFFT and effects induced by geometry and load eccentricity is presented. Figure 4-3 shows a generic dimensionless BCAB schematic of a coarse mesh illustrating the model in the global coordinate system (X,Y,Z). The FB element geometry within the corotational framework and element state-determination process are discussed. Incorporating a series of soil-spring elements connected to the nodes is detailed. Implementation procedures of multistage backfilling simulation and AASHTO HL-93 design load applications are discussed.

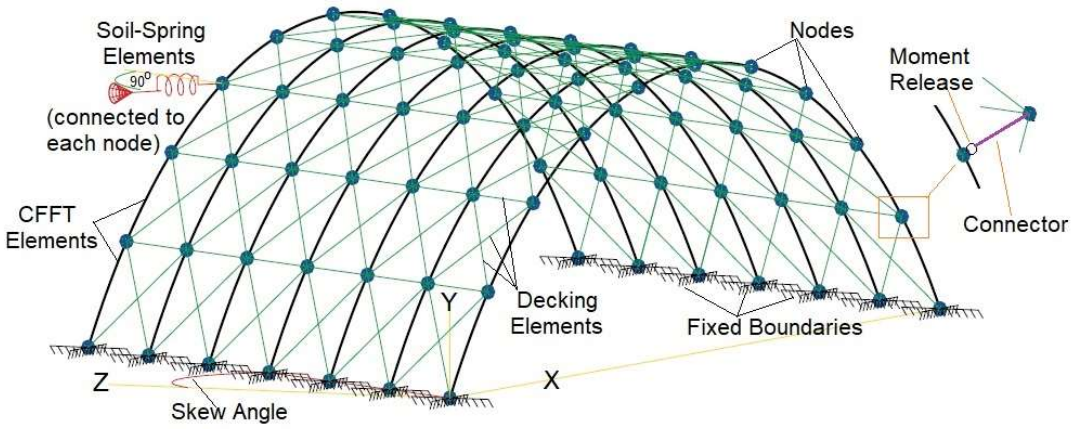

Figure 4-3. 3D Scheme of FE Model of BCAB including the Soil-Spring Element

The CFFT arches are represented using second-order nonlinear FB elements given an FRP-confined concrete stress-strain model that explicitly considers the effect of dilation of the concrete core and confinement provided by the FRP tube as summarized in Chapter 3 of this dissertation. The model also implements a bilinear concrete tensile stress-strain that considers the tension stiffening phenomenon and after-cracking concrete relaxation. The FRP decking diaphragm is implemented using a second-order linear elastic FB element that spans continuously in the transverse and diagonal directions. The diagonal bracing members have zero material density and are used to model diaphragm shear resistance that may have significant effects in the case of skewed BCAB. The decking elements are connected to the arch nodes with

beam elements to represent the fasteners (connectors). It is important to note that, in a real BCAB structure, these connecters are placed at discrete points wherever there is contact between the bottom side of the corrugated FRP deck and the top of the CFFT arches. To represent these connectors, a second set of nodes offset from the first set of nodes shown in Figure 4-3 is created with a specified distance to simulate the offset of the decking relative to the center of gravity of the arches. Each pair of offset nodes is connected with a rigid element having a moment release at the arch as detailed in Figure 4-3. In the proposed model, however, the number of connector elements is mesh-dependent because connections are placed at each arch node. Furthermore, any additional friction forces at the deck-to arch interfaces are not considered in this model, and these forces may be significant. The main function of the deck is to distribute soil load, dead load and live load to the arches. The soil-spring elements are connected to the deck elements and are activated during the staged backfill loading.

The BCAB loading simulation proceeds in steps: self-weight and soil backfilling loads, wearing surface load, and the subsequent application of AASHTO HL-93 design loads including impact. Since the principle of superposition is not applicable in the analyses due to the nonlinear response of the constituent materials, analysis of each loading step analysis must begin from the point at which the previous step was completed. The code was written specifically for simulations reported herein using MATLAB. Each loading stage was solved nonlinearly using the GDC solver discussed in Section 3.2.5 and Appendix C to calculate the unknown end displacements using an incremental-iterative trial-and-error procedure.

4.2.1 Second-Order Nonlinear Flexibility Based Element

4.2.1.1 Element Formulation

A spatial, FB frame element is adopted with two nodes and six degrees of freedom (DOF) in a local coordinate system (x, y, z). The local displacements **D** including one axial displacement, two rotations about y and z axes at each node and one torsional rotation about the x axis and the corresponding forces **P** are illustrated in Figure 4-4a and grouped in Equation 4.1 and Equation 4.2, respectively.

$$\mathbf{D} = [D_1, D_2, D_3, D_4, D_5, D_6]^T \quad \text{Equation 4.1}$$

$$\mathbf{P} = [P_1, P_2, P_3, P_4, P_5, P_6]^T \quad \text{Equation 4.2}$$

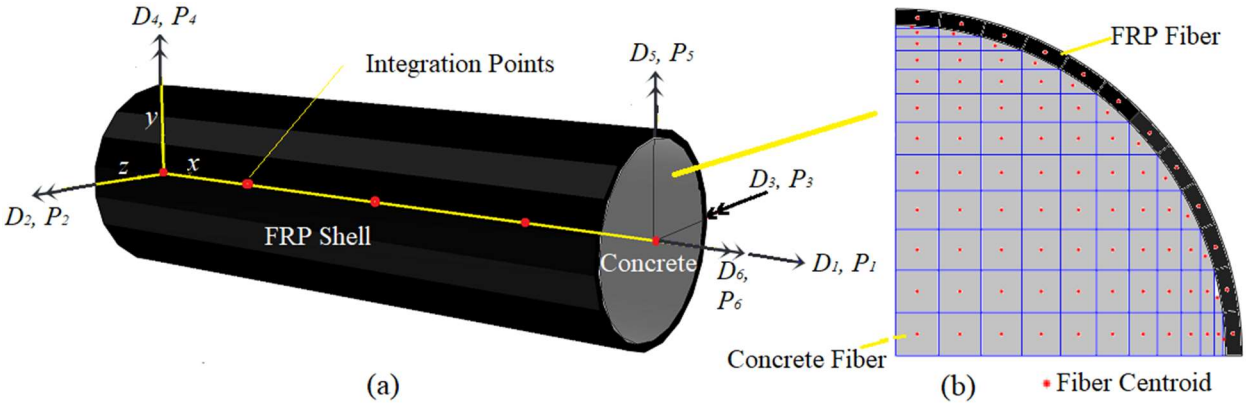

Figure 4-4. FB CFFT element (a) Distributed Plasticity Technique, (b) Fiber-Section Discretization

Based on the Bernoulli-Euler beam theory, the 3D response of such element is represented by the generalized strain field $\mathbf{d}(x)$ at each cross-section of the of the element, which consists of four DOFs including the axial strain at the reference axis $\varepsilon_0(x)$, curvatures $\kappa_z(x)$ and $\kappa_y(x)$ about z and y axes respectively, and the torsional angle $\varphi(x)$, as grouped in Equation 4.3. The corresponding section forces or the stress resultant vector $\mathbf{S}(x)$ consists of the axial force $N(x)$, bending moments $M_z(x)$ and $M_y(x)$ about z and y axes respectively, and torque $T(x)$ as grouped in Equation 4.4.

$$\mathbf{d}(x) = [\, \varepsilon_0(x)\ \kappa_z(x)\ \kappa_y(x)\ \ \varphi(x)]^{\,T} \quad \text{Equation 4.3}$$

$$\mathbf{S}(x) = [N(x)\ M_z(x)\ \ M_y(x)\ T(x)]^T \quad \text{Equation 4.4}$$

Each element is further divided into a number of sections (integration points) that are subdivided into fibers as shown in Figure 4-4b, in which a dimensionless quarter section of a coarse mesh is displayed to conceptually illustrate the CFFT element components, section fibers, and their centroids. It is observed

here that using such fiber-section discretization traces the behavior of CFFT arches better than using the radial discretization used in the analysis of circular columns and bridge piers confined with FRP jackets presented by Monti et al. (2001) and Hu and Barbato (2014). The uniaxial strain $\varepsilon(x, y, z)$ at any fiber is constant and related to the sectional deformation $\mathbf{d}(x)$ as $\varepsilon(x, y, z) = \mathbf{a}(y, z)\mathbf{d}(x)$, where $\mathbf{a}(y, z)$ is the compatibility matrix that relates the generalized section deformations with the uniaxial strain at any section neglecting the contribution of the torsion in the axial strain, as shown in Equation 4.5.

$$\mathbf{a}(y, z) = [1 \quad -y \quad z \quad 0] \qquad \text{Equation 4.5}$$

To satisfy equilibrium at any section in the deformed element of length L, the force interpolation function $\mathbf{b}(x)$ in Equation 4.6 proposed by de Souza (2000) was adopted to relate the section forces $\mathbf{S}(x)$ to the element end forces $\mathbf{P}$ by Equation 4.7.

$$\mathbf{b}(x) = \begin{bmatrix} 1 & 0 & 0 & 0 & 0 & 0 \\ v(x) & x/L - 1 & x/L & 0 & 0 & 0 \\ -w(x) & 0 & 0 & x/L - 1 & x/L & 0 \\ 0 & 0 & 0 & 0 & 0 & 1 \end{bmatrix} \qquad \text{Equation 4.6}$$

$$\mathbf{S}(x) = \mathbf{b}(x)\mathbf{P} \qquad \text{Equation 4.7}$$

Due to this interpolation function that strictly satisfies equilibrium in the deformed shape, there is no discretization error but only a numerical error in the FB element analysis (Neuenhofer and Filippou 1997). The lateral displacements $v(x)$ and $w(x)$ in y and z axes are employed to accurately capture the geometric nonlinearity in the section level caused by the interaction between the axial force and bending moment. The weak form of compatibility is enforced through the application of the Principle of Virtual Forces, which in the case of the FB frame element takes the form in the Equation 4.8. According to Du et al. (2017), Equation 4.9 represents the relations between the virtual section forces $\delta\mathbf{S}(x)$ and virtual end forces $\delta\mathbf{P}$ obtained using the composite matrix $\mathbf{b}^*(x)$ in Equation 4.10. By Substitution of Equation 4.9 in

Equation 4.8 and elimination of $\delta\mathbf{P}^T$ based on the arbitrariness argument, the element end displacement in terms of the section deformation along the element is shown in Equation 4.11.

$$\int_0^L \delta\mathbf{S}(x)^T\mathbf{d}(x)d(x) = \delta\mathbf{P}^T\mathbf{D} \qquad \text{Equation 4.8}$$

$$\delta\mathbf{S}(x) = \mathbf{b}^*(x)\delta\mathbf{P} \qquad \text{Equation 4.9}$$

$$\mathbf{b}^*(x) = \begin{bmatrix} 1 & 0 & 0 & 0 & 0 & 0 \\ v(x)/2 & x/L-1 & x/L & 0 & 0 & 0 \\ -w(x)/2 & 0 & 0 & x/L-1 & x/L & 0 \\ 0 & 0 & 0 & 0 & 0 & 1 \end{bmatrix} \qquad \text{Equation 4.10}$$

$$\mathbf{D}^{\boldsymbol{ele}} = \int_0^L \mathbf{b}^*(x)\mathbf{d}(x)d(x) \qquad \text{Equation 4.11}$$

4.2.1.2 Fiber Section Model and Element Flexibility matrix

The nonlinear stress-strain response of each one-dimensional element fiber at any cross-section of Figure 4-4a is described by the appropriate uniaxial nonlinear material constitutive model of a normal stress $\sigma(x,y,z)$ and the corresponding material tangent modulus is $E_t(x,y,z) = \frac{\partial\sigma(x,y,z)}{\partial\varepsilon(x,y,z)}$. Therefore, considering distributed plasticity by using the fiber-section technique makes the FB elements more efficient than the DB elements in geometrically nonlinear inelastic analyses (Du et al. 2017). Furthermore, using the fiber-section technique in FB elements can assist in capturing plastic hinges along the elements with reduced computation time due to the adopting of exact force interpolation function $\mathbf{b}(x)$.The section tangent stiffness matrix $\mathbf{k}^{\boldsymbol{sec}}(x)$ is obtained from Equation 4.12 with need to add the section torsional stiffness parameter of $\int_0^A (y^2+z^2)GdA$ as the last member of the matrix $\mathbf{k}^{\boldsymbol{sec}}(x)$, where G is the fiber shear modulus. The section flexibility matrix $\mathbf{f}^{\boldsymbol{sec}}(x)$ and its constitutive law are written in Equation 4.13 and Equation 4.14, respectively.

$$\mathbf{k}^{\boldsymbol{sec}}(x) = \int_0^A \mathbf{a}(y,z)^{\boldsymbol{T}} E_t(x,y,z)\mathbf{a}(y,z)dA \qquad \text{Equation 4.12}$$

$$\mathbf{f}^{\boldsymbol{sec}}(x) = \mathbf{k}^{\boldsymbol{sec}}(x)^{-\mathbf{1}} \qquad \text{Equation 4.13}$$

$$\mathbf{d}(x) = \mathbf{f}^{\boldsymbol{sec}}(x)\mathbf{S}(x) \qquad \text{Equation 4.14}$$

The element flexibility matrix $\mathbf{F}^{\boldsymbol{ele}}$ can be obtained by taking the derivative of the end nodal displacements $\mathbf{D}^{\boldsymbol{ele}}$ (Equation 4.11) with respect to the end nodal forces $\mathbf{P}$. Due to the existence of lateral displacement terms $v(x)$ and $w(x)$ in the matrix $\mathbf{b}^*(x)$, the flexibility evaluation is complex and leads to Equation 4.15. Finally, the element stiffness matrix without rigid body modes is given by Equation 4.16.

$$\mathbf{F}^{ele} = \frac{\partial \mathbf{D}}{\partial \mathbf{P}} = \int_0^L \{\mathbf{b}^*(x)^{\boldsymbol{T}}\mathbf{f}^{\boldsymbol{sec}}(x)[\mathbf{b}(x) + \mathbf{h}(x)] + \mathbf{g}(x)\}d(x) \qquad \text{Equation 4.15}$$

$$\mathbf{K}^{ele} = \mathbf{F}^{ele^{-1}} \qquad \text{Equation 4.16}$$

The matrices **h** and **g** are defined in Equation 4.17.

$$\mathbf{h}(x) = P_1[\mathbf{0} \;\; \mathbf{V}(x) \;\; -\mathbf{W}(x) \;\; \mathbf{0}]^T$$

$$\mathbf{g}(x) = \frac{\kappa_z(x)}{2}[\mathbf{V}(x) \;\; \mathbf{0} \;\; \mathbf{0} \;\; \mathbf{0} \;\; \mathbf{0} \;\; \mathbf{0}]^T - \frac{\kappa_y(x)}{2}[\mathbf{W}(x) \;\; \mathbf{0} \;\; \mathbf{0} \;\; \mathbf{0} \;\; \mathbf{0} \;\; \mathbf{0}]^T \qquad \text{Equation 4.17}$$

$$\mathbf{V}(x) = \left[\frac{\partial v(x)}{\partial P_1} \;\; \frac{\partial v(x)}{\partial P_2} \;\; \frac{\partial v(x)}{\partial P_3} \;\; \frac{\partial v(x)}{\partial P_4} \;\; \frac{\partial v(x)}{\partial P_5} \;\; \frac{\partial v(x)}{\partial P_6}\right]$$

$$\mathbf{W}(x) = \left[\frac{\partial w(x)}{\partial P_1} \;\; \frac{\partial w(x)}{\partial P_2} \;\; \frac{\partial w(x)}{\partial P_3} \;\; \frac{\partial w(x)}{\partial P_4} \;\; \frac{\partial w(x)}{\partial P_5} \;\; \frac{\partial w(x)}{\partial P_6}\right] \qquad \text{Equation 4.18}$$

The term $\mathbf{V}(x)$ and $\mathbf{W}(x)$ in Equation 4.18 are evaluated using the CBDI technique, in which the displacements $v(x)$ and $w(x)$ are obtained from the curvatures field $\kappa_z(x)$ and $\kappa_y(x)$ evaluated at *n*

integration points using a Lagrangian polynomial. The procedure is mathematically summarized in the Appendix A. Further details on the derivation of element flexibility matrix $\mathbf{F}^{ele}$ and the formulation of CBDI technique are omitted here but are thoroughly covered by de Souza (2000).

4.2.2 Soil-Spring Elements

One of the most important factors in the response of buried structures is the soil backfill, which both loads the structure due to its weight and restrains or loads the structure due to horizontal earth pressure. The vertical earth pressure σ_v acting at any node on the BCAB is computed based on soil density γ_{soil} and the soil depth at that node h as $\sigma_v = \gamma_{soil} \cdot h$ while its corresponding horizontal earth pressure σ_h was estimated based on earth pressure coefficient K_{soil} as $\sigma_h = K_{soil} \cdot \sigma_v$. In this study, the soil backfill was modeled as a series of nonlinear elastic horizontal soil-spring elements that only carried compressive axial loads. These individual horizontal springs were connected at each decking node, as seen in Figure 4-3. The spring force F_{spring} is computed based on the σ_h and the tributary area at the corresponding node (vertical projection) A_v as $F_{spring} = \sigma_h \cdot A_v$, i.e., $F_{spring} = K_{soil} \cdot \sigma_v \cdot A_v$. For each individual spring, K_{soil} and σ_v are unique and changing as functions of deflection and loading step (backfill, wearing surface or live load), respectively. The spring tangent stiffness k_{spring} has been estimated based on the same forward difference approximation employed by Walton et al. (2016b) taking into consideration the influence of skew on the mobilized resistance of the backfill soil and the behavior of SSI. However, this research has adopted an effective and unified displacement-dependent model proposed by Ni et al. (2018) to calculate the K_{soil}.The approach is directly effective and applicable for practical engineering design without prior knowledge of earth pressure measurements.

Based on the commonly observed lateral earth pressure (p_s) displacement (s) relationship shown in Figure 4-5, Ni et al. (2018) obtained Equation 4.19 to calculate displacement-dependent K_{soil} ranging from the fully active to the fully passive states for retaining walls. To define these boundary limits, the authors employed the traditional Rankine minimum active K_a and maximum passive K_p and the simplified

Jaky's at-rest K_0 earth pressure coefficients as shown in Equation 4.20, Equation 4.21, and Equation 4.22, respectively, in which, $\emptyset$ is the effective friction angle of the backfill soil. As part of their study, Ni et al. (2018) further recommend to use the displacement required to mobilize the full active earth pressure s_a.as a function of the height of the retaining wall H and type of backfill. For example, s_a is equal to $0.001H$, $0.002H$ and $0.004H$ for dense sand, medium sand and loose sand, respectively. In this study, $H$was taken as the depth of soil at a current stage of backfill, and K_0 (typically 0.4 for the granular backfill used in BCAB) was increased to 1.0 as the compaction modifies the at-rest state of the soil.

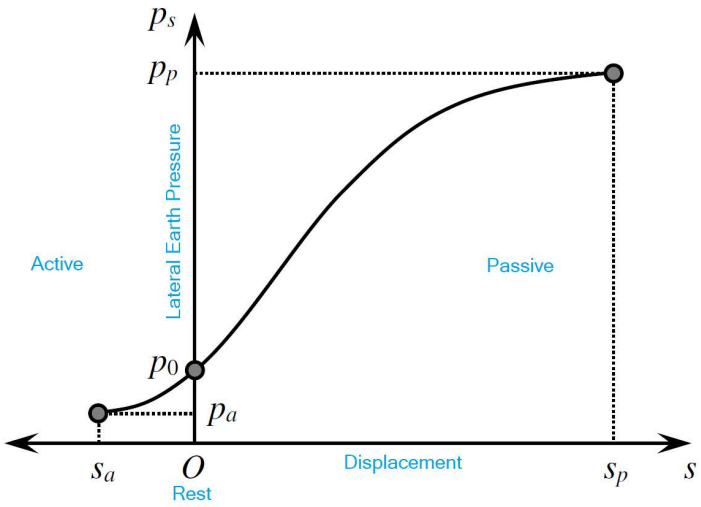

Figure 4-5. Variation of Earth Pressure with Displacement, (Ni et al. 2018)

$$K_{soil} = 2K_o - K_p + 2\frac{K_p - K_0}{1 + e^{\frac{s}{s_a}\cdot\ln(\frac{K_p - K_a}{K_p - 2K_0 + K_a})}} \quad \text{Equation 4.19}$$

$$K_a = \tan^2(\frac{\pi}{4} - \emptyset) \quad \text{Equation 4.20}$$

$$K_p = \tan^2(\frac{\pi}{4} + \emptyset) \quad \text{Equation 4.21}$$

$$K_0 = 1 - \sin\emptyset \quad \text{Equation 4.22}$$

4.2.3 Simulation of Staged Backfilling and Wearing Surface Loads Application

The backfilling process takes place after FRP decking is situated and the concrete fill in the arches has cured. The backfill is applied in lifts sequentially on alternating sides of the arch to maintain balanced loading. As recommended by AIT, 200 mm is the maximum compacted lift height, and no more than 600 mm of soil may be placed on one side of the arch without countering backfilling on the opposite side. Figure 4-6 illustrates backfill placement for a series of 200 mm layers corresponding to the maximum allowable unbalanced backfilling sequence. After backfilling is completed, the wearing surface is applied to the roadway. Accordingly, this study assumed the same sequence in the simulation of backfill and wearing surface applications.

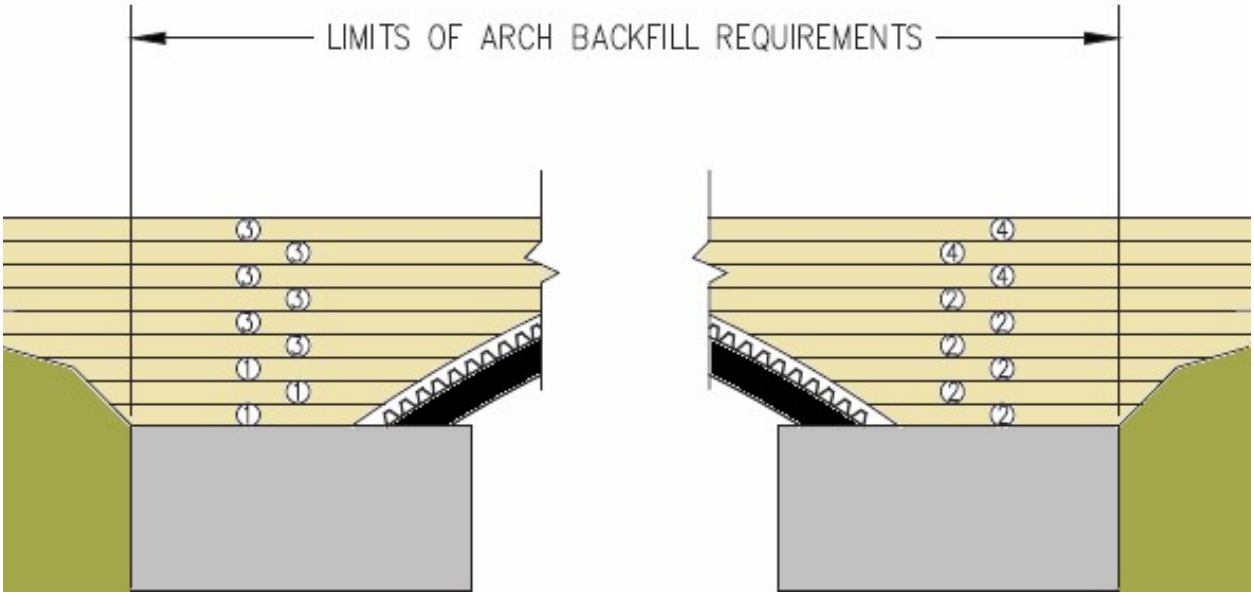

Figure 4-6. Uniform Backfill Placement (by AIT)

To mimic the backfill and wearing surface application, a progressive multistage simulation was used to capture the effect of backfilling. This study assumed that as each lift was installed, the soil vertical loads increase on each node below updated soil depth and new soil-spring elements are initialized for nodes covered by soil. The nodal soil vertical load at any node can be calculated based on σ_v and horizontal

tributary area A_h. Prior analysis by Walton et al. (2016b), considered that the new positions of the deformed nodes represent the at-rest state of the corresponding soil-springs. And for the next soil lift or any loading step, the structure has to be analyzed from the beginning with new total applied loads and activated springs. This may be inefficient with respect to computational time.

To achieve more computationally efficient multistage simulation, this study considers the advantage of both adopted incremental-iterative GDC solver and the FB element state determination detailed in Chapter 3 to analyze the pre-loaded structure under the application of a single layer of backfill, wearing surface placement, or live load application as new load increment. In other words, the model is brought into equilibrium under any current loading, and then only the load effect resulting from the next step must be analyzed. All initial variables required in the current loading stage are stored from the last local iteration of the last global increment of the previous converged state. The current analysis stores both force and stiffness of each soil-spring. Before performing the main steps of the element state determination in the framework of the overall analysis, initial variables need to be stored for each element before any local iteration is performed based on the previous converged state. The nodal soil vertical loads on the structure associated with the dead load of the wearing surface and the corresponding nodal lateral loads were simply based on tributary areas.

4.2.4 Simulation of Vehicular HL-93 Transient Loads

Loads on the BCAB structures are determined in accordance with AASHTO (2017) specifications. In addition to the force effects resulting from horizontal and vertical earth pressure and pavement load, AASHTO specifies that such a buried structure must be designed and analyzed for the force effects of live load and vehicular dynamic load allowance. Such transient load effects are affected by soil cover on the back of the buried arch and must be distributed through the earth fills. Further guidelines and specifications are provided to compute and distribute the live load effects when the soil cover exists as outlined in the provisions of Article 3.6.1.2.6. AASHTO (2017). Although the approach of distribution of the wheel loads

through the soil fill is very simple, this approach is overly conservative and does not account for variable load distribution with the depth of fill along the arc length of the arches (Bannon 2009). It is further noted here that this approach is not suitable for buried arch structures with a skew angle that affects both the longitudinal and transverse load distributions. However, the AASHTO (2017) specifications allow using more precise methods of analysis for these distributions.

In this study, both AASHTO HL-93 design uniform lane load and design vehicular live load (truck or tandem) including impact were applied at the road surface of the bridge and distributed through the earth fills as vertical loads. Each vertical live load p_{i_live} acting at node i is unique and calculated based on the well-known Boussinesq approach described by Das (2013). The Boussinesq approach accounts for variable load distribution with a depth of soil backfill in both the longitudinal and transverse directions. In contrast with the AASHTO simplified method, this approach also estimates the effects of the live load when the wheels are beyond the area of the bridge structure. It is observed throughout the model verification in the following section that the sum of the applied nodal force vector resulting from the Boussinesq method $\sum p_{i\_live}$ is less than the actual applied lane or tandem load P_{actual}. Presumably, this is due to the assumption of a semi-infinite soil medium made by Boussinesq. In case of BCAB (having non-infinite soil medium), however, some of the live loads is dissipated through the soil beyond the area of the bridge structure. To substitute that dissipated load in this analysis, any applied nodal live load vector was factored by $(\frac{P_{actual}}{\sum p_{i\_live}})$. The uniform lane load is applied separately from the live load because it is a constant load and it does not include impact loading and therefore it is not necessary to re-apply it for various truck positions in an envelope-type analysis.

4.3 Model Verification

4.3.1 Review of Previous Work by Walton et al. (2016)

The short subscale buried steel arch bridge tested and modeled by Walton et al. (2016a; b) was selected to verify the currently proposed model. The subscale bridge was tested in three phases to

investigate the SSI during the staged backfill, service live loading, and ultimate loading, (Walton et al. 2016a). The bridge structure was made of three circular-segment profile arches having a 6.1-m span and 1.22-m rise. The arches were solid square 51×51-mm cross sections fabricated from Grade 50 steel with experimentally determined 350-MPa yield strength. The arches were spaced 762 mm on center and set with no skew in 610×610×2130-mm concrete footing. Wood decking was attached on the top of the arches with 311-mm cantilever off the centerline of the outside arches to provide no torsion at arch locations under a uniform load. Figure 4-7 shows the overall test setup of the tested bridge. To mimic an in-service bridge, the subscale bridge was placed on a thick concrete floor inside a self-reacting heavy timber soil box for confinement. Bending strain gauges were distributed evenly at eight points along the arc length because buried arch bridge design is typically controlled by bending moment capacity.

Soil backfilling was performed in 19 lifts using a well-graded granular soil fill having a 44° friction angle and 2400 kg/m^3 compacted material density. Lift 1 was applied from the base of the foundation with a thickness of 400 mm on the south side and 200 mm on the north side. Lifts 2-16 were alternatingly placed in 200-mm thicknesses on each side of the bridge. North (N) and south (S) are relative to the apex as shown in Figure 4-7. Lifts 17-19 were applied across both sides. A scaled service live load of 84 kN was applied vertically using a hydraulic actuator with a spreader beam in order to equally loaded the three arches. The live loads were applied as three load cycles (loading up to 84 kN and unloading). The bridge was initially service loaded at the apex. Then, the load was alternatingly applied to each side of the bridge at offsets of percent of the span away from the apex including 10% N, 10% S, 20% N, 20% S, 30%N, and 30% S. After each service loading test, the strain gages mounted on the steel arches were reset. Finally, the bridge was loaded to failure at the apex with a pad made of timber placed over the soil to avoid driving the load beam into the soil under expected high loadings as shown in Figure 4-8.

Walton et al. (2016b) also developed a nonlinear soil-spring model to investigate SSI numerically and predict the bending moments during backfilling, service live and ultimate loadings. A structure consisting of a single arch with a tributary width of soil equal to the arch spacing was modeled with

conventional DB 2-noded 2D Euler beams and horizontal axial spring elements that represent soil. The experimentally measured and numerically predicted responses during different loading steps are summarized and illustrated later in the following section.

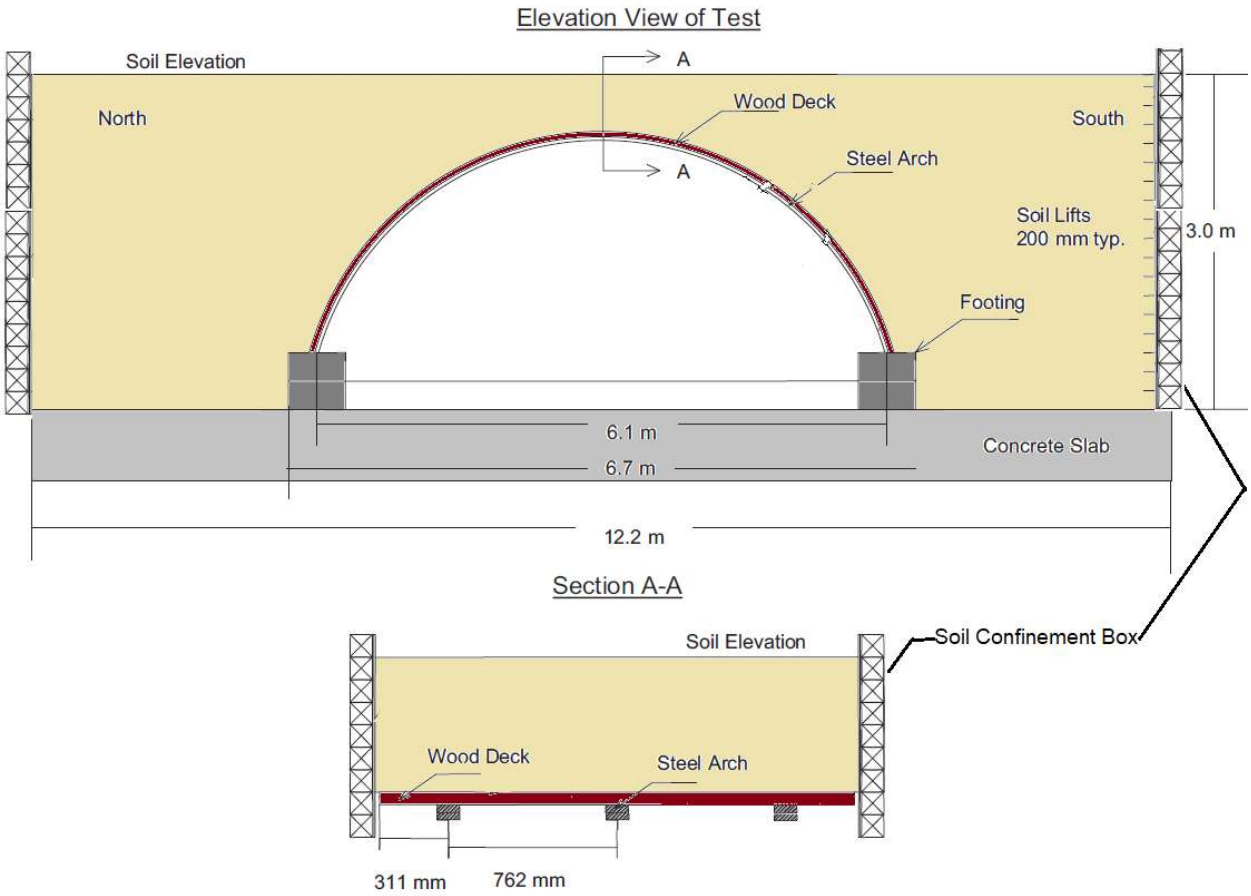

Figure 4-7. Elevation View of Arches with Apex Cross Section

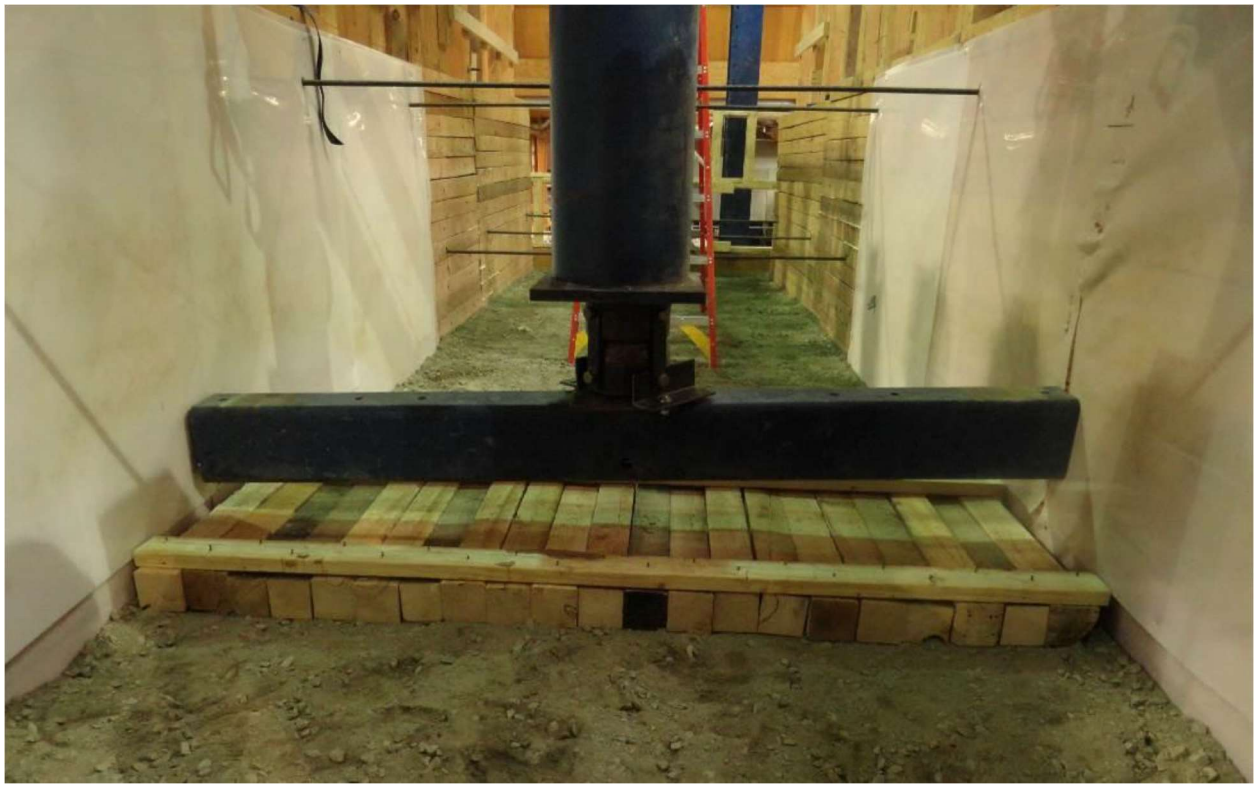

Figure 4-8. Load Beam before Ultimate Load Test (Walton et al. 2016a)

4.3.2 Simulation

Taking advantage of the structure symmetry, the central arch was simulated using the proposed model with an overhang transverse decking equal to the arch spacing. Figure 4-9 shows a representation of the model, in which a scaled schematic of a coarse mesh with a fictitious length given to each soil-spring element is displayed to conceptually illustrate the model components. Arch, decking, and foundation elements were modeled using the FB element formulation detailed previously with 5 Gauss-Lobatto integration points. Foundation and decking elements were given linearly elastic elements corresponding to their geometrical and physical properties. The steel elements were modeled as nonlinear elastic-perfectly plastic elements with 10×10 fibers used to discretize their cross-section.

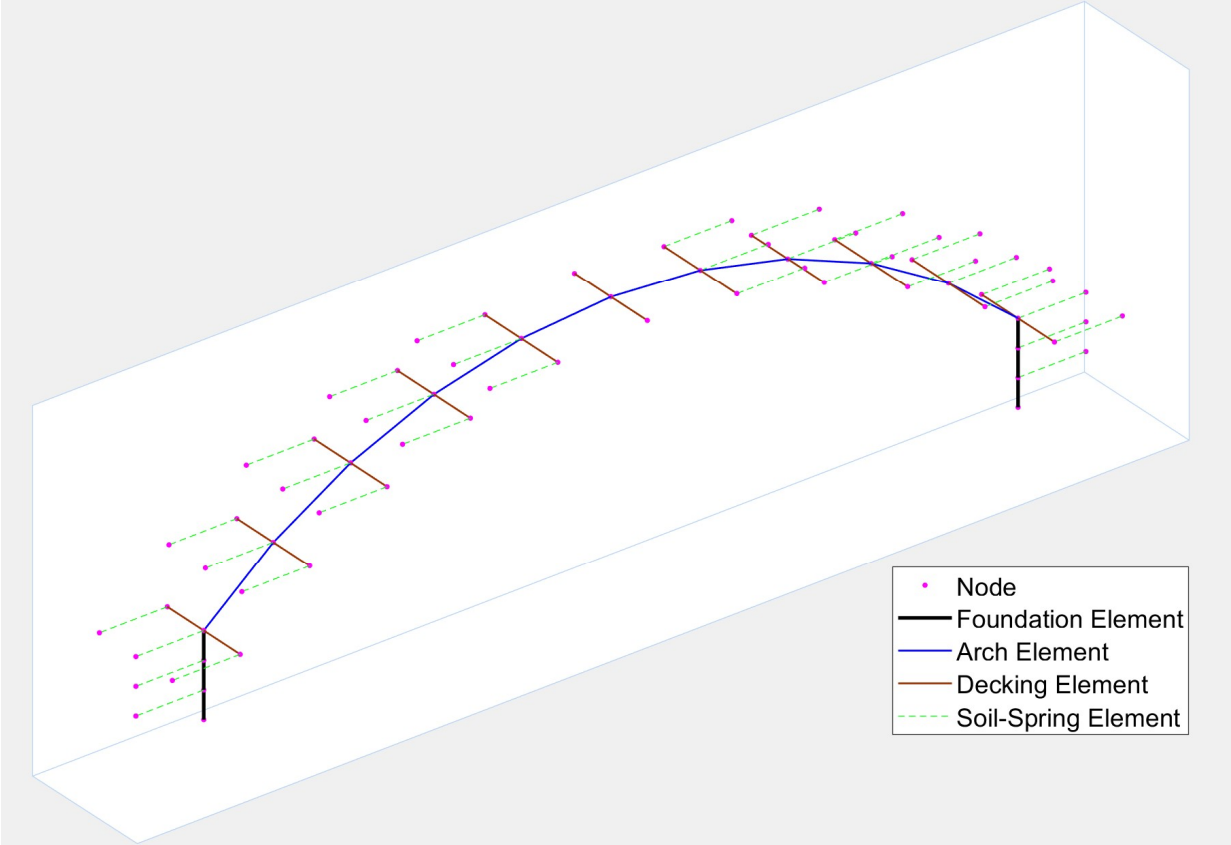

Figure 4-9. Schematic Model of Third Symmetry of Buried Steel Bridge

The bottom nodes of the foundations were modeled as clamped ends where the overhang nodes of the decking were modeled as symmetry faces having no transverse displacement and no rotation about the axis parallel to the arch span. All loads were gathered and represented as point loads applied at the nodes corresponding to their tributary areas, position and the soil depth above each node. Soil lifts were modeled and activated as soil-springs as discussed previously. The model was run with a mesh of 4 vertical elements per one footing, 2 elements per a single transverse row of a decking and 20 arch elements. Although the proposed model uses tributary areas to gather loads at nodes, the model accuracy is not limited by the small number of elements. Figure 4-10 shows a mesh convergence study conducted on the same arch bridge studying the apex moment and vertical displacement at the post-backfilling load and apex peak load against the number of arch elements. Figure 4-11 shows the arch deformed shapes resulted from the mesh convergence study.

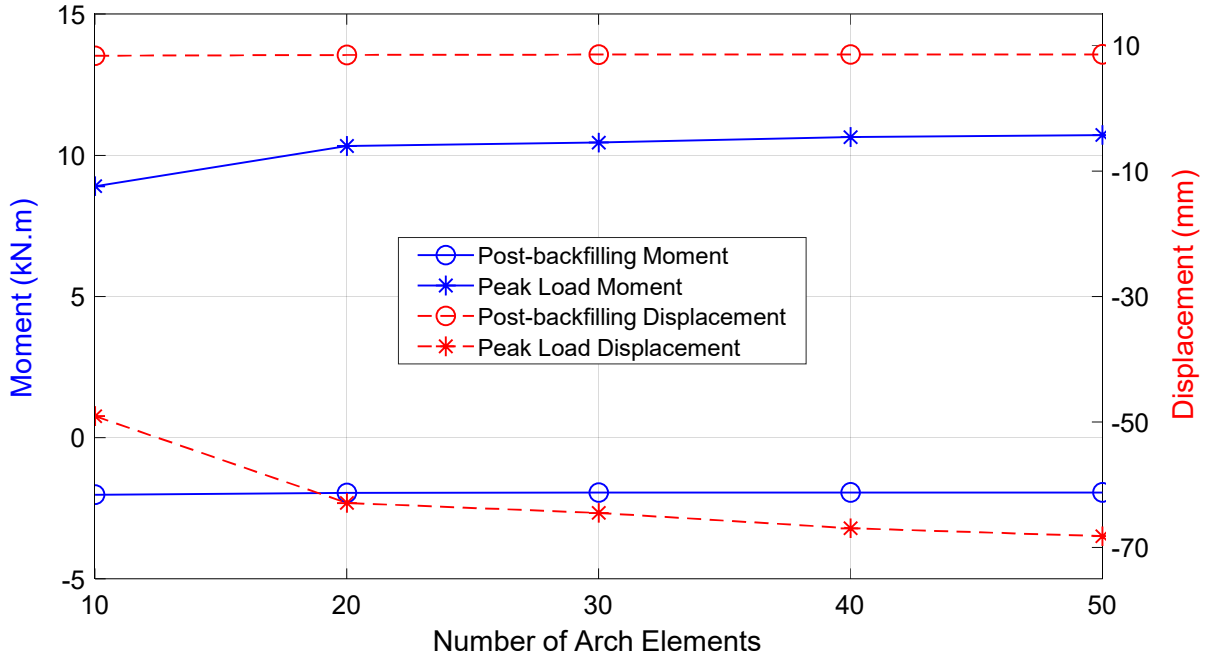

Figure 4-10. Mesh Convergence Study: Apex Moment and Vertical Displacement

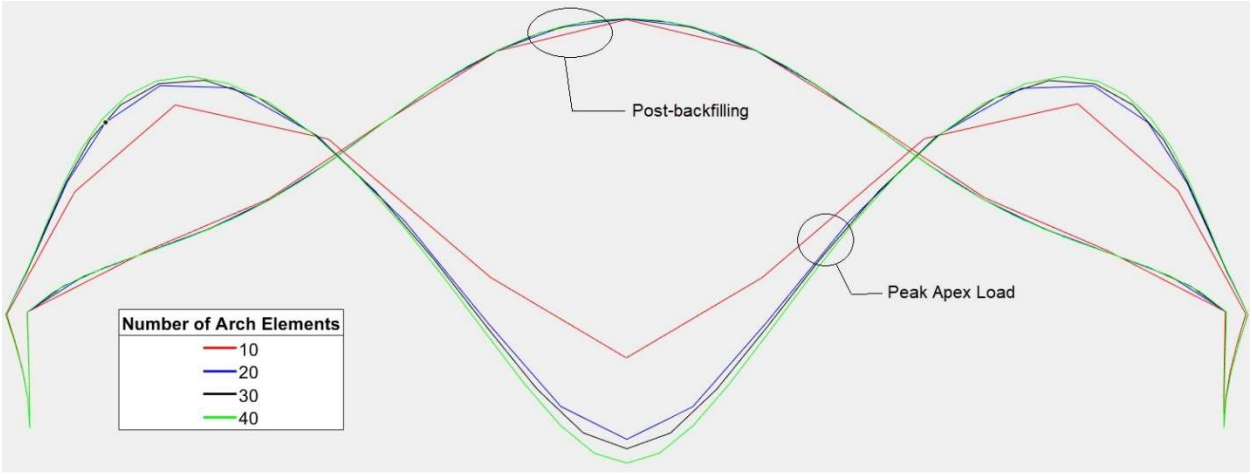

Figure 4-11. Mesh Convergence Study: Deformed Shape, (Deformations are magnified 30 times)

4.3.3 Predicted Responses

Different responses predicted by the proposed model for the three loading phases are illustrated against the experimental and model data of Walton et al. (2016a; b) in Figure 4-12 through Figure 4-19.

Figure 4-12 shows the apex moment during backfilling and comparisons between both experimental and Walton's model data. The experimental apex moment was computed from flexural strains measured over the depth of the steel arch section. The predicted apex moment shows good agreement with experimental results, including the peak moment as well as the reduction from peak during the last few backfill lifts. The proposed model better follows the trend indicated by experimental results as the soil loads above the apex induce an apex positive moment, reducing the negative moment from prior loading (positive moment produces compression on the outside face of the arch). However, the experiment response shows that the peak moment occurs after the first lift above the apex (Lift 17). On the other hand, the proposed model predicts the peak moment at Lift 16. The predicted apex moments corresponding to Lift 16, Lift 17 and Lift 19 (final lift) are 2014, 2007 and 1896 N-m, respectively. These predicted moments were within 1.6%, 7.6%, and 3.6% of corresponding experimentally observed apex moments of 1982, 2174 and 1967 N-m, respectively.

Figure 4-13 shows the apex displacements (positive upward) during backfilling and comparisons with the experimental data of the three steel arches measured by Walton et al. (2016a). The predicted displacement response shows good agreement with the experimental response and both show that the peak displacement of approximately 12 mm occurred at the Lift 16 and the final three lifts cause downward apex displacement of a final displacement approximately 7 mm. Figure 4-14 shows the moments along the arch arc length at the end of the backfilling process for both the proposed model, the experiments, and the model of Walton et al. (2016b). Generally, moments predicted by the proposed model follow a similar trend at the experimental moments better than Walton's model. As shown by the experiment, the proposed model indicates that the peak positive moment appears near 20% of the span away from foundations with a more symmetric response.

Following backfilling simulation, live loadings are applied corresponding to load points from laboratory experiments. Due to the non-hysteretic soil-spring model used in this study, the simulation of each cyclic live loading is represented by the first cycle taking place right after the backfilling simulation

and the proposed model does not account for any creep or relaxation between live loading tests. Figure 4-15 through Figure 4-18 show the comparison of live-load moments along the arch arc length at the end of each live loading simulation. Live-load moments are calculated from the difference between total moments at the end of each live load analysis and the moments at the end of backfilling.

Returning to Figure 4-14, the experimental and predicted post-backfilling moment responses are slightly un-symmetric. In Figure 4-15 through Figure 4-18, however, the experimental live-load moment responses are not identical for the same N and S offset loads due to the cyclic live-loading tests conducted on alternating sides of the bridge and the resulting un-symmetric, locked-in deformations of the soil and arch. On the other hand, the proposed model responses for both offset loading sides are identical because it does not account for any creep or relaxation between live loading tests as well as due to the assumption of non-hysteretic soil model that is not accounting for the effect of cyclic live-loading applications on the alternating sides of the bridge. Although Walton's model has the same two former assumptions, its responses for both offset loading sides were not identical and the reason for that is not interpreted. Furthermore, Walton et al. (2016b) conducted additional soil continuum model using Abaqus, not reported here, and this model also showed identical responses for both offsets loading sides. Consequently, each plot illustrates both N and S offset load responses on the same plot flipping the former response about the apex. As shown by the experiment, the model indicates that the peak positive moment is produced near the point of load application in all cases. Comparing with Walton's model, the FB model more accurately predicted the peak moment under the point of load application. For the larger load offsets of 20% and 40%, the FB model also more accurately predicted arch response away from the point of load application. Both the proposed and Walton's models over-predicted moments near the supports. This is likely because the model assumes a clamped support, and during the test, rotations were likely not fully restrained. However, none of the moments near the foundation exceed the maximum moment for the all loading conditions.

Figure 4-19 shows the predicted ultimate load total moment responses plotted against the experimental response which includes backfilling and hysteretic locked-in strains resulting from all prior

loads. Taking advantage of the GDC solver used in this study, the proposed model was able to predict the failure loads corresponding to snap through observed experimentally. The model was run after the backfilling simulation. Figure 4-20 shows the arch displaced shape, deformations are magnified 30 times, predicted by the proposed model at the loading of Lift 16 (soil backfilling within the arch apex) and Lift 19 (post-backfilling), and 27.8, 53.3, 74.7 and 100 percent of the ultimate applied apex load.

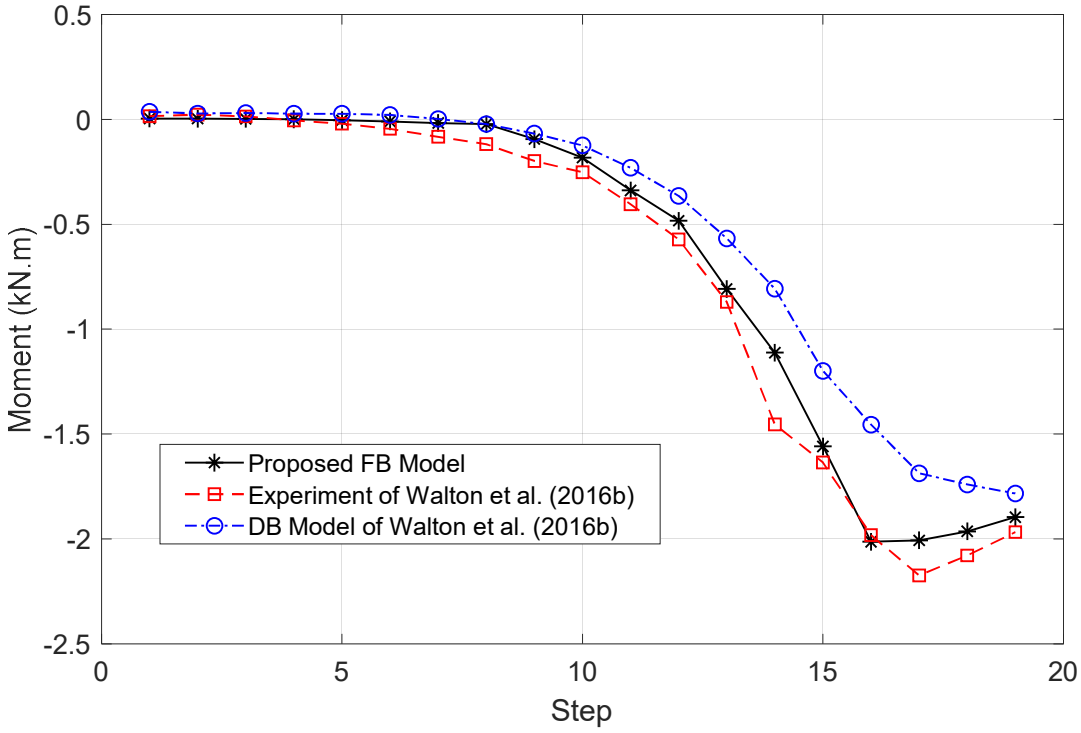

Figure 4-12. Apex Moment During Backfilling

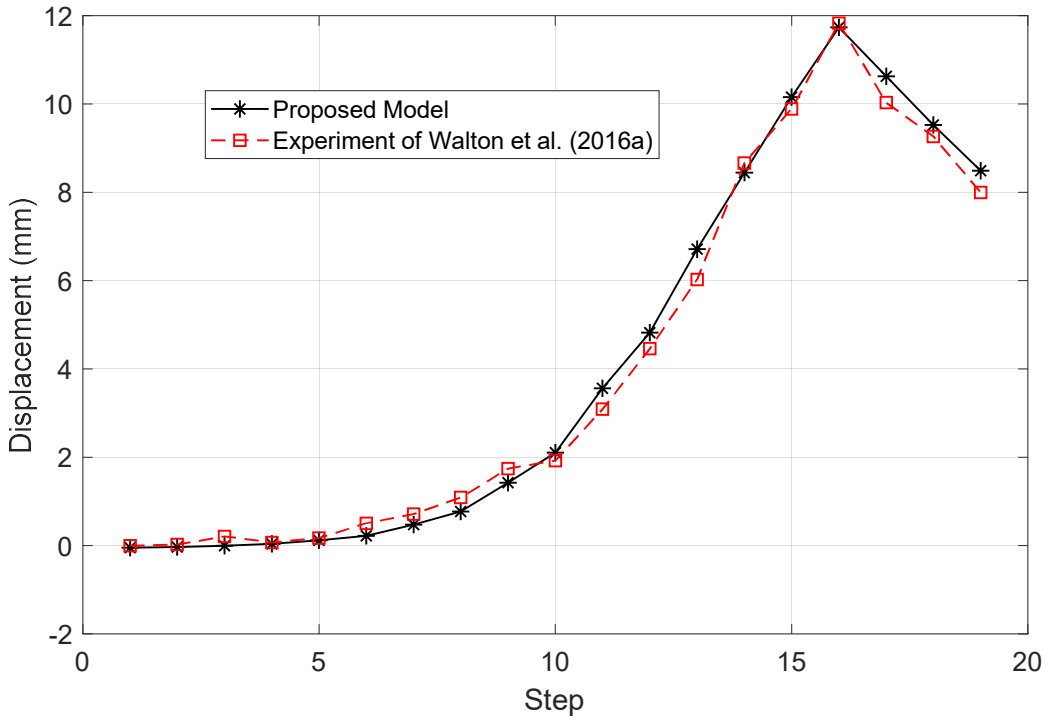

Figure 4-13. Apex Displacement During Backfilling

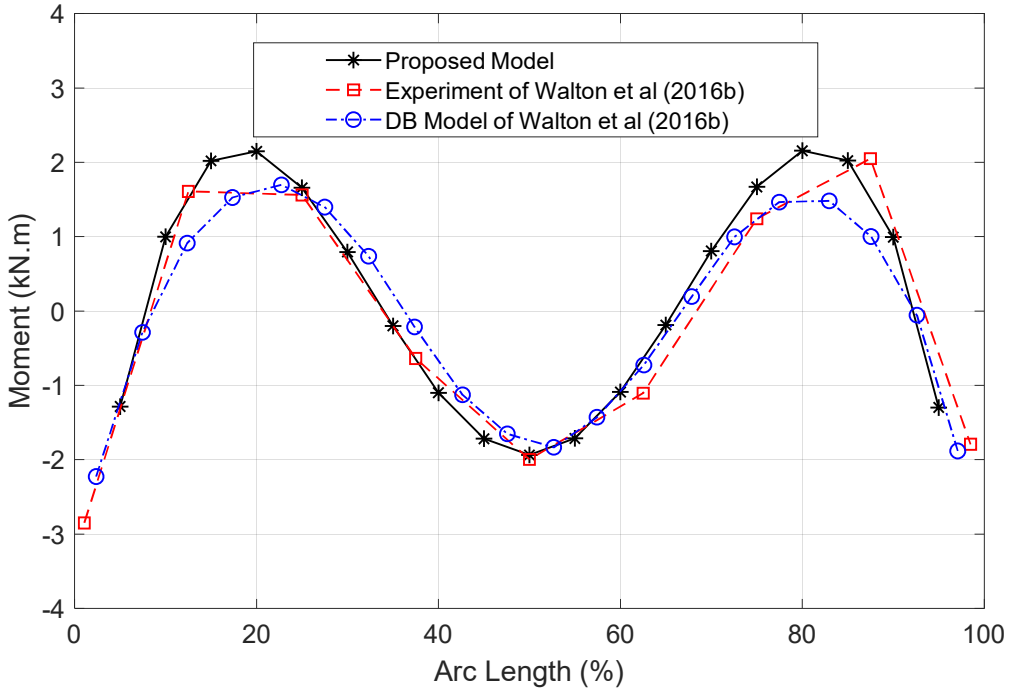

Figure 4-14. Moment at the End of Backfilling

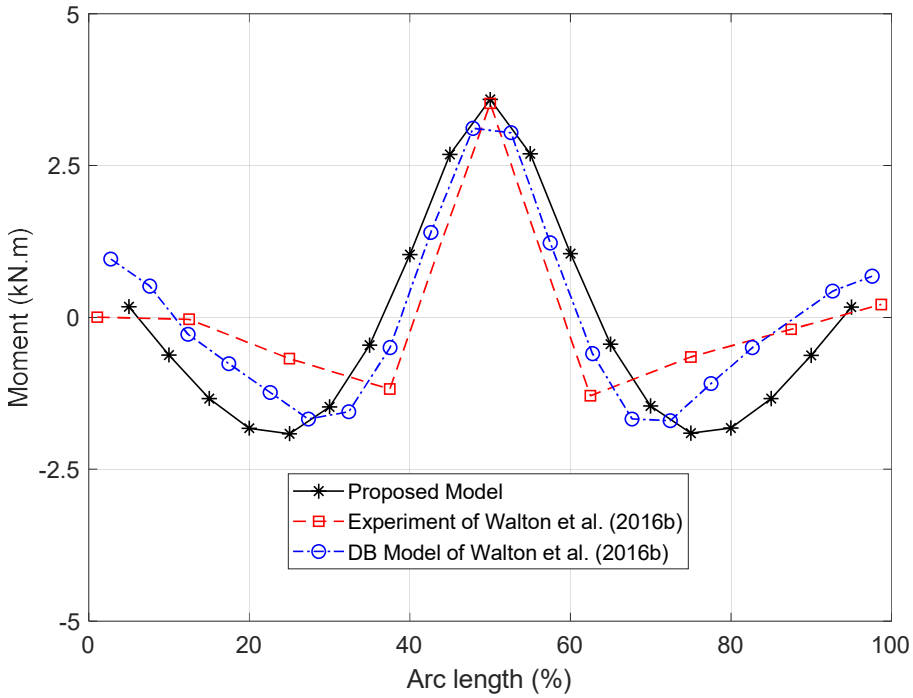

Figure 4-15. Apex Live-Load Moment Diagram

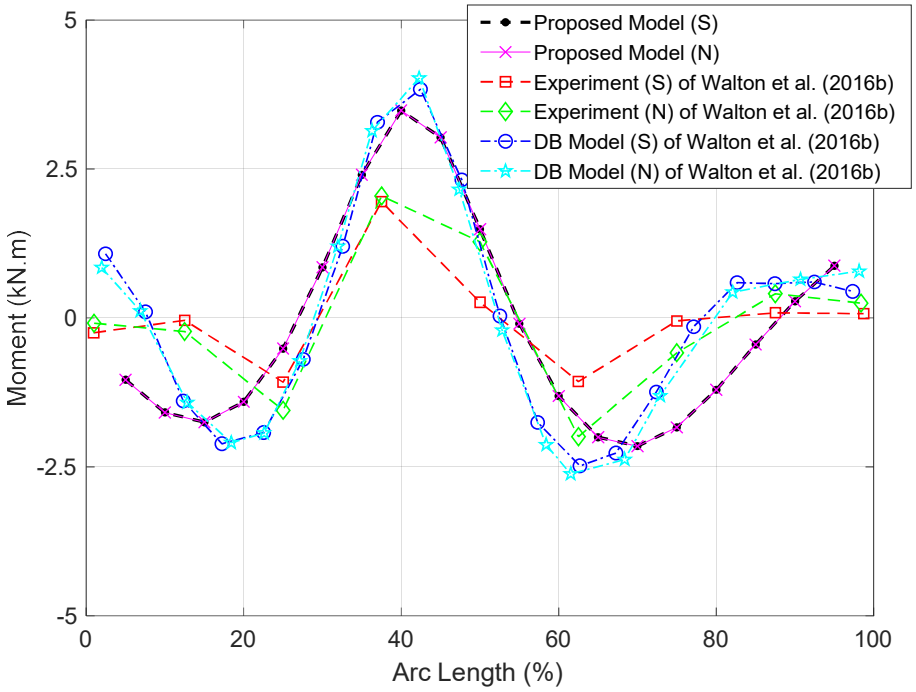

Figure 4-16. 10% Offset Live-Load Moment Diagram

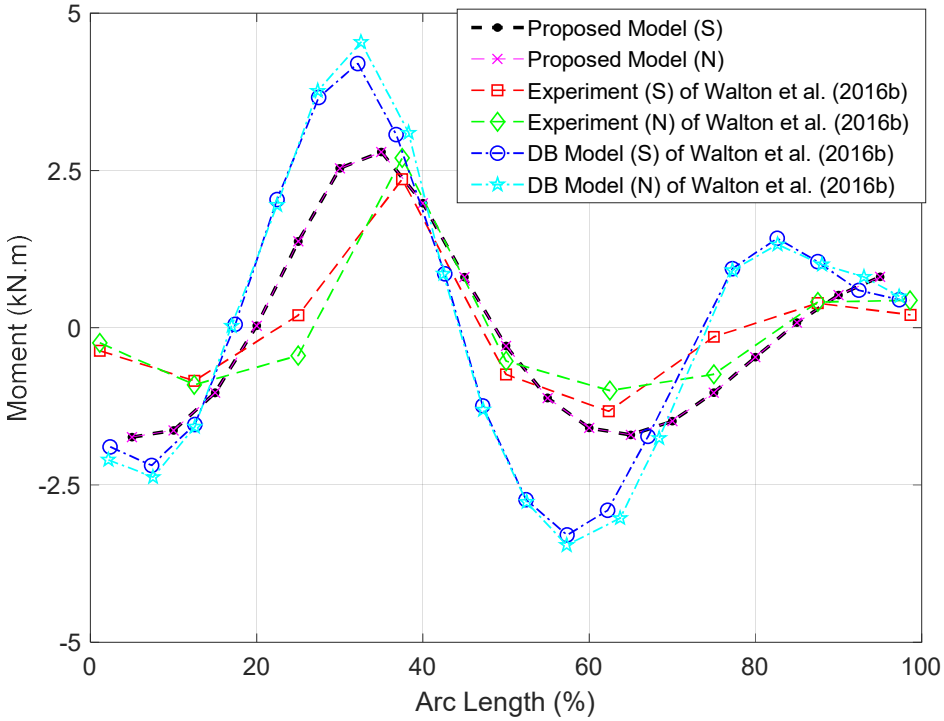

Figure 4-17. 20% Offset Live-Load Moment Diagram

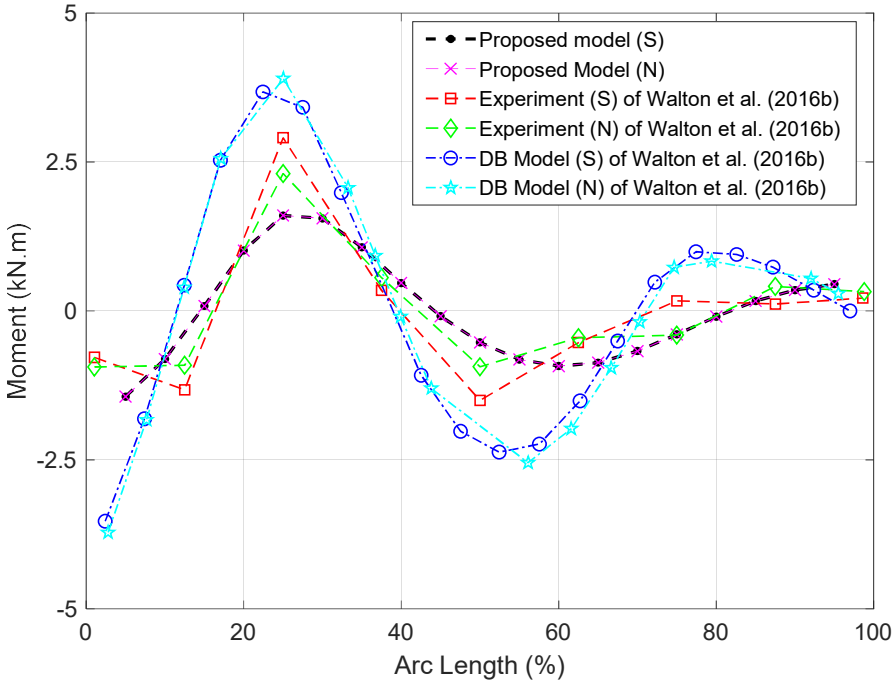

Figure 4-18. 30% Offset Live-Load Moment Diagram

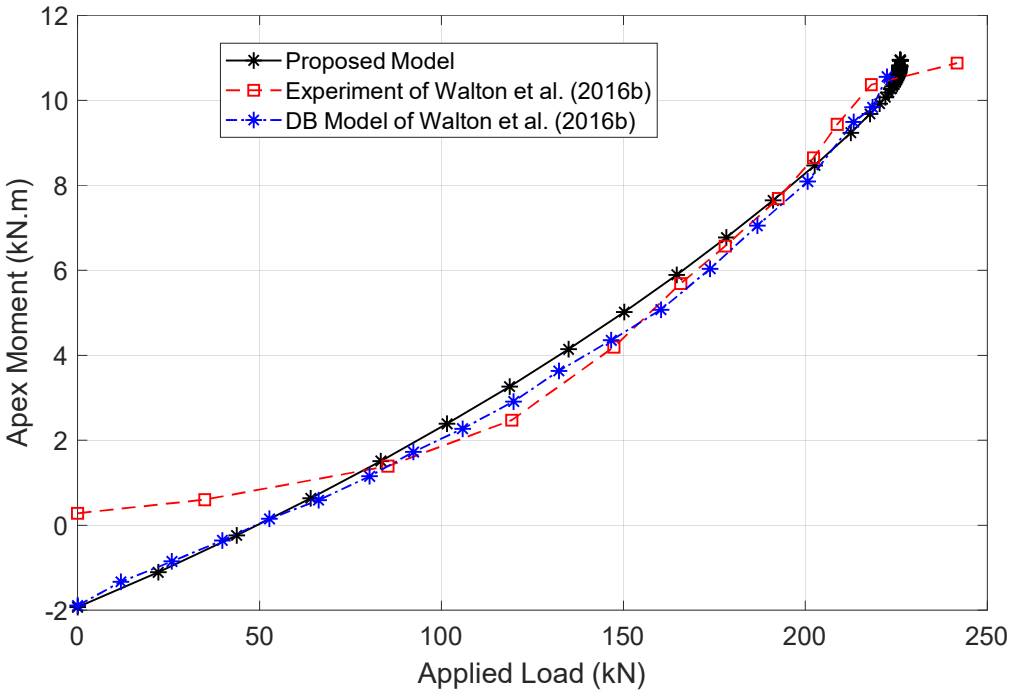

Figure 4-19. Ultimate total moment, apex load

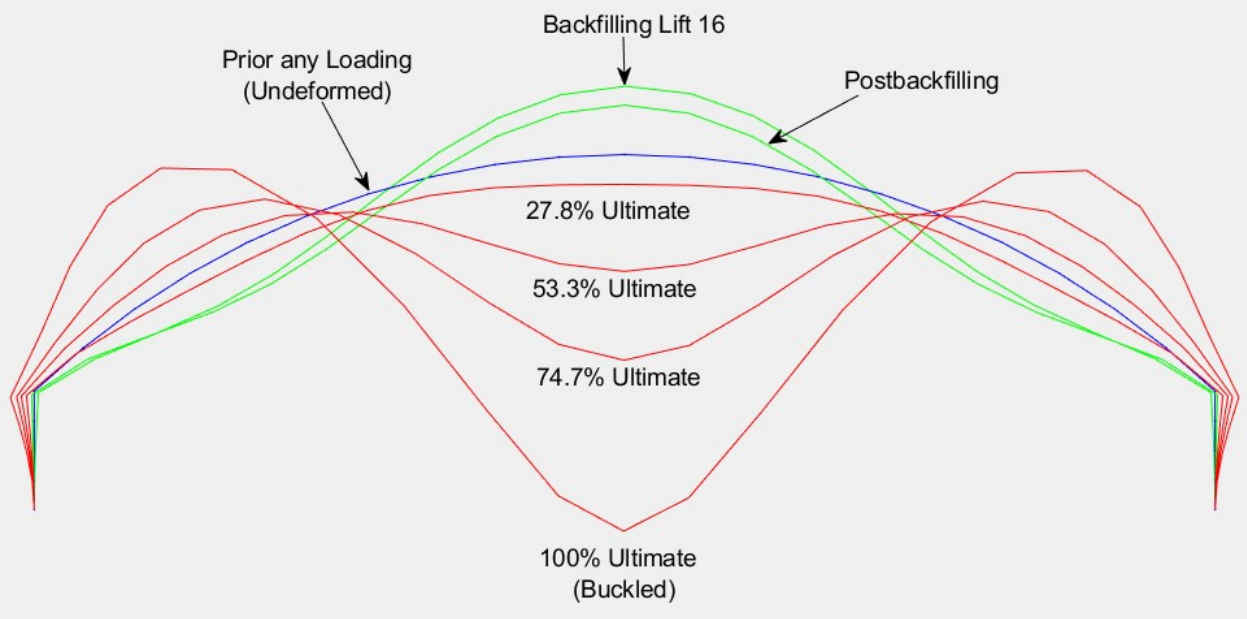

Figure 4-20. Shape of the Steel Arch with its Foundations during Several Loading Cases

4.4 Skew Effect Parametric Study

Skewed bridges, which have foundations that are not perpendicular to the bridge span, are common in roadway and railway networks. The faces of the bridge superstructure are not perpendicular to its abutments and its plan view is a parallelogram as shown in Figure 4-2. According to AIT (2019), the BCAB's superstructure can easily accommodate skews without increasing the bridge footprint. Orienting the CFTT arches and headwalls of a BCAB parallel to the roadway reduces right-of-way impact and softens horizontal curves in the roadway alignments. In 2012, for instance, the Maine DOT made a decision to use a skewed BCAB with a 25° skew angle and 11 CFFT arches instead of using a precast concrete bridge in Ellsworth, Maine as shown in Figure 4-21.

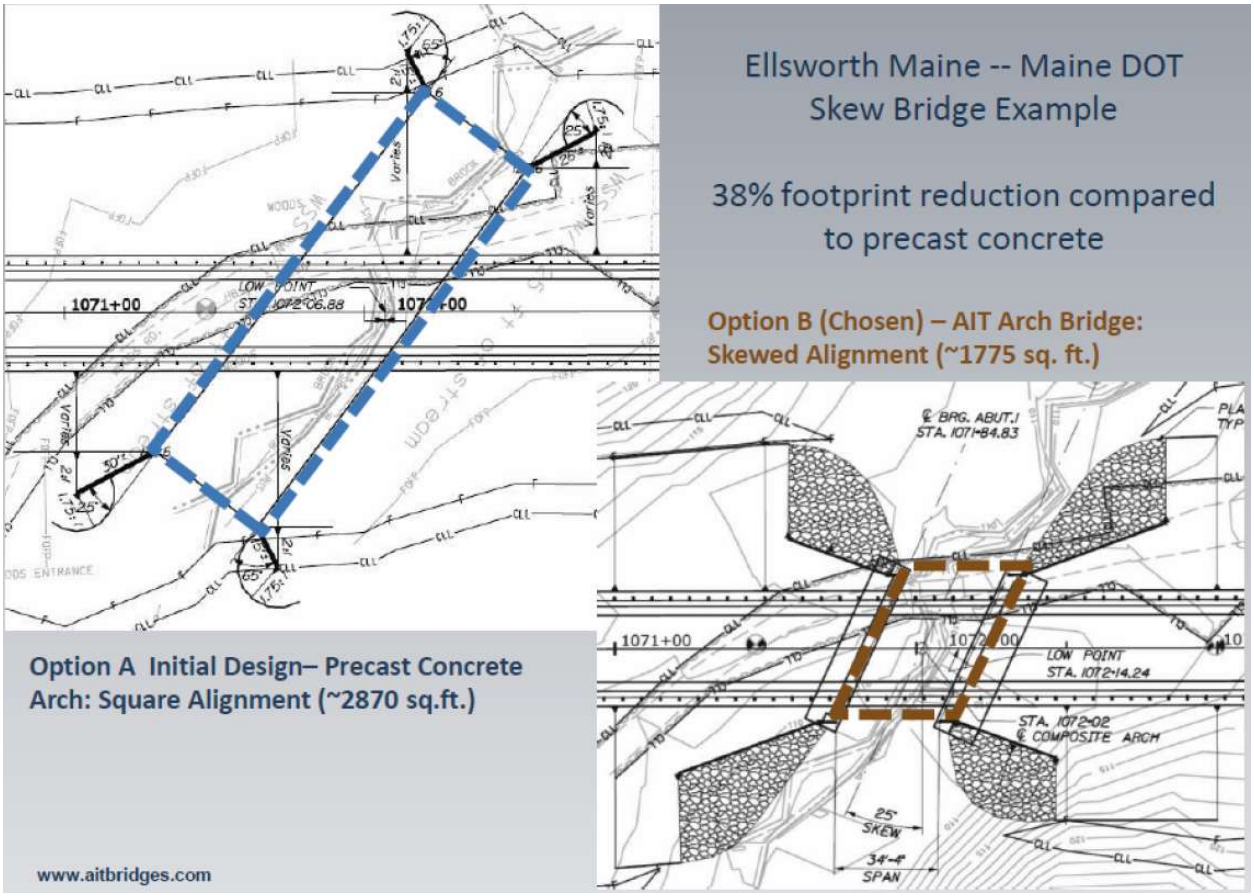

Figure 4-21. Skewed Bridge Comparison Example, Ellsworth, Maine, reported by AIT (2019)

Skewed BCABs will experience out-of-plane deformations which cannot be captured by conventional 2D analyses. For such a skewed buried structure, AASHTO (2017) specifies to extend the design and analyses to consider the influences of unsymmetrical forces on the structure as well as on the representation of conventional dead and service live loads. The sophisticated combined FE model presented and verified early in this chapter is used to investigate the effect of the skew angle that causes many difficulties in the implementation and analysis of BCABs.

4.4.1 Description of the Skewed Bridge

A generic, skewed, two-lane BCAB having a span of 12 m, a width of 9 m, and a rise of 3 m, consisting of nine circular-segmental profile CFFT arches as shown in Figure 4-2, was used in the

parametric studies presented here. This geometry is very typical of BCABs. The nine arches were considered to be parallel, spaced at 1.125 m on center, and cast into very stiff and strong footings. This type of stiff footing may not represent actual foundations of an in-service BCAB. According to Walton et al. (2016a), there is lateral resistance through basal shear and soil pressure behind the foundation such as is present in the in-service speared foundations. Other types of foundations are used in BCAB technology, such as piles, which provide horizontal resistance dependent on pile stiffness and *in situ* soil properties. Simulation of the BCAB foundation is beyond the scope of this parametric study. The skew angle was the single parameter and was varied from 0° to 50° in 10° increments. For the purpose of this investigation, the 12-m bridge span (parallel to the CFFT arches) has been kept constant in all skew angle cases. Consequently, the square span (S) of the bridges decreased as the angle of skew (φ) increased as shown in Figure 4-2, i.e., S= 12 m × cos(φ).

The CFFT arches were assumed to be fabricated from the same the FRP-tube and concrete used in the analysis of the isolated arch described in Section 3.4.5, which is typical for BCABs. An FRP corrugated decking, fabricated particularly for use in BCAB technology, was assumed to be fixed on the back of the arches. It is important to note that the corrugation of the FRP decking is always parallel to the footings for any skew angle as seen in Figure 4-1. Geometrical and material properties of the decking were provided by AIT as shown in Appendix D. The 200-mm height of soil lifts was treated as recommended previously considering the alternating sequence and the soil material properties used in Section 4.3.1. A wearing surface of 0.1 m was applied to the top of the backfill with a density of 2500 kg/m^3.

4.4.2 Loading Application

The bridges were considered to be subjected to loads defined by AASHTO (2017) for Strength I and Service I load limit states with load factors defined in Table 4-1 Service I is not reported here because Strength I load combination controlled in all load stages. In addition to the description of the skewed bridge above, this parametric study is limited to two cases of AASHTO HL-93 design live loading. Both cases

were two-lanes loaded with a uniform lane and design tandem loads transversely positioned as close as possible to the longitudinal centerline (CL) of the bridge. Longitudinally, the center of the two tandem loads was positioned at mid-span (Case 1) and the quarter-point of the span (Case 2). Figure 4-22 shows the two loading cases, in which the uniform lane load was applied as an infinite strip load over the roadway. Although the tandem has lower wheel loads than the HL-93 design truck, the tandem often controls the design for BCABs according to Walton (2015) and is generally critical for shorter span bridges like the BCAB considered here. The tandem is a 224 kN vehicle with two axles spaced at 1.2 m with a 1.8 m axle width.

Table 4-1 Strength I Limit State Load Combinations

Factor	Value	Definition
DC	1.25	Both CFFT arches and FRP decking self-weight
EV	1.30	Vertical earth pressure
EH	1.35	Horizontal earth pressure
DW	1.50	Wearing surfaces loads
LL	1.75	Live loads
m	1.00	Multiple Presence Factors (two lanes)
IM	0.17	Dynamic Load Allowance as $\mathrm{IM} = 33 \cdot \left(1.0 - \frac{0.125 \cdot D_E}{0.305}\right) \geq 0\%$ D_E is taken as 1.2 m the depth of the backfill above the crown

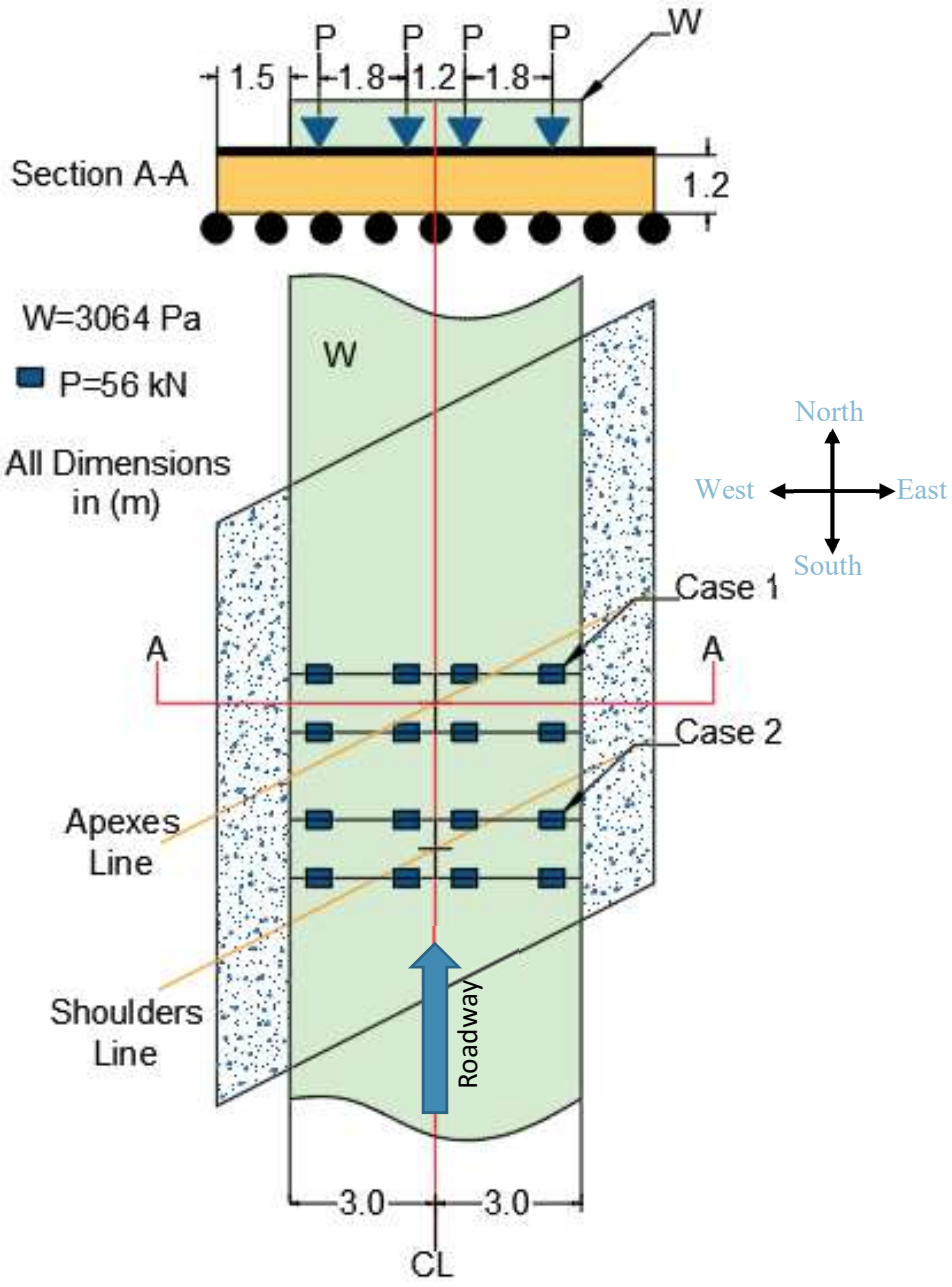

Figure 4-22. Two-Lane Skewed BCAB with Centered Loading

4.4.3 Analyses

The entire BCAB described above was simulated using the proposed model having rigid supports in the vertical and horizontal directions (fixed-fixed boundaries as seen in Figure 4-3). Arch and decking elements were modeled using the FB element formulation detailed previously with 5 Gauss-Lobatto integration points. The nonlinear FRP-confined concrete model presented in chapters 2 and 3 was implemented to simulate the CFFT elements with 80 equal sizes of FRP fibers and 840 differently sized concrete fibers used to discretize their cross-section as seen in Figure 4-4b.

All decking elements were assumed to be linearly elastic. The stiffness matrix of the transverse decking elements was calculated using to the geometrical and material properties of the corrugated decking given in Table D 1 and Figure D 1. In case of diagonal bracing elements and due to the corrugation of the FRP deck, it is difficult to perform an equivalent lattice analysis to find a satisfactory approximation for their stiffness matrix that works for different mesh sizes. For that reason, the diagonal element stiffness matrix was taken as a fraction of the transverse decking stiffness matrix and a sensitivity analysis was performed to evaluate the effect of that fraction on the analysis. A visual representation of this sensitivity analysis (Appendix D) shows that there is some effects of the fraction of the resultant bending and torque moments of CFFT arches cross-section. The sensitivity analysis shows that as that fraction increases, the factored ultimate moment M_u, which generally controls the design of BCAB, decreases. Thus, the stiffness matrix of the diagonal bracing elements was taken as10% of the stiffness of the transverse decking elements for in the subsequent analyses, which is expected to be a conservative assumption.

The model was run with a mesh of 24 circular-segment elements of equal length per single arch (25 nodes) and a single decking element between pairs of adjacent arch nodes. All loads were gathered and represented as point loads applied at the nodes corresponding to their tributary areas, position and the soil depth above each node. Soil lifts were modeled and activated as a soil-spring as discussed previously.

One of the advantages of the FB element formulation employed here is its ability to provide output for different variables at any node, integration point or section fiber of any element during all of the multistage simulation. These output variables include strains and stresses, displacements and rotations, forces and moments as an in-plane, out-of-plane, and torsion. Prior research showed that the in-plane moment capacity of CFFT arches typically controls the design of BCAB, and these arches are usually under combined axial compression and bending loading (Walton 2015). In the case of skewed BCAB, however, out-of-plane shear forces and flexural moments, as well as torsional moments, are produced during the backfilling process and under the service load. For the purpose of this investigation, the results and discussion focus on the effect of skew angle on shear forces and flexural moments of CFFT arches, the two most critical section forces for design.

Because of the circular configuration of the CFFT cross-section used in this study, the maximum resultant shear force and the maximum resultant flexural moment will control the design of CFFT arches in skewed BCABs. Therefore, the CFFT cross-section should be designed as a cylindrical section that has the same longitudinal properties in all radial directions (360°), i.e. under cylindrical envelopes of moments and forces. It is important to note that the CFFT cross-section used in this study has an experimentally-determined nominal moment capacity M_n of 156 kN-m (having a standard deviation of 21.17 kN-m and coefficient of variation of 6.91%) corresponding to 1.72% longitudinal tensile rupture strain at the tension face of the FRP shell as shown in Table 2-3. Although this moment capacity is for a section under pure bending, the axial force typically carried by CFFT arches has an advantageous effect on the bending capacity of such sections. According to a CFFT moment-curvature analysis that accounts for the effect of a fixed axial force, Dagher et al. (2012) generated multiple moment-curvature relationships corresponding to different values of the axial force. Due to the assumption of fixed axial force during the analysis, Dagher et al. (2012) found that the applied axial force has an obvious effect the earlier stage of the analysis rather than on the ultimate moment. Herein, a range of isolated CFFT arches having the same cross-section, material properties used for skewed brides and different span to rise ratios were analyzed using the FB

method detailed in Chapter 3. Figure 4-23a shows the predicted moment-curvature relationship for the apex cross-section of different isolated arches having the pinned-pinned supports and apex load configuration used in Section 3.4.4. Figure 4-23b shows the corresponding axial force occurred and increased gradually during the analysis. Further visual representation of the effect of the axial force is shown in Figure 4-24. For example, a value of 300 kN axial force at the end of the analysis increases the corresponding ultimate moment resistance by 10.3%. However, an M_n of 156 kN-m with a resistance factor ϕ of 0.65 are used herein as conservative comparison giving a design flexural moment capacity $\phi M_n = 101.4kN$.

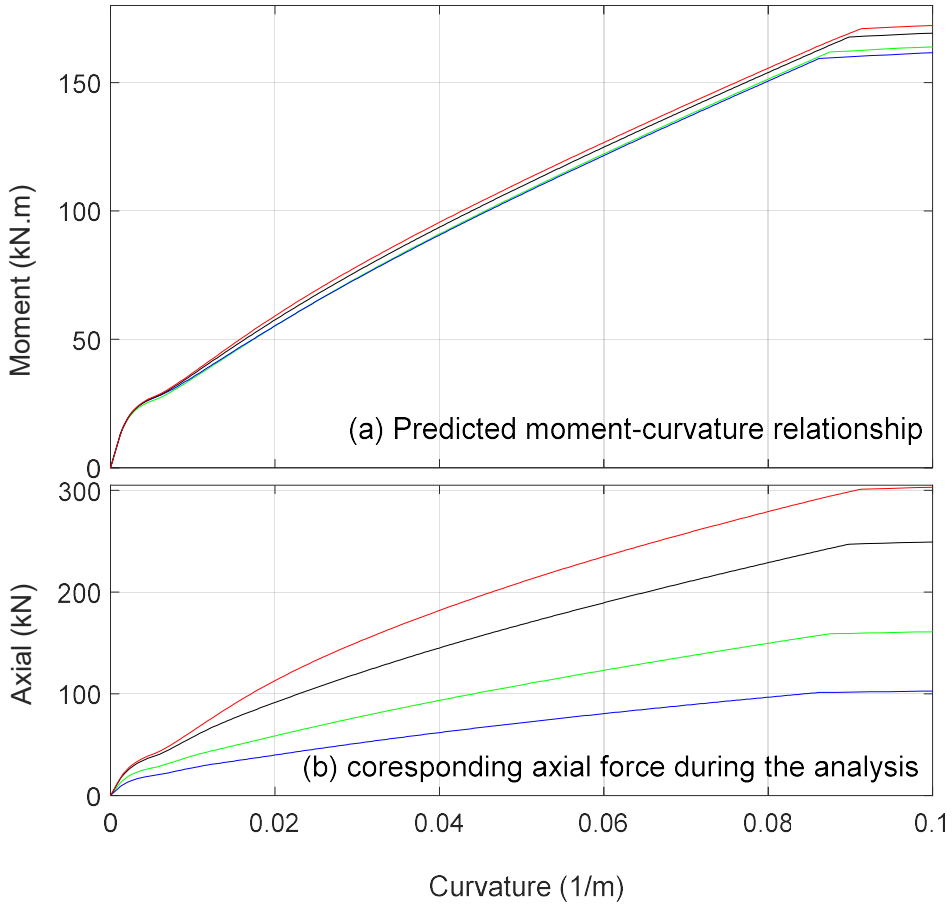

Figure 4-23. Axial Force Effect on the Resistance Moment of the CFFT Cross-Section

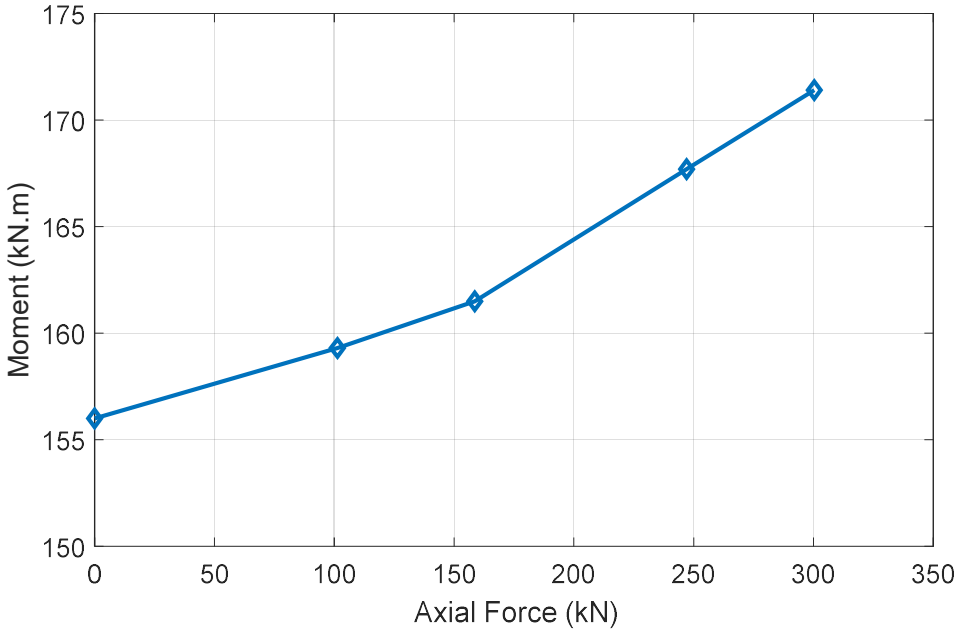

Figure 4-24. Axial Forces vs. Ultimate Resistance Moments of the Arch Cross-Section

4.4.4 Result and Discussion

The influence of the skew angle is investigated by comparing maximum flexural moments and maximum shear forces along the CFFT arches and the maximum shear force at the deck-arch interface of the skewed BCABs against the straight BCAB. The maximum total in-plane, out-of-plane and resultant of these parameters' forces are summarized in Table 4-2 through Table 4-4. In these tables, the location of any variable is given by the number of the corresponding CFFT arch over the percentage of the arc length of the arch (Arch/Arc %), where the Arches are numbered from 1 (West) to 9 (East) and arc% is from zero (South) to 100 (North) as illustrated in Figure 4-22. Results show that the skew angle has a significant effect on the magnitudes and locations of the maximum flexural moments as well as the shear forces in the CFFT arches. Both maximum in-plane moment and shear generally decrease as the skew angle increases. In contrast, both out-of-plane moment and shear force increase as the skew angle increases and for some larger skew angles, the out-of-plane moment and shear force exceed the corresponding in-plane moment and shear, respectively.

For the CFFT arches flexural moments and shear forces increase as the skew angle increases. An extreme loading event is expected to induce high lateral displacements and according to Figure 4-5, the slope of the soil-spring model becomes smaller under such high lateral displacements. Consequently, the superstructure will lose some of its soil restraint under high loadings. This is a good illustration of the need for a nonlinear soil-spring model in the simulation of BCABs responses. Furthermore, Figure 4-25 and Figure 4-26 illustrate the CFFT arches' absolute resultant moment and shear envelopes, respectively. The torsional moment and axial force envelopes are plotted in Figure 4-27 and Figure 4-28, which show the effect of the skew angle parameter on these variables. While both shear and torsional moments increase with increasing skew, the increase is more pronounced for torsion. This implies that for a skewed BCAB, the effect of torsion may need to be considered simultaneously with other stress resultants when checking arch capacity.

The effects of skew angle on the shear forces at the decking-to-CFFT arches interfaces is also assessed in this study as shown in Table 4-4. Although these shear forces do not realistically represent forces in individual connectors between the deck and arch for the reasons discussed in Section 4.2, the results show the significance of the skew angle on the resultant shear force and its components. The peak shear force increases significantly as skew angle increases. Therefore, the number and capacity of the fasteners used to attach the decking on the back of the CFFT arches must be considered for skewed BCAB bridges. If the fasteners between the deck and arches are insufficient, lateral bracing of the arches could be lost, significantly increasing the potential for arch global instability.

From the design point of view, the CFFT arch cross-section assumed here is not practical when it is skewed to more than 30° because the factored ultimate moment M_u of 102.54 kN-m (Table 4-2) exceeds the design moment capacity $\phi M_n = 101.4\ kN.m$ (pure bending) presented previously. In contrast, that Mu is for a section at the north footing of Arch 4 and this section has factored ultimate shear and axial forces of 75 kN and 750 kN, respectively. The comparison with that ϕM_n of pure bending moment is conservative

because of the existence of axial compression that increases moment capacity of the CFFT section (Figure 4-23 and Figure 4-24).

Additional visual representations of the effect of the skew parameter are given in Appendix E (Figure E 1 through Figure E 20). In those figures, more in-plane and out-of-plane flexural moments and shear forces at different BCABs cross-sections are plotted for dead and two cases live loads as. Due to the nonlinearity, the principle of superposition is not applicable. Therefore, live-load moments are calculated from the difference between total moments at the end of each live load analysis and the moments at the end of the dead load (after DW application) analysis.

In the following tables, all entries are absolute values and the resultant entry in any row is not necessarily equal to the resultant of in-plane and out-of-plane entries at that row. Bold entries indicate that in-plane and out-of-plane entries are at the same location. Underlined entries indicate that the out-of-plane moment exceeds the in-plane.

Table 4-2. Maximum Flexural Moments of the CFFT Arches

Load Case	Skew Angle (deg)	In-Plane		Out-of-Plane		Resultant	
		Value (kN-m)	Location Arch/Arc (%)	Value (kN-m)	Location Arch/Arc (%)	Value (kN-m)	Location Arch/Arc (%)
Case 1	0	40.95	5/50	1.32	5/58.33	40.97	5/50
	10	40.82	5/50	13.62	8/0	40.83	5/50
	20	41.14	5/50	28.33	9/0	41.15	5/50
	30	41.11	5/50	43.72	8/0	46.76	8/0
	40	40.21	5/50	62.01	8/0	65.15	8/0
	50	38.74	5/50	76.59	8/0	79.84	8/0
Case 2	0	99.47	5/100	1.29	7/100	99.48	5/100
	10	97.97	4/100	22.48	5/100	100.35	4/100
	20	90.87	4/100	40.85	4/100	99.59	4/100
	30	**85.50**	**4/100**	**56.60**	**4/100**	**102.53**	**4/100**
	40	76.40	3/100	69.65	4/100	103.21	4/100
	50	65.66	3/100	82.61	4/100	105.41	4/100

Table 4-3. Maximum Shear Forces of the CFFT Arches

Load Case	Skew Angle (deg)	In-Plane		Out-of-Plane		Resultant	
		Value (kN)	Location Arch/Arc (%)	Value (kN)	Location Arch/Arc (%)	Value (kN)	Location Arch/Arc (%)
Case 1	0	32.36	5/100	0.36	9/100	32.31	5/100
	10	32.31	5/100	10.89	9/0	33.08	5/100
	20	32.07	5/100	23.41	9/0	34.62	5/0
	30	31.22	5/0	36.55	1/100	37.62	1/100
	40	28.15	5/0	48.83	8/0	49.01	9/0
	50	25.82	5/0	63.36	2/100	63.74	2/100
Case 2	0	57.19	8/25	0.52	7/100	57.19	8/100
	10	60.72	2/100	14.54	3/100	62.28	2/100
	20	58.58	2/100	27.55	3/100	64.33	2/100
	30	55.31	2/100	40.69	4/100	66.94	2/100
	40	**49.58**	**3**/100	**54.43**	**3**/100	**73.68**	**3/100**
	50	**45.19**	**3**/100	**68.48**	**3**/100	**82.05**	**3/100**

Table 4-4. Maximum Shear Forces at the Decking-to-CFFT Arches Interfaces

Load Case	Skew Angle (deg)	In-Plane		Out-of-Plane		Resultant	
		Value (kN)	Location Arch/Arc (%)	Value (kN)	Location Arch/Arc (%)	Value (kN)	Location Arch/Arc (%)
Case 1	0	27.13	4/95.83	0.23	2/4.16	27.13	4/95.83
	10	27.29	8/4.16	3.36	2/4.16	27.43	8/4.16
	20	28.17	8/4.16	6.59	2/4.16	28.77	8/4.16
	30	29.12	8/4.16	10.96	3/4.16	30.69	8/4.16
	40	29.66	8/4.16	14.00	8/95.83	32.75	8/4.16
	50	31.10	3/4.16	19.27	2/4.16	35.67	2/95.83
Case 2	0	27.55	5/4.16	0.244	9/4.16	27.55	5/4.16
	10	27.57	8/4.16	3.83	3/95.83	27.71	8/4.16
	20	28.45	8/4.16	7.04	3/95.83	29.04	8/4.16
	30	29.40	8/4.16	11.27	3/4.16	31.08	3/4.16
	40	29.28	8/4.16	15.51	3/95.83	31.79	3/95.83
	50	30.41	4/95.83	21.20	3/95.83	35.71	3/95.83

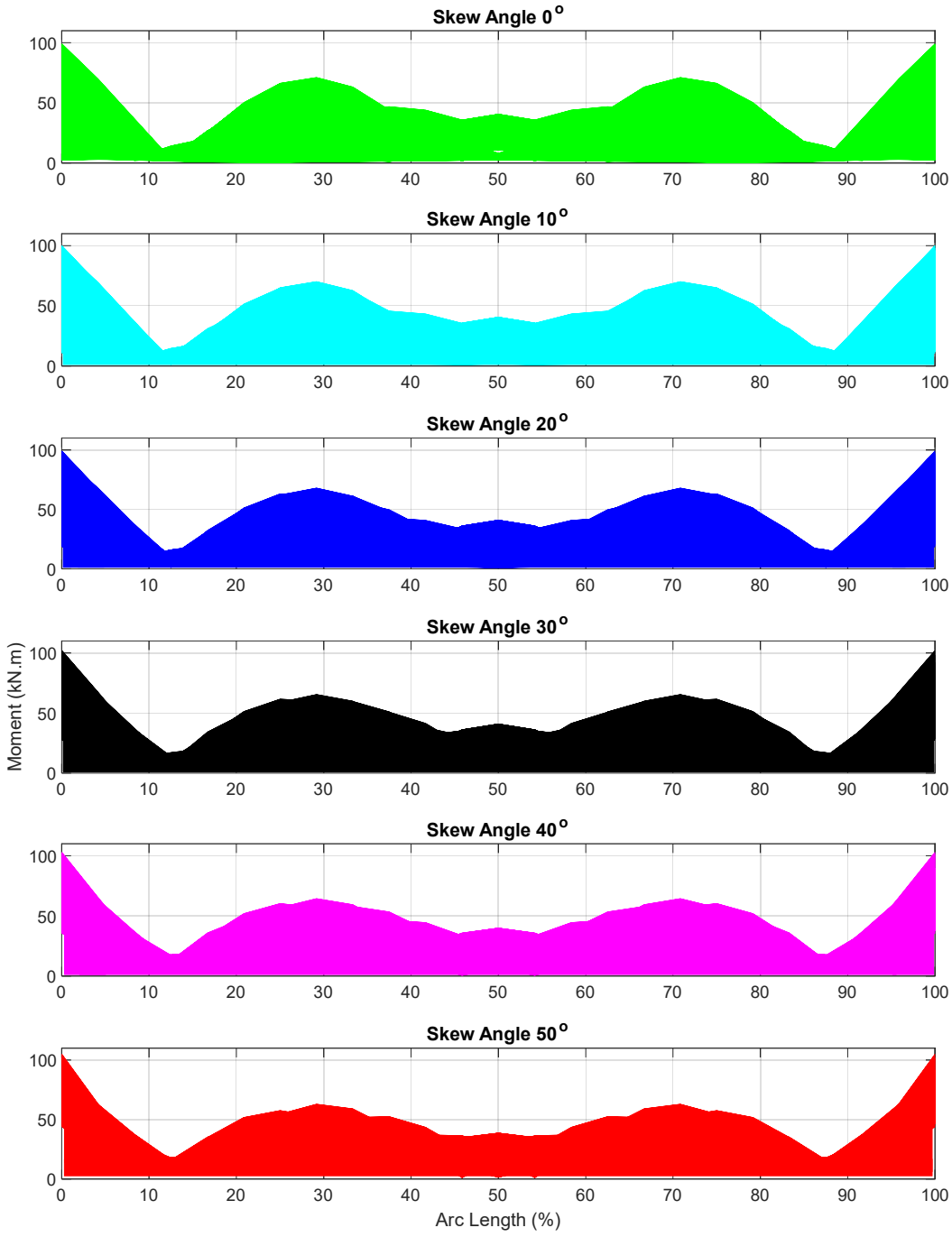

Figure 4-25. Resultant Moment Envelope

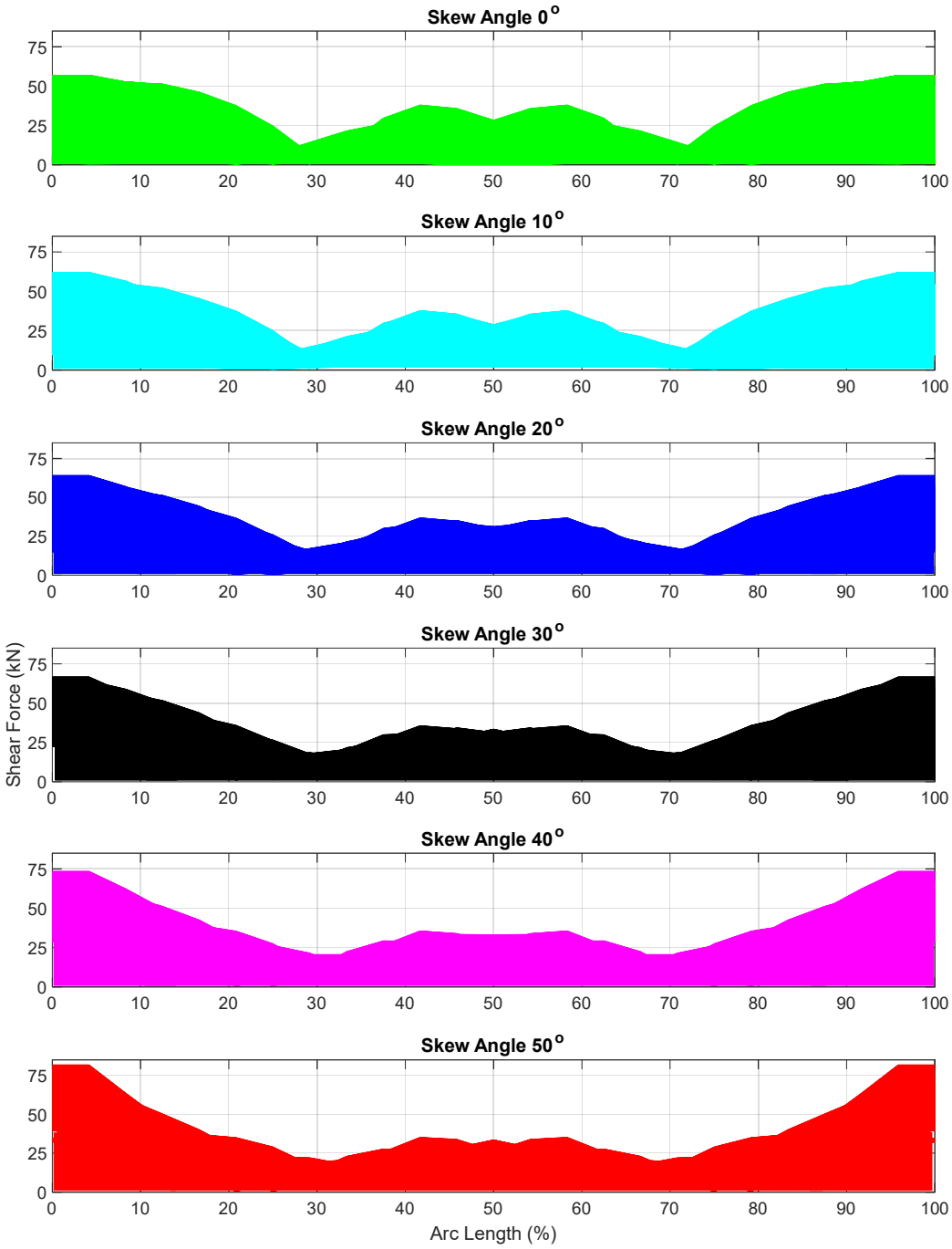

Figure 4-26. Resultant Shear Force Envelope

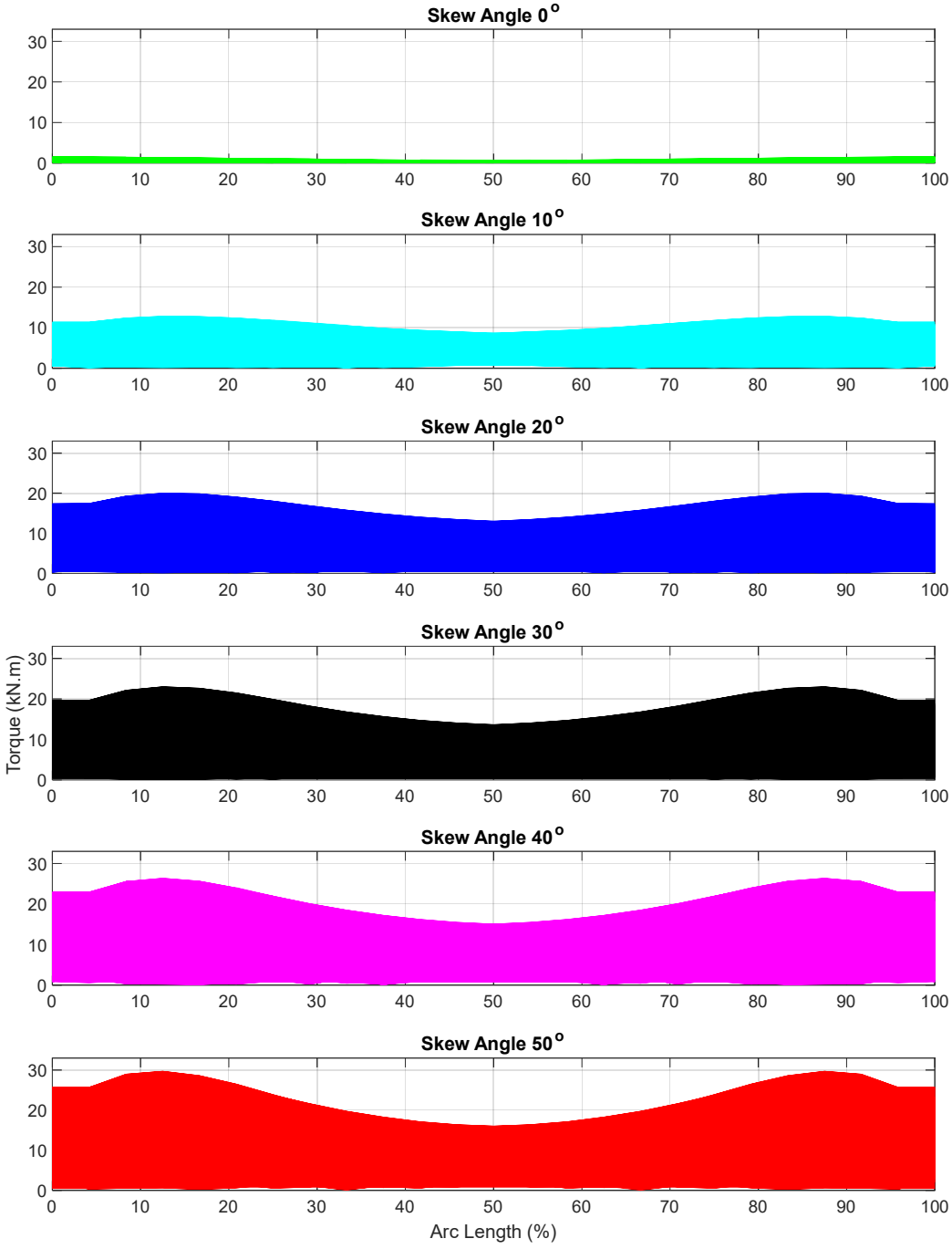

Figure 4-27. Torque Envelope

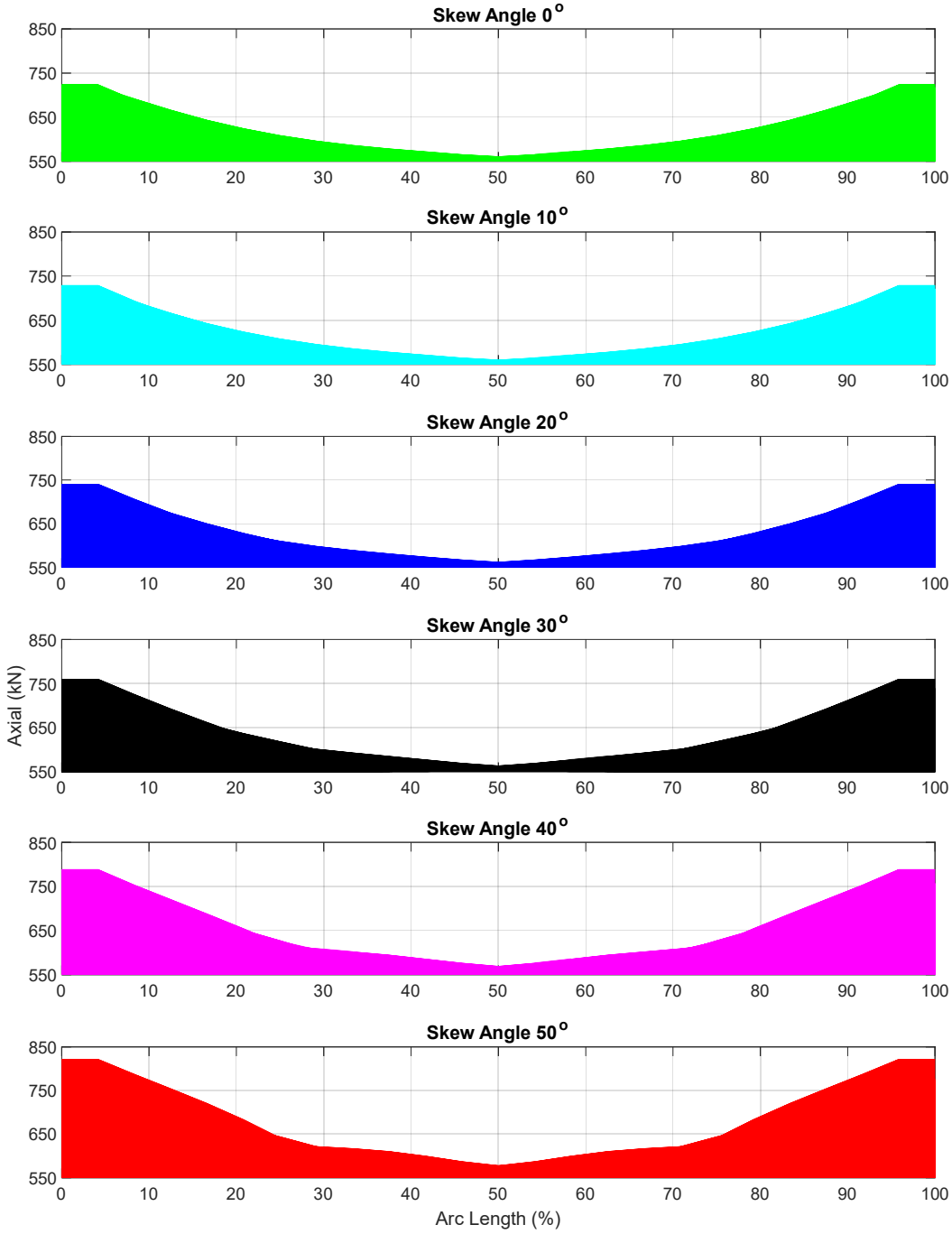

Figure 4-28. Axial Force Envelope (all compression forces)

4.5 Summary and Conclusions

A novel yet practical methodology for 3D simulation of an entire skewed BCAB, including SSI and staged backfilling has been presented. The analysis methodology reflects a computationally efficient structural analysis technique that uses a newly-developed combined FE model. The model consists of two types of elements that capture complexities in the structural response arising from the nonlinear behavior of the CFFT arches, SSI, and transverse effects induced by geometry and load eccentricity in skewed BCABs. The first element is a spatial, co-rotational, FB, fiber-frame element employed to discretize each of the arches and decking elements. This element has unique features for the analysis of CFFT arches that help resolve unique modeling challenges due to the effect of confinement of the concrete core on its stiffness and ductility, as well as the importance of large deformations. The second element is a soil-spring element used to idealize the soil with a series of one-dimensional, nonlinear, axial-only springs connected to each decking node. An effective and unified displacement-dependent model has been adopted to simulate the behavior of these compression-only springs under any state of soil between full active and full passive. Row sets of soil-spring elements are activated when their corresponding nodes are covered by soil during the backfilling process. An efficient multistage simulation was developed to analyze and capture the effect of progressive staged backfilling, wearing surface, and service load applications. To achieve this, the model is brought into equilibrium under any current loading. Subsequently, only the load effect resulting from the next step is required to be analyzed using the stress and loading from the previously resolved state as initial conditions. The well-developed Boussinesq approach with small modifications is adopted to distribute AASHTO HL-93 design uniform lane and vehicular live loads that are applied at the road surface of the bridge. All loads were gathered and represented as point loads applied at the nodes corresponding to their tributary areas, position and the soil depth above each node.

The features of the presented model include computational efficiency and high accuracy despite using coarse mesh. The computational efficiency is derived from the use of FB element formulation that distributes the plasticity and imposes equilibrium at specified integration points, the cross-section fiber

discretization that allows use of uniaxial material constitutive models, the one-dimensional, nonlinear springs and the unified displacement-dependent soil model to idealize soil-structure-interaction, and the multistage simulation that captures the effect of construction sequence. The accuracy of the model is derived from the use of the second order 3D element and the capability of the fiber section model and its discretization that characterize the nonlinear interaction between axial forces and bending moments.

Due to the lack of the experimental work, the analysis is verified by comparison with results measured during laboratory tests of straight buried steel arch bridges found in the literature for an un-skewed bridge. Although the model uses tributary areas to gather loads at nodes, a mesh convergence showed that the model accuracy is enough with a small number of arch elements. The verification analyses showed very good predictions of the proposed model against different responses under different types of loadings.

Finally, a parametric study was undertaken on a generic, two-lane BCAB to investigate the effect of abutment skew angle on bridge capacity, an important practical design concern. BCAB models with skew angles ranging from 0° to 50° were analyzed for different loading stages. The bridges were subjected to factored loads due to the AASHTO Strength I load combination. Although the study was limited to a relatively small number of load cases, the results clearly show the effects of the skew angle on the in-plane and out-of-plane flexural moments and shear forces of the CFFT arches. According to this parametric study, a skewed BCAB must be designed for the section resultant moment and shear envelopes (cylindrical envelopes). The proposed FB model neglected the contribution of torsion in the axial strains, however, the study showed that such contribution is important to be considered in case of skewed BCAB bridges. The proposed model showed that the shear forces at the decking-to-CFFT arches interfaces are most effected by the skew angle. The peak shear force increases significantly as skew angle increases. However, these shear forces do not realistically represent forces in individual connectors between the deck and arch due to the mimicking of FRP deck as transvers and diagonal FB element connected to the arch nodes. These nodes are not necessarily located at the real decking-to-CFFT arches interfaces in addition of neglecting the friction forces and the glue resistance force at these interfaces.

Besides the different sophisticated techniques used in the model presented (distributed plasticity, fiber-section, corotational formulation, FB element determination, displacement-dependent soil model, GDC solver, multistage simulation, etc.), there are some improvements that could further enhance the proposed model. Although the simplified section constitutive relation with adopted uniaxial FRP-confined concrete model was adequate for the parametric study, a 3D FRP-confined concrete model that addresses the interaction between the axial force, bidirectional shear, biaxial bending, and torsion can be implemented. Furthermore, a more practical hysteretic FRP-confined concrete model can be used that combines the envelope curve above with the unloading and reloading as well as the hysteretic rules. The full composite action at the interface between the FRP tube and the concrete core is required by CFFT design specifications and must be verified in accordance with ASSHTO (2012). On the other hand, the assumption of no relative slippage between different fibers is also required in order to use the fiber-section technique (Spacone et al. 1996). However, cylindrical FRP-to-concrete interaction can be implemented to model any level of the composite action at that interface that may exist in the case of a BCAB having a spliced CFFTs. Although the adopted soil model was unified and applicable for practical engineering vertical retaining walls with a free end, a modification on the model may be made to capture the arch curvature and the compaction effects. The proposed model demonstrates the significance of skew angle on the shear force at the decking-to-CFFT arches interfaces. Because the proposed model was largely intended to study the effect of skew angle, the representation of the connecters was not realistic and was affected by the beam element representation of corrugated deck. Therefore, improvements on the representation of connecters in the proposed model are demanding. Such improvements can be achieved by incorporating a shell element in the model to simulate the decking.

CHAPTER 5

RECOMMENDATIONS FOR FUTURE RESEARCH

For future research, there are several topics that warrant investigation to further expand our understanding of the behavior of BCABs and their structural components. That future work can be broadly divided into several topics as outlined below:

- **Splice Optimization**: The FE continuum models presented in Chapter 2 can be used for parametric studies that examine the effect of collar length, collar material and thickness, CFCC length and area, and other applicable factors that are likely to affect splice capacity and failure modes.
- **Foundation Simulation**: Different BCAB foundation configurations should be assessed and investigated. The lateral resistance due to basal shear and soil pressure behind the spread foundation as well as the horizontal resistance of the pile foundations can be included in the 3D presented model in Chapter 4. The effect of skew angle on the bridge abutments can be further investigated.
- **CFFT Arches Shape Optimization**: The shape of the CFFT arches is very important in the design of BCAB as it has a major effect on the way that the structure responds during different sequential loadings. Other geometries such as elliptic or multi-radius circular-segment arches can be investigated in future analyses. Parametric studies on the effect of the skew angle can be further conducted to optimize the shape of the CFFT arches. The shape optimization including the skew may tend to decrease the foundation thrust and increase the CFFT arch design capacities.
- **Backfill Crown Depth Optimization**: BCABs are considered as semi-rigid buried structures in well-compacted granular soil. Their design and analysis are based on SSI as that soil loads the structure due to its weight, restrains the structure due to horizontal earth pressure, and dissipate the vehicular live loads. Under a shallow depth of backfill, the structure may fail by initiating shear or tension failure in the backfill cover above BCAB crown. Therefore, an optimization of the minimum soil depth needs to be done in the future.

- **Incorporate More Realistic Models of Decking and Arch-Deck Connectors:** The model showed the significance of the skew effect on the shear force at the decking-to-CFFT arch interfaces. The idealization of the decking and the connectors using beam elements as done here is an approximation since the decking is constructed as a continuous diaphragm with glued and mechanically-fastened transverse joints. The inclusion of shell elements to model the decking would be more realistic and allow the assessment of in-plane shear-induced in the decking by abutment skew.
- **Model Verifications:** The presented model here has only been compared with previous experimental and numerical work relating to straight buried steel arch bridges. While those comparisons indicate reasonable accuracy of the model, additional experimental work should be performed to validate the response of the skewed structures assessed here.

In addition to the research topics detailed above, there may be value in extending the FE software developed here to become a design tool. The 3D combined model presented in Chapter 4 was developed as a research tool, and all its routines were written as MATLAB functions, i.e., the model inputs and outputs are text-based files. Integration of this FE software with a graphical user interface would give an integrated tool suitable for the analysis of multi-arch, skewed BCABs.

REFERENCES

AASHTO. (2012). *LRFD Guide Specifications for Design of Concrete-Filled FRP Tubes for Flexural and Axial Members*. 1st Edition, American Asociation of State Highway and Transportation Officials, Washington, DC, USA.

AASHTO. (2017). *LRFD Bridge Design Specifications*. 7th Edition, American Asociation of State Highway and Transportation Officials, Washington, DC, USA.

Abdelkarim, O., and ElGawady, M. (2015). "Concrete-filled-large deformable FRP tubular columns under axial compressive loading." *Fibers*, 3(4), 432–449.

ACI Committee 318. (2008). *Building Code Requirements for Structural Concrete*. *ACI 318-08*, American Concrete Institute, Farmington Hills, Michigan, USA.

ACI Committee 318. (2014). "Building code requirements for structural concrete." *ACI 318-14*, American Concrete Institute, Farmington Hills, Michigan, USA.

ACI Committee 440. (2015). *Guide for the design and construction of structural concrete reinforced with FRP bars*. *ACI 440.1R-15*, American Concrete Institute, Farmington Hills, Michigan, USA.

ACI Committee 440. (2017). *Guide for the design and construction of externally bonded FRP systems for strengthening existing structures*. *ACI 440.2R-17*, American Concrete Institute, Farmington Hills, Michigan, USA.

Ahmad, I., Zhu, Z., and Mirmiran, A. (2008). "Behavior of short and deep beams made of concrete-filled fiber-reinforced polymer tubes." *Journal of Composites for Construction*, 12(1), 102–110.

Ahmed, I. (1999). "Shear response and bending fatigue behavior of concrete -filled fiber reinforced polymer tubes." *PhD dissertation, North Carolina State University*.

AIT. (2019). "Resources Website." Advanced InfrastructureTechnologies, Orono, Maine, USA, <http://www.aitbridges.com/>.

Alshand Inc. (2016). *DERAKANE 610C Epoxy Vinyl Ester Resin*. In DERAKANE ® Epoxy Vinyl Ester Resins.

ARTBA. (2018). *Bridges Inventory of Maine*. American Road & Transportation Builders Association, Washington, D.C.,USA. https://www.artba.org/wp-content/uploads/bridge-inventory/ (Excel File).

Ashland Inc. (2016). *Technical Datasheet: Pliogrip 7770 Urethane Adhesive System*.

ASTM. (2008). *Standard test method for tensile properties of polymer matrix composite materials*. *D3039*, ASTM International, Pennsylvania, USA.

ASTM. (2015). *Standard test method for pullout strength of hardened Concrete*. *C900*, ASTM International, Pennsylvania, USA.

Ayranci, C., and Carey, J. (2008). "2D braided composites: A review for stiffness critical applications." *Composite Structures*, 85(1), 43–58.

Bannon, D. J. (2009). “Characterization of concrete-filled fiber-reinforced polymer arch members.” MS Thesis, University of Maine, Orono, Maine.

Barbero, E. J. (2011). *Introduction to Composite Materials Design*. Taylor & Francis Group, Florida.

Burgueño, R. (1999). “System Characterization and Design of Modular Fiber Reinforced Polymer (FRP) Short- and Medium-Span Bridges.” University of Calfornia.

Burns, J. (2016). “Splicing of concrete-filled fiber reinforced polymer tubes for structural applications.” MS Thesis, University of Maine, Orono, Maine.

Chung, W., He, Y., and An, Z.-O. (2010). “Numerical and experimental investigation of concrete-filled FRP tube.” *CICE 2010 - The 5th International Conference on FRP Composites in Civil Engineering September 27-29, 2010*, Beijing, China.

Cole, B., and Fam, A. (2006). “Flexural load testing of concrete-filled FRP tubes with longitudinal steel and FRP rebar.” *Journal of Composites for Construction*, 10(2), 161–171.

Cox, B. N., and Flanagan, G. (1997). “Handbook Composites of Analytical Methods for Textile.” *NASA Contractor Report*, (March 1997), 176.

Crisfield, M. A. (1990). “A consistent co-rotational formulation for non-linear, three-dimensional, beam-elements.” *Computer Methods in Applied Mechanics and Engineering*, 81(2), 131–150.

Dagher, H. J., Bannon, D. J., Davids, W. G., Lopez-Anido, R. A., Nagy, E., and Goslin, K. (2012). “Bending behavior of concrete-filled tubular FRP arches for bridge structures.” *Construction and Building Materials*, Elsevier Ltd, 37, 432–439.

Das, B. M. (2013). *Advanced soil mechanics*. Crc Press.

Davol, A., Burgueño, R., and Seible, F. (2001). “Flexural behavior of circular concrete FRP shells.” *Structural Engineering*, 127(7), 810–817.

Demkowicz, M. (2011). “Environmental durability of hybrid braided polymer matrix composites for infrastructure applications.” MS Thesis, University of Maine, Orono, Maine.

Du, Z. L., Liu, Y. P., and Chan, S. L. (2017). “A second-order flexibility-based beam-column element with member imperfection.” *Engineering Structures*, Elsevier Ltd, 143, 410–426.

Echevarria, A., Zaghi, A. E., Christenson, R., and Accorsi, M. (2016). “CFFT bridge columns for multihazard resilience.” *Journal of Structural Engineering*, 142(8), C4015002.

ElGawady, M. A., and Dawood, H. M. (2012). “Analysis of segmental piers consisted of concrete filled FRP tubes.” *Engineering Structures*, Elsevier Ltd, 38, 142–152.

Fam, A. Z., Greene, R., and Rizkalla, S. H. (2003a). “Field applications of concrete-filled FRP tubes for marine piles.” *ACI Special Publication*, (SP-215-9), 161–180.

Fam, A. Z., Pando, M., Filz, G., and Rizkalla, S. H. (2003b). “Precast piles for Route 40 bridge in Virginia using concrete filled FRP tubes.” *PCI journal*, 48(3), 32–45.

Fam, A. Z., and Rizkalla, S. H. (2002). “Flexural Behavior of Concrete-Filled Fiber-Reinforced Polymer Circular Tubes.” *Journal of Composites for Construction*, 6(2), 123–132.

FHWA. (2018). *National Bridge Inventory*. The Federal Highway Administration, U.S. Department of Transportation, Washington D.C., USA. https://www.fhwa.dot.gov/bridge/nbi/no10/yrblt.pdf.

Goslin, K., Davids, W., Lopez-Anido, R., Walton, H., and Clapp, J. (2015). *Bridge-in-a-Backpack™, Monitoring and Load Rating*.

Hany, N. F., Hantouche, E. G., and Harajli, M. H. (2016). “Finite element modeling of FRP-confined concrete using modified concrete damaged plasticity.” *Engineering Structures*, Elsevier Ltd, 125, 1–14.

Helmi, K., Fam, A., and Mufti, A. (2005). “Field installation, splicing, and flexural testing of hybrid FRP/concrete piles.” *ACI Special Publication*, Vol. SP-23, 1103–1120.

Helmi, K., Fam, A., Mufti, A., and Hall, J. M. (2006). “Effects of driving forces and bending fatigue on structural performance of a novel concrete-filled fibre-reinforced-polymer tube flexural pile.” *Canadian Journal of Civil Engineering*, 33(6), 683–691.

Hu, D., and Barbato, M. (2014). “Simple and efficient finite element modeling of reinforced concrete columns confined with fiber-reinforced polymers.” *Engineering Structures*, 72, 113–122.

Hussein Abdallah, M., Shazly, M., Mohamed, H. M., Masmoudi, R., and Mousa, A. (2017). “Nonlinear finite element analysis of short and long reinforced concrete columns confined with GFRP tubes.” *Journal of Reinforced Plastics and Composites*, 36(13), 972–987.

Jafari, V., Abyaneh, M. A., Vahdani, S. H., and Rahimian, M. (2009). “Improved displacement-field approximation for geometrical nonlinear flexibility-based planar curved element in state space.” *Mechanics Based Design of Structures and Machines*, 37(4), 475–502.

Kabir, M. Z., and Shafei, E. (2012). “Plasticity modeling of FRP-confined circular reinforced concrete columns subjected to eccentric axial loading.” *Composites Part B: Engineering*, Elsevier Ltd, 43(8), 3497–3506.

Karbhari, V. M., Seible, F., Burgueño, R., Davol, A., Wernli, M., and Zhao, L. (2000). “Structural characterization of fiber-reinforced composite short-and medium-span bridge systems.” *Applied Composite Materials*, 7(2–3), 151–182.

Leon, S. E., Paulino, G. H., Pereira, A., Menezes, I. F. M., and Lages, E. N. (2011). “A Unified Library of Nonlinear Solution Schemes.” *Applied Mechanics Reviews*, 64(4), 040803.

Li, Z. X. (2006). “A mixed co-rotational formulation of 2D beam element using vectorial rotational variables.” *Communication in Numerical Methods in Engineering*, 23, 45–69.

MaineDOT. (2018). *Maine Public Bridge Structurs in the Municipality of Lagrange*. https://www.maine.gov/mdot/bridges/docs/bridgereports/Lagrange.pdf.

MathWorks Inc. (2018). “MATLAB 2018a.” Massachusetts, USA.

Mirmiran, A., and Shahawy, M. (1997). “Fiber reinforced plastic (‘FRP’)-concrete composite structural members, United States Patent.” United States Patent, United States Patent.

Mirmiran, A., Zagers, K., and Yuan, W. (2000). “Nonlinear finite element modeling of concrete confined by fiber composites.” *Finite elements in analysis and design*, 35(1), 79–96.

Mohamed, H. M., and Masmoudi, R. (2010). “Flexural strength and behavior of steel and FRP-reinforced concrete-filled FRP tube beams.” *Engineering Structures*, Elsevier Ltd, 32(11), 3789–3800.

Monti, G., Nistico, N., and Santini, S. (2001). “Design of FRP Jackets for Upgraded of Circular Bridge Pires.” 5(May), 94–101.

Neuenhofer, A., and Filippou, F. C. (1997). “Evaluation of nonlinear frame finite element models.” *Journal of Structural Engineering*, 123(7), 958--966.

Neuenhofer, A., and Filippou, F. C. (1998). “Geometrically Nonlinear Flexibility-Based Frame Finite Element.” *Journal of Structural Engineering*, 124(6), 704–711.

Ni, P., Ph, D., Mangalathu, S., Ph, D., Asce, A. M., Song, L., Ph, D., Mei, G., Ph, D., Zhao, Y., and Ph, D. (2018). “Displacement-Dependent Lateral Earth Pressure Models.” 144(6), 1–12.

Parry, H. (2013). “Splicing and local reinforcement of concrete filled FRP tubes (CFFTS).” MS Thesis, University of Maine, Orono, Maine.

Qasrawi, Y., Heffernan, P. J., and Fam, A. (2016). “Numerical Modeling of Concrete-Filled FRP Tubes’ Dynamic Behavior under Blast and Impact Loading.” *Journal of Structural Engineering*, 142(2), 04015106.

Simulia Inc. (2017). “Abaqus/CAE [Computer Software].” Rhode Island, USA.

Son, J. K., and Fam, A. (2008). “Finite element modeling of hollow and concrete-filled fiber composite tubes in flexure: Model development, verification and investigation of tube parameters.” *Engineering Structures*, 30(10), 2656–2666.

de Souza, R. M. (2000). “Force-based finite element for large displacement inelastic analysis of frames.” PhD dissertation, University of California, Berkeley, California.

Soykasap, O. (2011). “Analysis of plain-weave composites.” *Mechanics of Composite Materials*, 47(2), 161–176.

Spacone, E., Filippou, F. C., and Taucer, F. F. (1996). “Fibre Beam Column Model for Nonlinear Analysis of R/C Frames: Part I. Formulation.” *Earthquake Engineering and Structural Dynamics*, 25, 711–725.

Tao, Y., and Chen, J. F. (2015). “Concrete damage plasticity model for modeling FRP-to-concrete bond behavior.” *Journal of Composites for Construction*, 19(1), 1–13.

Teng, J. G., Huang, Y. L., Lam, L., and Ye, L. P. (2007). “Theoretical model for fiber-reinforced polymer-confined concrete.” *Journal of Composites for Construction*, 11(2), 201–210.

Teng, J. G., Jiang, T., Lam, L., and Luo, Y. Z. (2009). “Refinement of a design-oriented stress strain model for FRP confined concrete.” *Journal of Composite Construction*, 13(4), 269–278.

Tokyo Rope Inc. (2017). *CFCC carbon fiber composite cable*. Tokyo, Japan.

Walton, H. J. (2011). "Response of FRP arches to concrete filling loads." MS Thesis, University of Maine, Orono, Maine.

Walton, H. J. (2015). "Behavior of buried composite buried arch bridges." PhD dissertation, University of Maine, Orono, Maine.

Walton, H. J., Davids, W. G., Landon, M. E., and Clapp, J. D. (2016a). "Experimental Evaluation of Buried Arch Bridge Response to Backfilling and Live Loading." *Journal of Bridge Engineering*, American Society of Civil Engineers, 21(9), 4016052.

Walton, H. J., Davids, W. G., Landon, M. E., and Clapp, J. D. (2016b). "Simulation of buried arch bridge response to backfilling and live loading." *Journal of Bridge Engineering*, 21(9), 1–11.

Wang, H., Chen, H., Zhou, Y., Wang, P., Zhou, J., and Fan, H. (2019). "Blast responses and damage evaluation of CFRP tubular arches." *Construction and Building Materials*, Elsevier Ltd, 196, 233–244.

Yang, Y. B., Lin, S. P., and Leu, L. J. (2007). "Solution strategy and rigid element for nonlinear analysis of elastically structures based on updated Lagrangian formulation." *Engineering Structures*, 29(6), 1189–1200.

Yang, Y. B., and Shieh, M. S. (1990). "Solution method for nonlinear problems with multiple critical points." *AIAA Journal*, 28(12), 2110–2116.

Youssf, O., ElGawady, M. A., Mills, J. E., and Ma, X. (2014). "Finite element modelling and dilation of FRP-confined concrete columns." *Engineering Structures*, Elsevier Ltd, 79, 70–85.

Yu, T., Teng, J. G., Wong, Y. L., and Dong, S. L. (2010a). "Finite element modeling of confined concrete-II: Plastic-damage model." *Engineering Structures*, Elsevier Ltd, 32(3), 680–691.

Yu, T., Teng, J. G., Wong, Y. L., and Dong, S. L. (2010b). "Finite element modeling of confined concrete-I: Drucker-Prager type plasticity model." *Engineering Structures*, Elsevier Ltd, 32(3), 665–679.

Yuan, F., Wu, Y. F., and Li, C. Q. (2017). "Modelling plastic hinge of FRP-confined RC columns." *Engineering Structures*, Elsevier Ltd, 131, 651–668.

Zhu, Z., Ahmad, I., and Mirmiran, A. (2006). "Splicing of precast concrete-filled FRP tubes." *Journal of Composites for Construction*, 10(4), 345–356.

Zhu, Z., Ahmad, I., and Mirmiran, A. (2009). "Fatigue modeling of concrete-filled fiber-reinforced polymer tubes." *Journal of Composites for Construction*, 13(6), 582–590.

APPENDICES

Appendix A: Curvature Based Displacement Interpolation (CBDI)

The CBDI formulas used to interpolate the curvatures field $\boldsymbol{\kappa}_z$ and $\boldsymbol{\kappa}_y$, and to evaluate the lateral displacements **v** and **w** at the FB element integration points using the influence matrix $\mathbf{I}^*$ are summarized in Table A 1. For further details, see de Souza (2000).

Table A 1.Summary of CBDI

Planar FB Element Chapter 3	**Spatial FB Element Chapter 4**
$\mathbf{v} = \mathbf{I}^*\boldsymbol{\kappa}$	$\mathbf{v} = \mathbf{I}^*\boldsymbol{\kappa}_z$ $\mathbf{w} = \mathbf{I}^*\boldsymbol{\kappa}_y$
$\mathbf{v} = [\, v(\xi_1) \quad v(\xi_2) \quad \dots \quad v(\xi_n)]^T$	$\mathbf{v} = [\, v(\xi_1) \quad v(\xi_2) \quad \dots \quad v(\xi_n)]^T$ $\mathbf{w} = [\, w(\xi_1) \quad w(\xi_2) \quad \dots \quad w(\xi_n)]^T$
$\boldsymbol{\kappa} = [\kappa(\xi_1) \quad \kappa(\xi_2) \quad \dots \kappa(\xi_n)]^T$	$\boldsymbol{\kappa}_z = [\, \kappa_z(\xi_1) \quad \kappa_z(\xi_2) \quad \dots \kappa_z(\xi_n)]^T$ $\boldsymbol{\kappa}_y = [\, \kappa_y(\xi_1) \quad \kappa_y(\xi_2) \quad \dots \kappa_y(\xi_n)]^T$
$\mathbf{I}^* = \mathbf{L^2}\begin{bmatrix} \frac{1}{2}({\xi_1}^2 - \xi_1) & \frac{1}{6}({\xi_1}^3 - \xi_1) & \cdots & \frac{1}{n(n+1)}({\xi_n}^{n+1} - \xi_1) \\ \frac{1}{2}({\xi_2}^2 - \xi_2) & \cdots & \ddots & \vdots \\ \vdots & \ddots & \ddots & \vdots \\ \frac{1}{2}({\xi_n}^2 - \xi_n) & \frac{1}{6}({\xi_n}^3 - \xi_n) & \cdots & \frac{1}{n(n+1)}({\xi_n}^{n+1} - \xi_n) \end{bmatrix}\mathbf{G^{-1}}$	
$\mathbf{G} = \begin{bmatrix} 1 & \xi_1 & \cdots & {\xi_1}^{n-1} \\ 1 & \xi_2 & \cdots & \vdots \\ \vdots & \vdots & \ddots & \vdots \\ 1 & \xi_n & \cdots & {\xi_n}^{n-1} \end{bmatrix}$	

$\frac{\partial \mathbf{v}}{\partial \mathbf{P}} = \mathbf{B}\mathbf{a}^*$	$\begin{Bmatrix} \frac{\partial \mathbf{v}}{\partial \mathbf{P}} \\ \frac{\partial \mathbf{w}}{\partial \mathbf{P}} \end{Bmatrix} = \begin{bmatrix} \mathbf{A_z} & \mathbf{B} \\ \mathbf{B} & \mathbf{A_y} \end{bmatrix}^{-1} \begin{Bmatrix} \mathbf{I}^* \mathbf{a_z} \\ -\mathbf{I}^* \mathbf{a_y} \end{Bmatrix}$
$\mathbf{B} = \mathbf{A}^{-1}\mathbf{I}^*$	$\mathbf{B} = \mathbf{I}^*(\mathbf{If_{23}})P_1$
$\mathbf{A} = \mathbf{I} - \mathbf{I}^*(\mathbf{If_{22}})P_1$	$\mathbf{A_z} = \mathbf{I} - \mathbf{I}^*(\mathbf{If_{22}})P_1$ $\mathbf{A_y} = \mathbf{I} - \mathbf{I}^*(\mathbf{If_{33}})P_1$
$\mathbf{a}^* = [\mathbf{f_{21}} + (\mathbf{If_{22}})\mathbf{v} \quad (\mathbf{If_{22}})(\boldsymbol{\xi} - \mathbf{1}) \quad (\mathbf{If_{22}})\boldsymbol{\xi}]$	$\mathbf{a_z} = [\mathbf{a_{z\_\xi_1}} \quad \mathbf{a_{z\_\xi_2}} \quad \cdots \quad \mathbf{a_{z\_\xi_n}}]^T$ $\mathbf{a_y} = [\mathbf{a_{y\_\xi_1}} \quad \mathbf{a_{y\_\xi_2}} \quad \cdots \quad \mathbf{a_{y\_\xi_n}}]^T$ $\mathbf{a_{z\_\xi_i}} = \mathbf{f_{2_{\xi_i}}}\mathbf{b}_{\xi_i}$ and $\mathbf{a_{y\_\xi_i}} = \mathbf{f_{3_{\xi_i}}}\mathbf{b}_{\xi_i}$
$\mathbf{f_{21}} = [f_{2,1}^{sec}(\xi_1) \quad f_{2,1}^{sec}(\xi_2) \quad \cdots \quad f_{2,1}^{sec}(\xi_n)]^T$ $\mathbf{f_{22}} = [f_{2,2}^{sec}(\xi_1) \quad f_{2,2}^{sec}(\xi_2) \quad \cdots \quad f_{2,2}^{sec}(\xi_n)]^T$ $\mathbf{f_{23}} = [f_{2,3}^{sec}(\xi_1) \quad f_{2,3}^{sec}(\xi_2) \quad \cdots \quad f_{2,3}^{sec}(\xi_n)]^T$ $\mathbf{f_{33}} = [f_{3,3}^{sec}(\xi_1) \quad f_{3,3}^{sec}(\xi_2) \quad \cdots \quad f_{3,3}^{sec}(\xi_n)]^T$ $\mathbf{f_{2_{\xi_i}}} = [f_{2,1}^{sec}(\xi_i) \quad f_{2,2}^{sec}(\xi_i) \quad f_{2,3}^{sec}(\xi_i) \quad f_{2,4}^{sec}(\xi_i)]$ $\mathbf{f_{3_{\xi_i}}} = [f_{3,1}^{sec}(\xi_i) \quad f_{3,2}^{sec}(\xi_i) \quad f_{3,3}^{sec}(\xi_i) \quad f_{3,4}^{sec}(\xi_i)]$	
$\boldsymbol{\xi} = [1 \quad 2 \quad \ldots \quad n]^T$ $\mathbf{I}$ is $(n \times n)$ identity matrix, and $\mathbf{1}$ is a column vector of ones of a length n. $\mathbf{f}^{sec}$ is the section flexibility matrix shown in Equation 3.16 (planar) or Equation 4.13 (spatial) for the ith integration point. $\mathbf{b}_{\xi_i}$ is the force interpolation function shown in Equation 4.6 for the ith integration point.	

Appendix B: The Global Incremental-Iterative Solver

The simplified step-by-step solution algorithm is summarized below in accordance with the GDC as a nonlinear iterative-incremental solver including the element state determination process is as the following:

1. Define the initial state: $\mathbf{U}_0$, $\mathbf{R_0}$ and $\mathbf{Q}_0$ then assemble the initial tangent stiffness matrix $\widehat{\mathbf{K}}_0$.
2. Select a reference load vector $\widehat{\mathbf{Q}}$, the first load increment λ_1 and set the reference load factor $\Lambda = 0$.
3. Start loop over the load increments.
4. Start loop over iteration at the structure level.

   4.1. For the first iteration at each incremental step:

      4.1.1. Solve $\Delta\widehat{\mathbf{U}} = \widehat{\mathbf{K}}_0^{-1}\widehat{\mathbf{Q}}$

      4.1.2. For the first increment, set GSP = 1; for other increments, use Equation 3.29 to determine GSP.

      4.1.3. Use Equation 3.28 to determine λ as the sign of λ_1.

      4.1.4. Check the value of GSP. If GSP is negative, then multiply obtained in step (4.13) by −1.

      4.1.5. Evaluate the displacement increments as $\Delta\mathbf{U} = \lambda\Delta\widehat{\mathbf{U}}$.

   4.2. Compute the structural displacements $\mathbf{U}$ and the corresponding total external loads $\mathbf{Q}$ using Equation 3.25 and Equation 3.26, respectively.

   4.3. Start loop over all the elements of the structure.

      4.3.1. Element State Determination algorithm as presented in Appendix C.

      4.3.2. Assemble the tangent stiffness matrix and set it as $\widehat{\mathbf{K}}_0$.

      4.3.3. Assemble the vector of residual loads and set it as $\mathbf{R}_0$.

   4.4. Updated history variables for the next iteration: $\mathbf{Q}_0 = \mathbf{Q}$, $\mathbf{U}_0 = \mathbf{U}$.

   4.5. $\Lambda = \Lambda + \lambda$

   4.6. For the remaining iterations ($iteration \neq 1$):

      4.6.1. Evaluate $\Delta\widehat{\mathbf{U}}$ and $\Delta\overline{\mathbf{U}}$ through Equation 3.22 and Equation 3.23, respectively.

      4.6.2. Use Equation 3.29 to determine λ.

      4.6.3. Compute the displacement increments $\Delta\mathbf{U}$ through Equation 3.24.

4.7. Repeat steps (4.2-4.5)

4.8. If ($\boldsymbol{R} < tolerance$), exit loop; otherwise, next iteration and go to steps (4.6 and 4.7).

5. If ($\Lambda > 1$), exit loop; otherwise, the next increment and go to step (4.6).

Appendix C: State Determination Algorithm

Iterations at the element level were performed such that the residual displacements fall below a specified tolerance within each global iteration. The iterative procedure is accomplished with the following state determination algorithm.

1. Gather the total end element forces without rigid body modes: $\mathbf{P} = \mathbf{P}_0 + \Delta\mathbf{P}$;
2. Compute corresponding sections force increments: $\Delta\mathbf{S} = \mathbf{b}_0\mathbf{P}$;
3. Determine trial sections deformations: $\Delta\mathbf{d} = \mathbf{k}_0^{sec\,-1}\Delta\mathbf{S}$;
4. Store accumulated section deformations: $\mathbf{d} = \mathbf{d}_0 + \Delta\mathbf{d}$;
5. Determining the corresponding lateral displacement $\mathbf{v}$, through;
6. Update the force interpolation matrices $\mathbf{b}$ and the composite matrices $\mathbf{b}^*$ using Equation 3.8 and Equation 3.12, respectively;
7. Updated section stiffness matrices $\mathbf{k}^{\boldsymbol{sec}}$ and corresponding flexibility matrices $\mathbf{f}^{\boldsymbol{sec}}$ using Equation 3.15 and Equation 3.16, respectively;
8. Determine updated element end displacement $\mathbf{D}^{\boldsymbol{ele}}$ and element flexibility matrix $\mathbf{F}^{\boldsymbol{ele}}$ using Equation 3.13 Equation 3.18, respectively;
9. Compute trial section forces $\mathbf{S} = \mathbf{bP}$;
10. Determine the residual displacements: $\mathbf{r} = \mathbf{D} - \mathbf{D}^{\mathbf{ele}}$, where $\mathbf{D}$ obtained from Equation 3.3;
11. Compute the residual end forces: $\Delta\mathbf{P} = \mathbf{F}^{ele\,-1}\mathbf{r}$;
12. Update history variables for the next iteration: $\mathbf{P}_0 = \mathbf{P}$, $\mathbf{b}_0 = \mathbf{b}$, $\mathbf{d}_0 = \mathbf{d}$, $\mathbf{k}_0^{sec} = \mathbf{k}^{sec}$, and $\mathbf{S}_0 = \mathbf{S}$;
13. If ($\mathbf{r} <$ tolerance), exit loop; otherwise, go to step (1).

For the next load step, the stiffness matrix $\mathbf{K}^{ele}$ and the geometric stiffness matrix $\mathbf{K}_G{}^{ele}$ can be determined through Equation 3.19 and Equation 3.31, respectively. Then, the element resisting forces $\widehat{\mathbf{P}}$ and the tangent stiffness matrix $\widehat{\mathbf{K}}^{ele}$ in the global system can be calculated according to Equation 3.32 and Equation 3.33, respectively.

Appendix D: FRP Decking Properties and Diagonal Elements Stiffness Sensitivity Analysis

Table D 1. Geometrical and Material Properties Provided by AIT

Support Spans	5ft
Load Condition:	Projected Uniform Pressure (12.5psi)
Part Resin System:	4000 Series Urethane

Material Properties	Standard Structurals
Lengthwise Modulus (Msi):	2.98
Crosswise Modulus (Msi):	2.88
Inplane Shear Modulus (Msi):	0.65

Material Strengths	Unconditioned Strength Values	Strength Reduction Factor (♦)	Allowable Strength Values[1] w/ Phi Factors	Allowable Strength Values[1] w/o Phi Factors
Lengthwise Tensile Strength (psi):	64,000	0.65	14,976	23,040
Lengthwise Compression Strength (psi):	64,000	0.70	16,128	23,040
Crosswise Tensile Strength (psi):	43,000	0.65	10,062	15,480
Crosswise Compression Strength (psi):	43,000	0.70	10,836	15,480
Inplane Shear Strength (psi):	22,000	0.65	5,148	7,920
Interlaminar Shear Strength (psi):	14,000	0.65	3,276	5,040

Environmental Considerations	
Strength Knockdown Factor for Temperature:	1.00
Strength Knockdown Factor for Moisture:	0.90
Time Effect Factor (λ)[2]:	0.40

	6" Wide Rigid PVC Support			2" Wide Rigid PVC Support		
	FEA Predicted Values	Factor of Safety Against Allowable Strength Values w/ Phi Factor	Factor of Safety Against Allowable Strength Values w/o Phi Factor	FEA Predicted Values	Factor of Safety Against Allowable Strength Values w/o Phi Factor	Factor of Safety Against Allowable Strength Values w/o Phi Factor
Flange						
Lengthwise Tension:	8,883	1.69	2.59	10,198	1.47	2.26
Lengthwise Compression:	13,334	1.21	1.73	17,524	0.92	1.31
Crosswise Tension:	3,030	3.32	5.11	3,966	2.54	3.90
Crosswise Compression:	7,956	1.36	1.95	12,718	0.85	1.22
Inplane Shear:	1,822	2.83	4.35	2,207	2.33	3.59
Interlaminar Shear:	1,647	1.99	3.06	2,579	1.27	1.95
Radius						
Lengthwise Tension:	6,341	2.36	3.63	6,453	2.32	3.57
Lengthwise Compression:	16,749	0.96	1.38	22,403	0.72	1.03
Crosswise Tension:	3,013	3.34	5.14	4,734	2.13	3.27
Crosswise Compression:	9,136	1.19	1.69	15,166	0.71	1.02
Inplane Shear:	3,138	1.64	2.52	4,805	1.07	1.65
Interlaminar Shear:	4,439	0.74	1.14	7,249	0.45	0.70
Web						
Lengthwise Tension:	6,341	2.36	3.63	9,995	1.50	2.31
Lengthwise Compression:	16,749	0.96	1.38	11,952	1.35	1.93
Crosswise Tension:	971	10.36	15.94	1,539	6.54	10.06
Crosswise Compression:	11,477	0.94	1.35	14,818	0.73	1.04
Inplane Shear:	3,084	1.67	2.57	4,360	1.18	1.82
Interlaminar Shear:	2,477	1.32	2.03	695	4.71	7.25
Global Buckling Factor:	4.60	1.33	1.66	10.82	3.12	3.89
Displacement Vector Sum (in):	0.291			0.311		

FRP decking cross-section is shown in Figure D 1 having 20.924-in width, 7.561-in2 cross-sectional area, and 15.237-in4 and 264.205-in4 second moment of area about the weak and strong axes, respectively

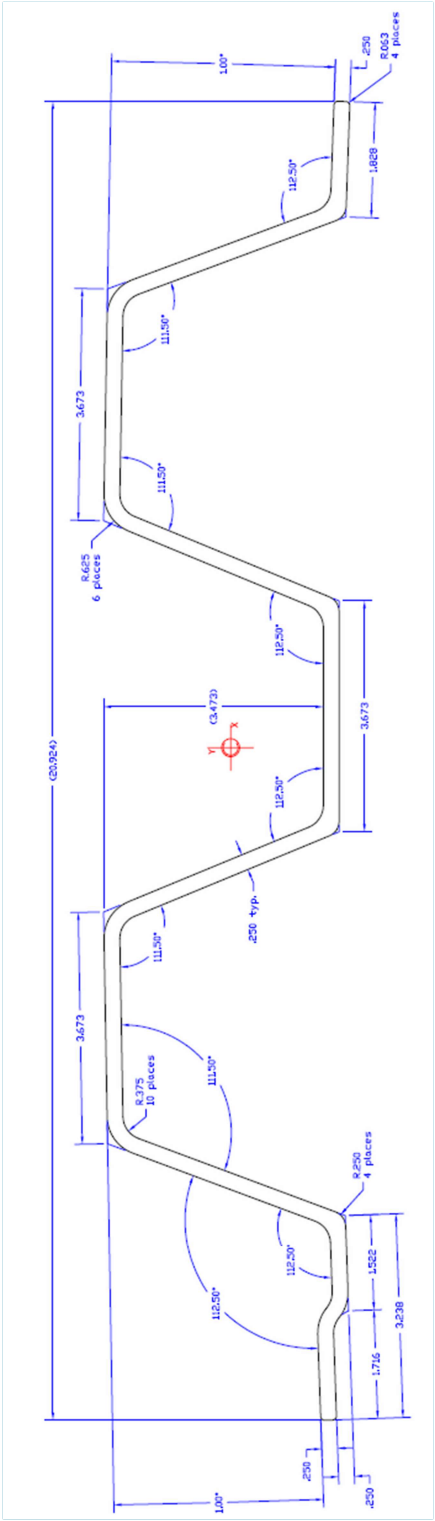

Figure D 1. FRP decking cross-section Provided by AIT

The following figures were plotted according to a 40° skew angle.

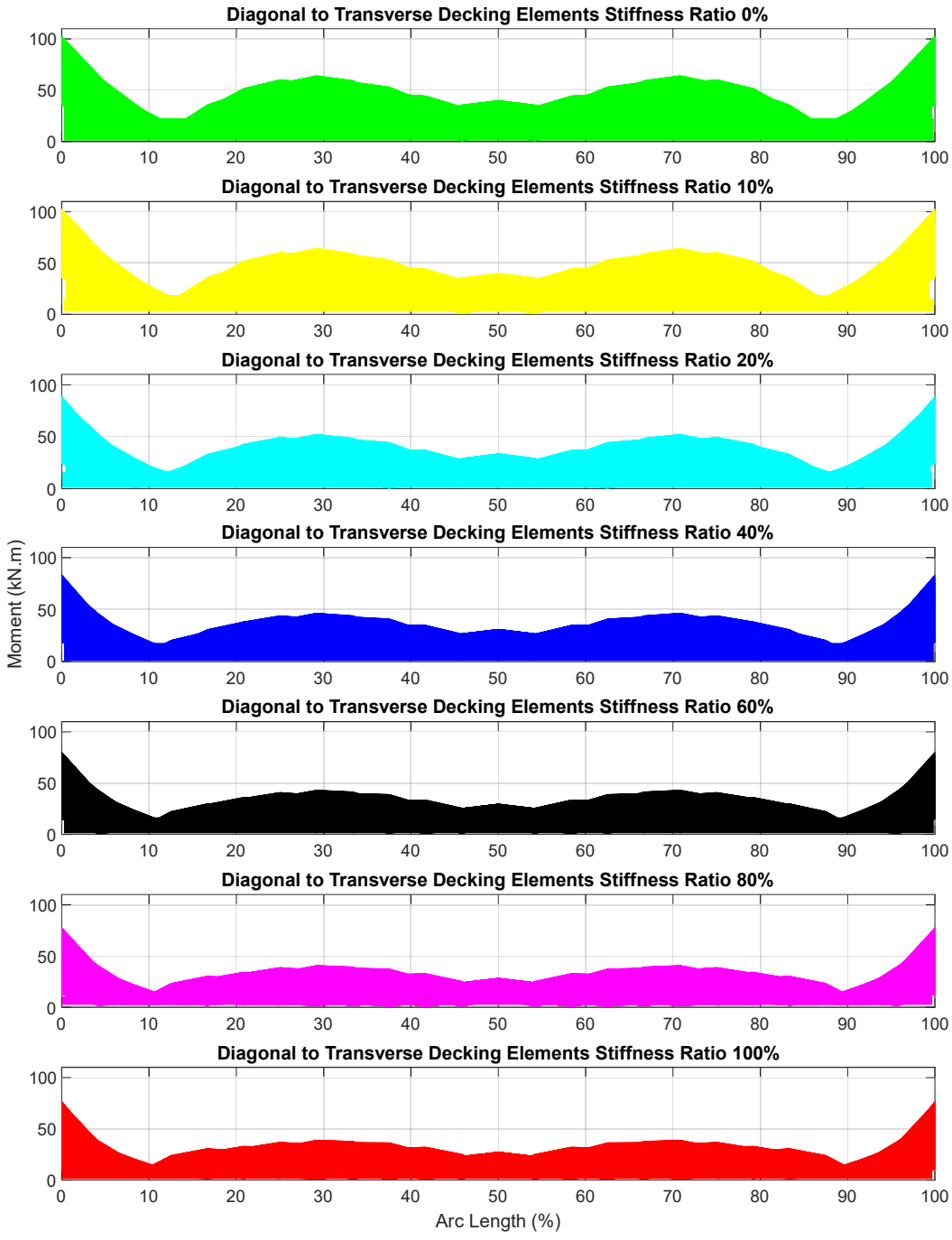

Figure D 2.. Resultant Moment Envelope

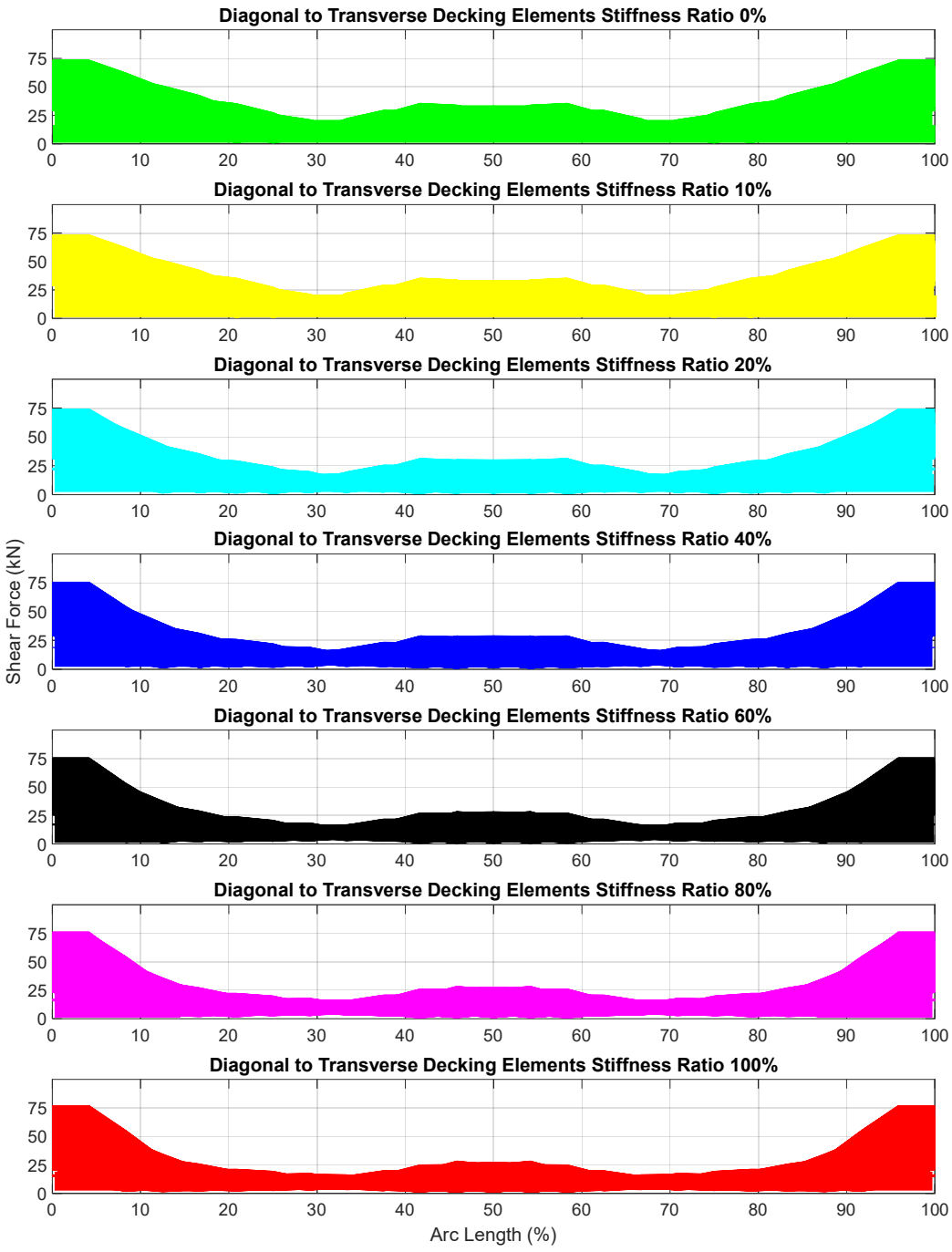

Figure D 3. Resultant Shear Force Envelope

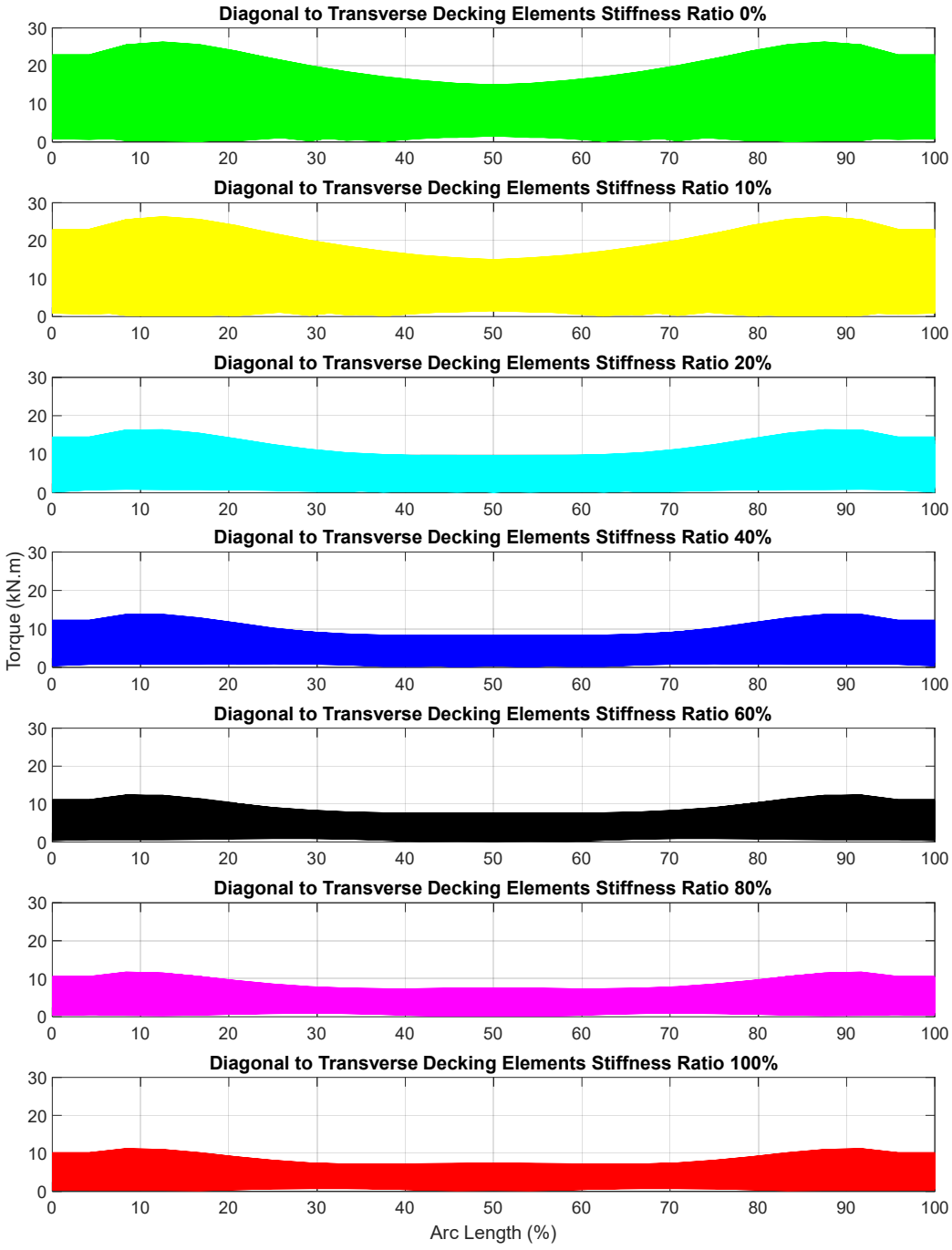

Figure D 4. Torque Envelope

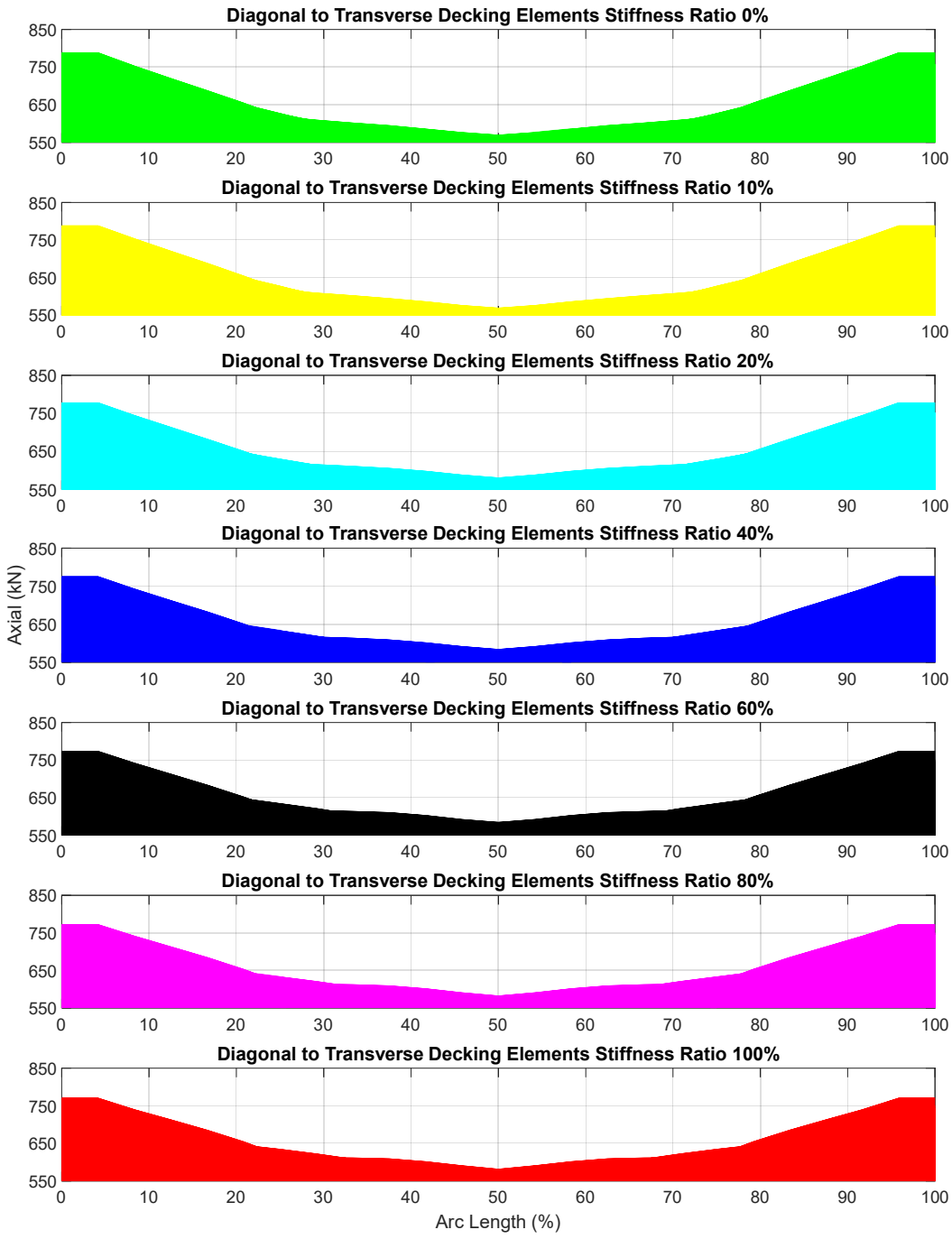

Figure D 5. Axial Force Envelope (all compression forces)

Appendix E: Visual Representation of the Influence of the Skew Angle

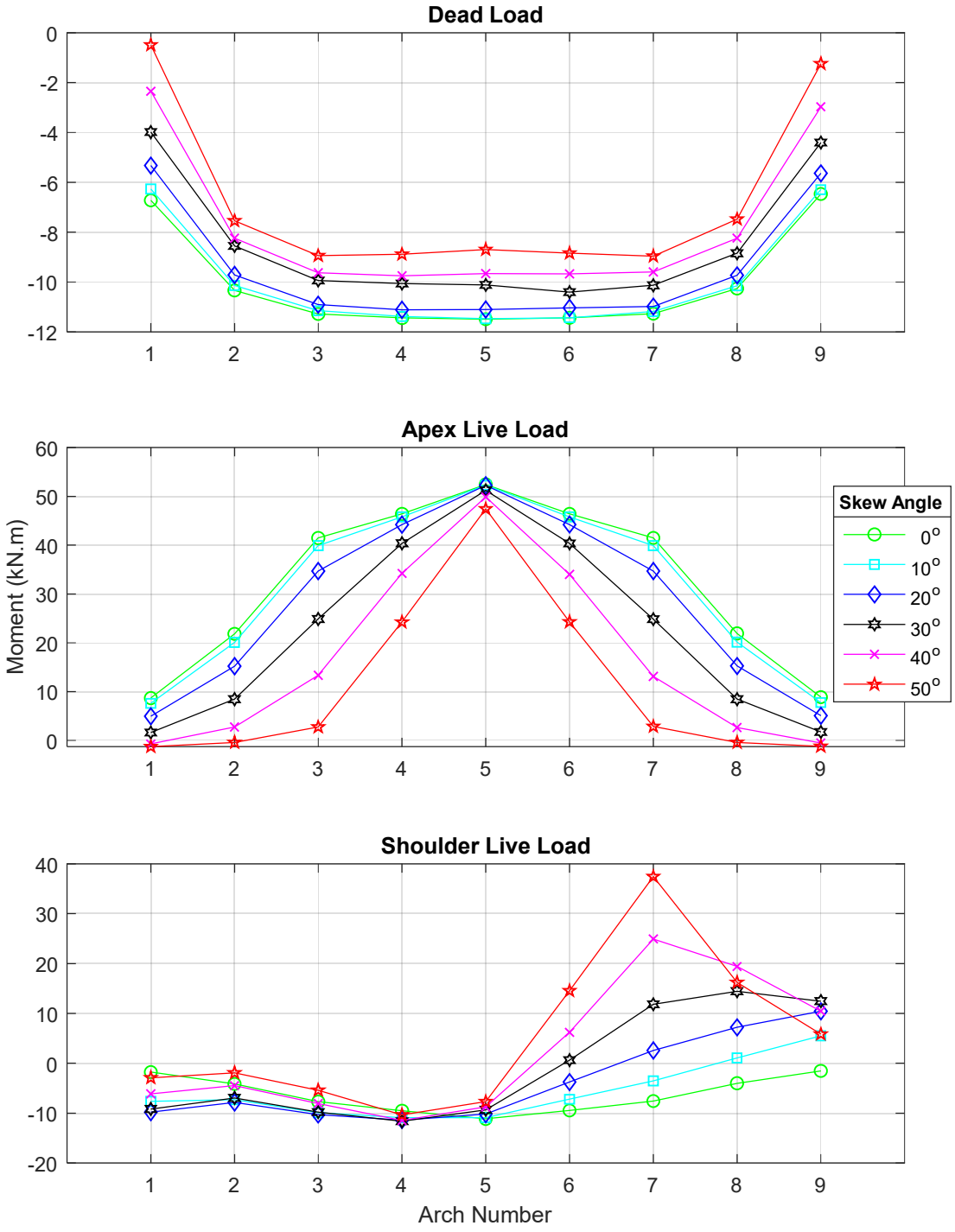

Figure E 1. Strength I: Apexes In-plane Moment

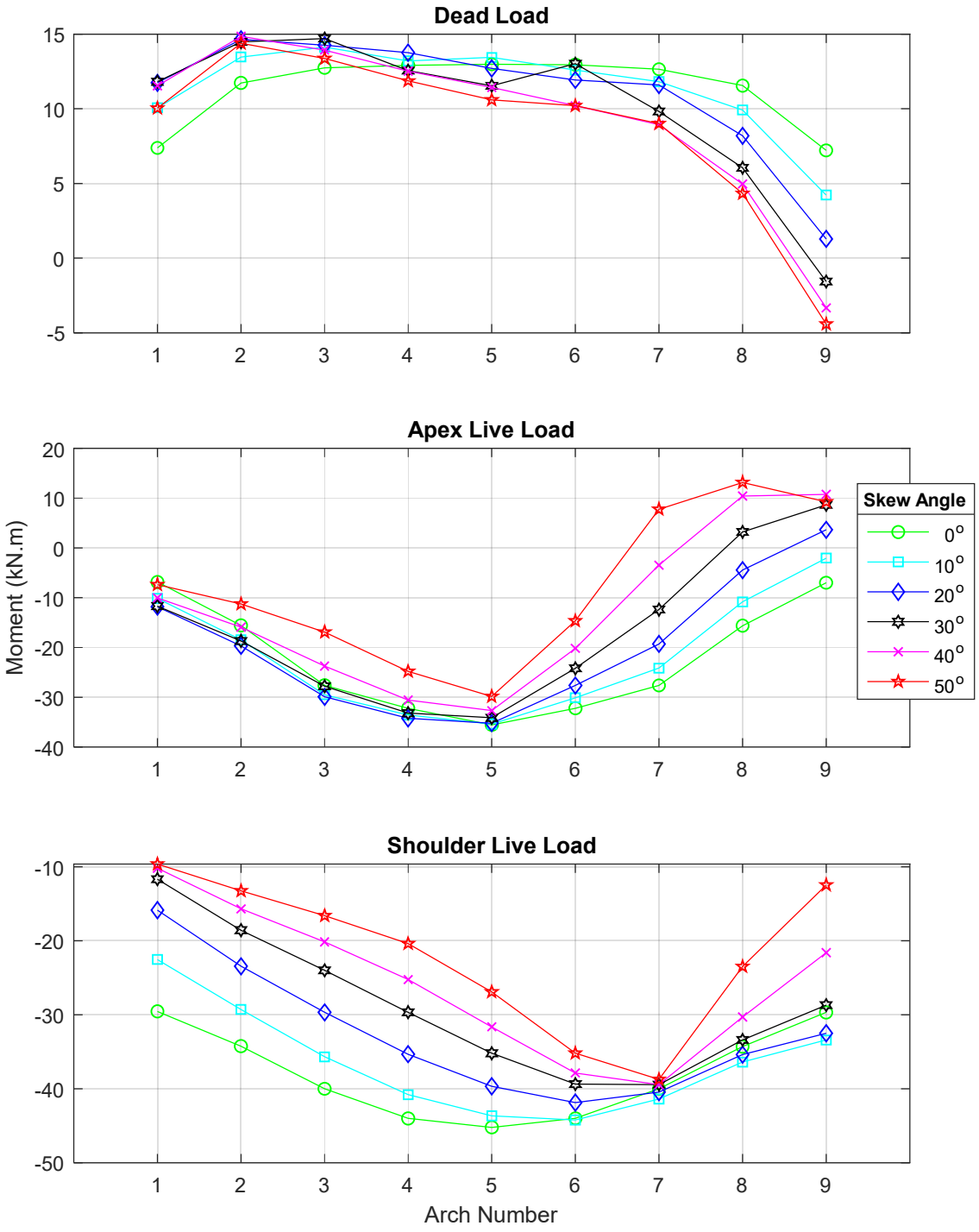

Figure E 2. Strength I: South Shoulders In-Plane Moment

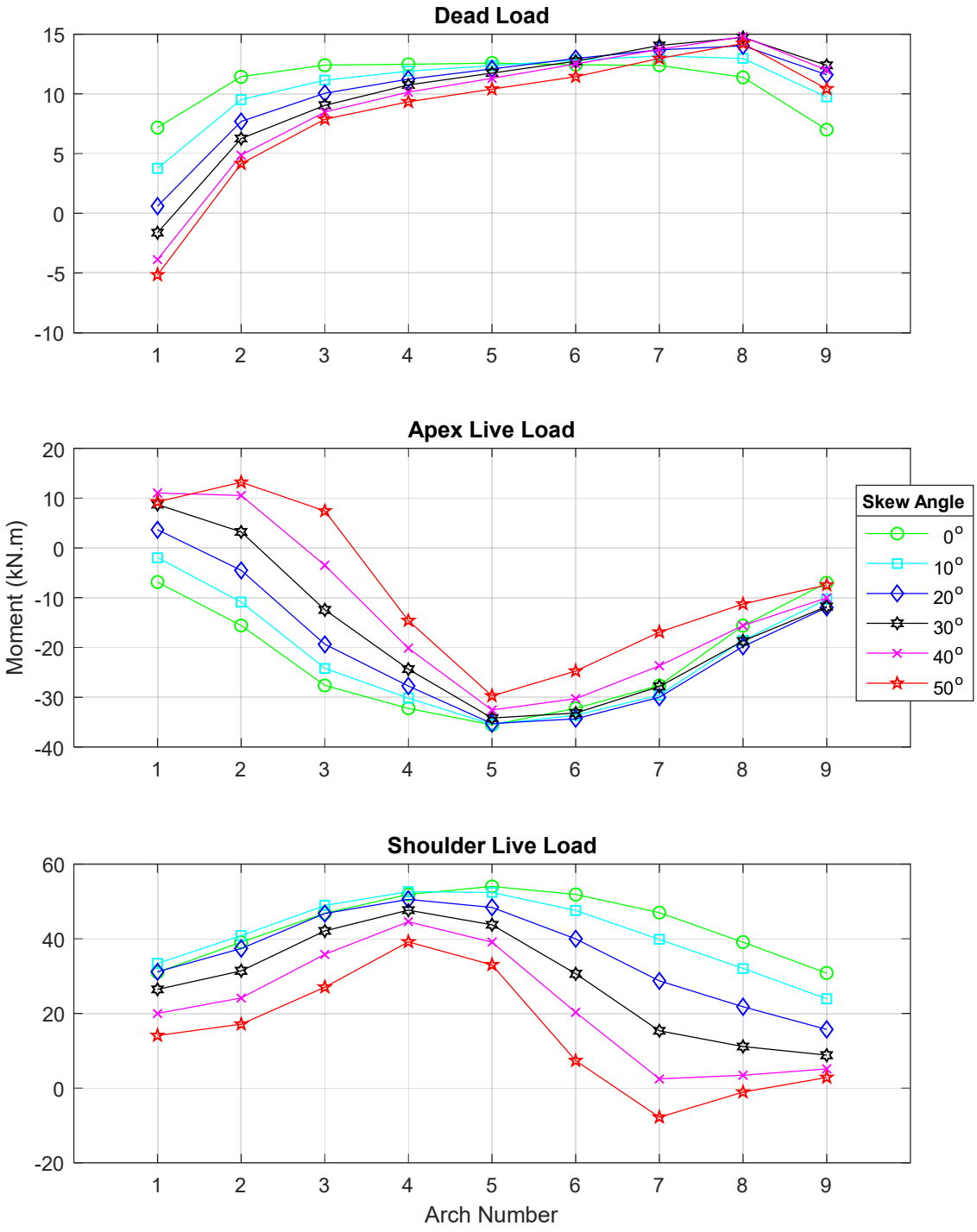

Figure E 3. Strength I: North Shoulders In-Plane Moment

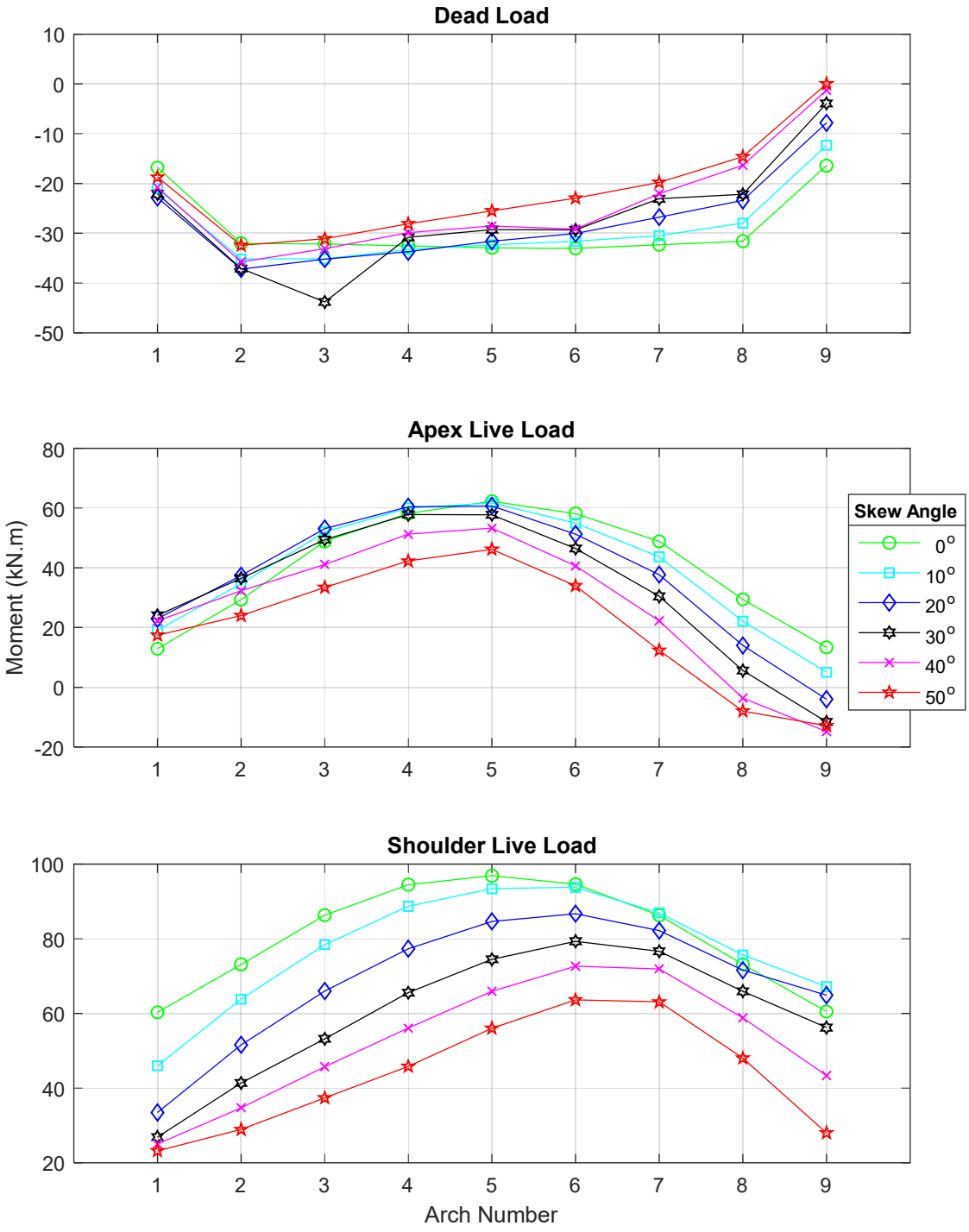

Figure E 4. Strength I: South Footings In-Plane Moment

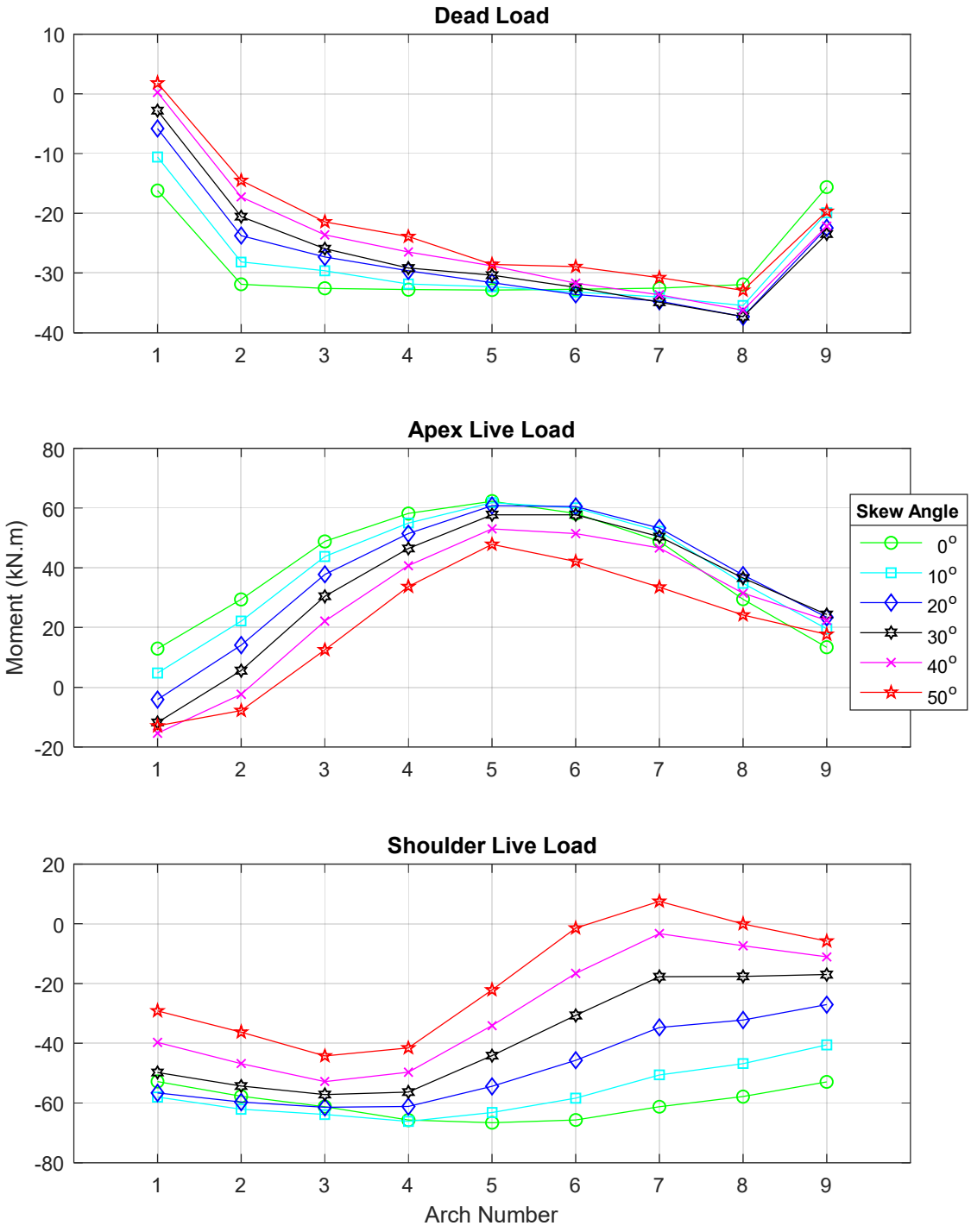

Figure E 5. Strength I: North Footings In-Plane Moment

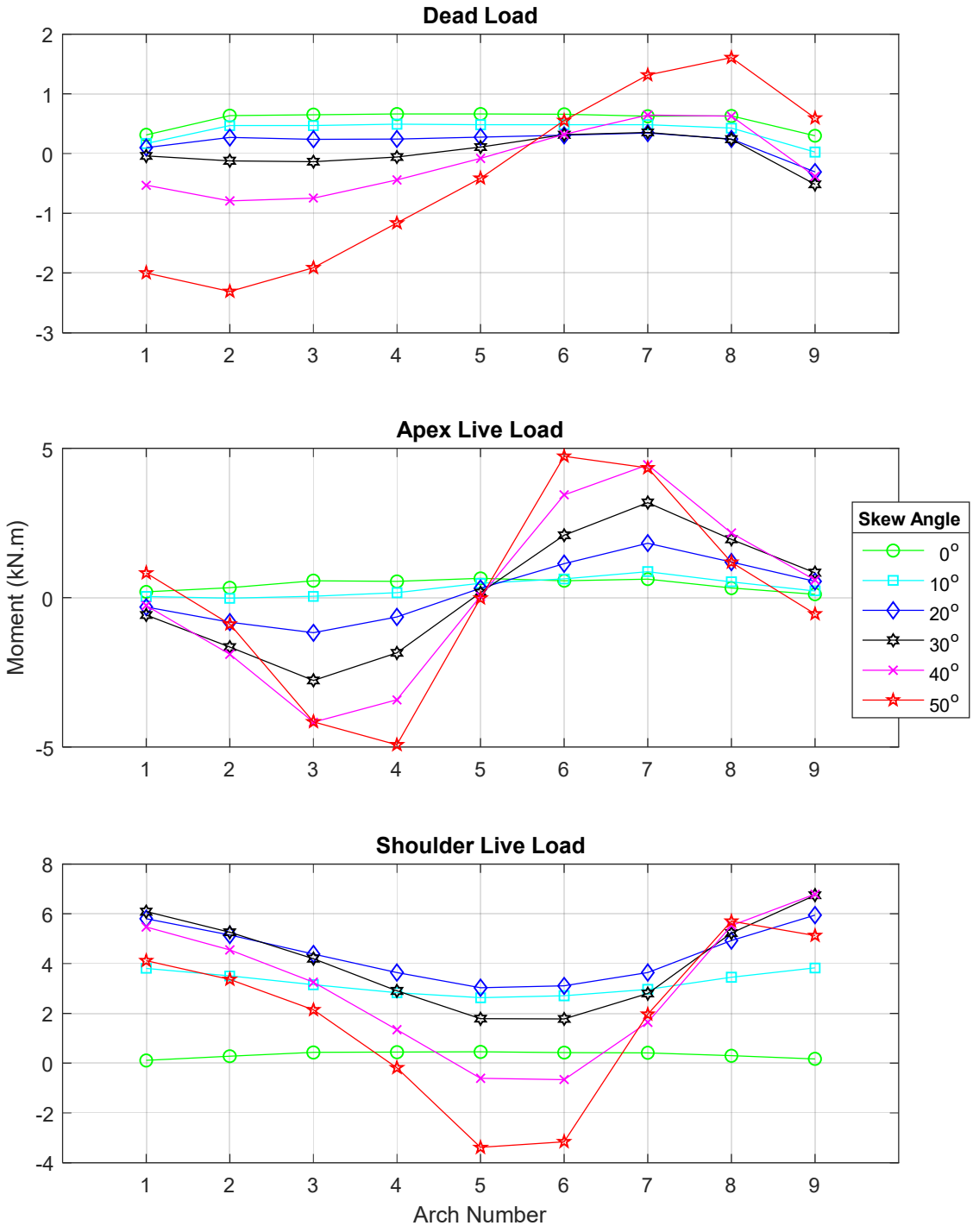

Figure E 6. Strength I: Apexes Out-of-Plane Moment

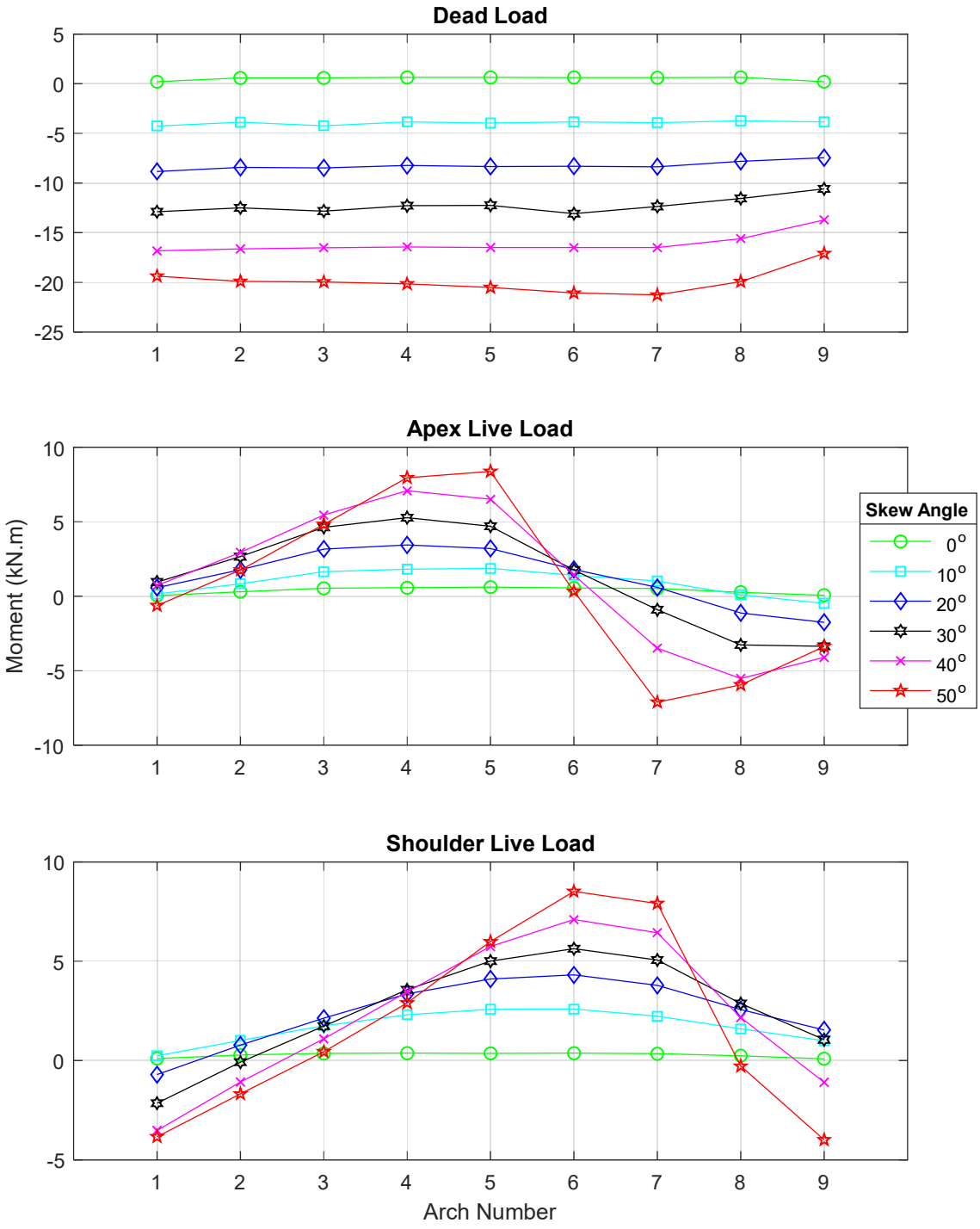

Figure E 7. Strength I: South Shoulders Out-of-Plane Moment

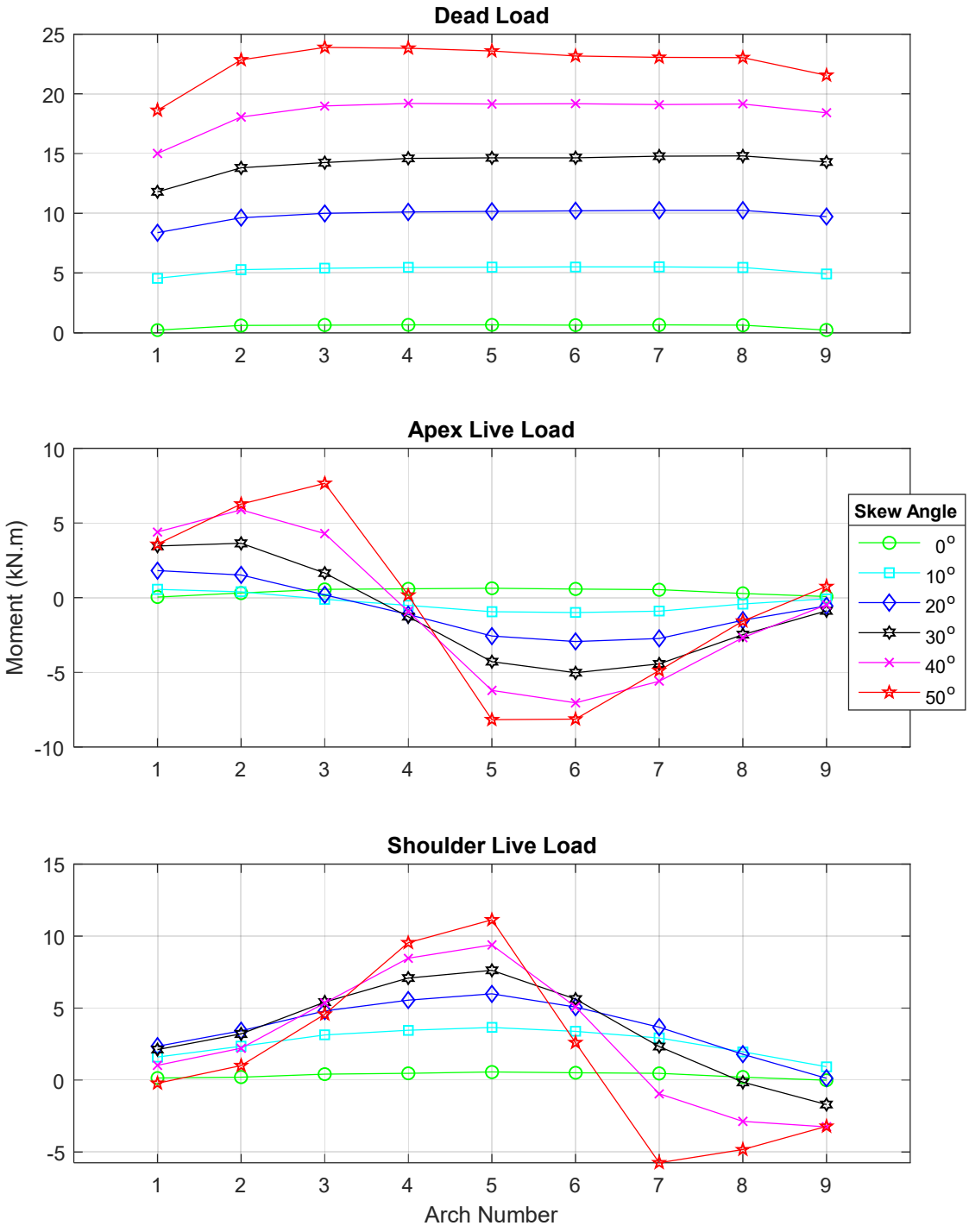

Figure E 8. Strength I: North Shoulders Out-of-Plane Moment

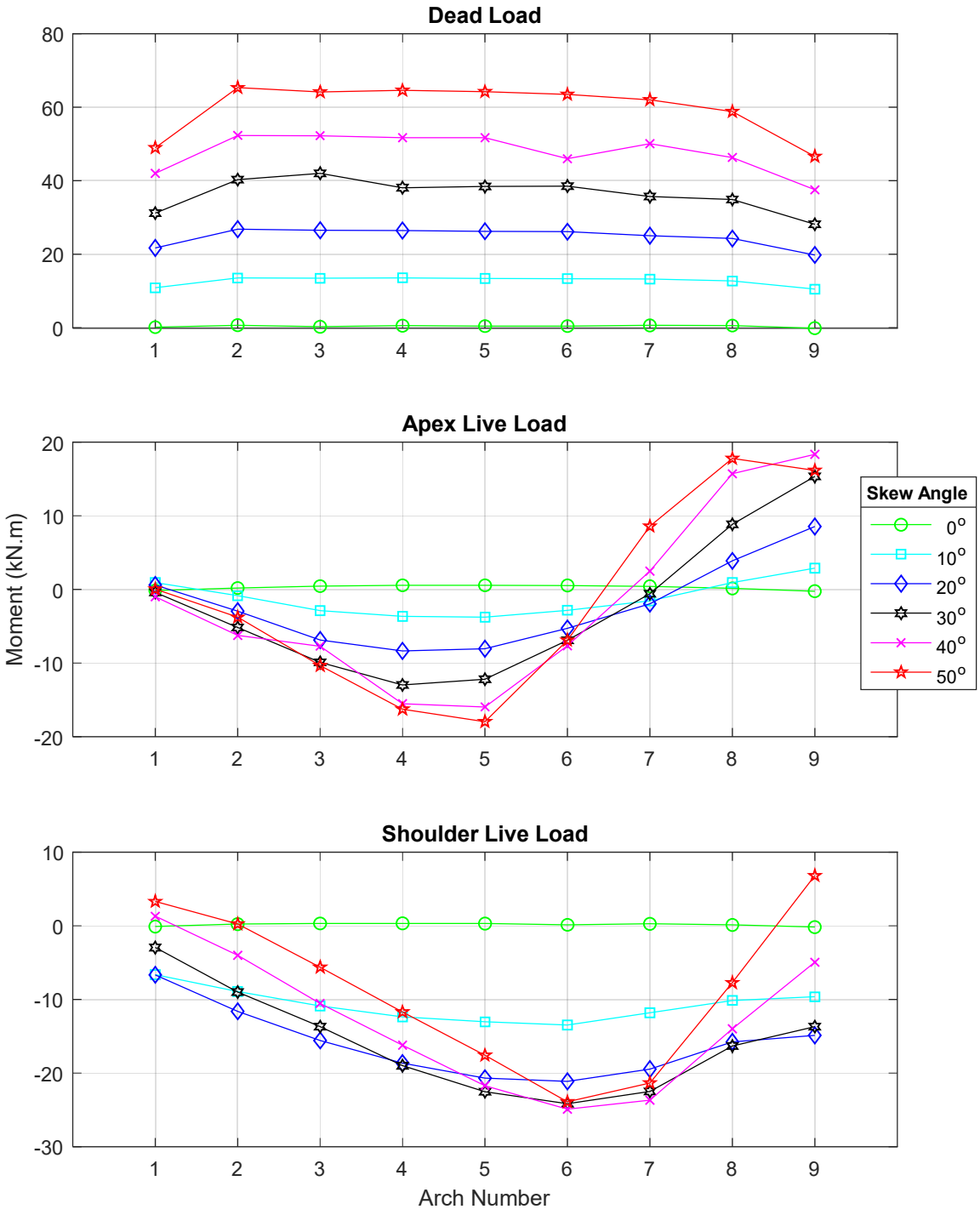

Figure E 9. Strength I: South Footings Out-of-Plane Moment

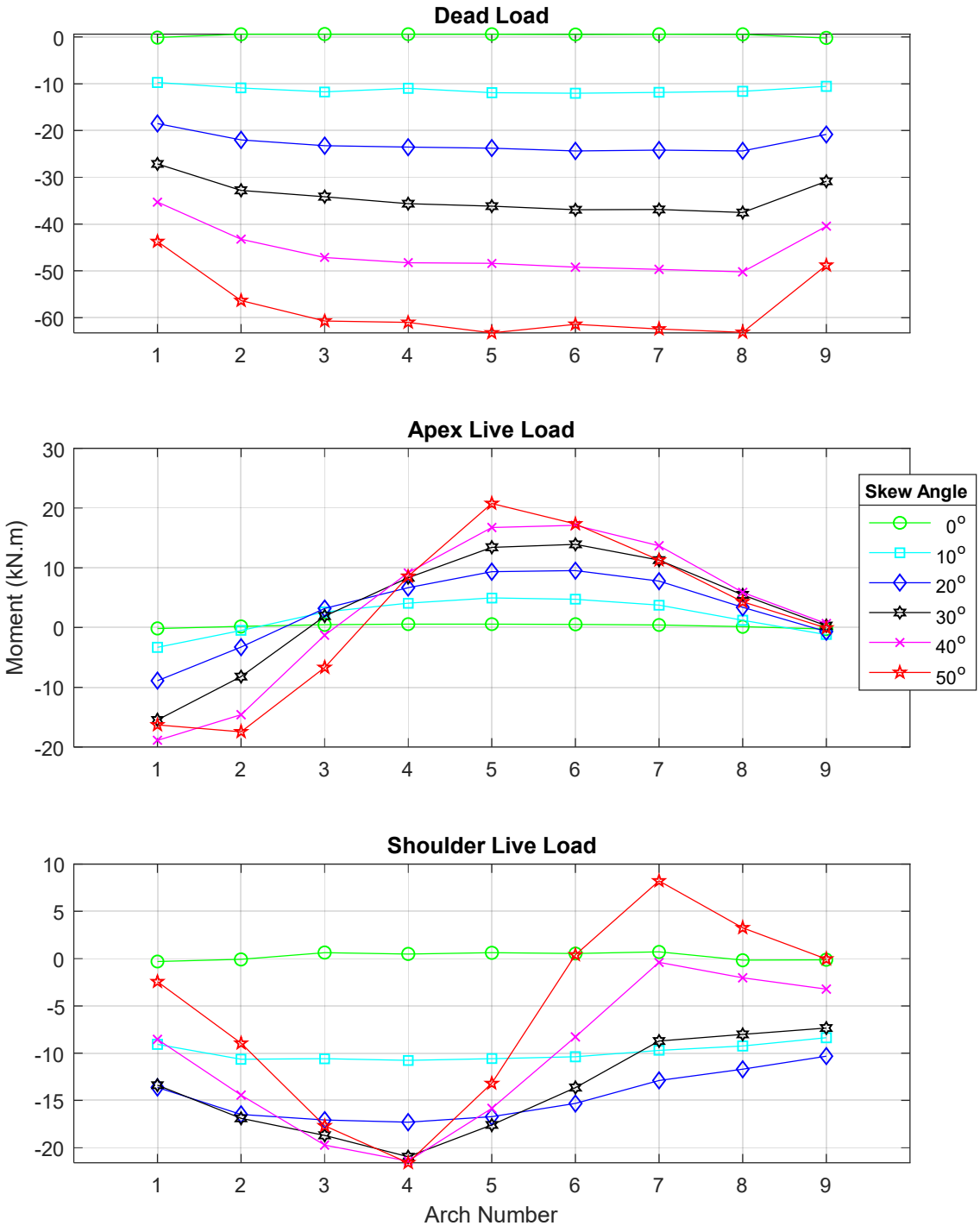

Figure E 10. Strength I: North Footings Out-of-Plane Moment

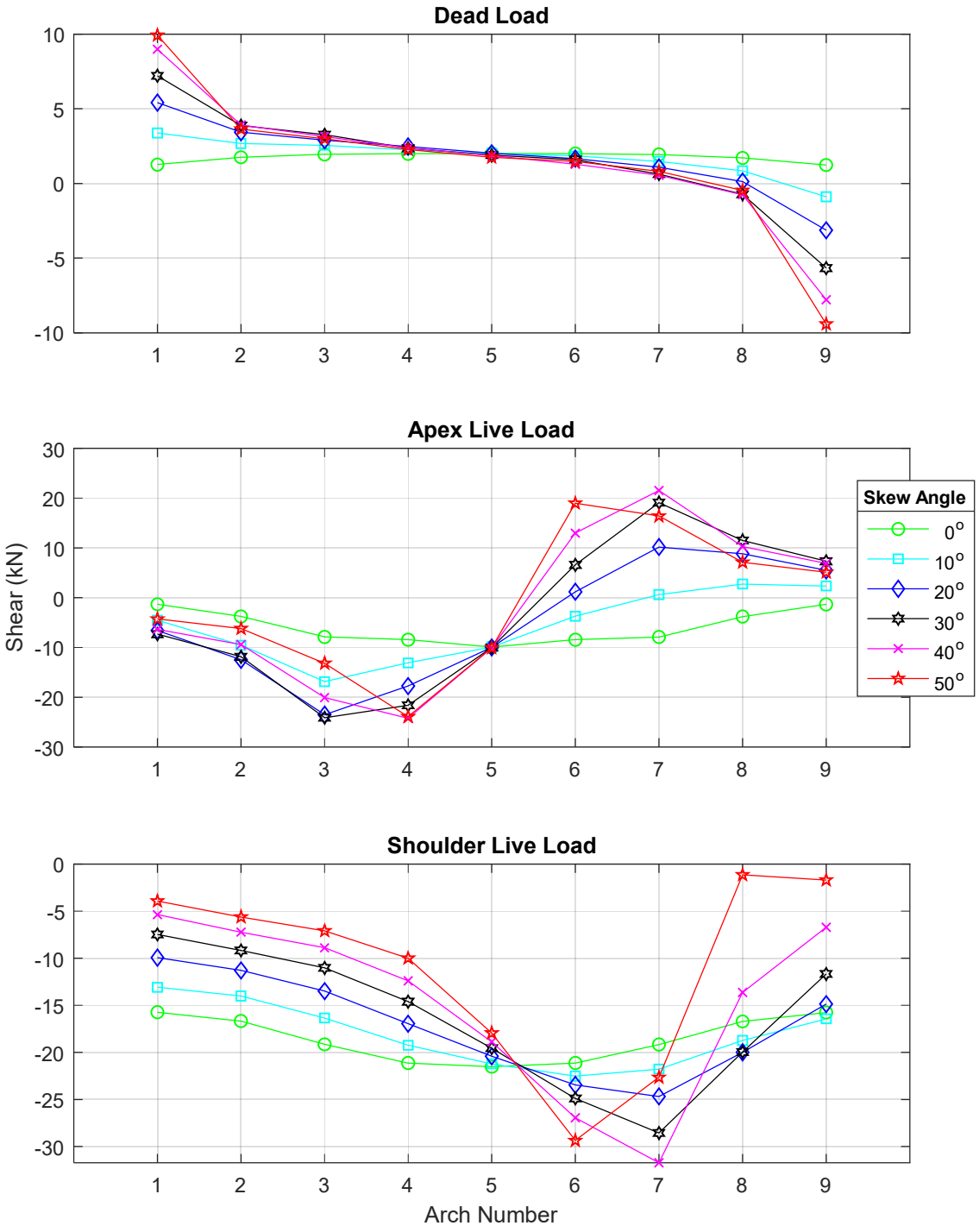

Figure E 11. Strength I: Apexes In-Plane Shear Force

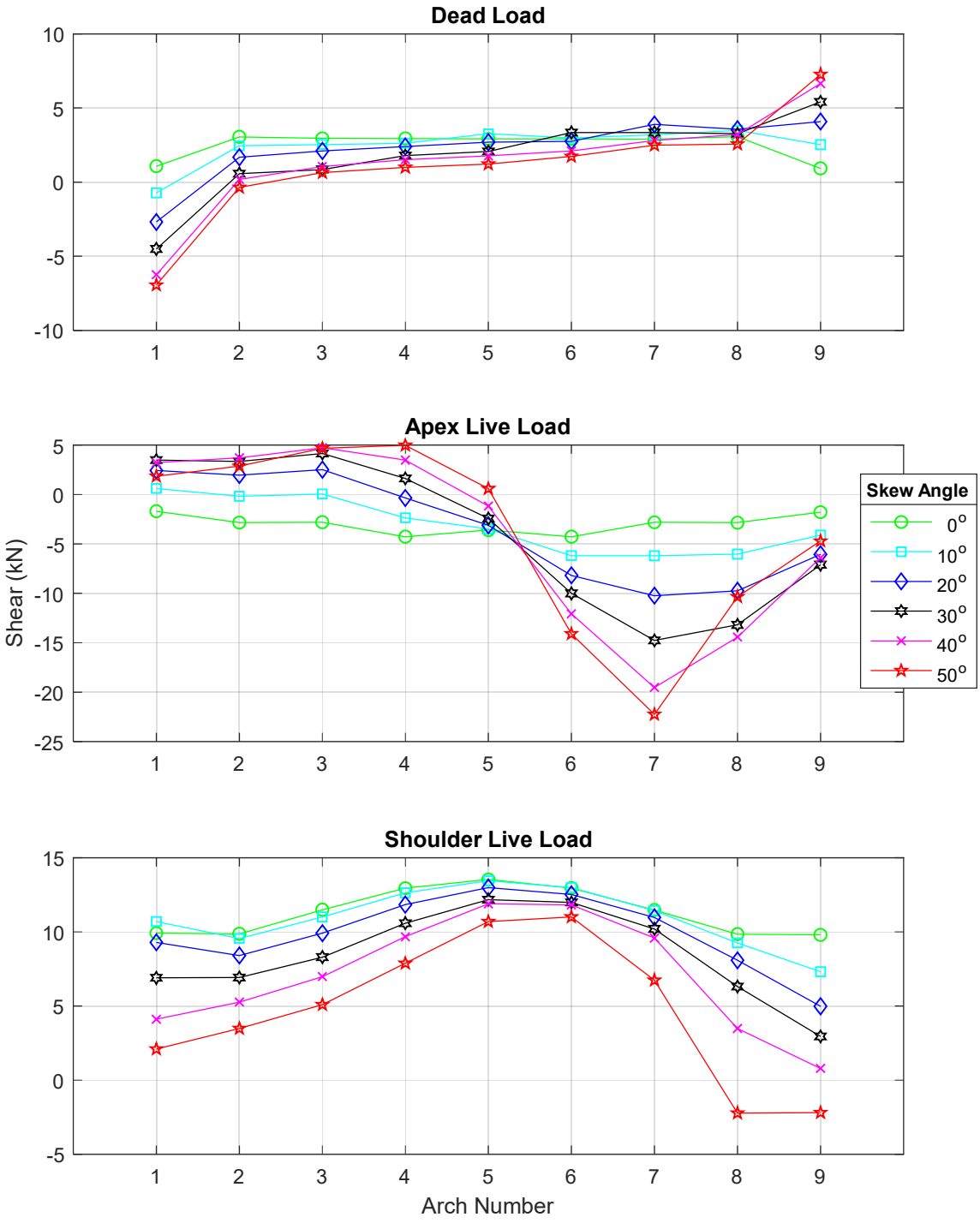

Figure E 12. Strength I: South Shoulders In-Plane Shear Force

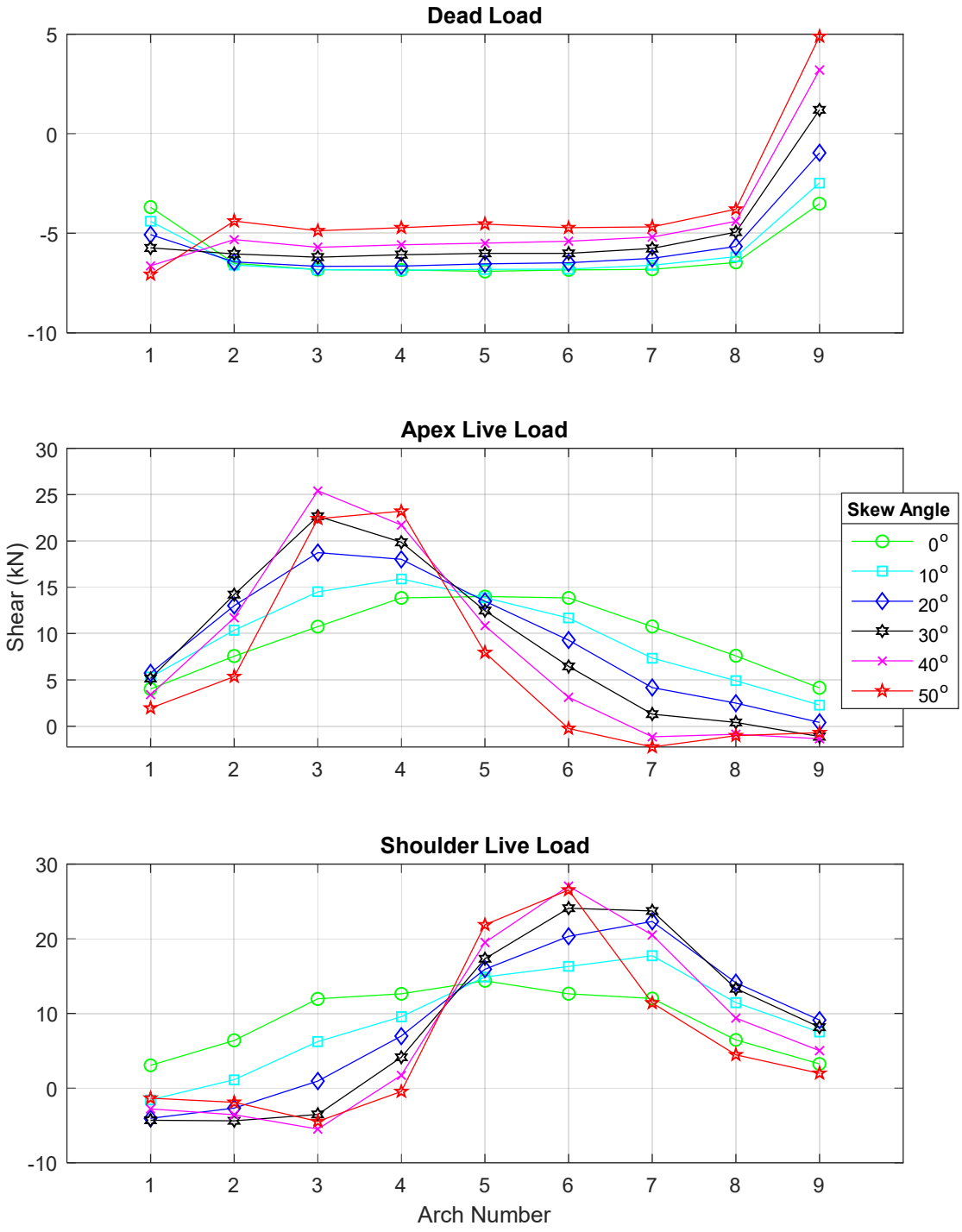

Figure E 13. Strength I: North Shoulders In-Plane Shear Force

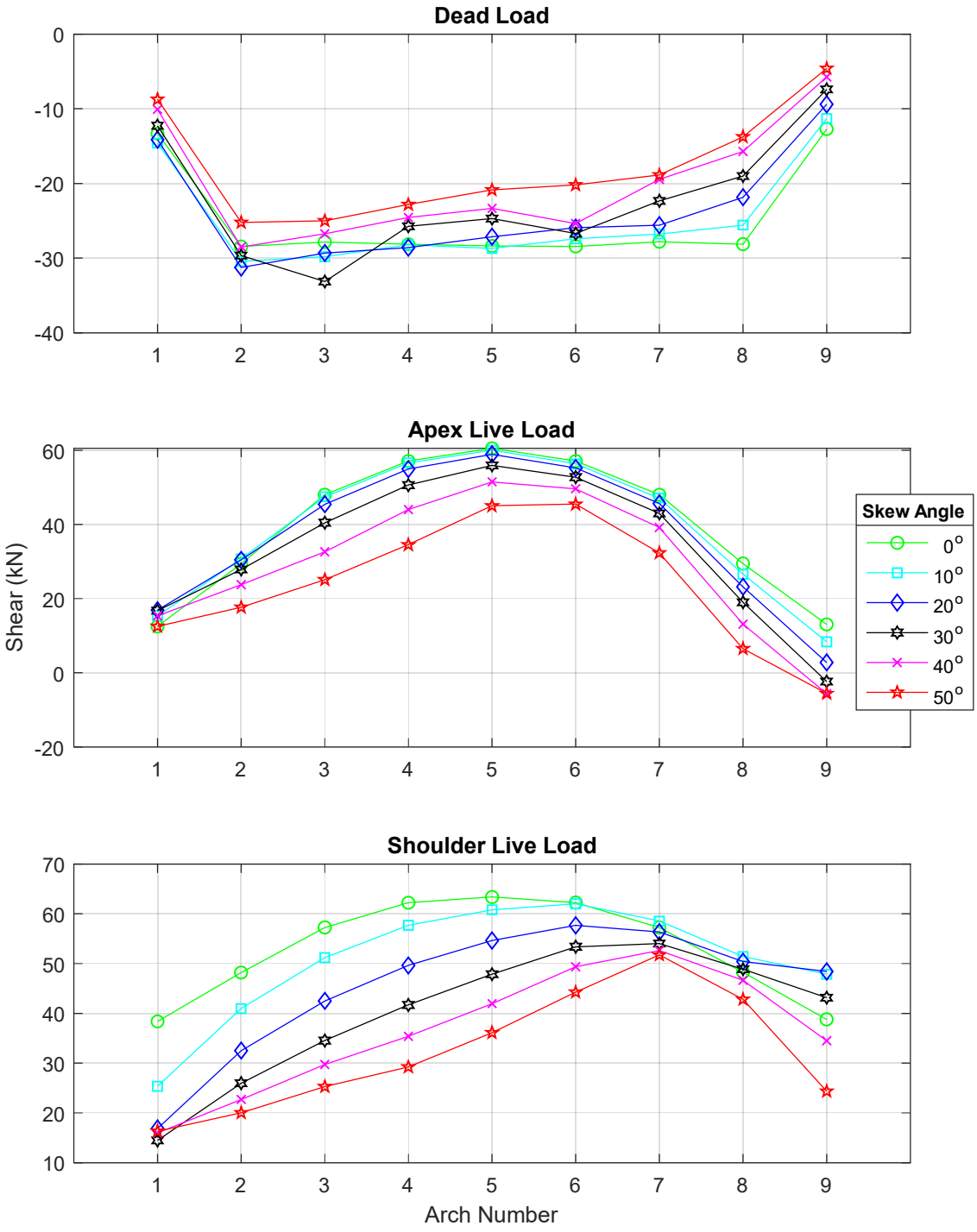

Figure E 14. Strength I: South Footings In-Plane Shear Force

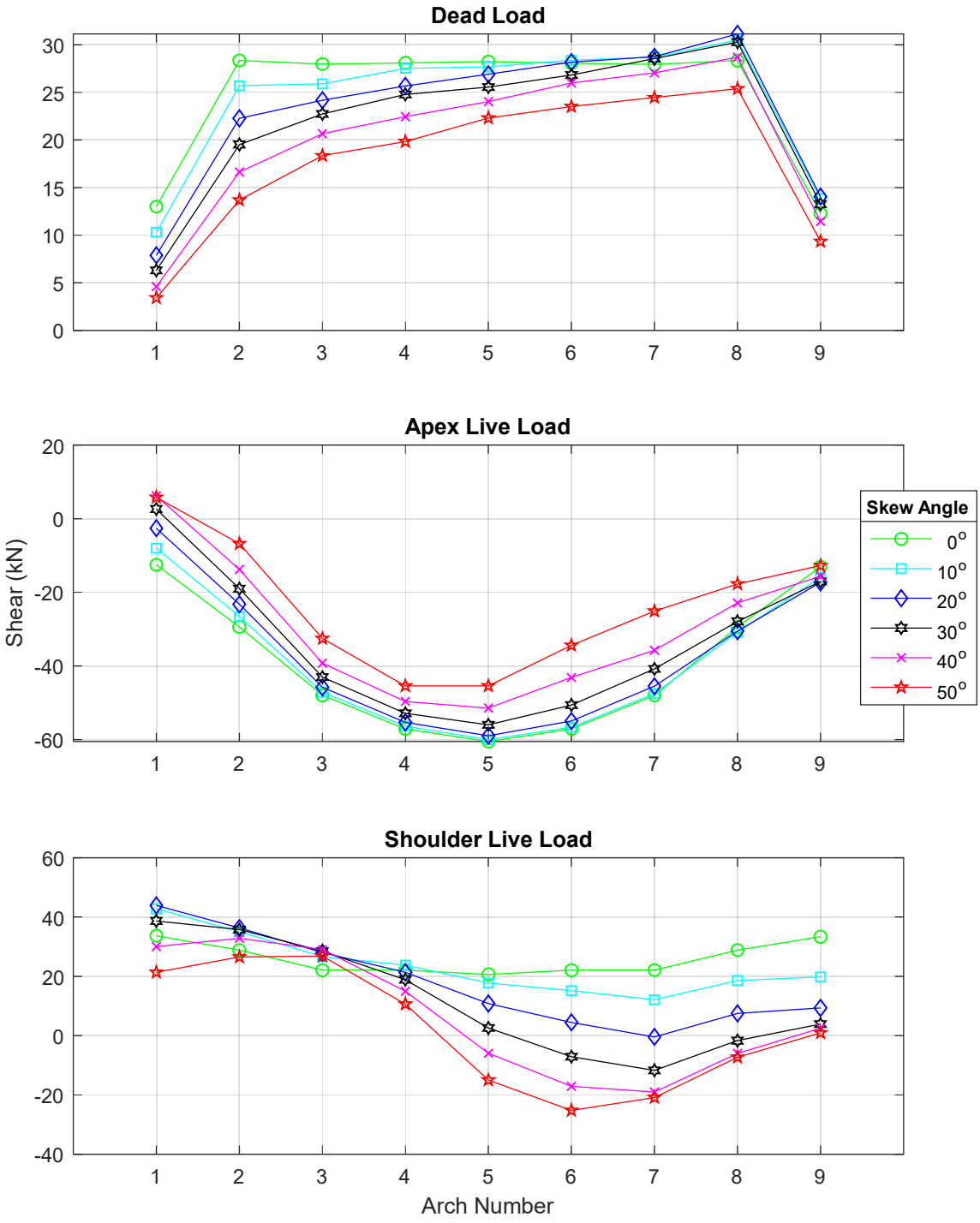

Figure E 15. Strength I: North Footings In-Plane Shear Force

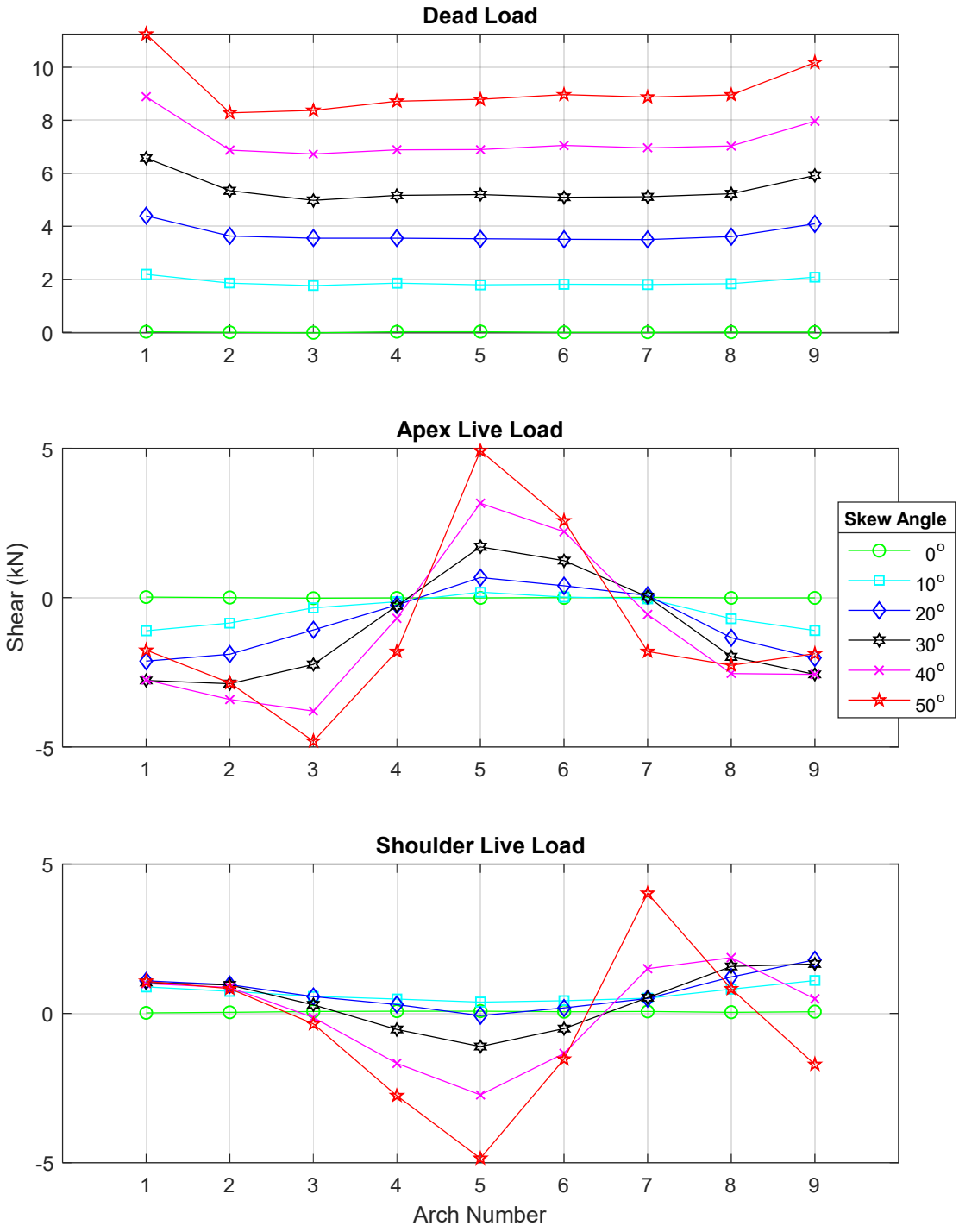

Figure E 16. Strength I: Apexes Out-of-Plane Shear Force

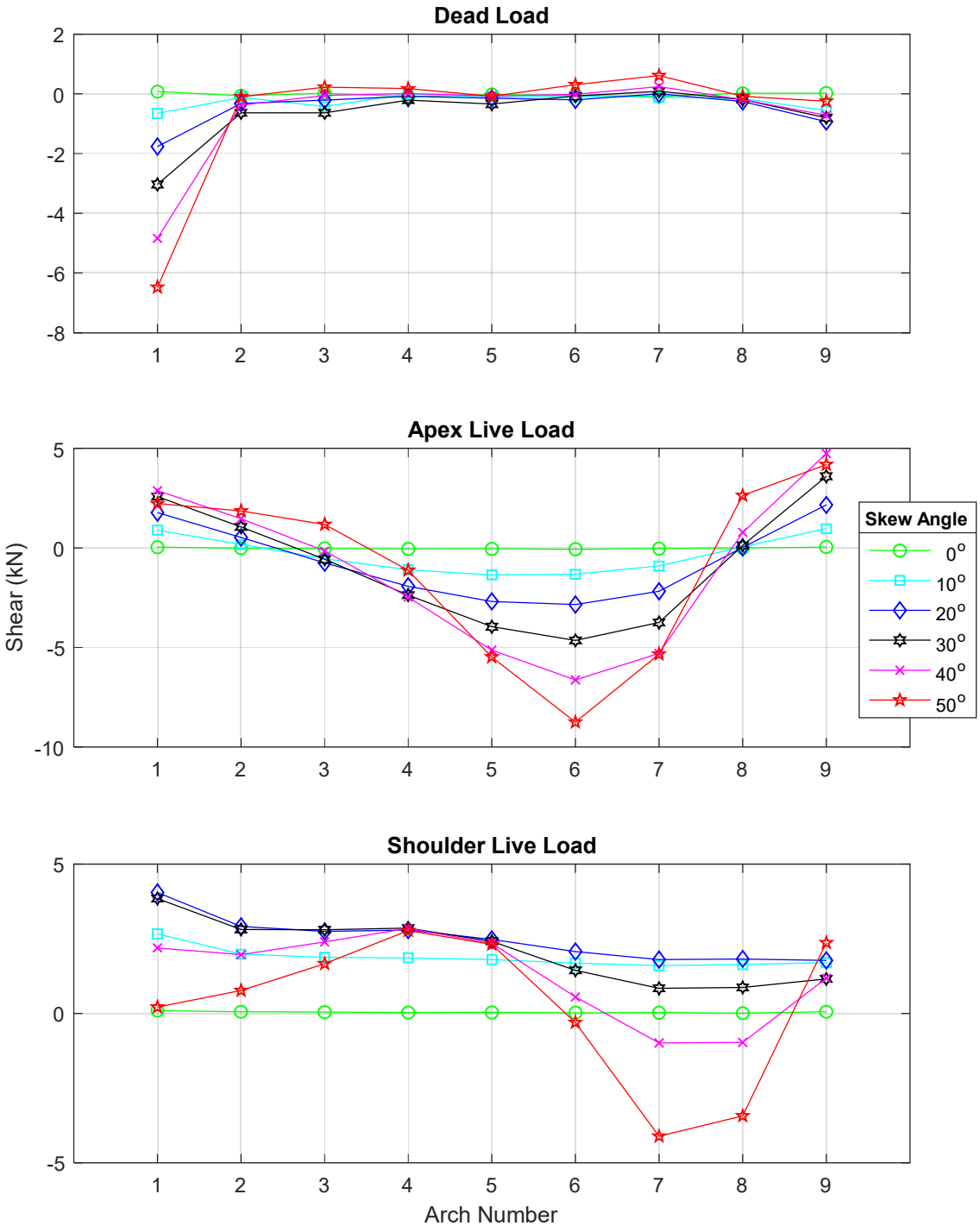

Figure E 17. Strength I: South Shoulders Out-of-Plane Shear Force

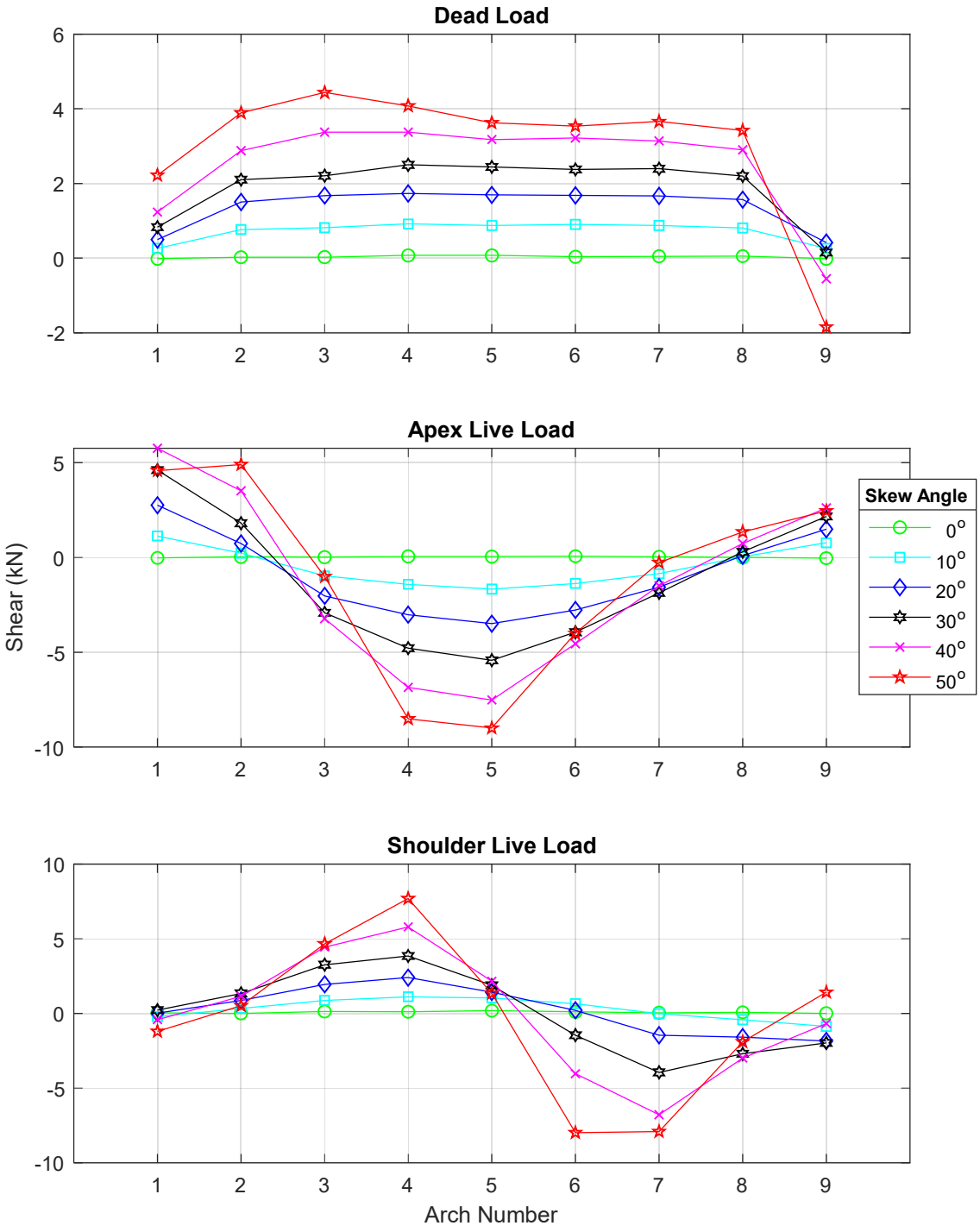

Figure E 18. Strength I: North Shoulders Out-of-Plane Shear Force

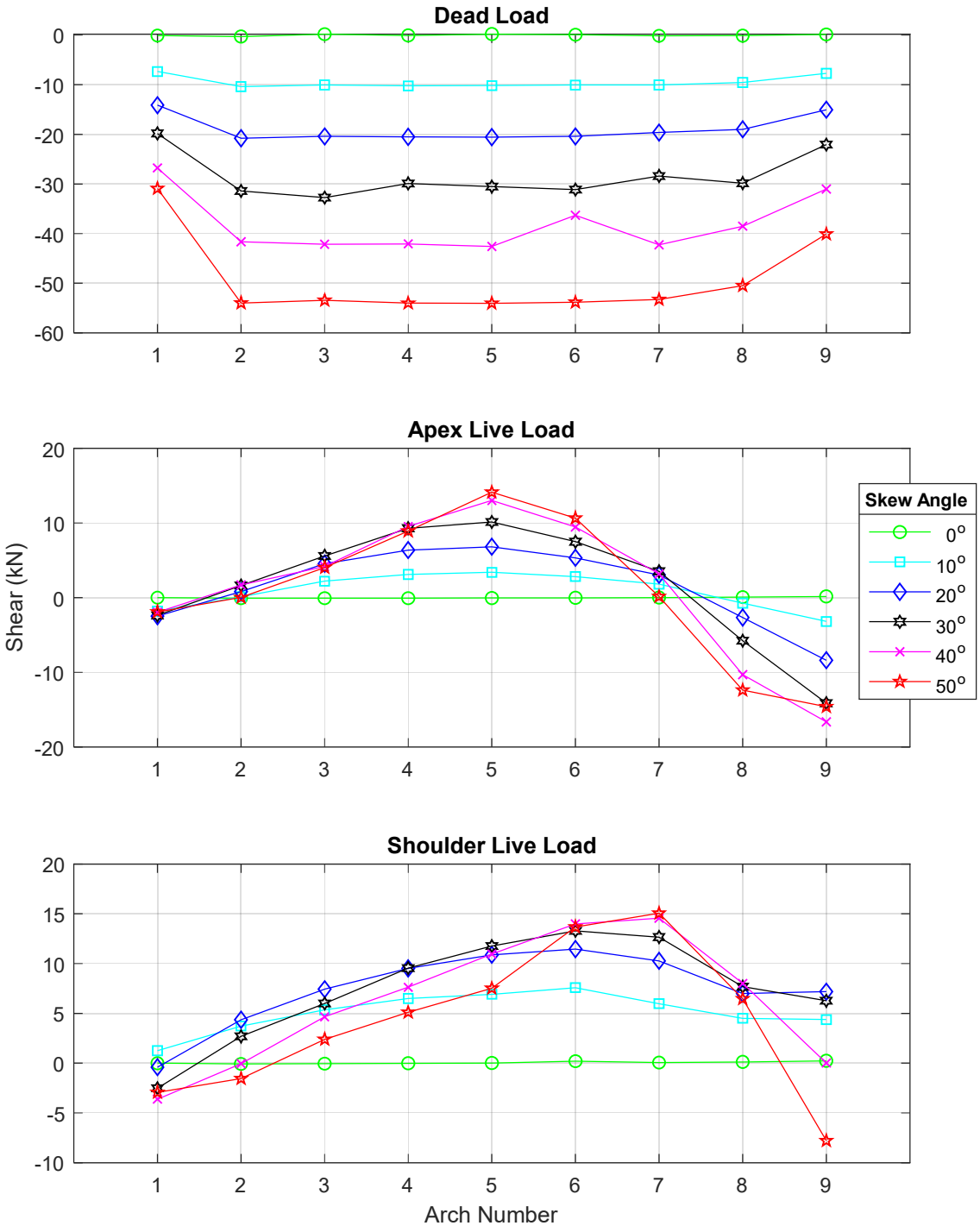

Figure E 19. Strength I: South Footings Out-of-Plane Shear Force

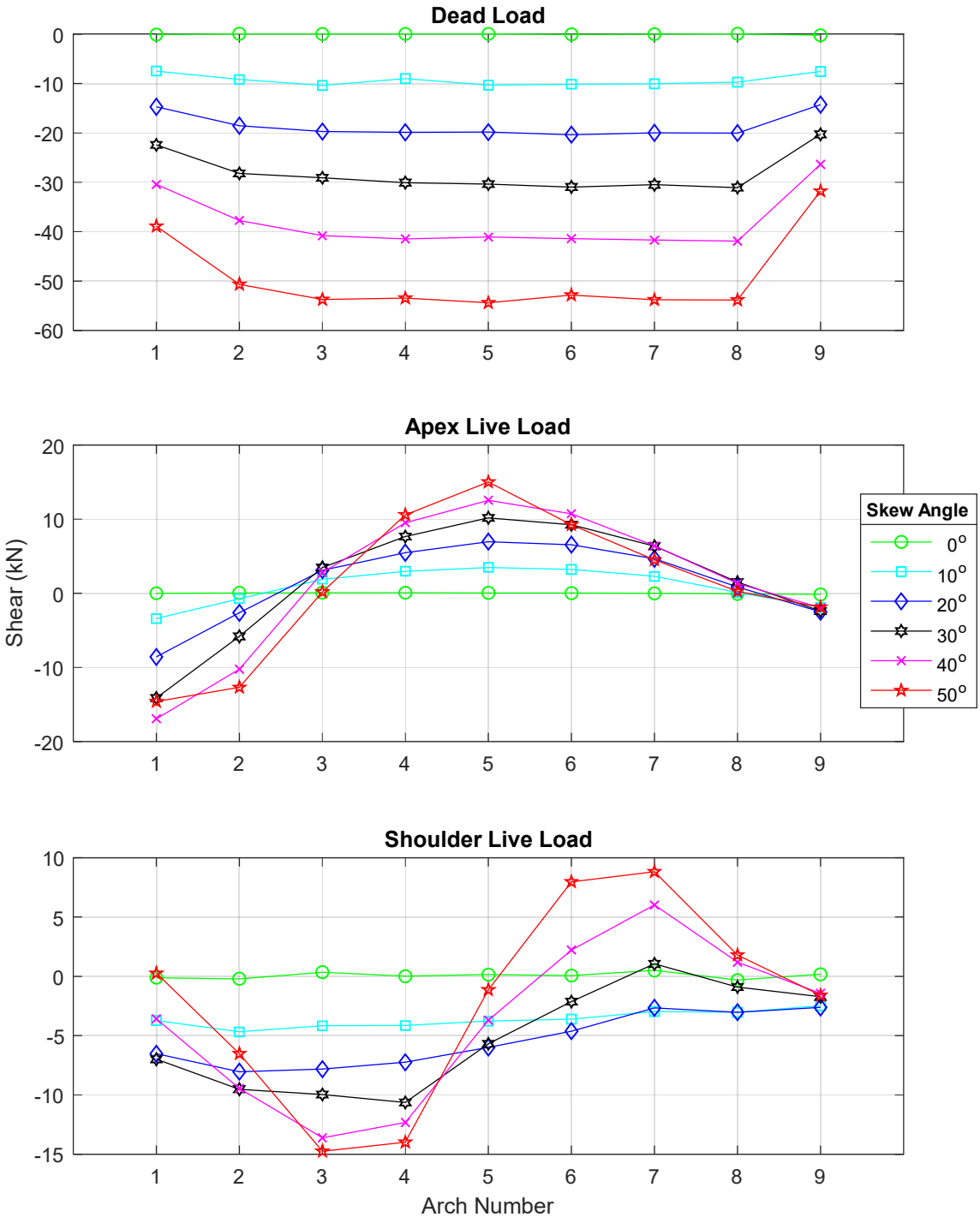

Figure E 20. Strength I: North Footings Out-of-Plane Shear Force

BIOGRAPHY OF THE AUTHOR

Hakeem Salih Majeed was born in Baghdad, Iraq on January 5, 1983. He grew up in Baghdad and graduated from one of its high schools in 2000. Hakeem enrolled at the College of Engineering, Alnahrain* University, fall 2000 and graduated in 2003 with a B.S. in Civil Engineering. He showed a clear superiority and ranked 1st out of 18 graduates. After that, Hakeem continued at the same College and earned a M.S. in Civil Engineering in October 2007. He is a Member of Iraqi Engineers Association since 2003.

The senior engineer Hakeem was appointed at Ministry of Agriculture as an Official of the Division of Engineering at the State Board of Agricultural Extension and Cooperation from March 2007 until May 2014. On the period between 2003-2014, he worked as a site engineer, supervising engineer, resident engineer, quality control engineer, and project manager at several fields with many construction companies in Iraq.

On 2014, Hakeem was awarded a scholarship from the Higher Committee for Education Development in Iraq to read for a Ph.D. in Civil Engineering in the University of Maine. He is a candidate for the Doctor of Philosophy degree in Civil Engineering from the University of Maine in December 2019.

*Alnahrain: The Two-Rivers, *Tigris and Euphrates.*